QUANTIFYING THE EFFECT OF ROCK MASS QUALITY ON PEAK PARTICLE VELOCITY FOR UNDERGROUND DRIFT DEVELOPMENT

by

Cristian Andres Caceres Doerner

A THESIS SUBMITTED IN PARTIAL FULLFILMENT OF
THE REQUIREMENTS FOR THE DEGREE OF

DOCTOR OF PHILOSOPHY

in

The Faculty of Graduate Studies
(Mining Engineering)

THE UNIVERSITY OF BRITISH COLUMBIA
(Vancouver)

December 2011

ABSTRACT

In prior research the existence of the strong relation between peak particle velocity (*PPV*), as a result of blasting, and damage to civil structures and mining excavations has been well established. In essence, the higher the *PPV* levels, the greater has been the observed damage to a structure or excavation.

The first part of this thesis examines, through case studies in four underground mines, the relationship observed between measured *PPV* and induced overbreak. These developed relationships were established through a blast monitoring campaign of drift development headings of markedly dissimilar rock mass qualities, varying from fair/poor to extremely competent.

In the second part of this thesis is developed of a new methodology to estimate *PPV*, which incorporates input parameters that are characteristic of different rock mass qualities, such as propagation velocity and resonance frequency, and explosive characteristics such as velocity of detonation (*VOD*). This methodology makes use of waveforms to determine vibration levels from which the *PPV* of a blasthole is established. The developed model estimates *PPV* by taking into consideration the spatial location of the blasthole with respect to both the drift face, and the point of interest, and the arrival time difference of every incremental charge (or packet) within a blasthole based on the travel distance of the seismic wave, the *VOD*, and the rock mass propagation velocities.

Current state of the art methodologies are solutions to a particular blasting situation; they either consider a specific close range geometry, where they have limited applicability, or they tend to be over simplified in the far-field by considering the explosive charge as a point source. The proposed methodology considers a more realistic close range geometric solution that can be applied specifically to a drifting situation, and improves some of the drawbacks of current methodologies in the far-field range.

Finally, a more reliable estimation of *PPV* levels can help in the assessment of the damage potential of a particular structure or excavation and therefore should help toward preventive measures to make the working environment more safe and cost effective.

TABLE OF CONTENTS

LIST OF TABLES

LIST OF FIGURES

LIST OF ABBREVIATIONS AND SYMBOLS

a	-	Acceleration
A	-	Amplitude
ANFO	-	Ammonium nitrate and fuel oil
c	-	Characteristic propagation velocity of P/S/Raleigh wave
CMRI	-	Central Mining Research Institute
d	-	Displacement
D	-	Distance
E	-	Original energy stored in a wave
ELOS	-	Equivalent linear overbreak slough
ER	-	Energy ratio
f	-	Frequency
f_{dom}	-	Dominant frequency
FFT	-	Fast Fourier transform
GPR	-	Ground penetrating radar
HCF	-	Half cast factor
ISP	-	Indian Standard Predictor
Ja	-	Joint alteration number
Jn	-	Joint set number
Jr	-	Joint roughness number
Jv	-	Volumetric joint count
Jw	-	Joint water reduction factor
l	-	Linear charge concentration
LIDAR	-	Light Detection and Ranging

NIOSH	-	National Institute for Occupational Safety and Health
POD	-	Point of diffraction
PPV	-	Peak particle velocity
Q	-	Barton’s rock tunnelling quality index
Q_E	-	Mass of explosive charge
Q_f	-	Quality factor
RMR	-	Bieniawski's rock mass rating
RQD	-	Deere’s rock quality designation
SD	-	Scaled distance
SRF	-	Stress reduction factor
t	-	Time
T	-	Period
TDR	-	Time domain reflectometry
u	-	Harmonic displacement
USBM	-	U.S. Bureau of Mines
V	-	Velocity
V_P	-	Particle velocity
VOD	-	Velocity of detonation
Z_{POD}	-	Z coordinate at the point of diffraction
α_P	-	P-Wave velocity
β_{ith}	-	Angle formed between the i_{th} packet (elemental charge) and the horizontal
β_S	-	S-Wave velocity
ΔE	-	Energy lost in one cycle
ε	-	Strain

θ - longitudinal shear displacement vector

λ - Wavelength

ψ - rotational shear displacement vector

ω - angular frequency

ϕ - phase shift

ACKNOWLEDGEMENTS

I would like to thank the committee members for all the support they gave me throughout all these years without which it would have been impossible to complete this research and thesis. My greatest thanks goes to my supervisor Dr. Rimas Pakalnis for the immense and invaluable amount of knowledge he has shared with me, for his trust and friendship, patience and financial support.

To my co-supervisor Dr. Michael Hitch for his editing support and his exchange of knowledge and ideas, which improved my research findings and helped to produce a better thesis document.

To Dr. Malcolm Scoble for his directions and detailed assessment of my research and his key and precise editing contributions.

To Dr. Scott Dunbar and David Sprott for their supervision and fundamental directions.

The author would like to thank immensely *NIOSH* Spokane Research Laboratory and the blasting research team for their financial support, and their contribution of knowledge, as well as the support of their qualified personnel, these being fundamental components in the completion of this research. They have also made available their state of the art equipment and assisted in the organization of the field investigations. The author is particularly grateful to the following: Jami Dwyer, Steve Iverson, Bill Hustrulid, Ed McHugh, Ted Williams, Tom Brady, and Joel Warneke.

To Trent McColl for his editorial support. With his English expertise, the thesis is now much more comprehensible as before.

The author would also like to thank the following mining companies and their personnel involved: Stillwater Mining Company, Queenstake Resources, Barrick Gold Corp. and Newmont Mining Corp., and Goldcorp Inc.. They provided invaluable assistance during the data acquisition phase of the research, and allowed the use of their time, facilities, and equipment, without which this research could not have been conducted.

DEDICATION

To my wife Veronica and my daughters Victoria and Javiera and to my son Tomas. To my parents Ximena and Alberto. To my family and friends. They all gave me the strength and confidence necessary to pursue this incredible endeavor.

1 INTRODUCTION

1.1 Motivation and Significance of the Proposed Research

Since the beginning of the twentieth century, more than 50,000 mining related fatalities have occurred in the U.S. alone (which is approximately half of all fatalities in metal and non-metal mining, excluding coal), according to *NIOSH*'s Information Circular 9520 (Breslin, 2010). A significant portion of these fatalities would be related to ground falls and pillar failures. According to the U.S. Department of Labor, the incidence of fatal injuries fell dramatically during the period 2006 to 2010 (31 fatalities total due to face/rib/highwall falls of roof and back, pertaining to both surface and underground mining). Reducing fatalities and injuries across the mining industry remains a principle concern.

A strong relationship between peak particle velocity (*PPV*) – as a result of blasting – and damage to civil structures and mining excavations has been well established by previous research. In essence, the higher the *PPV*, the greater the observed damage to a structure or excavation. Estimating *PPV* levels occurring at any given location (with respect to the explosive charge) as accurately as possible thus becomes critical toward making better, more reliable predictions of the potential for damage to existing structures and excavations.

The primary motivation of this research is to make the drifting process safer by preventing injuries and fatalities from roof and rib falls in underground mines. The triggering of these failures can have diverse origins but one major factor is the excessive vibration levels resulting from blasting.

In addition, this research aims to make the drifting process more cost effective by ensuring a better understanding of the working environment, in terms of particle velocity, which has the potential to cause rock instabilities, as a result of the blasting process. From a geotechnical perspective, cost effective solutions are reached when support designs can prevent all potential instabilities from occurring at the minimum possible cost. Hence, if this process can establish a reliable estimation of the maximum vibration levels, and

therefore, an estimate of the degree of damage caused by blasting, then there will be advances in the optimization of drift support designs.

1.2 Scope and Objective

The information produced by this research can be used by geotechnical and blasting personnel for a more comprehensive analysis of a particular situation, as this information relates to various rock mass conditions existing at their sites. This research provides empirical relationships relating *PPV*, scaled distance (*SD*), and overbreak obtained throughout the analysis of data gathered. Mine sites were selected in order to cover a broad range of rock mass qualities assessed in terms of *RMR* and *Q*, ranging from fair/poor to extremely competent.

In the author's opinion, there is a lack of tools available to the geotechnical and blasting community that can be used to determine *PPV*, specifically in a drifting situation. The existing tools produce overly simplistic solutions, which can lead to large calculation errors in *PPV* value estimation. This research is oriented to the geotechnical and blasting personnel who are engaged in analysis of the stability of development drifts. The proposed methodology, which has been developed specifically for a drifting situation, can have positive impacts in the reduction of underground rock failure. This methodology considers important geometric and geophysical features not necessarily addressed by traditional methodologies. Moreover, the methodology is also applicable to surface and underground production blasting when the surface layout is similar to that existing in drift development.

The proposed methodology has been verified experimentally using a modeling tool developed and tested with commonly used spreadsheet software and is presented by the author to be more accurate than current methodologies, as it incorporates parameters that are characteristic of the quality of the rock mass and the explosives utilized.

The main objective is the development of a new methodology and modeling tool that, once calibrated, can be used by the blasting engineer to improve and optimize designs of blasting rounds. A reliable estimation of the *PPVs* determined at any given location, some distance from the blast or within the blast round, can then be related to the potential for

overbreak and damage occurring at these locations and can therefore assess the potential risk to mining personnel.

1.3 Methodology

A total of four underground mines located in North America were investigated, and their drill and blast operations monitored with respect to blasthole location, explosive distribution, delay sequence, seismic vibration monitoring, ground support employed, overbreak assessment, and rock mass quality assessment. Each of the four sites investigated showed clear differences with respect to the other three, in that the sites exhibit a broad range of rock mass qualities, all of which were subsequently analyzed in terms of measured *PPV* and the associated frequency content. Two widely used rock mass classification systems to assess rock mass quality were employed at the mine sites investigated. These are Bieniawski's Rock Mass Rating, *RMR* (1976) and Barton's Rock Tunnelling Quality Index, *Q* (1974).

The seismic records of particle velocity versus time were recorded via high-frequency geophones and dataloggers that were installed along the walls of the monitored drifts, some distance from the blast.

Measurements of blast-induced overbreak were estimated from laser scanner profiles and planned surface of excavation. A less accurate method using a handheld laser distance meter was also employed to estimate overbreak in those situations where laser scanner equipment was not available.

Site-specific characteristic curves were then obtained from the records of *PPV* versus *SD* data. These site-specific characteristic curves present further evidence that as rock mass quality improves, the *PPV* required for fragmenting and displacing the rock increases.

From the records of the particle velocity measured over time, frequency spectrum graphs were derived employing the fast Fourier Transform (*FFT*). The peak frequency and frequency ranges obtained in this way indicate that there is a strong relationship between frequency ranges and rock mass quality, where high frequencies are undetectable and/or decay more rapidly with decreasing rock mass quality.

In an attempt to reduce the large scatter of the recorded *PPV* versus *SD* data, a modification and improvement to the Hustrulid-Lu method (Hustrulid and Lu, 2002) used for the near-field *PPV* prediction, was made by the incorporation of geophysical components into the proposed methodology. This methodology – and the result of it, the developed modeling tool – utilizes a waveform seed generator to determine the peak velocities of individual packets that pertain to a single blasthole of the round. *PPV* for each blasthole can then be calculated from the linear superposition of all individual packet waveforms whose phases are shifted by their respective arrival time differences, that is, when they arrive at the geophone location. The methodology takes into account the travelled distance, and the travelled time of the seismic wave (between the packet centroid and the geophone), which differs for each packet. The methodology also takes into account the vibration frequency of the given rock mass which has an effect on the waveform generated. These three considerations should lead to greater accuracy in the determination of the final *PPV* values.

The properties and characteristics employed in the model are as follows: the location, length, and diameter of every blasthole in the round with respect to the geophone's location; the explosive's linear charge density and *VOD*; the rock mass medium's body and surface wave velocities and its main resonant frequency; and, the travelled length of the wavefront comprising every individual packet originating at the blasthole. In principle, only the shortest path travelled by the seismic vibration, measured from the packet location to the geophone location, would generate the *PPV* and any other path would merely add to the residual portion of the original particle velocity.

As a result of the frequency content analysis, the importance of analyzing the combined particle velocity determined for a single blasthole from the combination of a wide range of frequencies can be recognized, however, to simplify the analysis performed, only a single predominant resonance frequency was used. To ascertain the model's capabilities, an example of a waveform generated from the linear superposition of a range of waveforms each with a different frequency, was conducted and documented.

The implemented model was constructed keeping in mind that the seismic wavefront originating at the packet location travels through a body of rock at the body wave

velocity, and once it has reached the face-wall contact of the blasting round, the wavefront passes through a point of diffraction (*POD*); from there on, it travels through the surface of the drift's wall, at the surface wave velocity, to the geophone location. In the proposed methodology, of the two decomposed *PPV* vectors, the vector parallel to the wall, and, the vector perpendicular to the wall (i.e., the vertical projection of the original *PPV* vector before it passes through the *POD*), only the *PPV* magnitude of the vector parallel to the wall is accounted for, while the other, the *PPV* magnitude of the vector perpendicular to the wall, is discarded. This was done by the application of a factor to the length of every packet ray trajectory. This factor is a function of the incidence angle of the packet's trajectory to the *POD*, explained in more detail below.

1.4 Statement of Contributions

As a result of the field investigation and subsequent analysis of the data gathered, graphs of *PPV* versus *SD* were developed for a wide range of rock mass qualities (Figure 4.38 and Figure 4.40). In addition, the corresponding average overbreak determination is also provided for each of the mine sites investigated. These graphs were obtained using existing methodologies but the innovation lies in the fact that the *PPV* versus *SD* relations were obtained for a broad range of rock mass qualities, varying from fair/poor to extremely competent and these empirical relations are combined into a single graph from which the importance of rock mass quality on the *PPV* versus *SD* relations is emphasized.

Also, a set of graphs showing the content of resonance frequencies (Figure 4.10, Figure 4.19, Figure 4.28, and Figure 4.37), obtained from the particle velocity versus time records, provides additional evidence of the strong relation existing between resonance frequencies and rock mass quality. The main resonance frequency is also used as an input parameter for the proposed methodology to determine *PPV*.

The primary contribution of this research is to present a new semi-empirical methodology to determine *PPV* at any given location from any particular blasthole of the round. This methodology was especially designed for a drifting situation and includes analytical formulations (Eq. 41 through Eq. 45) and the development of a computer based modeling tool. This computing tool was validated and tested using spreadsheet software, and applied to determine *PPV* values at any distance from a given blasthole location. The

model takes into consideration the arrival times of a number of individual packets forming the blasthole column, as well as the predicted path of the seismic wavefront. In certain cases, the seismic wave diffracts at the face-wall contact and this phenomenon is also incorporated into the new methodology. The specifics are explained in detail in subsequent sections.

In summary, the provided empirical data relating *PPV*, *SD*, overbreak, and resonance frequency with rock mass quality constitute valuable information to the reader for whom similar rock mass condition could be present at their sites. In addition, the new methodology proposed to estimate *PPV* and subsequently the validation and testing of the modeling tool developed, may have a noteworthy positive impact on safety, as well as on cost optimization of drift developments, both being key factors in underground mine operations.

1.5 Thesis Outline

The manuscript has been divided into 9 main chapters and a brief summary of each one is given as follows:

Chapter 2 Literature Research, presents the theory and background of the main aspects this thesis is focused on, particularly rock blasting and rock mechanics. It describes crucial aspects with regard to *PPV*, rock mass quality, overbreak, and frequency spectrum. A discussion of limitations of current methodologies follows, as they are employed to assess near-field *PPV*, close to the blasthole's perimeter, and also in the intermediate- and far-field case. Also, the scarce number of alternative methods that can be used on a regular basis, other than seismic monitoring, to assess damage caused by an explosive charge of known properties and its relation to the quality of the rock mass, will be addressed. The analytical and applied background regarding ground vibrations, wave theory, seismic monitoring, particle velocity, damage potential, *SD*, near- and far-field *PPV* prediction, frequency spectrum, and rock mass quality is also covered in this chapter.

Chapter 3 Field Data Collection and Analysis , describes the procedures and processes involved in the data acquisition and analysis of field measurements. The characteristics of

the equipment employed are described, as well as the processes of data gathering including examples of a typical rock mass quality logging sheet, a laser scanner profile, a structural mapping record, particle velocity and vector sum versus time records, and a plot of frequency spectrum, among others. The *ELOS* concept is introduced, normally applied to the determination of the average overbreak thickness of large open stopes, but employed here for drift development type excavations. An example is also presented, of the scatter that could be found in the delay time of pyrotechnic detonators, along with an example of a *PPV* versus *SD* graph recorded for a given rock mass quality.

Chapter 4 Case Studies, presents details of the information gathered at the four mines investigated including their locations, a brief description of the mining methods employed to extract the ore, the types of ore and rock types under investigation, as well as plan views of the monitoring area, and general descriptions of rock mass quality including pictures of the rock mass conditions and the support system being employed. Results of the analysis of the gathered data, *PPV* versus *SD* charts, are presented along with best-fit curves and equations obtained from the point cloud of the recorded data, including the range of frequencies at which a particular rock mass vibrates.

Chapter 5 *PPV* Modeling – The Proposed Methodology, presents the methodology itself including a new set of analytical equations to determine *PPV* at any location in the vicinity of a blasting round, either at the face where the detonation of the blastholes occurs, or on the walls some distance away from the blast. Details of the semi-empirical modeling tool, including the geophysical and analytical background, are also presented. The geophysical and analytical background provides the working ground for the analysis of the data gathered in the field campaigns, as was presented in Chapter 4 Case Studies. Validation of the modeling tool against current methodologies is performed in this chapter as well as a series of tests to determine potential applications for the model, e.g., *PPV* analysis based on different rock mass qualities.

Chapter 6 Model Testing, tests the proposed semi-empirical modeling tool on one of the four mine sites visited by estimating *PPV* values and comparing them against the field data gathered. Three-axial plots of the recorded *PPV* determined for each blasthole location are compared against surface contour plots obtained via the modeling tool. No

statistical analysis was performed to compare the modeled and field data owing to the fact that some of the properties and constants used in the model were obtained from literature (due to cost constraints on the data acquisition in the field).

Chapter 7 Applications of the Proposed Model, proposes other potential applications for the modeling tool, such as estimation of the *PPV* values in the boundaries immediately adjacent to the explosive charge. The model can also be used, for example, to perform *PPV* decay contour plots in the vicinity of blastholes loaded with different types of explosives. The interaction between two or more charges could also be a part of potential applications making use of the analysis of the modeling results. In this chapter the limitations of the modeling tool are also provided.

Chapter 8 Conclusions, includes a summary of the main findings and the contributions made by this research.

Chapter 9 Recommended Future Work, describes a number of ideas to implement in future studies for the continuation of the research presented herein, in order to expand knowledge in the field of rock blasting. A good portion of the ideas mentioned in this chapter point toward improving the model's capability and tackling its shortcomings (as mentioned in Chapter 7).

2 LITERATURE RESEARCH

2.1 Falls of Ground – A Latent Threat to Miners

From time to time, news appears of miners trapped, injured, or becoming part of fatalities statistics that flood the media. News of injuries is a main concern to the families and the community, to the mine, the industry, industrial health and safety organizations, and the public in general. So any effort toward reducing injuries in the workplace should be forefront.

Figure 2.1 - Figure 2.3 show percentage injuries and fatalities in the U.S. mining industry occurring in underground (conventional stoping and caving) mining during the period 2000-2011.

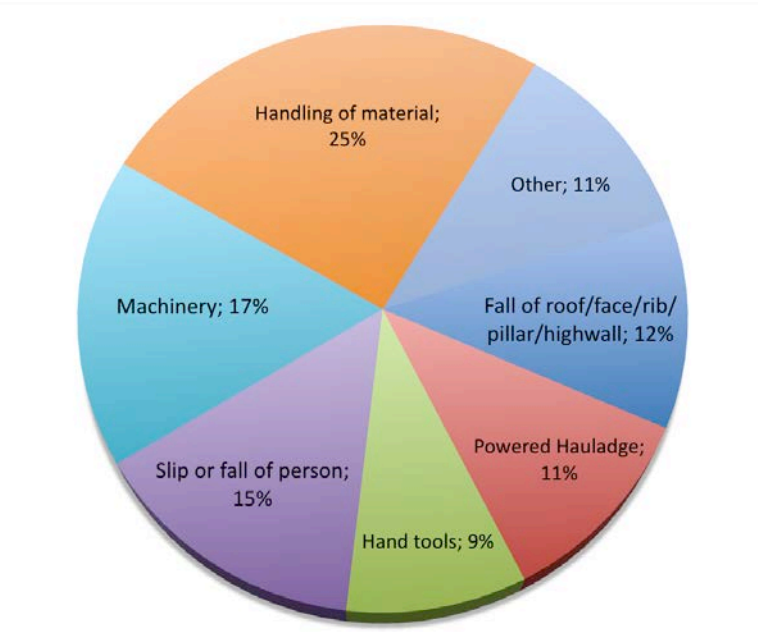

Figure 2.1 Percentage of underground mining injuries in U.S. classified by accident type (source: U.S. Department of Labor: Bureau of Labor Statistics (http://www.bls.gov/iif/, June 2011))

Figure 2.2 shows the percentage of fatalities that occurred in the U.S. in underground mining for the same period.

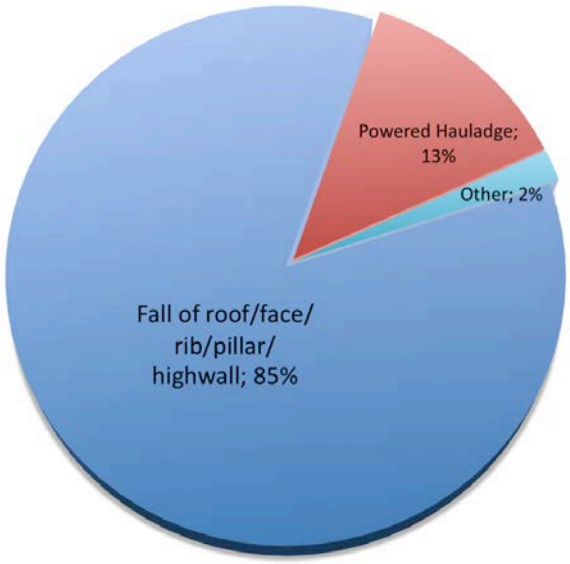

Figure 2.2 Percentage of underground mining fatalities in U.S. classified by accident type (source: U.S. Department of Labor: Bureau of Labor Statistics (http://www.bls.gov/iif/, June 2011))

Figure 2.3 shows the total number of injuries related only to fall of roof and fall of face/rib/pillar that occurred in the U.S. during the period January 2000 to June 2011.

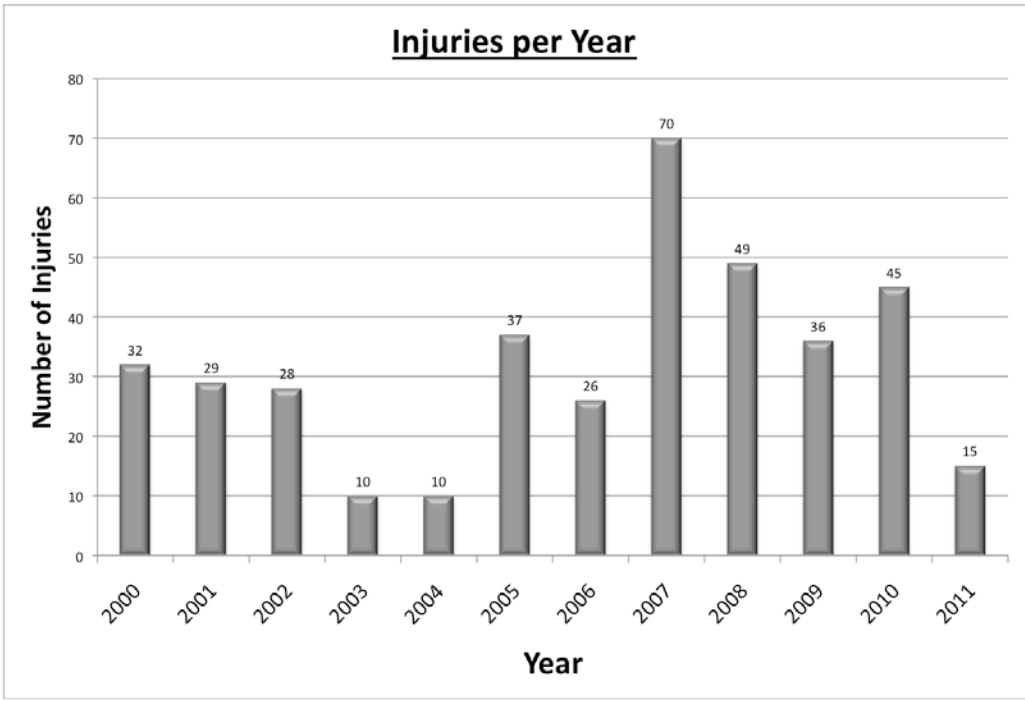

Figure 2.3 Fall of ground related injuries in U.S. (source: U.S. Department of Labor: Bureau of Labor Statistics (http://www.bls.gov/iif/, June 2011))

The information provided in the previous figure was obtained from the "Accident Injuries Data Set" database. This information was filtered to show only conventional stoping and caving underground mining methods, from which only injury records classified as fall of roof or back and fall of face/rib/pillar/side/highwall is reflected. Underground locations include faces, intersections, vertical, sloping and inclined shafts, underground shops and offices, and others. Coal mining including shortwall, longwall, and continuous miner methods do not form part of the data analyzed as they bear little relation to the drilling and blasting techniques under study.

2.2 Ground Vibrations and Damage Assessment

2.2.1 Introduction

It is widely understood that the degree of damage sustained by a given rock mass as a result of blasting is proportional to the quality of that rock mass (Bieniawski, 1989; Barton et al. 1974; Hoek et al., 1980) as well as proportional to the quantity of explosives fired per delay. Logically, the higher the quantity of explosives fired per delay, the higher

the resultant seismic vibration, and this vibration has a direct effect on the magnitude of the damage sustained by the rock mass.

Given that it is nearly impossible to take measurements of peak vibration levels in the immediate vicinity of a given blasthole, i.e., where the greater damage to the rock actually occurs, these vibration levels have always been estimated by extrapolating measured vibrations at considerable distances from the source. From statistical and physical points of view, the greater the distance from the blast that data points are used for extrapolation, the greater the error generated, thus the lower the reliability of predicting the peak vibration levels responsible for the damage to the rock mass. This is probably the greatest shortcoming of most of the research undertaken so far in this area, and there are several relevant examples (Dey, 2004; Adamson et al., 1999, Murty et al., 2003). Moreover, those who have attempted to monitor vibration levels nearer to a given blast, have not done so for more than a single rock mass quality. Notably, for some of the research undertaken, the methods employed require extra or special operations, such as drilling perpendicular to the strike direction of the drift, which generally conflict with production schedules, and for this reason, are not used on a regular basis. Boreholes for instrumentation drilled in a different orientation than the blastholes, in many cases require bringing in other drilling equipment, and even though they can prove to be useful, the extra setup time may not allow the mining cycle to fit the constraints of the shift. On the other hand, the installation of blast monitoring instrumentation can operate during parts of the mining cycle where they produce insignificant interruptions to the operation.

In Murty (2003), peak vibration levels were predicted in the near-field, at a distance of 1m from the blast, while the nearest actual measurements were taken at a distance of 43m from the blast. On the other hand, some research involving single blasthole firing has attempted to monitor in the near-field using experimental rather than real-world mine drift developments (Yang et al., 1994). Yang employed accelerometers rather than the more direct measurement method utilizing geophones, requiring subsequent integration of the acceleration versus time records in order to derive the corresponding particle velocity, which involves an implicit approximation error as well as the use of a much higher frequency band (accelerometers) to record the seismic data.

2.2.2 Beyond the Detonation Process

The author considers the following two quotes to be representative of a fundamental vision toward a safer and cost effective blasting process. The damage produced to the remaining excavation might not be completely avoidable, but it can be engineered so as to be minimized.

“The innocent rock mass is often blamed for insufficient stability that is actually the result of rough and careless blasting. Where no precautions have been taken to avoid blasting damage, no knowledge of the real stability of the undisturbed rock can be gained from looking at the remaining rock wall. What one sees are the sad remains of what could have been a perfectly safe and stable rock face.” Holmberg and Persson (1980).

“Blasting for underground construction purposes is a cutting tool, not a bombing operation.” Svanholm et al. (1977).

When an explosive charge is detonated inside a borehole, the rock in the periphery of the charge will sustain irreversible plastic deformation. As the seismic wave continues its outwards propagation, its energy will decay very rapidly, up to the point that only elastic stress waves will remain propagating through the volume of rock. From the total available energy produced by the detonation of the explosive charge, only a portion of the energy is transformed into seismic waves, which then propagate as body waves, and also on the surface of the ground as surface waves. These elastic stress waves or seismic waves, as they propagate through the whole volume of rock including its surface, are felt as ground vibrations.

Blasting operations inevitably produce ground vibrations that, for the majority of cases, are undesirable and unavoidable. Therefore, it has always been an important consideration in blast design, to control and maintain within acceptable limits the magnitude of these ground vibrations, since they can induce excessive damage to nearby excavations and equipment. Ground vibrations may also dislodge rock wedges that are difficult to recognize but become a latent threat to the safety of personnel and equipment.

In the book “Rock Blasting and Explosives Engineering” the authors Persson, Holmberg, and Lee, provided pertinent information regarding the blasting process. The information is summarized as follows: Only a fraction, ranging between 50%-70%, of the detonating

energy corresponds to the effective expansion work used for breaking the rock, and this occurs up to the point when pressures on the order of 1000 bar have been reached, and when the blasting products have expanded 10 to 20 times the initial volume. When the rock breakage process is taking place, new and existing cracks are being extended, as extremely high-induced tangential stresses overcome the tensile strength of the rock, triggered by the radial expansion of the borehole walls. Also, new and existing cracks are being formed by the injection of high-pressure gases. The breakage process continues until the pressures have reached approximately 100 bars, then the expanding gases get vented until they reach atmospheric pressure. During this process, the remaining 50%-30% of the original explosive energy is transformed into heat, seismic energy, and airblast.

The seismic energy propagates outward in all directions from the source charge as an expanding sphere or ovoid, and the rate of decay of these seismic waves will vary depending on how the rock mass medium interacts with the vibrations being generated.

An explosive charge initiated in a cylindrical column can at best propagate at its maximum propagation velocity, theoretically the stable detonation velocity D_{CJ} (Chapman-Jouguet detonation velocity) that is intrinsic to the explosive type and the diameter and condition of the blasthole. In this sense, the larger the blasthole diameter, the higher the *VOD*, and similarly, a confined explosive charge will produce a higher *VOD* as compared to an unconfined charge. Figure 2.4 shows the relation existing between explosive diameter and *VOD* for an unconfined charge (blue dashed line) and a confined charge (red continuous line).

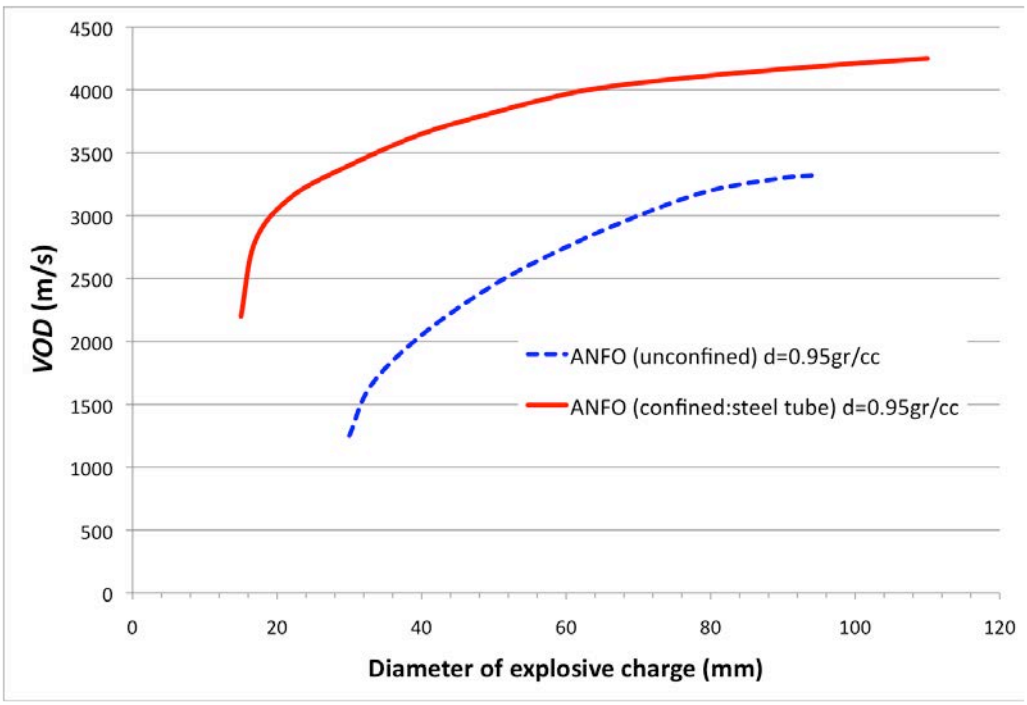

Figure 2.4 Detonation velocity for *ANFO* versus charge diameter (modified from source: "Rock Blasting and Explosives Engineering" pg. 101)

Given that the explosive's propagation velocity is limited to its maximum velocity, the contribution that each infinitesimal portion of the charge column adds to the ground vibrations generated, and measured some distance from the blast, will be comprised of a complex combination of waves including direct, refracted, reflected, body, and surface waves of the compressive, shear, and tensile types.

From a practical point of view, the complex combination of wave types is nearly impossible to separate out, however, this separation is not really necessary since the resultant vibration can be measured directly with seismic instrumentation (for this research, only the magnitude of the particle velocity is relevant. The reader is encouraged to check Green's paper for a complete discussion of the wave types comprising ground vibration (Green, 1984)).

The character of ground vibrations can be fully described by measurements in three orthogonal or mutually perpendicular directions, that of the time history of the acceleration, the velocity, or the displacement at a point (particle) in the ground. These quantities are interrelated, as shown in the following expression where a is acceleration, V is velocity, d is displacement, t is time, and f is the frequency of vibration:

$$a = \frac{dV}{dt} = \frac{d^2d}{d^2t} \qquad \text{Eq. 1}$$

and for sinusoidal motion takes the form:

$$a = 2 \cdot \pi \cdot f \cdot V = (2 \cdot \pi \cdot f)^2 \cdot d \qquad \text{Eq. 2}$$

In practice, it is generally easier to measure either the velocity or the acceleration. Most commercial blast vibration monitoring equipment is used to record particle velocity (i.e., velocity of ground movement), given that the maximum or *PPV* of ground movement is closely related to the potential for structural/rock damage, as noted by Forsyth (Forsyth, 1993); Pusch (Pusch et al. 1993), Holmberg (Holmberg, 1993), and Siskind (Siskind, 2000), among others.

2.2.3 The Harmonic Seismic Wave Equation

The following equations provided in this section form part of many basic physics and geophysics textbooks. These equations in particular were obtained from "Fundamentals of Geophysics" by William Lowrie, Second Edition, pp. 133-135.

Two characteristics of wave motion are important to consider, first, that the wave transmits energy by means of elastic displacement of its particles in the medium, that is, the particles will be displaced momentarily by the shaking of the ground, where there is no net transfer of mass, and subsequently, that they will return to their initial position, once the shaking has ended. The second characteristic is that there is a repetition of the wave pattern in space and time.

Because there is such harmonic repetition of the wave pattern, the amplitude variation can be expressed by a sine or cosine function. The amplitude of the disturbance is repeated at regular time intervals (known as the period of the wave), *T*, while the wave passes through a point in space. Frequency is defined by the number of times the amplitude is repeated per second. Thus, the frequency, *f*, is equal to the inverse of the period *T* (*f=1/T*). The regular repetition distance of the wave motion along the direction of travel is known as the wavelength, λ. The disturbance of the medium by the passage of a wave motion can be expressed by the harmonic displacement, *u*, of a particle from its initial position, by:

$$u = A \cdot \sin\left(2 \cdot \pi \cdot \left(\frac{x}{\lambda} - \frac{t}{T}\right)\right) \quad \text{Eq. 3}$$

Where A is the amplitude, x is the position, and t is the time.

The angular frequency ω and the wave number k can be expressed by:

$$\omega = 2 \cdot \pi \cdot f = \frac{2 \cdot \pi}{T} \quad \text{Eq. 4}$$

$$k = \frac{2 \cdot \pi}{\lambda} \quad \text{Eq. 5}$$

The displacement equation, u, can be written as:

$$u = A \cdot \sin(k \cdot x - \omega \cdot t) \quad \text{Eq. 6}$$

The first and second derivation over time t and position x gives the following:

$$\frac{\partial u}{\partial t} = -A \cdot \omega \cdot \cos(k \cdot x - \omega \cdot t) \quad \text{Eq. 7}$$

$$\frac{\partial^2 u}{\partial t^2} = -A \cdot \omega^2 \cdot \sin(k \cdot x - \omega \cdot t) = -\omega^2 \cdot u \quad \text{Eq. 8}$$

$$\frac{\partial u}{\partial x} = -A \cdot k \cdot \cos(k \cdot x - \omega \cdot t) \quad \text{Eq. 9}$$

$$\frac{\partial^2 u}{\partial x^2} = -A \cdot k^2 \cdot \sin(k \cdot x - \omega \cdot t) = -k^2 \cdot u \quad \text{Eq. 10}$$

Which corresponds to solutions to the more general seismic wave equation for the primary or compressional P-Wave, and the secondary or shear S-Wave, respectively:

$$\frac{\partial^2 \theta}{\partial t^2} = \alpha_P{}^2 \cdot \left(\frac{\partial^2 \theta}{\partial x^2} + \frac{\partial^2 \theta}{\partial y^2} + \frac{\partial^2 \theta}{\partial z^2}\right) \quad \text{Eq. 11}$$

$$\frac{\partial^2 \psi}{\partial t^2} = \beta_S{}^2 \cdot \left(\frac{\partial^2 \psi}{\partial x^2} + \frac{\partial^2 \psi}{\partial y^2} + \frac{\partial^2 \psi}{\partial z^2}\right) \quad \text{Eq. 12}$$

Where α_P and β_S are the P-Wave and S-Wave velocities and θ and ψ are the longitudinal and rotational shear displacement vectors.

2.2.4 Seismic Wave Attenuation

As the seismic wave travels away from its source, its intensity becomes weaker. The attenuation of a wave refers to the decrease of the amplitude with increasing distance. This decrease of intensity is partly due to geometric propagation and partly due to absorption of energy due to imperfect elastic properties of the medium.

As the seismic wave propagates through a medium, the anelastic properties of this medium – in which the particles that comprise it do not react as though perfectly elastic with their neighbors – has negative effects on the intensity of the seismic wave. In anelastic damping, part of the total seismic energy is transformed into, for example, frictional heat and other sources of energy loss.

The most important reduction of the intensity of a seismic wave is due to geometric attenuation, where, if considered that there is no anelastic damping, as the wavefront propagates, the original seismic energy amplitude is now distributed over an increasingly larger surface.

The attenuation of the waveform equation can be expressed from a modification of the Knopoff (1963) equation, but where the independent variable is converted from offset to arrival time and the dominant wavelength to dominant frequency (Huang et. al, 2009):

$$A(t) = A(t_o) \cdot \exp\left(\frac{-t \cdot f_{dom} \cdot \pi}{Q_f}\right) \qquad \text{Eq. 13}$$

Where f_{dom} is the dominant frequency and t is the arrival time of peak amplitude. The parameter Q_f is called the quality factor defined by the fractional energy loss per cycle:

$$\frac{2 \cdot \pi}{Q_f} = -\frac{\Delta E}{E} \qquad \text{Eq. 14}$$

Where ΔE is the energy lost in one cycle and E is the original energy stored in the wave. A similar approach is used in the proposed methodology to determine the pre-peak attack and post-peak attenuation of the waveform. This approach is introduced in Chapter 5, where the parameter Q_f has been replaced by $+1/(2\delta_1)$ or $-1/(2\delta_2)$, which are the pre-peak attack or post-peak decay factors, defined later.

2.2.5 Seismic Wave Diffraction

When the wavefront plane of a seismic wave hits an acute obstacle, a sharp corner or a more general discontinuous boundary, it experiences a phenomenon called diffraction, which allows the wave to follow a path that is in the shadow zone of the source of the seismic vibration. This discontinuous boundary acts as a source of secondary wavelets in which part of the total energy contributes to the reflected wave and part diffracts into the shadow zone where its intensity is lower than the original wavefront. As the angle away from the incident wavefront progressively increases, the intensity progressively decreases.

2.2.6 Seismographs

The vibration waveform generated by the detonation of a blasthole can be directly recorded with the use of motion sensing transducers that are connected to a datalogger, whose function is to record digital or analog data into its internal memory, and to provide the geophone or set of geophones with an electrical power source.

The geophones utilized in this research were a class of high frequency, high particle velocity range sensors with a frequency range of between 28Hz and 1000Hz, and particle velocities of up to 2540 mm/s.

The seismographs record ground movement in three mutually perpendicular orientations or motion components, with one vertical orientation component and two horizontal components. When properly aligned, the horizontal components are labeled longitudinal and transverse components to measure ground movement parallel, and perpendicular to the direction where the vibration source is coming from, respectively. The datalogger also incorporates a separate channel to record airblast.

A series of recommendations and requirements on the installation of seismographs in buildings, soils, and rock structures is specified in various documents (Siskind et al., 1985; Duvall, 1961; USBM RI 5708; Stagg and Engler, 1980; and USBM RI 8506, 17th Edition Blasters' Handbook (ISEE, 2000)) to avoid slippage, rotation, and tipping, due to insufficient gripping of the seismograph-structure contacting surfaces. A faulty

installation would provoke the measurement of unwanted motion not representative of the motion being recorded.

Recommendations on appropriate distances from the source of vibration to the seismographs are given in USBM Bulleting 656 (Nicholls et al., 1971), RI 8507 (Siskind, et al., 1980b) and RI 9226 (Siskind, et al., 1989). These recommendations were not followed entirely as recommended as the selection of the location for the installation of the geophones was based on maximum proximity to the blast but at the same time the spot selected gave some protection from the shock wave and fly rock.

Performance standards and technical specifications of blasting seismographs are provided in the Blast Vibration and Seismograph section of the International Society of Explosive Engineers September 30, 1990. These specifications are presented in terms of the required accuracy for frequency and vibration records, their minimum and maximum range levels, calibration, range of operating temperatures, sampling rate, and over-swing ratio, among others. The technical specifications of the geophones utilized are given in Chapter 3.

A geophone is the mechanism inside these transducers that measures ground vibrations by the movement of a magnet within a field of magnetic flux lines. The speed at which these flux lines are traversed, is proportional to the induced voltage. In principle, as the magnet or the surrounding coil is free to move, when the ground vibrates, it will shake the transducer casing that is coupled to the ground, and the coil or the magnet due to its inertia, will tend not to move. The speed at which the magnet versus coil motion vibrates, results in an induced voltage proportional to the particle velocity in units of Volts/millimeters/seconds. This information gets recorded in the internal memory of the unit.

The term geophone is also referred to herein as the instrument capable of monitoring and recording seismic vibrations with all the required components.

2.2.7 Geophone Damping

Geophones make use of damping to retard the tendency of the mass and spring to oscillate at its natural vibration frequency. If the sensor has no damping, the amplitude

peaks at its natural or resonance frequency and the oscillation of the spring-mass system will eventually stop due to gravity and friction. If a low resonant frequency is desirable, this can be accomplished through a modification of its design by a stiffer spring or a heavier mass. A shorter impulse provided by heavy damping has direct impact on the sensitivity of the sensor.

Critical damping of a sensor, measured as a damping ratio, happens when the mass-spring system returns to the rest position with no oscillation or over-swing after being displaced by the seismic vibration. A geophone can be over-damped or under-damped when its ratio is either over or under the critical damping value. Normal damping for geophones is in the range of 70% of critical (source: High Frequency Geophone manual).

2.2.8 Frequency of Vibration

Vibration is the mechanical oscillation around an equilibrium point. These oscillations can be periodic in time or random, depending on the object being analyzed and the source of the oscillation.

When the detonation of an explosive charge is set off within a mechanical system such as the rock, the initial input vibration will be allowed to vibrate freely. The mechanical system will vibrate at one or more of its natural vibration frequency or frequencies and then damp down to zero over time and distance.

Vibration analysis can be explained by a simple mass-spring-damper model, which is indeed an example of a simple harmonic oscillator. Even a more complex system could possibly be modeled by the superposition of simple mass-spring-damper models.

2.2.9 Frequency Spectrum

The representation of a time-domain signal in its frequency domain is called a frequency spectrum. The Fourier transformation can be applied to any time domain signal to obtain its frequency spectrum yielding a plot of amplitude and phase against frequency.

The seismic vibration occurring in a volume or surface of rock can be specified by the spectral composition of its vibrations and predominant periods in the rock and their dependence on the intensity of the blast effects, the distance to the source, the depth of

the explosive charge, the geological conditions of the rock, and the nature of the reduction of intensity of the seismic waves over distance and time from the source.

The frequency spectrum as applied in this analysis is the determination of the range of frequencies (or frequency content) that the rock vibrates at as a result of the high intensity detonation process. After the blast, the rock vibrates in its natural vibration frequencies and a significant part of this frequency range is recorded in the internal memory of the geophones. A frequency spectrum is determined through the application of the fast Fourier Transform (*FFT*) to the particle velocity versus time records.

The *FFT* can be used to compute the frequency distribution of the seismic records, which are considered non-periodic time series (Nicholls et al., 1971). *FFT* computes a continuous spectrum without preserving the amplitude of the time signal. Blair (2004) suggests the use of time-frequency analysis to determine the distribution of frequencies over a period of time, although this is impractical for small charges where the entire vibration waveform occurs in a fraction of a second. Blair demonstrated that the popular zero-crossing method could yield invalid results for the frequency obtained at the *PPV*. For the present work, it is sufficient that *FFT* be used to obtain the dominant frequency (or range of frequencies) of the peak of the vibration waveform.

It is important to mention that the implications of vibration frequency in the damage potential of building type structures have been well established (Siskind, 2000), but there is limited information available for rock type structures using high frequency and high particle velocity instruments, and of records of *PPV* levels measured in close proximity to an explosive charge.

2.2.10 Scaling and Prediction of Ground Vibrations

Spathis (2010) categorized vibration predictions into five procedures that can be used independently of each other or in combination with one or more procedures. Vibration predictions were categorized as:

- historical data review,
- charge weight scaling laws,
- waveform superposition,

- scaled charge weight superposition, and
- analytical and/or numerical methods such as finite difference or finite element.

Of these categories, the last four have direct relation to the research undertaken and they will be addressed in this chapter as well as in the following chapters.

Charge weight scaling laws have two types of scaling prediction formulations that can be used to assess *PPV* values for the purpose of estimating potential damage to rock subjected to blasting. In general, they can be classified as the near-field and far-field scaling formulations, and they are routinely employed to determine *PPV* at some distance from the explosive source.

Particle velocity of the vibration due to blasting is a function of the following: borehole pressure, confinement, and charge weight, as well as, distance from the blast site, how the compressive wave decays through the rock mass, superposition of the stress created by the firing sequence within the blasthole column, and superposition of the stress created by the firing sequence of adjacent holes.

For the far-field case, where the explosive charge can be considered a spherical charge, *PPV* (in millimeters per second, mm/s), experienced at some distance, *D* (in meters, m), from an explosive source of given mass, Q_E (in kilograms, kg), loaded into a volume of rock, is conveniently expressed in the general form of a power law as follows:

$$PPV = K\left(\frac{Q_E{}^{\alpha}}{D^n}\right) \qquad \text{Eq. 15}$$

Where *K*, α, and *n* are constants controlled mainly by the geology and the type of blasting.

In most cases, the three-parameter model above reduces to a more convenient, two-parameter form by combining the distance and charge mass into a single *SD* variable of the form:

$$SD = \left(\frac{D}{Q_E^{\alpha}} \right) \qquad \text{Eq. 16}$$

The explosive's quantity, Q_E, is determined by the summation of all equivalent explosive weight charges with the same delay number, however, it is commonly accepted that an initiation time difference of 9 milliseconds or greater is required if constructive interference is to be avoided from neighboring charges (Dick et al., 1983). Timing analysis of long period detonators will reveal a large scatter in their delay time, which translates into the absence of constructive interference in the individual particle velocity waveform, reducing the overall vibration intensity (as will be demonstrated in later chapters).

The normalizing factor, D/Q_E^{α}, accounts for changes in the mass of the charge and variations in the propagation distance from the source to the reference point. Square-root scaling (α = 1/2) characterizes the approach normally used in studies of surface blasting. Square root scaling takes into consideration cylindrical wave propagation (two-dimensional) such as that of a body wave close to a cylindrical charge, or, at greater distances, that of a surface wave. Given that the charge mass is proportional to the square of the hole radius, this distance ratio, or *SD*, can be written as $D/Q_E^{1/2}$. Likewise, where three-dimensional wave propagation closely represents the real world situation, cube-root scaling should apply. At substantial distances from a charge, where wave propagation is three-dimensional through an extended medium, cylindrical charges can be approximated as a spherical source. Here, explosive mass varies with the cube of the equivalent spherical-charge radius. Hence, in this case the *SD* is represented as $D/Q_E^{1/3}$.

In practical situations, other factors come into play, for example, a higher attenuation rate of high-frequency vibration components in cases where propagation distance is significant. The most appropriate scaling factor for use in a specific application is generally the one that provides the best statistical fit of the experimental data. Square-root scaling is normally used when propagation curves are being developed for vibrations from surface blasting as measured at the surface (which is a common situation). Cube-root scaling provides the best fit of experimental measurements for instances where wave propagation is approximately three-dimensional in reports such as those by Duvall and

Atchison (1957), Rupert and Clark (1977), and Naismith (1982); the last two studies measured vibration in underground coal mines from surface mine blasting.

General blast vibration prediction formulae have been presented by Du Pont (1977) and by Abraseys and Hendron (1968). Singh and Vogt (1998) gave a classification of the most common blast prediction formulas, some of which are presented in the following set of equations:

USBM[1] $$PPV = K\left(\frac{D}{\sqrt{Q_E}}\right)^{-\beta}$$ Eq. 17

AMHEN[2] $$PPV = K\left(\frac{D}{\sqrt[3]{Q_E}}\right)^{-\beta}$$ Eq. 18

LANKH[3] $$PPV = K\left(\sqrt{\frac{Q_E}{D^{\frac{3}{2}}}}\right)^{\beta}$$ Eq. 19

ISP[4] $$PPV = K\left(\frac{Q_E}{D^{\frac{2}{3}}}\right)^{\beta}$$ Eq. 20

CMRI[5] $$PPV = n + K\left(\frac{D}{\sqrt{Q_E}}\right)^{-1}$$ Eq. 21

USBM[1] = U.S. Bureau of Mines (Duval and Fogelson, 1962); AMHEN[2] (Ambrasey and Hendron, 1968); LANKH[3] (Langefors-Kihlstrom, 1978); and ISP[4] (Indian Standard Predictor, 1973); CMRI[5] (Central Mining Research Institute, Dhanbad, 1993).

Where K, β, and n are site-specific experimental constants.

However, given that the absolute charge mass, and the distance, geology, rock mass quality and types of blasting vary widely from site to site, the propagation equation should be developed from measurements taken at the particular site of interest. Where this is not possible, as in planning of the drilling and blasting operation for a new area, the findings obtained from empirical data obtained at other sites, under similar conditions, will provide a reasonable approximation.

When distances from the blast and explosive quantities are being determined for a large number of measurements of *PPV*, the best-fit criterion for the 3-parameter model is based on the minimization of the sum of the square residuals, ssr (Wetherelt et al., 2003):

$$ssr = \sum_{i=1}^{N} \left(PPV_i - K \cdot D_i^n \cdot Q_{Ei}^{\alpha} \right)^2 \qquad \text{Eq. 22}$$

Where PPV_i, D_i, and Q_{Ei}, is the *i* triad, and *N* is the number of data points. Alternatively, for the two-parameter model, the sum of the square residuals, *ssr*, is:

$$ssr = \sum_{i=1}^{N} \left(PPV_i - K \cdot SD_i^{-\beta} \right)^2 \qquad \text{Eq. 23}$$

It is common practice to express equation 17 in the log/log form:

$$\log PPV = \log K - \beta \cdot \log SD \qquad \text{Eq. 24}$$

And to determine the parameters *K* and β by minimizing *ssr* for equation 24, where:

$$ssr = \sum_{i=1}^{N} \left(\log PPV_i - \log K + \beta \cdot \log SD \right)^2 \qquad \text{Eq. 25}$$

The resulting *PPV-SD* equation is considered to be the best-fit equation, which can then be employed for on-site prediction purposes (Dowding, 1985; Wetherelt et al., 2003).

For the near-field case, Holmberg and Persson (1978) proposed a generalized *PPV* equation (Eq. 26) valid solely for distances that are short in comparison to charge length, such that the explosive charge can no longer be considered as concentrated at a point. For an extended charge of linear charge concentration, *l* (kg/m), a first approximation of the resulting *PPV* is obtained by integrating the generalized equation over the total charge length. This equation for near-field vibration particle velocity assumes that the vibration *PPV* resulting from the detonation along the entire column charge is numerically additive:

$$V = K \cdot \left[l \cdot \int_{x_s}^{x_s + H} \frac{dx}{\left[r_0^2 + \left(x - x_0 \right)^2 \right]^{n/2 \cdot \alpha}} \right]^{\alpha} \qquad \text{Eq. 26}$$

Where

- V = vibration velocity (mm/s, in/s),
- K, α, n = site specific constants,
- l = linear charge concentration (kg/m),
- x_s = start length of charged blasthole (m),
- $x_s + H$ = end length of charged blasthole (m), and
- r_o = length between explosive charge and measuring point measured perpendicular to the longitudinal axis of the blasthole.

They pointed out that resultant vibration *PPV* is representative of the stress caused by the vibration. One clear shortcoming of this method is that it is time independent (or basically a static approach). This method does not incorporate the arrival times of waveforms within a blasthole or the arrival times of waveforms from different blastholes within the blast, which limits its applicability for real-world examples.

Figure 2.5 illustrates the corresponding dimensions for the estimation of the near-region vibration particle velocity.

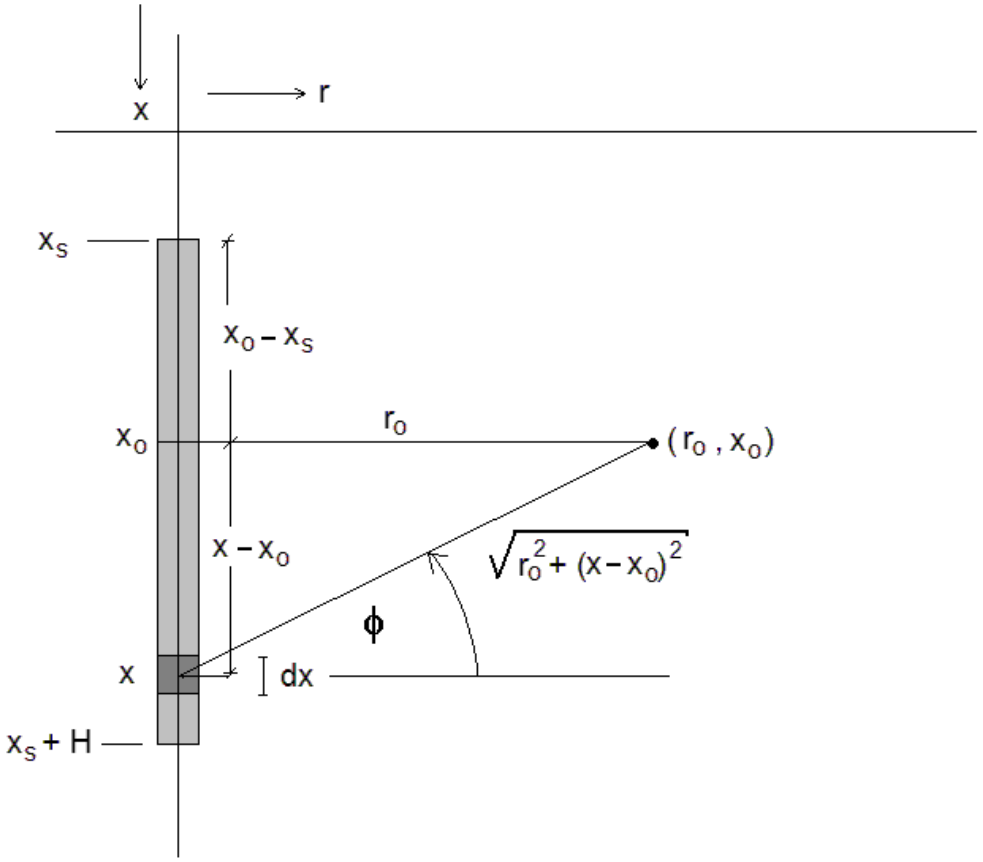

Figure 2.5 Integration of the surface wave effect in the near region of an extended charge (After Persson et. al., 2001) pg. 245

Holmberg and Persson (1978) found that for competent Swedish bedrock masses the applicable constants are K = 700, α = 0.7, and n = 1.5. The limits of the damage zones can then be estimated from a plot of particle velocity vs. distance.

Blair et al. (1996) suggested that the Holmberg-Persson equation requires further investigation. One problem is the way in which the Holmberg-Persson model deals with vibration peaks. For example, the model derives total peak vibration, V_T, by the scalar summation of the individual vibration peaks (i.e., $V_1+V_2+V_3\ldots$). Blair argued that the model is incapable of providing the correct near-field analysis as this model does not incorporate any time delay for the vibration peaks at a given point and the peaks should be summed as vectors and not as scalar magnitudes. In the same context, Baird et al. (1992) shows that a cylindrical column of explosive does not propagate in a spherical radiating pattern as the Holmberg-Persson model. Blair subsequently developed a

dynamic finite element model to assess the damage zone and later developed simple analytical tools to assess the non-linear behavior (Blair, 2008) occurring in the very-near-field between charges of the same blasthole or among different blastholes separated by small distances.

Persson (1997) showed from comparison of theoretical and experimental values that the effective parts of elemental waves arrive at a given point nearly simultaneously, i.e., the entire charge length detonates instantaneously. This assumption overlooks effects of the timing differences of the arrival of elemental waves originating at different parts of charge.

The Holmberg-Persson near-field vibration particle velocity formula (Eq. 26) has been widely used since its introduction, however, Blair and Minchinton (1996) showed that it did not correctly integrate the contribution from each charge element. Later Hustrulid and Lu (2002) showed that the equation was developed using an embedded error, meaning that the Holmberg-Persson equation is mathematically incorrect.

Hustrulid and Lu established that the *SD* equation can be written in differential form, as:

$$dV = K \cdot (l \cdot dx)^{\alpha} \cdot D^{-n} \qquad \text{Eq. 27}$$

Where l is the linear charge concentration (kg/m) and dx is the incremental charge length (m). The incremental form of equation 27 can be expressed as:

$$\Delta V = K \cdot (l \cdot \Delta x)^{\alpha} \cdot D^{-n} \qquad \text{Eq. 28}$$

If the cylindrical charge is divided into N incremental charges, then the total *PPV* produced by the overall cylindrical charge should be expressed as:

$$PPV = K \cdot l^{\alpha} \cdot \sum_{i=1}^{N} \frac{(\Delta x)^{\alpha}}{\left[r_o^2 + (x_i - x_o)^2\right]^{n/2}} \qquad \text{Eq. 29}$$

Which differs from the Holmberg-Persson equation (Eq. 26) written in the incremental form:

$$PPV = K \cdot l^{\alpha} \cdot \left(\sum_{i=1}^{N} \frac{(\Delta x)}{\left[r_o^2 + (x_i - x_o)^2 \right]^{n/2}} \right)^{\alpha} \qquad \text{Eq. 30}$$

One possible explanation for the good estimation capabilities of the Holmberg-Persson equation (Eq. 26) is the fact that the constants (or unknowns) *K*, *α*, and *n* are estimated from the best-fit relation as determined from actual records of seismic data. Even if the equation includes an error, this error is reduced by the fine-tuning of the constants toward those values that minimize the error against the provided data. This can be accomplished, for example, by means of a built-in Microsoft® Excel™ linear equation solver, using the Gauss-Jordan method, which solves systems of equations with two or more unknowns.

2.2.11 Rock Mass Damage from Blasting

Extensive research undertaken by many investigators has verified that civil and rock structure damages have a direct relationship with the ground vibrations originating from blasting.

The studies conducted by Swedish Detonic Foundation (Holmberg and Persson, 1978) resulted in a damage model, wherein damage to a rock mass is indicated if post-blast cracks exceed the pre-blast cracks. Holmberg (1993) concluded that damage was inflicted mainly in the rock structural discontinuities and joints, cracks, and other weak planes in the rock mass. Paventi's work (Paventi, 1995), introduces a similar approach for characterizing rock mass damage based on petrofabric rock mass classification and rock units at the Birchtree mine, although the lack of blast monitoring data to relate rock mass damage to the energies generated by the blast makes a comparison to the work presented in this research impractical.

The rock mass was considered disturbed through the following mechanisms:

- near hole crushing due to high shock wave amplitudes,
- generation of radial cracks due to high-pressure gas in the drill hole,
- opening of the existing joints because of high-pressure gases produced from detonation of explosive,
- fractures through spalling,

- reduction of shear strength due to blast induced rock movement, and
- vibration induced displacement affecting the local slope stability or tunnel perimeter.

Early investigations of blast damage of surface structures performed by the U.S. Bureau of Mines (Thoenen et al., 1937, 1938b and 1942) used criteria relating acceleration, frequency, charge size, and distance. Later research by Duvall (Duvall et al., 1957) established a criterion of 50mm/s (2in/s) particle velocity related to *SD*s, the latter utilizing a square-root power scaling law as discussed in Section 2.2.10.

Crandell (1949) proposed that the damage caused by the blast vibrations was proportional to the energy ratio. The energy ratio, *ER*, was defined as a ratio of the squares of the acceleration *a*, and the frequency *f*:

$$ER = \frac{a^2}{f^2} \qquad \text{Eq. 31}$$

Edwards et al. (1960), Langefors et al. (1973), Bauer et al. (1978), Holmberg et al. (1978) Mojitabai et al. (1996), and several others proposed particle velocity as a blast damage criterion.

In general terms, a simple, single-term criterion such as *PPV* of ground vibrations can be used to determine the damage potential of rock and civil structures. Dowding (1985) successfully applied elastic theory for plane waves (Kolsky, 1963) to blasting problems from which it was deduced that particle velocity was directly proportional to the strain, ε. Therefore, an increase in the particle velocity should directly translate to an increase in ground strain which, in turn, generally induces greater damage to the structure.

Holmberg and Persson (1978) stated that damage is a result of induced strain (ε):

$$\varepsilon = \frac{V_P}{c} \qquad \text{Eq. 32}$$

Where,

- V_P = particle velocity, and
- c = characteristic propagation velocity of P/S/Raleigh wave.

Furthermore, the relationship between *PPV* and rock breakage performance has also been established (Cunningham, 1983). Breakage performance indicators include size distribution of the rock fragments, muck pile placement, and oversize occurrence, among others. *PPV* is also associated with the damage inflicted onto the surroundings of the blasted excavation (Holmberg and Persson, 1978; Holmberg and Persson, 1979, Holmberg and Hustrulid, 1981).

2.2.12 Particle Velocity Estimates in Relation to Structural Damage

For the construction industry, the consensus is that a *PPV* of less than 50mm/s would have low probability of structural damage to residential buildings.

Some general data relating *PPV* to rock damage in underground openings is currently available but is scarce. Even so, Langefors and Kihlstrom (1973) have proposed the following specific criteria for tunnels: *PPV*'s of 305mm/s and 610mm/s shall result in a fall of rock in unlined tunnels, and the formation of new cracks, respectively.

Bauer and Calder (1970) observed that no fracturing of intact rock will occur for a *PPV* of 254mm/s, *PPV* of 254 - 635mm/s results in minor tensile slabbing and *PPV* of 635 - 2540mm/s would cause strong tensile and some radial cracking. Break up of rock mass will occur at a *PPV* of 2540mm/s.

Bogdanhoff (1995) monitored near-field blast acceleration of an access tunnel in Stockholm. Vibration measurements were done at distances between 0.25 and 1.0 meters, outside tunnel perimeter holes with accelerometers. Altogether eight blasts were monitored. The *PPV* in the assumed damage range was found to be between 2000 and 2500mm/s.

2.2.13 Blast Damage Measurement Techniques

Both direct and indirect techniques have been used in the past to measure the amount damage adjacent to the blasted area. Direct measurements include the use of:

- visual inspection,
- half-cast factor (*HCF*),
- bore hole camera to determine the fractures before and after blasting, and

- measurements of overbreak (and underbreak) using survey measurements or laser profiling.

Some other less common techniques include the use of borehole dilatometer (Scoble et al., 1987) to measure rock deformation modulus and relate it to the extent of excavation disturbance surrounding an underground opening and also locate open fracture within a rock mass (Koopmans and Hughes, 1985).

Indirect measurements are conducted using mainly geophysical techniques to assess the blast damage which include:

- vibration analysis,
- cross hole seismic scanning,
- surface seismic tomography,
- ground penetrating radar (*GPR*), and
- time domain reflectometry (*TDR*), among others.

In the author's opinion, visual inspection, overbreak, *HFC*, and vibration analysis associated with rock mass characterization are reliable, simple and robust techniques to measure blast damage, and can easily and routinely be carried out by mine personnel. Although the other techniques have their own merits for the purpose of assessing blast damage, these are considered more academic than practical, and thus are less likely to be performed on a regular basis.

2.2.14 Blast Overbreak

The Equivalent Linear Overbreak Slough (*ELOS*) introduced by Clark (1998), is a damage criterion used to assess the stability of open stopes by defining an average thickness of over-broken material. It considers an average thickness of the excess material and can be estimated independently for back and walls. *ELOS* is an appropriate method to define overbreak since it is relatively simple to determine and yields a linear measure – in length units – and makes it easy to plot and compare. Figure 2.6 shows the design/planned profile, the final profile, and the average overbreak thickness (as per *ELOS*). A drawback of using *ELOS* is the apparently small amount of average overbreak

even for cases where there is a large localized overbreak zone since that volume is then divided by the surface area of the excavation where this value dilutes over the entire surface excavation. The problem of estimating overbreak in specific locations where the actual overbreak occurred, rather than employing the *ELOS* method, is the fact that these kinds of estimations are unable to explain why in other cases such overbreak did not occur where a different blasthole was detonated with the same explosive type and quantities. In this sense, *ELOS* generalizes well the amount of overbreak, whereas overbreak measured in a particular location would not always be explainable.

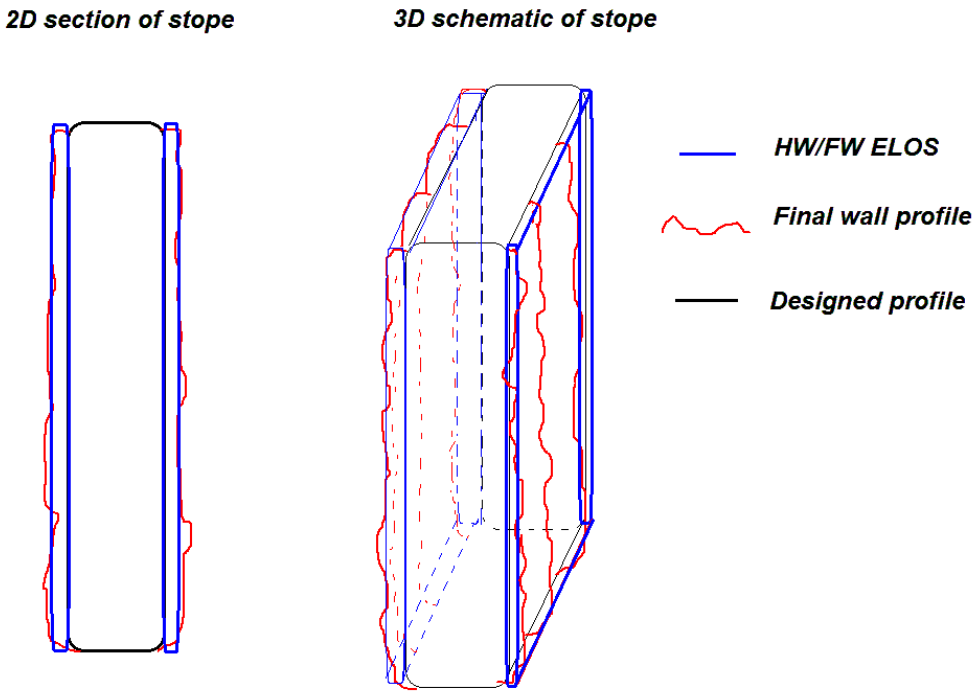

Figure 2.6 *ELOS* concept to measure average stope overbreak

2.3 Rock Mass Classification

2.3.1 Introduction

For the purposes of producing preliminary assessments, evaluating support requirements, estimating degrees of deformation, and determining the magnitude of the strength of a given rock mass, among others, two complimentary rock mass classification systems are widely used in the field: Bieniawski's *RMR* (1976, 1989) and Barton et al.'s *Q* (1974).

Such classification is highly effective in the development of a comprehensive picture of the nature and structure of rock masses.

Whether using *RMR* or *Q*, it is essential first to describe the rock mass in detail, and from there translate this description into either classification index, rather than simply recording rating values during mapping. Without a fully described rock mass, cost evaluations, stability analysis, and studies of the effectiveness of support systems are almost impossible to carry out.

These two classification systems employ somewhat similar parameters – geological, geometric, and design/engineering – where the main differences are the weighting assigned to those parameters, along with differentiations of the use of each parameter found in either system. Both methods evaluate quantitatively the quality of the assessed Rock Quality Designation

The *Rock Quality Designation* (*RQD*) index (Deere et al., 1967) provides a quantitative estimate of the rock mass quality using logs of rock cores. *RQD* is defined as the percentage of intact core pieces longer than 100mm (4 inches) within the total length of the core, where the cored samples should be at least NW size (54.7mm or 2.15 inches in diameter), to somehow standardize the sample's competency. Samples are drilled and extracted with a double-tube core barrel. Figure 2.7 summarizes the measurement procedures of the length of the core pieces and a calculation example of the *RQD*.

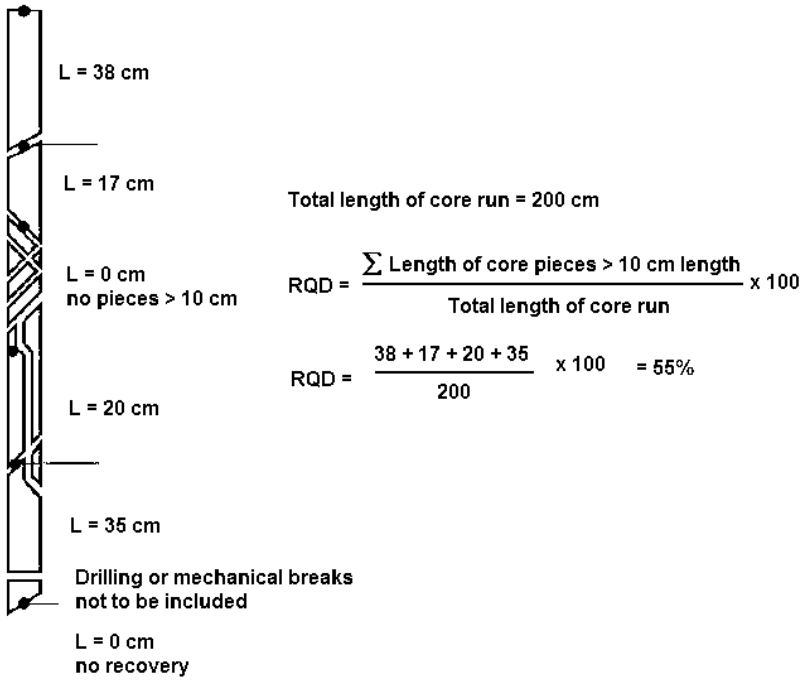

Figure 2.7 Procedure for measurement and calculation of *RQD* (after Deere, 1989)

Palmström (1982) suggested that when core samples are not available, the rock discontinuities visible in surface exposures or exploration addits could be used to estimate *RQD* from the number of discontinuities per unit volume. With respect to clay-free rock masses, the suggested relationship is:

$$RQD = 115 - 3.3 \cdot Jv \qquad \text{Eq. 33}$$

where *Jv* is the sum of the number of joints per unit volume for all joint (discontinuity) sets. *Jv* is known as the volumetric joint count.

Given that *RQD* is a directionally dependent parameter, its value may change substantially with respect to borehole orientation. To reduce such directional dependence, a volumetric joint count is recommended.

In cases of diamond drill core, because *RQD* is intended to represent rock mass quality in-situ, it is imperative that fractures caused by handling or the drilling process itself are identified and subsequently ignored.

Where Palmström's relationship is used for structural mapping of undisturbed rock masses and in estimating *Jv*, blast induced fractures should be ignored.

With regard to the research conducted for the present study, *RQD* is estimated and employed as a parameter of the *RMR* and *Q* rock mass classifications systems, covered later.

2.3.2 Bieniawski's Geomechanics Classification - *RMR*

Bieniawski (1976) produced a rock mass classification called the Geomechanics Classification or Rock Mass Rating (*RMR*). The five parameters used to classify a rock mass quality under the *RMR* system are:

- uniaxial compressive strength of rock material,
- rock quality designation (*RQD*),
- spacing of discontinuities,
- condition of discontinuities, and
- groundwater conditions.

To employ *RMR*, a given rock mass is first divided into a number of structural regions. Each region is subsequently classified separately. The boundaries of the structural regions may be determined by consideration of major structural features, such as a fault, or by examining changes in rock type. In some cases, the rock mass will need to be subdivided into a number of small structural regions, where significant changes in discontinuity spacing or characteristics must be accounted for within the same rock type.

The system is presented in Table 2.1, which gives ratings for each of the five relevant parameters. These ratings are summed to produce a value of *RMR*.

Table 2.1 Rock Mass Rating System (After Bieniawski, 1976)

PARAMETER			RANGE OF VALUES						
1	Strength of intact rock material	Point-load strength index	> 8 MPa	4-8 MPa	2-4 MPa	1-2 MPa	For this low range uniaxial compressive test is preferred		
		Uniaxial compressive strength	> 200 MPa	100-200 MPa	50-100 MPa	25-50 MPa	10-25 MPa	3-10 MPa	1-3 MPa
	Rating		15	12	7	4	2	1	0
2	Drill core quality RQD		90% - 100%	75% - 90%	50% - 75%	25% - 50%	< 25%		
	Rating		20	17	13	8	3		
3	Spacing of joints		> 3 m	1 - 3 m	0.3 - 1 m	50 - 300 mm	< 50 mm		
	Rating		20	25	20	10	5		
4	Condition of joints		Very rough surfaces Not continuous No separation Hard joint wall contact	Slightly rough surfaces Separation < 1 mm Hard joint wall contact	Slightly rough surfaces Separation < 1 mm Soft joint wall contact	Slickesided surfaces or Gouge < 5 mm thick or Joint open 1 - 5 mm Continuous joints	Soft gouge > 5 mm thick or Joint open > 5 mm Continuous joints		
	Rating		25	20	12	6	0		
5	Ground water	Inflow per 10m tunnel length	None	< 25 liters/s	25 - 125 liters/s	> 125 liters/s			
		Ratio of joint water pressure and major principal stress	0	0.0 - 0.2	0.2 - 0.5	> 0.5			
		General condition	Completely dry	Moist only (interstitial water)	Water under moderate pressure	Severe water problems			
	Rating		10	7	4	0			

The value of *RMR* can vary from nearly 10 to 100, with values of approximately 25 representing extremely poor ground and values rating around 100 representing exceptionally good, competent unjointed ground.

Bieniawski (1989) includes a set of guidelines as an aid to the selection of support for tunnels excavated in rock where *RMR* is employed.

2.3.3 Barton's Rock Tunneling Quality Index, *Q*

Using a large number of underground excavation case histories, Barton et al. (1974) of the Norwegian Geotechnical Institute, introduced a Tunneling Quality Index (*Q*) used to evaluate the characteristics of rock mass employed for the design of the tunnel support requirements. The index *Q* varies on a logarithmic scale from 0.001 to a maximum of 1,000, and is defined by:

$$Q = \frac{RQD}{Jn} \cdot \frac{Jr}{Ja} \cdot \frac{Jw}{SRF} \qquad \text{Eq. 34}$$

Where *RQD* is the Rock Quality Designation, *Jn* is the joint set number, *Jr* is the joint roughness number, *Ja* is the joint alteration number, *Jw* is the joint water reduction factor and *SRF* is the stress reduction factor.

To give an explanation of the meaning of the parameters involved in determining *Q*, Barton et al. (1974) offer the following description:

The first quotient (*RQD/Jn*), representing the structure of the rock mass, is a crude measure of the block or particle size, with the two extreme values (100/0.5 and 10/20) differing by a factor of 400. If the quotient is interpreted in units of centimeters, the extreme 'particle sizes' of 200 to 0.5cm are seen to be crude but fairly realistic approximations. Probably the largest blocks should be several times this size and the smallest fragments less than half the size. (Clay particles are of course excluded.)

The second quotient (*Jr/Ja*) represents the roughness and frictional characteristics of the joint walls or filling materials. This quotient is weighted in favor of rough, unaltered joints in direct contact. It is to be expected that such surfaces will be close to peak strength, that they will dilate strongly when sheared, and that they will therefore be especially favorable to tunnel stability.

The third quotient (*Jw/SRF*) consists of two stress parameters. *SRF* is a measure of:

1) loosening load in the case of an excavation through shear zones and clay bearing rock, 2) rock stress in competent rock, and 3) squeezing loads in plastic incompetent rocks.

It can be regarded as a total stress parameter. The parameter *Jw* is a measure of water pressure, which has an adverse effect on the shear strength of joints due to a reduction in effective normal stress. Water may, in addition, cause softening and possible outwash in the case of clay-filled joints. The quotient (*Jw/SRF*) is a complicated empirical factor describing the 'active stress'.

It appears that the rock tunneling quality *Q* can now be considered to be a function of only three parameters, which are crude measures of:

- block size (*RQD/Jn*),
- inter-block shear strength (*Jr/ Ja*), and
- groundwater and active stress (*Jw/SRF*).

The numerical value of the index *Q* varies on a logarithmic scale from 0.001 for exceptionally poor ground to a maximum of 1,000 for exceptionally good, competent, practically unjointed ground. Table 2.2 gives the classification of individual parameters used to obtain the Tunneling Quality Index *Q* for a rock mass.

Table 2.2 Classification of individual parameters used in the Tunneling Quality Index *Q* (After Barton et al 1974)

DESCRIPTION	VALUE	NOTES
1. ROCK QUALITY DESIGNATION	***RQD***	
A. Very poor	0 - 25	1. Where *RQD* is reported or measured as ≤ 10 (including 0),
B. Poor	25 - 50	a nominal value of 10 is used to evaluate *Q*.
C. Fair	50 - 75	
D. Good	75 - 90	2. *RQD* intervals of 5, i.e. 100, 95, 90 etc. are sufficiently
E. Excellent	90 - 100	accurate.
2. JOINT SET NUMBER	J_n	
A. Massive, no or few joints	0.5 - 1.0	
B. One joint set	2	
C. One joint set plus random	3	
D. Two joint sets	4	
E. Two joint sets plus random	6	
F. Three joint sets	9	1. For intersections use ($3.0 \times J_n$)
G. Three joint sets plus random	12	
H. Four or more joint sets, random,	15	2. For portals use ($2.0 \times J_n$)
heavily jointed, 'sugar cube', etc.		
J. Crushed rock, earthlike	20	
3. JOINT ROUGHNESS NUMBER	J_r	
a. Rock wall contact		
b. Rock wall contact before 10 cm shear		
A. Discontinuous joints	4	
B. Rough and irregular, undulating	3	
C. Smooth undulating	2	
D. Slickensided undulating	1.5	1. Add 1.0 if the mean spacing of the relevant joint set is
E. Rough or irregular, planar	1.5	greater than 3 m.
F. Smooth, planar	1.0	
G. Slickensided, planar	0.5	2. J_r = 0.5 can be used for planar, slickensided joints having
c. No rock wall contact when sheared		lineations, provided that the lineations are oriented for
H. Zones containing clay minerals thick	1.0	minimum strength.
enough to prevent rock wall contact	(nominal)	
J. Sandy, gravely or crushed zone thick	1.0	
enough to prevent rock wall contact	(nominal)	
4. JOINT ALTERATION NUMBER	J_a	ϕr degrees (approx.)
a. Rock wall contact		
A. Tightly healed, hard, non-softening,	0.75	1. Values of ϕr, the residual friction angle,
impermeable filling		are intended as an approximate guide
B. Unaltered joint walls, surface staining only	1.0	25 - 35 to the mineralogical properties of the
C. Slightly altered joint walls, non-softening	2.0	25 - 30 alteration products, if present.
mineral coatings, sandy particles, clay-free		
disintegrated rock, etc.		
D. Silty-, or sandy-clay coatings, small clay-	3.0	20 - 25
fraction (non-softening)		
E. Softening or low-friction clay mineral coatings,	4.0	8 - 16
i.e. kaolinite, mica. Also chlorite, talc, gypsum		
and graphite etc., and small quantities of swelling		
clays. (Discontinuous coatings, 1 - 2 mm or less)		

Table 2.2 (cont'd.) Classification of individual parameters used in the Tunneling Quality Index *Q* (After Barton et al 1974)

4, JOINT ALTERATION NUMBER	J_a	ϕr degrees (approx.)	
b. Rock wall contact before 10 cm shear			
F. Sandy particles, clay-free, disintegrating rock etc.	4.0	25 - 30	
G. Strongly over-consolidated, non-softening clay mineral fillings (continuous < 5 mm thick)	6.0	16 - 24	
H. Medium or low over-consolidation, softening clay mineral fillings (continuous < 5 mm thick)	8.0	12 - 16	
J. Swelling clay fillings, i.e. montmorillonite, (continuous < 5 mm thick). Values of J_a depend on percent of swelling clay-size particles, and access to water.	8.0 - 12.0	6 - 12	
c. No rock wall contact when sheared			
K. Zones or bands of disintegrated or crushed	6.0		
L. rock and clay (see G, H and J for clay	8.0		
M. conditions)	8.0 - 12.0	6 - 24	
N. Zones or bands of silty- or sandy-clay, small clay fraction, non-softening	5.0		
O. Thick continuous zones or bands of clay	10.0 - 13.0		
P. & R. (see G.H and J for clay conditions)	6.0 - 24.0		
5. JOINT WATER REDUCTION	J_w	approx. water pressure (kgf/cm^2)	
A. Dry excavation or minor inflow i.e. < 5 l/m locally	1.0	< 1.0	
B. Medium inflow or pressure, occasional outwash of joint fillings	0.66	1.0 - 2.5	
C. Large inflow or high pressure in competent rock with unfilled joints	0.5	2.5 - 10.0	1. Factors C to F are crude estimates; increase J_w if drainage installed.
D. Large inflow or high pressure	0.33	2.5 - 10.0	
E. Exceptionally high inflow or pressure at blasting, decaying with time	0.2 - 0.1	> 10	2. Special problems caused by ice formation are not considered.
F. Exceptionally high inflow or pressure	0.1 - 0.05	> 10	
6. STRESS REDUCTION FACTOR ***a. Weakness zones intersecting excavation, which may cause loosening of rock mass when tunnel is excavated***		***SRF***	
A. Multiple occurrences of weakness zones containing clay or chemically disintegrated rock, very loose surrounding rock any depth)		10.0	1. Reduce these values of *SRF* by 25 - 50% but only if the relevant shear zones influence do not intersect the excavation
B. Single weakness zones containing clay, or chemically disintegrated rock (excavation depth < 50 m)		5.0	
C. Single weakness zones containing clay, or chemically disintegrated rock (excavation depth > 50 m)		2.5	
D. Multiple shear zones in competent rock (clay free), loose surrounding rock (any depth)		7.5	
E. Single shear zone in competent rock (clay free). (depth of excavation < 50 m)		5.0	
F. Single shear zone in competent rock (clay free). (depth of excavation > 50 m)		2.5	
G. Loose open joints, heavily jointed or 'sugar cube', (any depth)		5.0	

Table 2.2 (cont'd.) Classification of individual parameters used in the Tunneling Quality Index *Q* (After Barton et al 1974)

DESCRIPTION	VALUE			NOTES
6. STRESS REDUCTION FACTOR			***SRF***	
b. Competent rock, rock stress problems				
	σ_c/σ_1	$\sigma_t\sigma_1$		2. For strongly anisotropic virgin stress field
H. Low stress, near surface	> 200	> 13	2.5	(if measured): when $5 \le \sigma_1/\sigma_3 \le 10$, reduce σ_c
J. Medium stress	200 - 10	13 - 0.66	1.0	to $0.8\sigma_c$ and σ_t to $0.8\sigma_t$. When $\sigma_1/\sigma_3 > 10$,
K. High stress, very tight structure	10 - 5	0.66 - 0.33	0.5 - 2	reduce σ_c and σ_t to $0.6\sigma_c$ and $0.6\sigma_t$, where
(usually favourable to stability, may				σ_c = unconfined compressive strength, and
be unfavourable to wall stability)				σ_t = tensile strength (point load) and σ_1 and
L. Mild rockburst (massive rock)	5 - 2.5	0.33 - 0.16	5 - 10	σ_3 are the major and minor principal stresses.
M. Heavy rockburst (massive rock)	< 2.5	< 0.16	10 - 20	3. Few case records available where depth of
c. Squeezing rock, plastic flow of incompetent rock				crown below surface is less than span width.
under influence of high rock pressure				Suggest *SRF* increase from 2.5 to 5 for such
N. Mild squeezing rock pressure			5 - 10	cases (see H).
O. Heavy squeezing rock pressure			10 - 20	
d. Swelling rock, chemical swelling activity depending on presence of water				
P. Mild swelling rock pressure			5 - 10	
R. Heavy swelling rock pressure			10 - 15	

ADDITIONAL NOTES ON THE USE OF THESE TABLES

When making estimates of the rock mass Quality (*Q*), the following guidelines should be followed in addition to the notes listed in the tables:

1. When borehole core is unavailable, *RQD* can be estimated from the number of joints per unit volume, in which the number of joints per metre for each joint set are added. A simple relationship can be used to convert this number to *RQD* for the case of clay free rock masses: $RQD = 115 - 3.3\,J_v$ (approx.), where J_v = total number of joints per m^3 ($0 < RQD < 100$ for $35 > J_v > 4.5$).
2. The parameter J_n representing the number of joint sets will often be affected by foliation, schistosity, slaty cleavage or bedding etc. If strongly developed, these parallel 'joints' should obviously be counted as a complete joint set. However, if there are few 'joints' visible, or if only occasional breaks in the core are due to these features, then it will be more appropriate to count them as 'random' joints when evaluating J_n.
3. The parameters J_r and J_a (representing shear strength) should be relevant to the weakest significant joint set or clay filled discontinuity in the given zone. However, if the joint set or discontinuity with the minimum value of J_r/J_a is favourably oriented for stability, then a second, less favourably oriented joint set or discontinuity may sometimes be more significant, and its higher value of J_r/J_a should be used when evaluating *Q*. The value of J_r/J_a should in fact relate to the surface most likely to allow failure to initiate.
4. When a rock mass contains clay, the factor *SRF* appropriate to loosening loads should be evaluated. In such cases the strength of the intact rock is of little interest. However, when jointing is minimal and clay is completely absent, the strength of the intact rock may become the weakest link, and the stability will then depend on the ratio rock-stress/rock-strength. A strongly anisotropic stress field is unfavourable for stability and is roughly accounted for as in note 2 in the table for stress reduction factor evaluation.
5. The compressive and tensile strengths (σ_c and σ_t) of the intact rock should be evaluated in the saturated condition if this is appropriate to the present and future in situ conditions. A very conservative estimate of the strength should be made for those rocks that deteriorate when exposed to moist or saturated conditions.

2.3.4 Rock Support Under Dynamic Loading

It is evident that the rock support employed should be designed to withstand the dynamic loading of nearby blasts. This is especially important when the ground being supported is of weak rock mass, in which the rock excavation is only held up by the supporting elements acting against an otherwise extreme deformation, to the point of caving. For this type of weak ground, where the use of shotcrete is very common, in combination with other means of rock support, there has been extensive work done in the field in terms of

empirical design (Pakalnis et. al., 2010), numerical modeling (Zhou and McNeary, 2007; Caceres et. al., 2010), and laboratory testing of shotcrete panels (Bernard and Pireher, 2000; Martin et. al. 2010). In any case, there remains a need for better understanding of the behavior of shotcrete under the instantaneous dynamic stresses exerted during the blasting process.

2.3.5 Support Design Requirements

A better understanding of the dynamic behavior of different rock mass qualities should provide fundamental information to define the type of ground support that requires a specific set of rock mass conditions. Input parameters, such as *PPV* values and ground vibration frequencies coupled with dynamic (and static) rock support strength, should be regularly assessed to provide the safest and most cost-effective ground support design.

3 FIELD DATA COLLECTION AND ANALYSIS

3.1 Introduction

There are two main purposes of drifting in underground mining, the first is that the drift itself as driven into ore material constitutes economic benefit to the mine; and the second is to gain access to an orebody. Secondary purposes may include ventilation and material transportation, among others. The main objective of the drifting process is to achieve the desired excavation profile as safely and cost-effective as possible. In this process, key factors include minimizing overbreak and damage to the remaining rock mass, hence reducing the support requirements up to an acceptable risk level while achieving the desired fragmentation for cost-effective material handling.

3.2 The Drifting Process

The process of drift development, also known as drifting, comprises a series of tasks performed sequentially. Briefly, the process starts by defining and delineating the direction of the drift and the blasthole location. This is followed by the drilling of blastholes and, subsequently, the loading of explosives. Once personnel and equipment have been vacated from the area, the round is blasted. After gases produced by the chemical reaction of the detonated explosives and the dust are ventilated, mucking of the broken material takes place. Manual and/or mechanical scaling of loose material to ensure there is a safe entrance to the workplace follow this. Once the support system and mining services are installed, the process repeats itself. The drifting process is summarized in the following flow chart. The whole process is guided by planning and engineering and regulated by human, economic, and workplace factors.

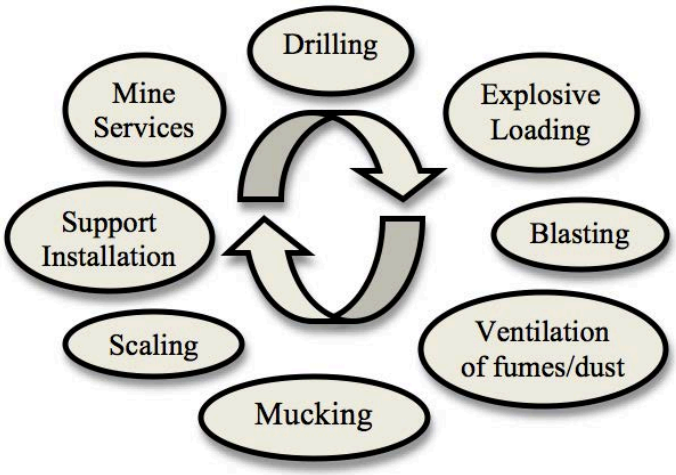

Figure 3.1 Sequential tasks of the drifting process

3.3 Methods of Field Data Collection

3.3.1 Process of Field Data Collection

Data was obtained through a field measurement process and a data collection process, followed by analysis and interpretation of the results. Details of each step and the logistics involved are given below. The following flow chart shows the different tasks involved in the pre-blast site investigation. These tasks can be executed in any given sequence, but they obviously depend on the availability of the workforce operating the machinery in the drift. Ideally, the site investigation should disrupt the drifting process as little as possible.

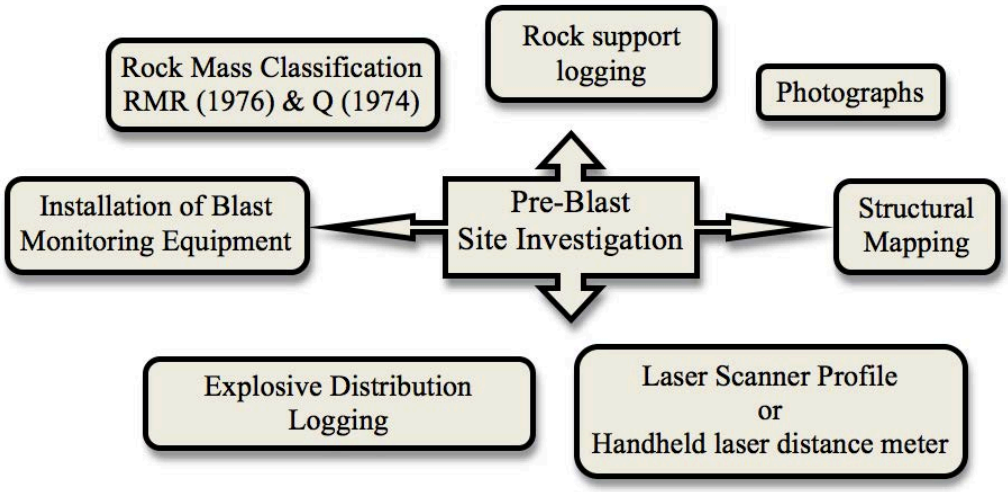

Figure 3.2 Pre-blast data collection process

The post-blast site investigation is concentrated in the newly created excavation and includes the following tasks:

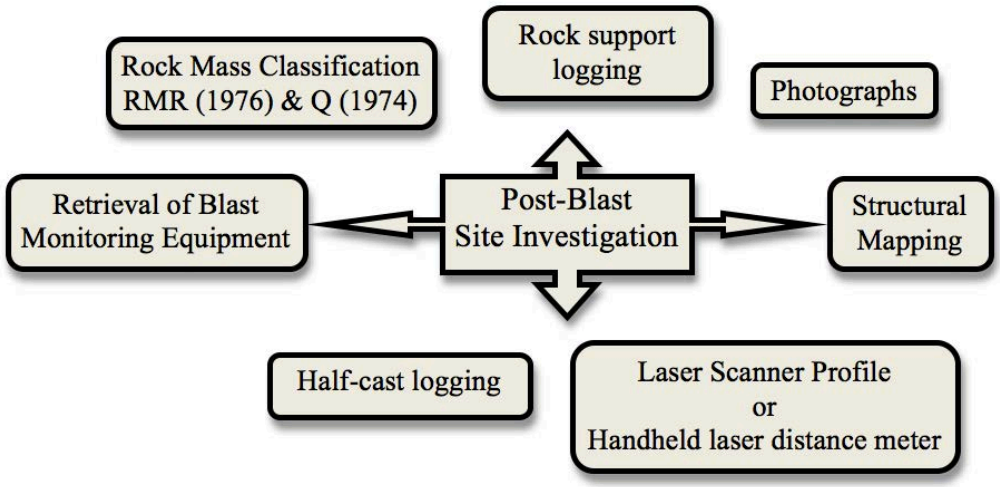

Figure 3.3 Post-blast data collection process

Although not included as part of the flow chart, a visual inspection to record any extra features that can help future analysis of the information, such as excessive break out in parts of the drift or the condition of the support in use to address rock bolt plate conditions and bagging of mesh with broken material, is performed.

During the pre- and post-blast site investigation it was necessary to take extra precautions to avoid injuries as there was more exposure to unsecure conditions like working right at the face or during the drilling and explosive loading of the blasthole round.

3.3.2 Rock Mass Quality Assessments

Two systems were employed to characterize rock mass quality: Bieniawski's Rock Mass Rating, *RMR* (1976), and Barton's Rock Tunneling Quality Index, *Q* (1974). See Sections 2.3.2 and 2.3.3 for explanations.

Uniaxial compressive strength values were obtained from laboratory test reports (previously completed on similar rock types for each of the mines investigated). No unconfined compressive strength tests had been performed at those particular sites. It is a common practice among geotechnical engineers and technicians to quantify the strength of a rock mass based on a hammer blow to the exposed rock for the purpose of analyzing its soundness. This method was employed along the entire, actual monitored drifts in order to confirm that the values obtained were consistent with those from previous tests performed on similar rock types.

RQD values were determined based on the average spacing of the joint sets and the relation existing between average spacing and *RQD*. As in the case of the strength of the rock mass, it is common practice to assess the *RQD* values based on average joint set spacing, in the absence of diamond drill core. The graph shown in Figure 3.4 presented by Bieniawski (1989), was used to determine approximated *RQD* values.

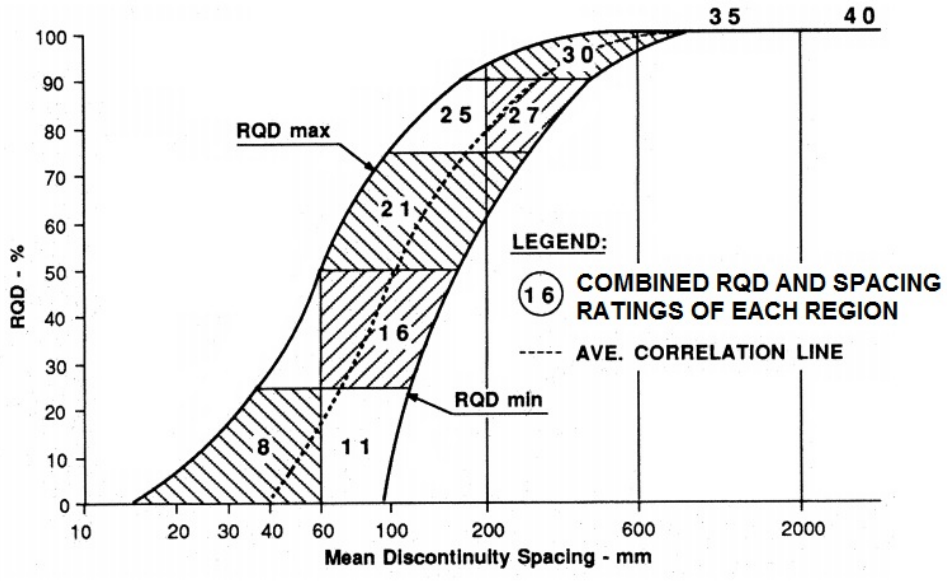

Figure 3.4 Relationship between discontinuity spacing and *RQD*, after Bieniawski (1989)

Barton et al. (1974) Tunneling Quality Index (*Q*) was also determined for the purpose of assessing the rock mass quality. The numerical value of the index *Q* is defined by:

$$Q = \frac{RQD}{Jn} \cdot \frac{Jr}{Ja} \cdot \frac{Jw}{SRF} \qquad \text{Eq. 35}$$

All of the values prescribed by the *Q* system, such as *RQD*, *Jn* (joint set number), *Jr* (joint roughness number), *Ja* (joint alteration number), *Jw* (joint water reduction factor), and *SRF* (stress reduction factor), were determined based on visual inspection of the sites being monitored. The data was subsequently reported as three separate ratios *RQD/Jn*, *Jr/Ja*, and *Jw/SRF*. As is the case in *RMR*, the larger the index *Q*, the more competent the rock mass.

Figure 3.5 shows the rock mass quality information sheet used for each mapped cell, featuring independent descriptions for both walls and back. Each cell constitutes a surface of a previously blasted round. Cells include Bieniawski's (1976) Rock Mass Rating (*RMR*), Barton's (1974) Tunneling Quality Index *Q*, Deere's (1976) Rock Quality Designation (*RQD*), dip and dip direction of major joint sets including persistence, spacing and number of occurrences, as well as field notes of type and condition of support installed, and any other description that may enhance the information detailed, such as number and length of half-barrels visualized, and a visual assessment of the

amount of overbreak that might have occurred (obtained with the help of a handheld laser distance meter).

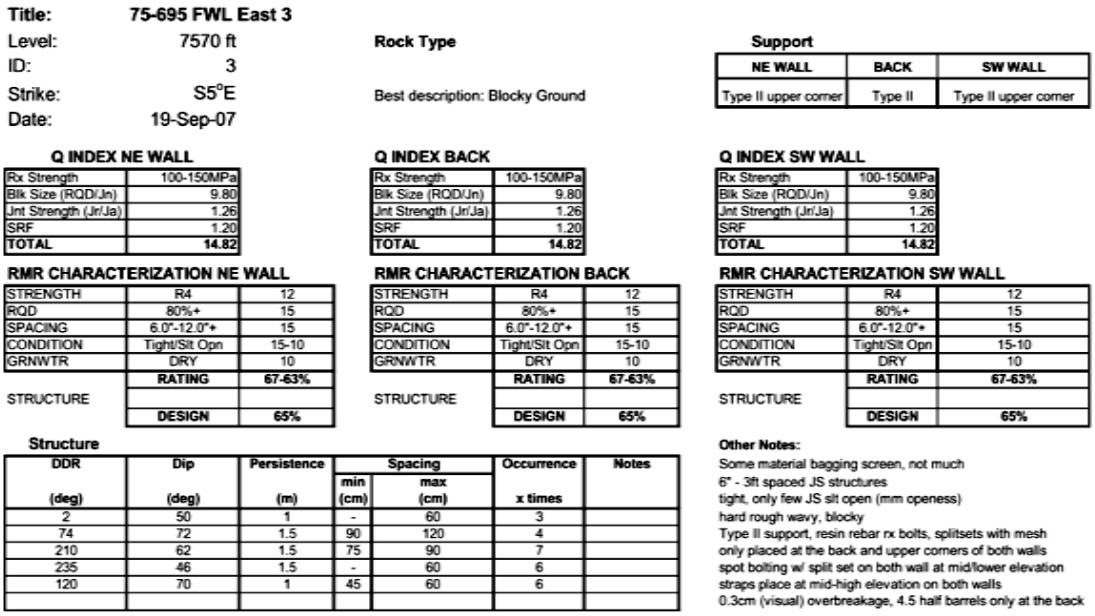

Title: 75-695 FWL East 3
Level: 7570 ft
ID: 3
Strike: S5°E
Date: 19-Sep-07

Rock Type
Best description: Blocky Ground

Support

NE WALL	BACK	SW WALL
Type II upper corner	Type II	Type II upper corner

Q INDEX NE WALL

Rx Strength	100-150MPa
Blk Size (RQD/Jn)	9.80
Jnt Strength (Jr/Ja)	1.26
SRF	1.20
TOTAL	**14.82**

Q INDEX BACK

Rx Strength	100-150MPa
Blk Size (RQD/Jn)	9.80
Jnt Strength (Jr/Ja)	1.26
SRF	1.20
TOTAL	**14.82**

Q INDEX SW WALL

Rx Strength	100-150MPa
Blk Size (RQD/Jn)	9.80
Jnt Strength (Jr/Ja)	1.26
SRF	1.20
TOTAL	**14.82**

RMR CHARACTERIZATION NE WALL

STRENGTH	R4	12
RQD	80%+	15
SPACING	6.0"-12.0"+	15
CONDITION	Tight/Slt Opn	15-10
GRNWTR	DRY	10
	RATING	**67-63%**
STRUCTURE		
	DESIGN	**65%**

RMR CHARACTERIZATION BACK

STRENGTH	R4	12
RQD	80%+	15
SPACING	6.0"-12.0"+	15
CONDITION	Tight/Slt Opn	15-10
GRNWTR	DRY	10
	RATING	**67-63%**
STRUCTURE		
	DESIGN	**65%**

RMR CHARACTERIZATION SW WALL

STRENGTH	R4	12
RQD	80%+	15
SPACING	6.0"-12.0"+	15
CONDITION	Tight/Slt Opn	15-10
GRNWTR	DRY	10
	RATING	**67-63%**
STRUCTURE		
	DESIGN	**65%**

Structure

DDR (deg)	Dip (deg)	Persistence (m)	Spacing min (cm)	Spacing max (cm)	Occurrence x times	Notes
2	50	1	-	60	3	
74	72	1.5	90	120	4	
210	62	1.5	75	90	7	
235	46	1.5	-	60	6	
120	70	1	45	60	6	

Other Notes:
Some material bagging screen, not much
6" - 3ft spaced JS structures
tight, only few JS slt open (mm openess)
hard rough wavy, blocky
Type II support, resin rebar rx bolts, splitsets with mesh
only placed at the back and upper corners of both walls
spot bolting w/ split set on both wall at mid/lower elevation
straps place at mid-high elevation on both walls
0.3cm (visual) overbreakage, 4.5 half barrels only at the back

Figure 3.5 Cell mapping of both walls and back for each round

In order to have a visual record for future analysis and interpretation of rock mass quality and type and condition of the rock support employed, three pictures of the right and left walls and the back were taken for every round length. As an example, Figure 3.6 shows the left wall of the drift, where the face of the round represents the front.

Figure 3.6 Photograph of the left wall showing structures and rock mass condition

The dip and dip direction of the structures and joint sets were measured using a Brunton® compass, for which the declination had been previously set up to measure the strike of rock features with respect to mine North.

3.3.3 Blast Monitoring and Equipment

High frequency triaxial geophones were installed along drifts to measure particle velocity. These instruments are capable of measuring ground velocities up to 2540mm/s (100in/s) between the 28Hz to 1000Hz range. The geophones were bolted to the ribs of one or both walls, preferentially on solid rock or mounted on an aluminum bracket, and on shotcrete when the circumstances required doing so. The data loggers or monitors were set to begin recording triggered by ground motion exceeding 10mm/s. The location for the installation of each geophone was selected after a thorough inspection, to avoid intersecting rock features that could cause faulty readings (because of loosening of the coupling of the geophone to the rock). Because the geophones were installed as near to the face as possible, in some close distance cases a protective metal box was used to shield the instruments from the shock wave, and from the ejected rock from the blast (Figure 3.7).

Figure 3.7 Protective metal box with geophone and datalogger installed

The seismic data, consisting of the measurement of particle velocity over a period of time, was recorded on an Instantel™ MiniMate Plus® datalogger (seismic monitor). Figure 3.8 shows the MiniMate Plus®, along with a high frequency triaxial geophone used to monitor blast-produced seismic vibrations.

Figure 3.8 Minimate Plus® and high frequency triaxial geophone

The geophones were connected to the dataloggers using cables of various lengths, permitting coverage of long lengths (up to 25 meters) with the use of a single datalogger. A maximum of two geophones can be connected to each datalogger of the series employed.

The internal batteries of the datalogger were fully charged to ensure that they were able to record during the blasting event, which could be hours after the instruments were installed. Also, they required the setup of the sampling rate (the number of samples recorded per second) to a maximum of 16,384 samples per second, along with the length of time of the measurement once triggered, to ensure that all blastholes of a round were recorded. Ten seconds is sufficient to record all the events of a round when long-period delay detonators are used.

In many cases, the dataloggers recorded events other than the blasting episode, triggered by vibration levels in excess of 10mm/s, such as when heavy machinery was passing close to the geophone. As these instruments have a limited memory capacity, it was imperative that the useable records were downloaded immediately following each event, in order to clear and free up available memory.

At the end of the monitoring process, all instruments were retrieved, in some cases many hours after the event occurred, when personnel were allowed access to the monitored drift.

The technical specifications of the geophones utilized were obtained from the product instruction sheet Table 3.1 – High Frequency Triaxial Geophone – Instantel® web page.

Table 3.1 High Frequency Triaxial Geophone – Instruction Sheet (source: www.instantel.com, June 2011)

Specifications	
Amplitude Range	100in/s (2540mm/s)
Frequency Range	28Hz to 1000Hz
Sensitivity	0.0012674V/in/s (0.33222605V/mm/s)
Resolution	0.00310in/s (0.0788mm/s)
Trigger Levels	0.05 to 100in/s (1.27 to 2540.00mm/s)
Sensor Density	145lb/ft^3 (2.33g/cc)
Recommended Sample Rate	4096 samples per second
Cable Length	100ft (30.48m)

The frequency response curve and the phase lag for model type SM-7 30Hz geophone sensors are shown in Figure 3.9 and Figure 3.10 respectively. The SM-7 sensors are manufactured by Ion Geophysical Corporation. From the response curve it can be seen that sensitivity rapidly decreases for frequencies lower than 30Hz and is negligible below 10Hz. On the upper side, the sensitivity shows an almost flat response for frequencies in the range 30-1000Hz. The equipment utilized is incapable of recording accurately frequencies below the 30Hz threshold and has zero sensitivity for frequencies lower than 8Hz where an important portion of the low frequency particle velocity is to be found. However, rock breakage occurs not because of the *PPV* at a particular frequency level, but occurs due to the cumulative particle velocity over a wide range of frequencies.

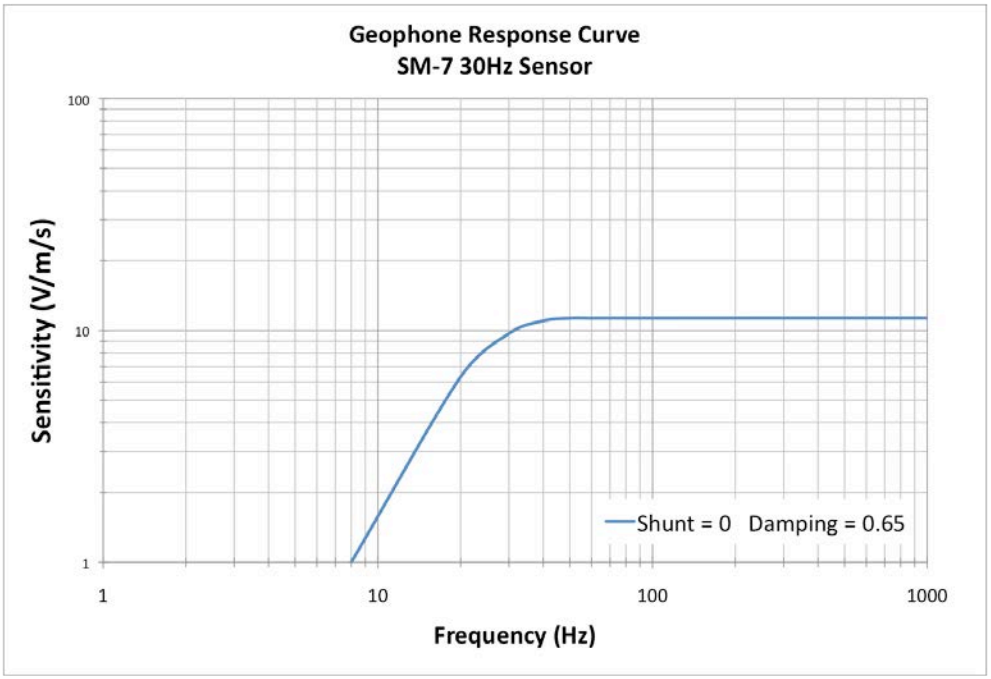

Figure 3.9 SM-7 30Hz geophone response curve (modified from www.iongeo.com, June 2011)

The phase response starts around 0 degrees at approximately 0Hz, then reaches 90 degrees at 30Hz, ascending to approximately 160 degrees at 100Hz.

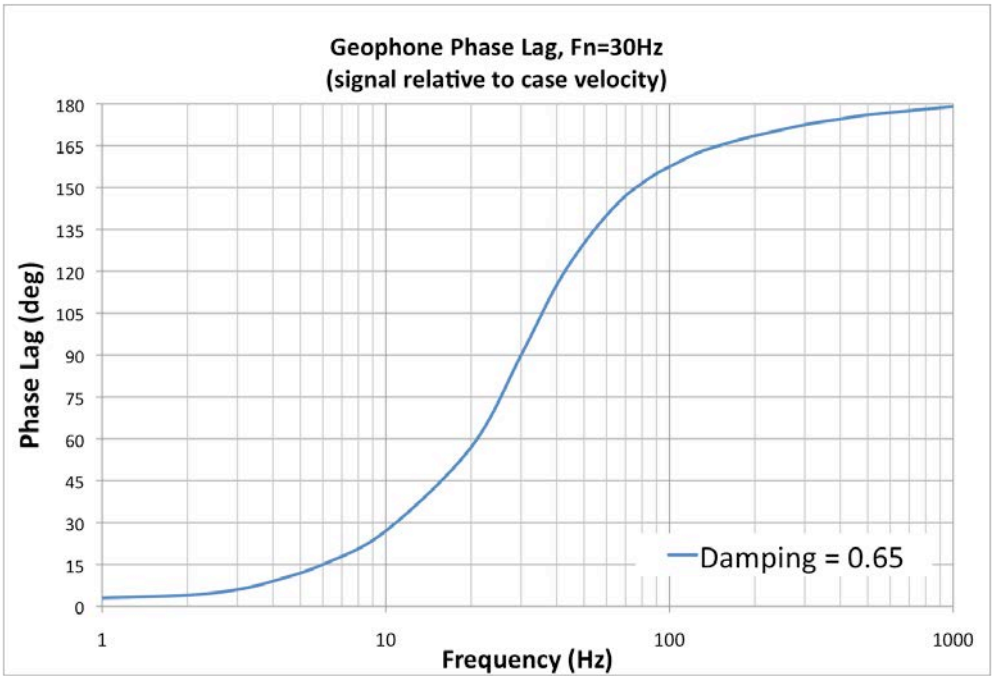

Figure 3.10 SM-7 30Hz geophone phase lag (modified from www.iongeo.com, June 2011)

3.3.4 Explosives Characteristics

The following table (Table 3.2) lists the technical specifications of the explosives utilized in the blasting of development rounds. Some of these specifications can only be taken as average values since they could vary due to a variety of factors. Some of these factors are inherent to the explosive itself, and some are external, dependent upon the surrounding rock, and the size and condition of the blasthole.

Table 3.2 Explosive utilized – Main specifications (source: www.dynonobel.com, June 2011)

Specifications	***ANFO***	***Dyno® AP***	***Dynosplit®***
Density (g/cc)	0.84	1.15	1.40
Energy (cal/g) **(cal/cc)**	880 720	775 890	995 1,440
Relative Weight Strength	1.00	0.88	1.13
Relative Bulk Strength	1.00	1.24	2.00
Velocity (m/s)	3,400	4,700	2,600
Detonation Pressure (kbars)	31	63	25
Gas Volume (moles/kg)	43	41	32
Water Resistance	None	Excellent	24 hrs

The relative weight strength is a specified explosive characteristic used to compare the energy content and the production of gases of different explosives with respect to an explosive considered standard. In many cases, including in this research, the standard explosive used is *ANFO*, a combination of ammonium nitrate and fuel oil, which at a certain percentage, maximizes energy delivered and balances oxygen consumption (i.e., minimizing production of CO and NOx gases).

3.4 Methods of Analysis of Field Data

3.4.1 *PPV* and *SD*

PPV measurements of each blasthole or combination of blastholes were determined directly from the vector sum of the three independent and perpendicular particle velocities versus time velocities.

The larger the amount of explosives detonated per delay, the higher the *PPV* measured for similar excavation geometries and rock mass conditions, although the quantities of explosive and the distances to the blast must be normalized in order to compare them with different explosive types and quantities, used within the same blasthole or blastholes in the round. It is common practice to use *SD* (Dowding, 1985), which can be defined as the relation existing between the standardized explosive quantities to its equivalent quantity of *ANFO* – or any other explosive used as a reference – measured in kilograms or pounds, and the distance to the explosive source measured in meters or feet, from an arbitrary point. For the analysis herein, the standardization of different explosive types was performed using their relative weight strength to that of *ANFO*, based on information obtained and documented by the explosives companies. Figure 3.11 portrays an example of a section of the combination of explosives loaded into individual blastholes for body, perimeter (contour), and lifter blastholes at the Stillwater mine.

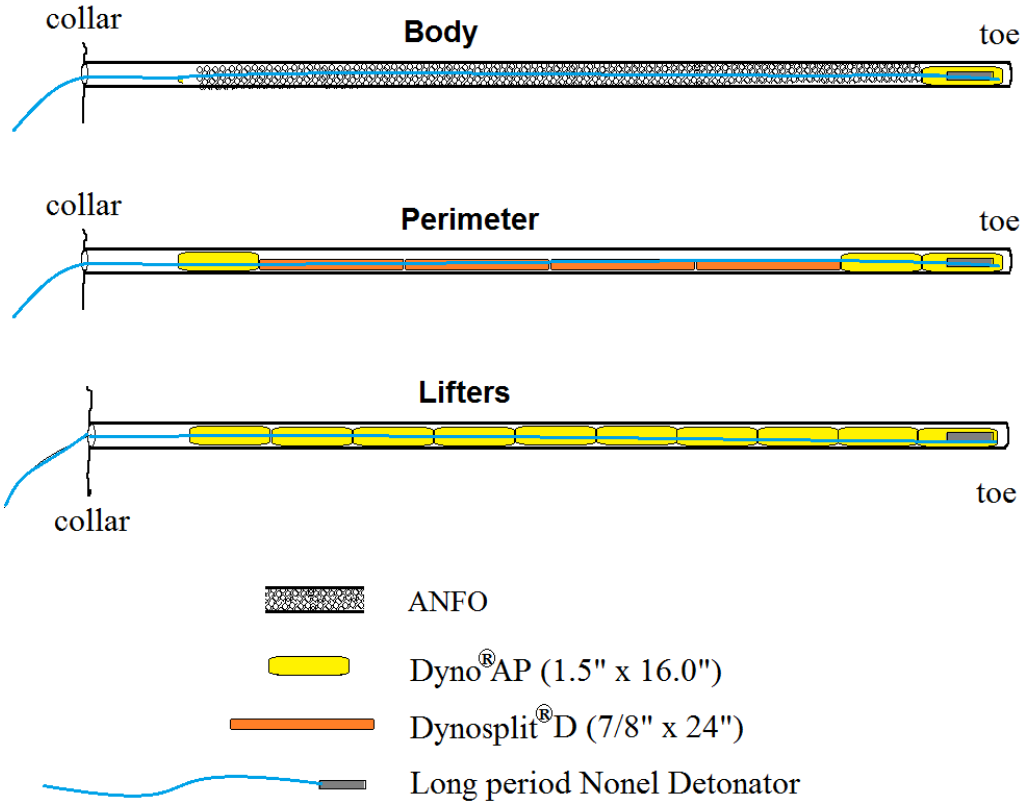

Figure 3.11 Perimeter and lifter blastholes - Explosive's distribution – Stillwater mine

The *PPV* relationship is presented with respect to the *SD* as an equation of the type shown in equation 26.

$$PPV = K\left(\frac{Q^{\alpha}}{D^{n}}\right) \qquad \text{Eq. 36}$$

Where n, α, and K are the site-specific constants, D is the distance to the source, and Q is the weight of explosives detonated per delay. In this analysis, it was assumed that $\alpha=0.5$, and so only K and n are the unknowns to be determined based on the best-fit power law relation, as applied to the cloud of data points recorded.

Once these constants are determined (and incorporated back into the Holmberg-Persson equation (Eq. 26)), it then is possible to establish the near-field *PPV* necessary to produce the measured amount of overbreak, for any given rock mass quality.

3.4.2 Frequency Content of a Waveform

The frequency content was obtained from the particle velocity versus time records, and then compared to the differences existing among the range of rock mass qualities being analyzed. As determined in the proposed semi-empirical model, in the upcoming pages, only the main, predominant frequency will be used to assess *PPVs*.

3.4.3 *PPV* Analysis using Band-Pass Filter

The following figures display the resultant *PPV* waveforms (after the original waveform has been filtered using a band pass filter). The set of ranges analyzed were 0-100Hz, 100-500Hz, 500-1000Hz, and 1000-1500Hz. The scale of each pair of graphs, i.e., with and without band pass filtering, is the same.

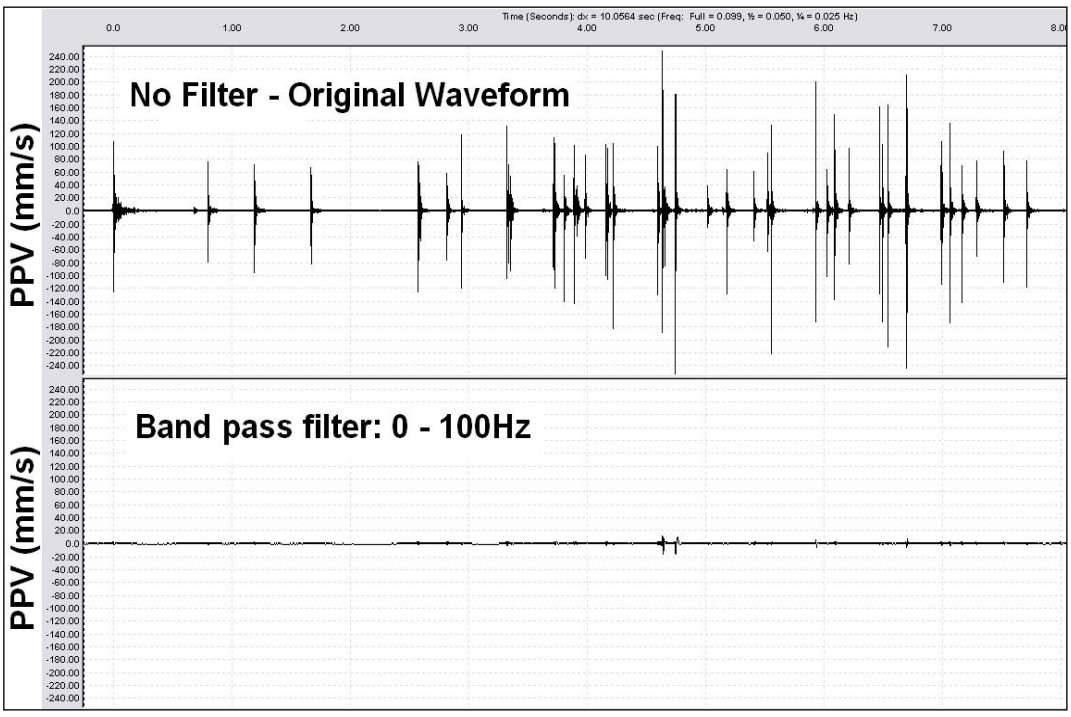

Figure 3.12 *PPV* versus time record – With and without band pass filter (0-100Hz)

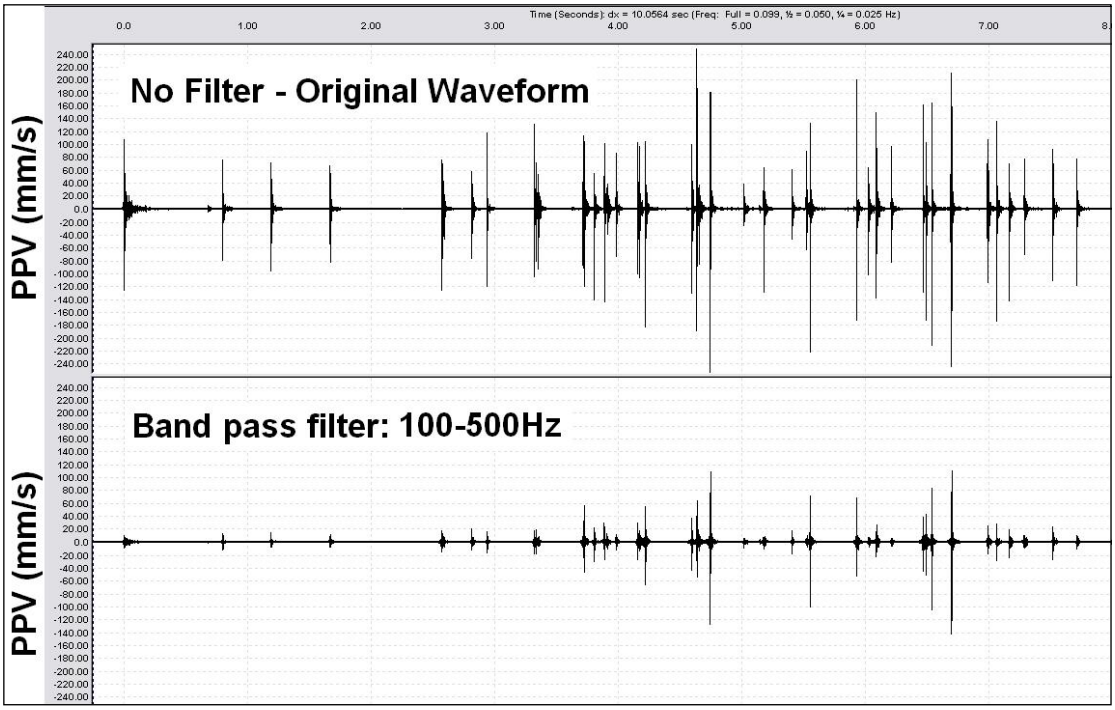

Figure 3.13 *PPV* versus time record – With and without band pass filter (100-500Hz)

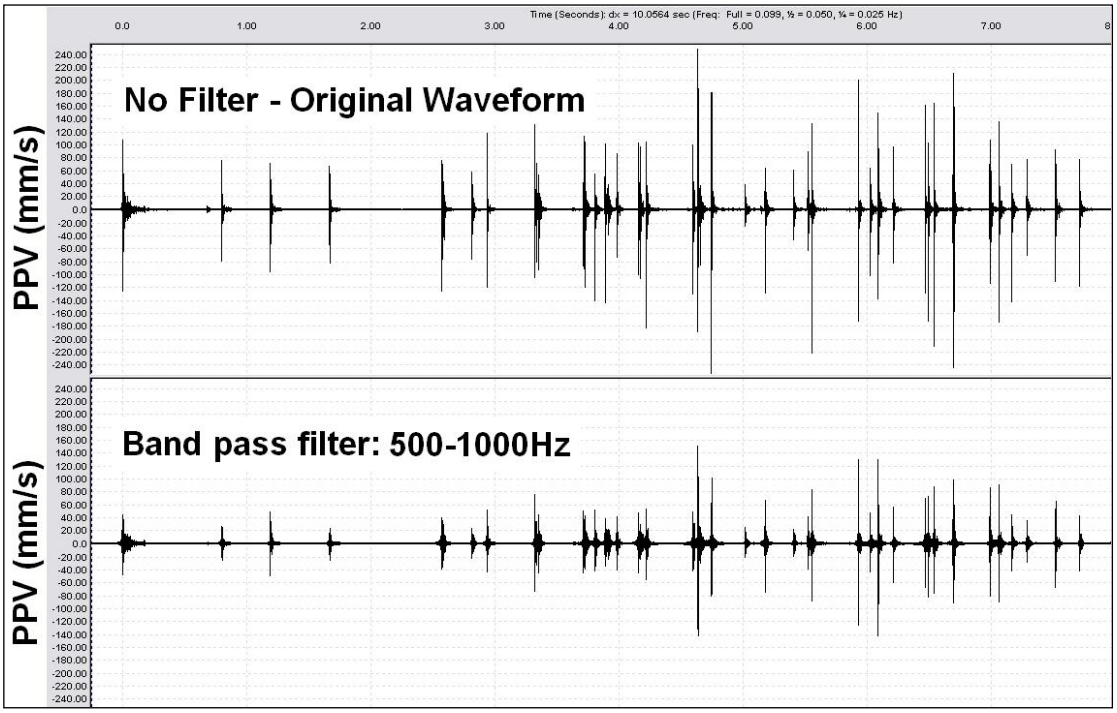

Figure 3.14 *PPV* versus time record – With and without band pass filter (500-1000Hz)

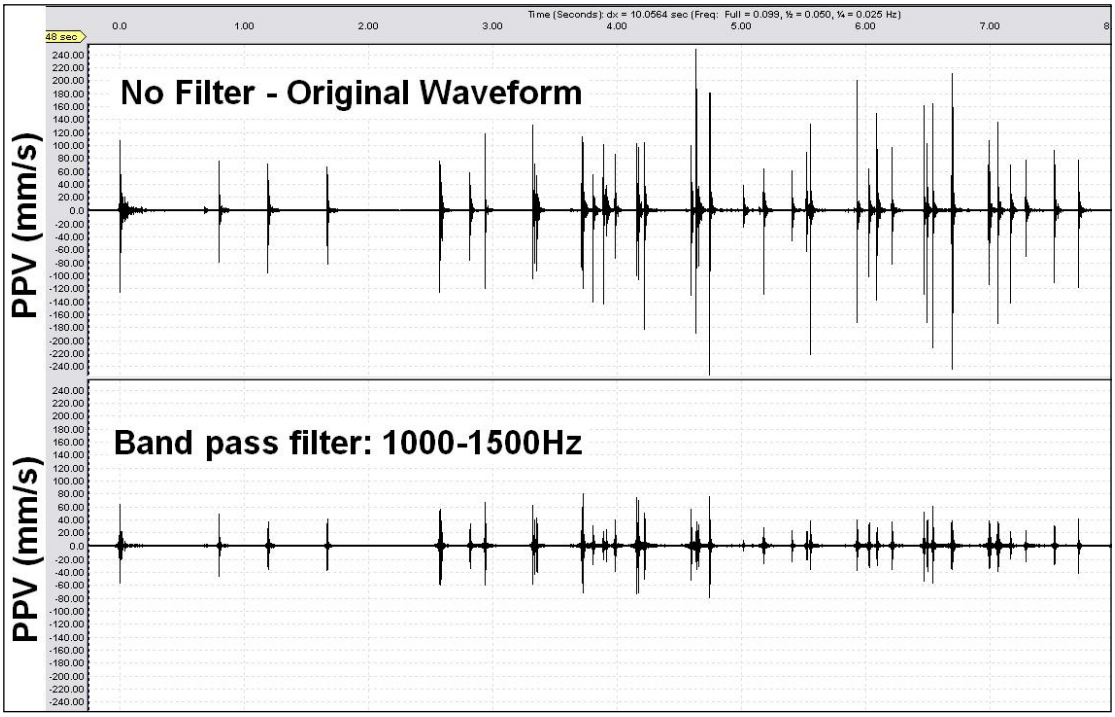

Figure 3.15 *PPV* versus time record – With and without band pass filter (1000-1500Hz)

It is clear from the above graphs that, when the seismic monitors are in close proximity to the blast, the largest *PPV* values are determined in the high frequency range of the spectrum. In particular, for the Musselwhite Mine case study, this range was between 500-1500Hz yielding an average of more than 90% of the original *PPV* value. It is important to note that there is practically no literature available regarding such high frequency readings and high levels of *PPV* measurements. This is because the majority of existing, available data had been recorded at considerable distances from the blast.

3.4.4 Data Processing

Data processing included analysis of the various seismic records obtained from each geophone installed along a given drift. The results of the *PPV* for several events were combined on a single spreadsheet. Seismic data processing was by Instantel® Blastware™ software (v. 4.37). Each seismic record included three independent particle velocity measurements (in millimeters per second), one for each axis (horizontal, vertical, and transversal) of the triaxial geophone, as depicted in Figure 3.16.

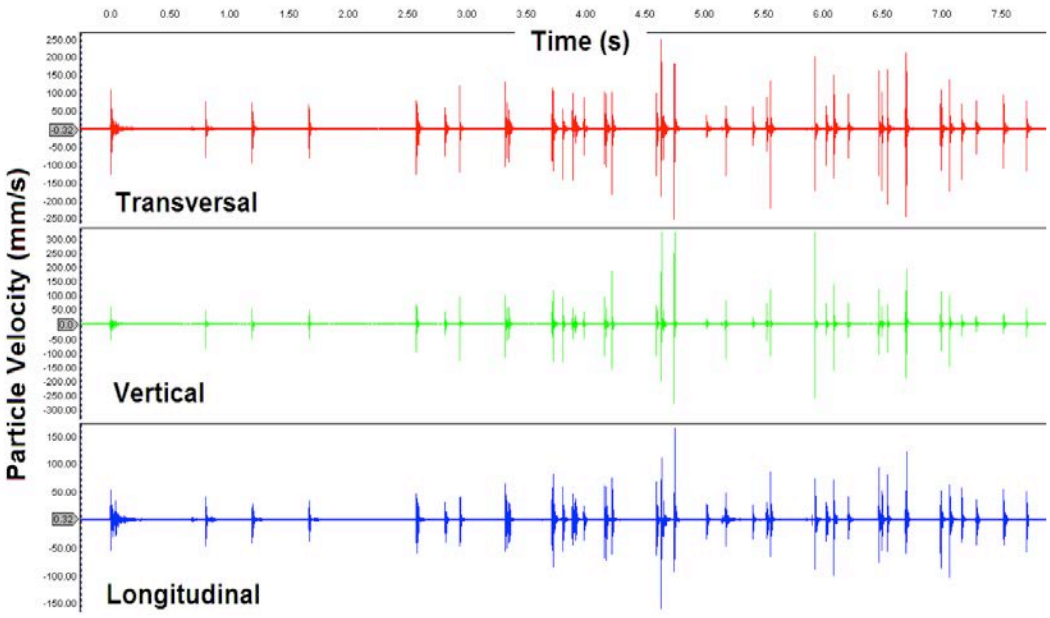

Figure 3.16 Transversal, vertical and longitudinal particle velocity record

The vector sum of the three components is obtained by applying the square root of the sum of the square of the horizontal, vertical, and transversal particle velocity component measurements at any given time, from which *PPVs* for each individual blasthole or sets of blastholes are determined, as shown in Figure 3.17. Each seismic record has an associated standardized explosive quantity and length, and from each peak (using the vector sum), a single point on the *PPV* versus *SD* graph is determined. It is important to note that the vector sum *PPV* might not coincide with the peak velocity of each of the three individual records.

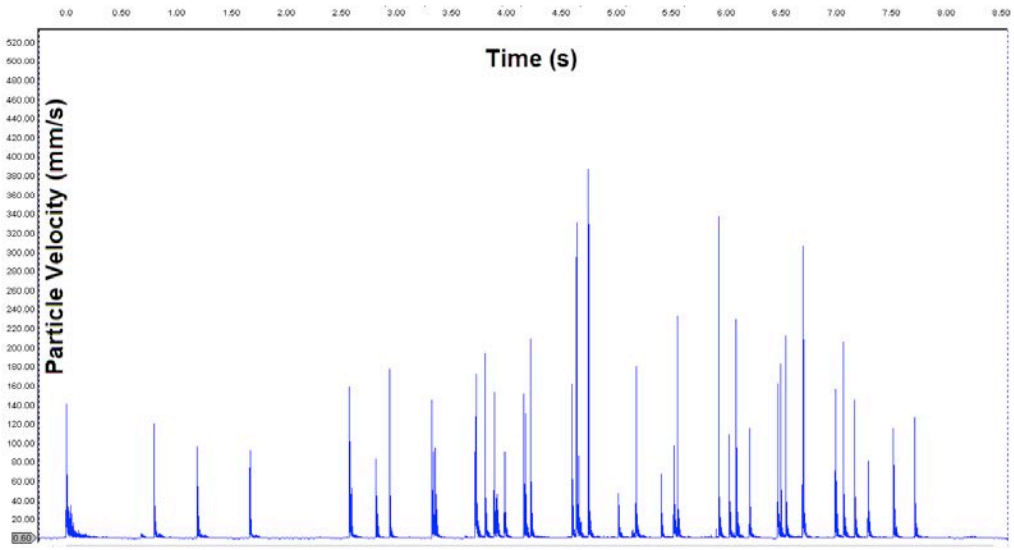

Figure 3.17 Vector sum of the three individual particle velocity components

In order to illustrate the relationship that exists between the frequency spectrum range and the rock mass quality assessed, the seismic record waveform of a single blasthole was isolated from the waveforms pertaining to other blastholes, as shown in Figure 3.18. Background noise, which is also mixed with the seismic events, distorts the overall frequency content, and can lead to ambiguous results. It is for these reasons that filtering and isolating individual blasthole waveform are important to determine the most significant frequency range where the *PPV* is the highest. The fast Fourier transformation was applied to this isolated portion, and the frequency spectrum was thus obtained (Figure 3.19).

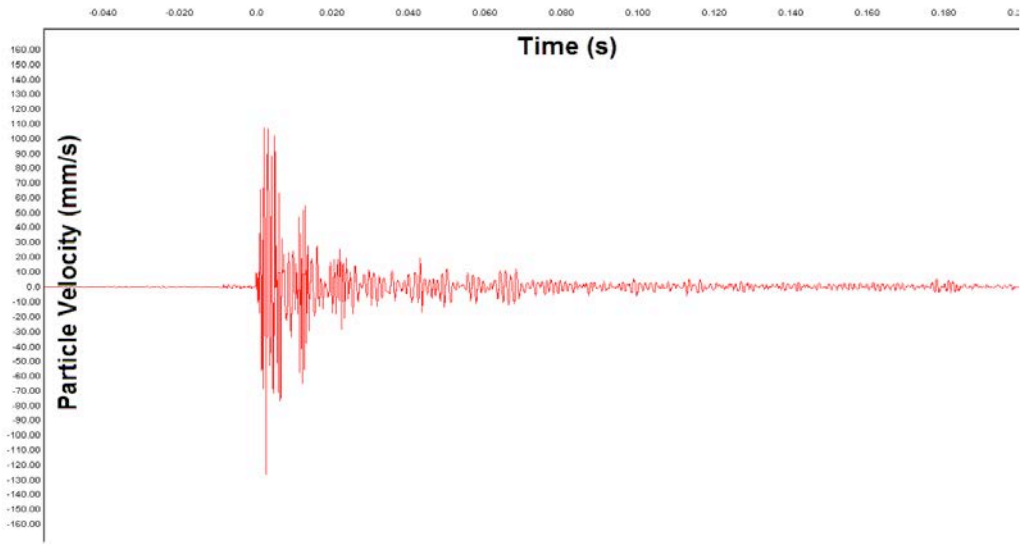

Figure 3.18 Isolated seismic waveform

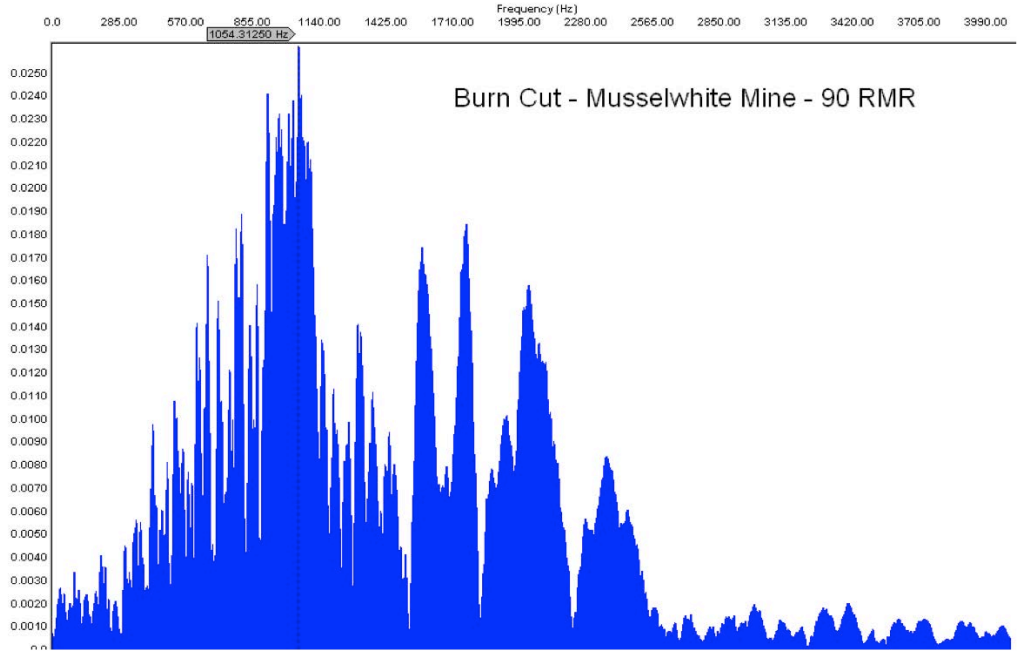

Figure 3.19 Frequency content for burn cut blasthole

A number of examples regarding the frequency content obtained for various experiments performed on the information gathered can be found in Appendix B – Particle Velocity and Frequency Content - Case Studies. There, the frequency content of an isolated waveform compared to the frequency content of the entire blast, the frequency content of the blast compared to the quiet portion in between blast records, is shown. Also, the

frequency content of an original waveform compared to the frequency content of various filtered waveforms using the smoothing function, which averages successive particle velocity records using a moving box, used to decrease the standard deviation of the original waveform, can be found in Appendix B as well. Also, the frequency content of the waveforms of a number of successive blastholes given by their respective delay number, and the frequency content for the same blasthole measured from different geophone locations at increasingly longer distances from the blast, is included.

3.4.5 Overbreak Assessments – Scanner Profiles

Overbreak (as defined for this specific research), consists of the average thickness of excess rock, for one section of a blasted round, beyond its design perimeter. Figure 3.20 shows the planned profile, the final profile, and the estimated average thickness of overbreak/underbreak, for a single section of the drift.

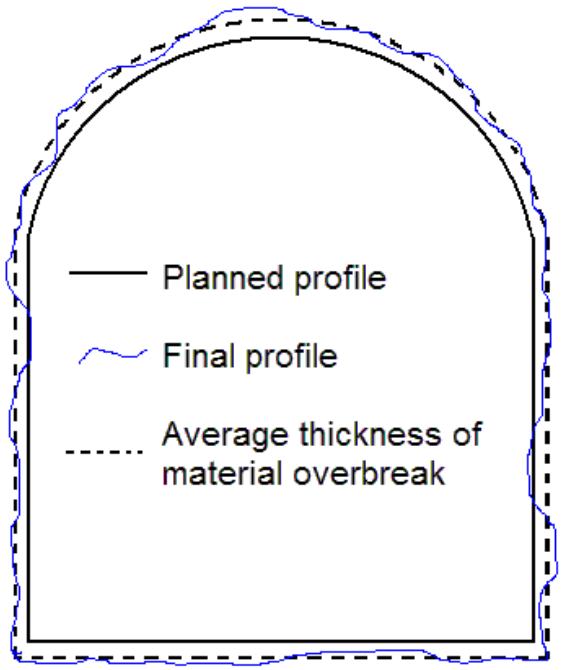

Figure 3.20 Planned or as-built profile against final profile

The average overbreak/underbreak comprises a number of sections of measurements of overbreak/underbreak as depicted in Figure 3.21.

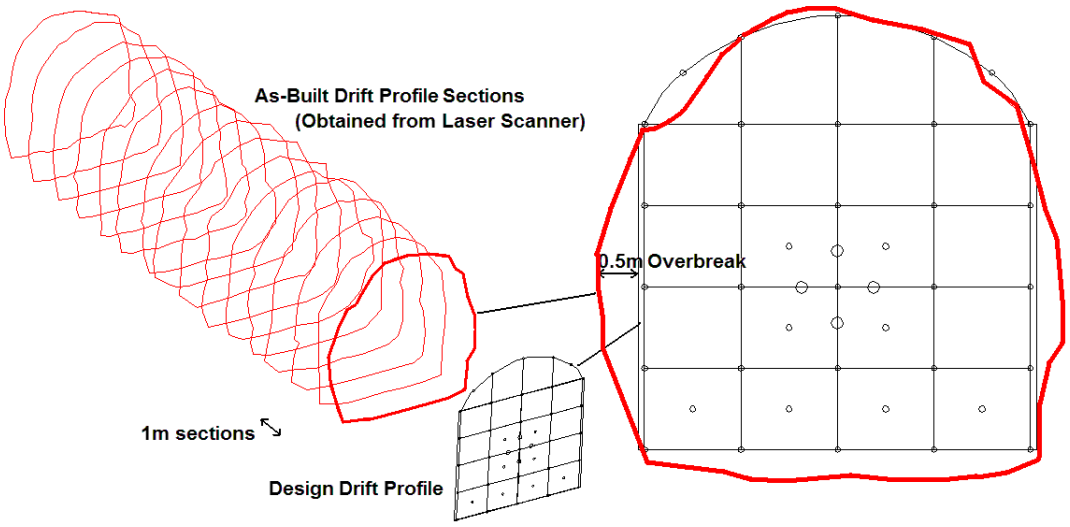

Figure 3.21 Average overbreak measurement over an entire blasted round section

To calculate overbreak values, a series of three-dimensional digital profiles were generated utilizing a laser scanner computerized surveying unit (Leica™ Geosystems HDS 3000® (Figure 3.22)) of the family of *LIDAR* systems. *LIDAR* stands for Light Detection and Ranging.

Figure 3.22 Leica™ HDS3000® laser scanner

This *LIDAR* unit can not only obtain a three-dimensional point cloud image with the actual size and shape of the volume being surveyed, but also detect and record different colorations of the surfaces, depending on their reflective properties (when hit by the laser device), as shown in Figure 3.23. In this particular image, several features can be detected in great detail: the contour of the excavation, the welded mesh installed, a pool of water, and wood pieces in left lower corner of the drift.

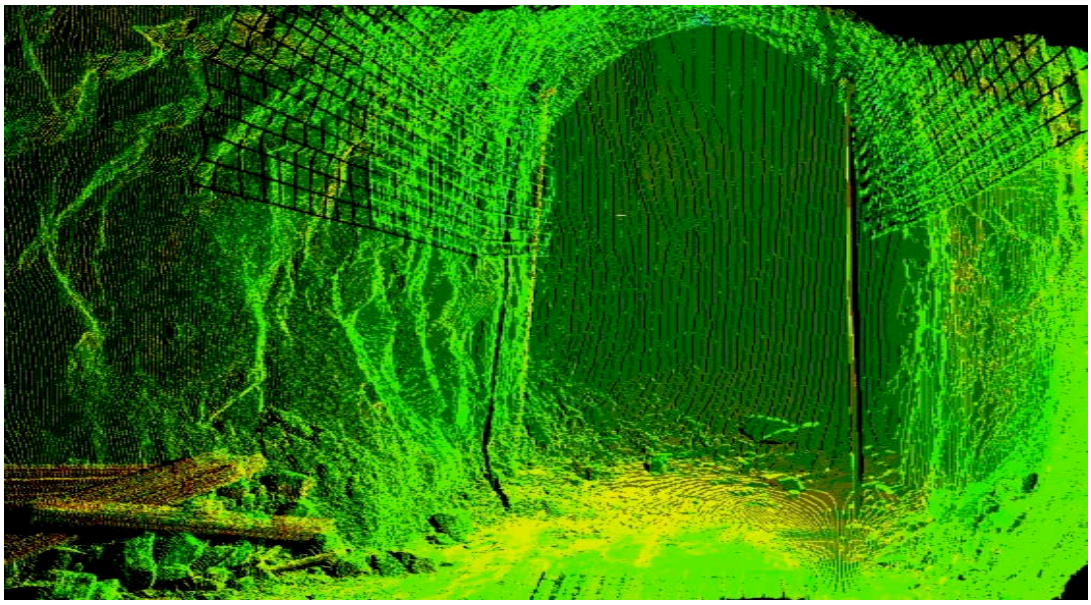

Figure 3.23 Laser scanned profile of a development drift

A less accurate technique was also employed in the absence of the *LIDAR* surveying system, by using a high-precision handheld laser distance meter. Readings were taken across the drift and the results were recorded manually.

3.4.6 Other Analysis of Field Data

Part of the whole field data collection process included photographing the face loaded with the explosives, prior to blasting, and marking the location of each blasthole in the round with the detonator delay numbers. These numbers were subsequently superimposed to the loaded face to track changes to the original design, as shown in Figure 3.24. This helped reconcile the delay numbers and the different explosives loaded within the same round, e.g., *ANFO* for production holes, Dyno Split D® for perimeter holes, and Dyno AP® for lifter holes.

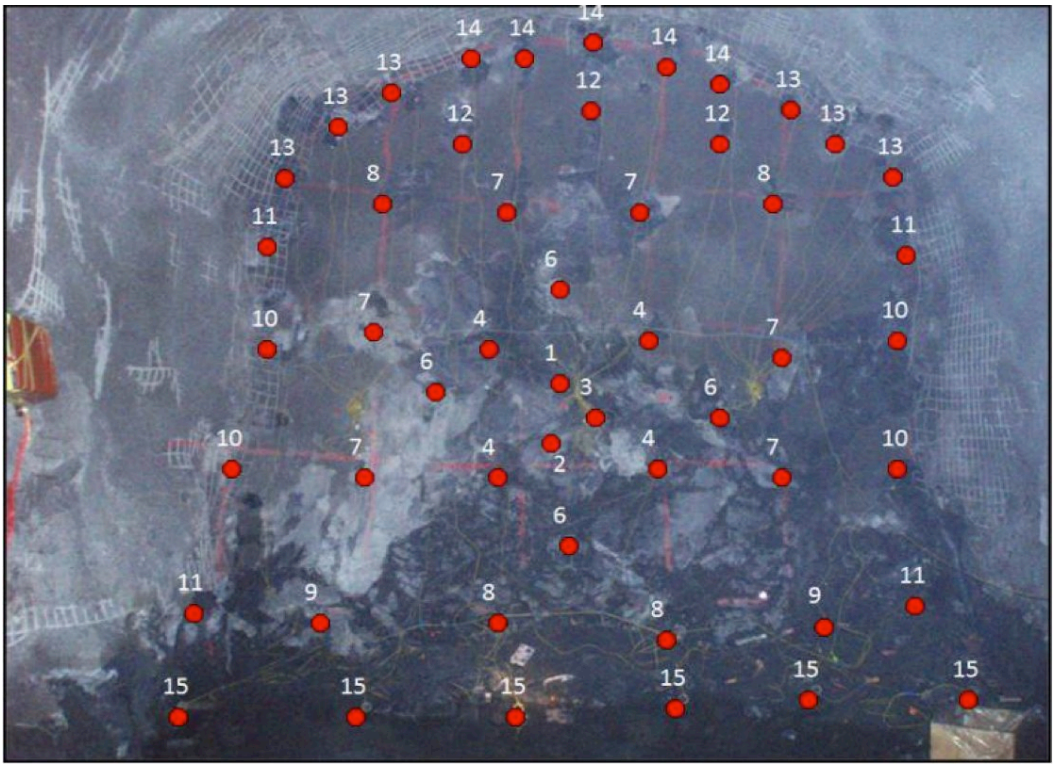

Figure 3.24 Picture of the face showing dimensions and blasthole long period delay number

3.4.7 Structural Mapping

The equal area Schmidt stereonet projection shown in Figure 3.25 was obtained using Rocscience™ Dips® software, from the records of dip and dip direction, of all major structures present in every cell mapped. The projection permits visualization and analysis of structures present, in order to examine the potential for wedge failures (which may raise safety concerns or increase the amount of overbreak material that is not in direct relation to the detonation process).

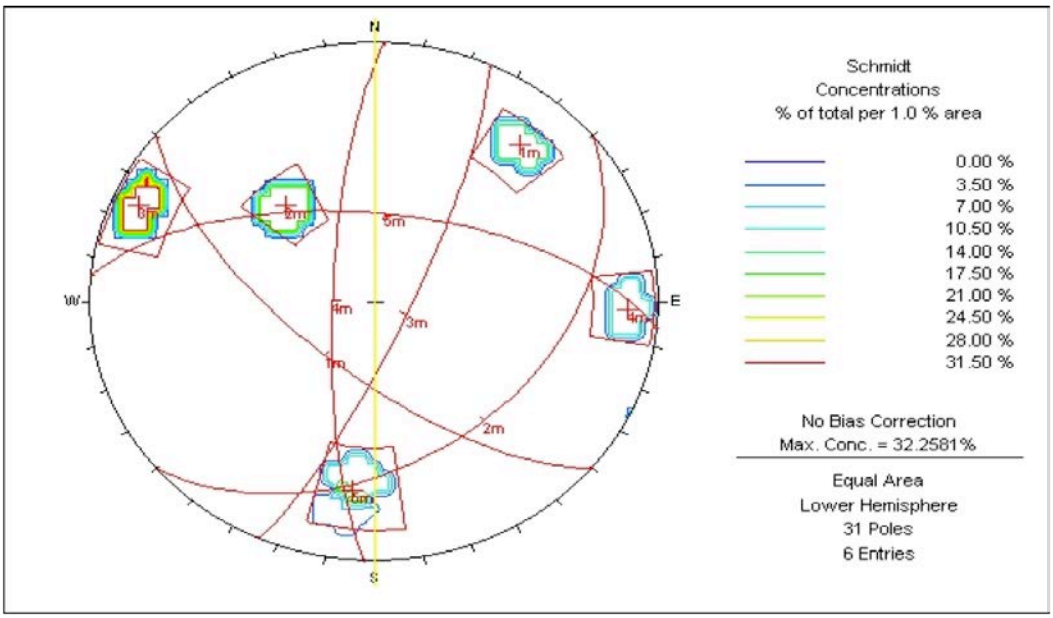

Figure 3.25 Representation of major structures on Schmidt stereonet

3.4.8 Detonator Delay Scatter

Figure 3.26 shows the measured scatter of the defined delay numbers of the explosive detonators. Zero cap delay scatter implies that the total weight of explosives fired with the same delay number should be numerically summed. Linear superposition of individual particle velocity waveforms would produce constructive interference, generating greater peak values versus peaks of blastholes fired independently of each other.

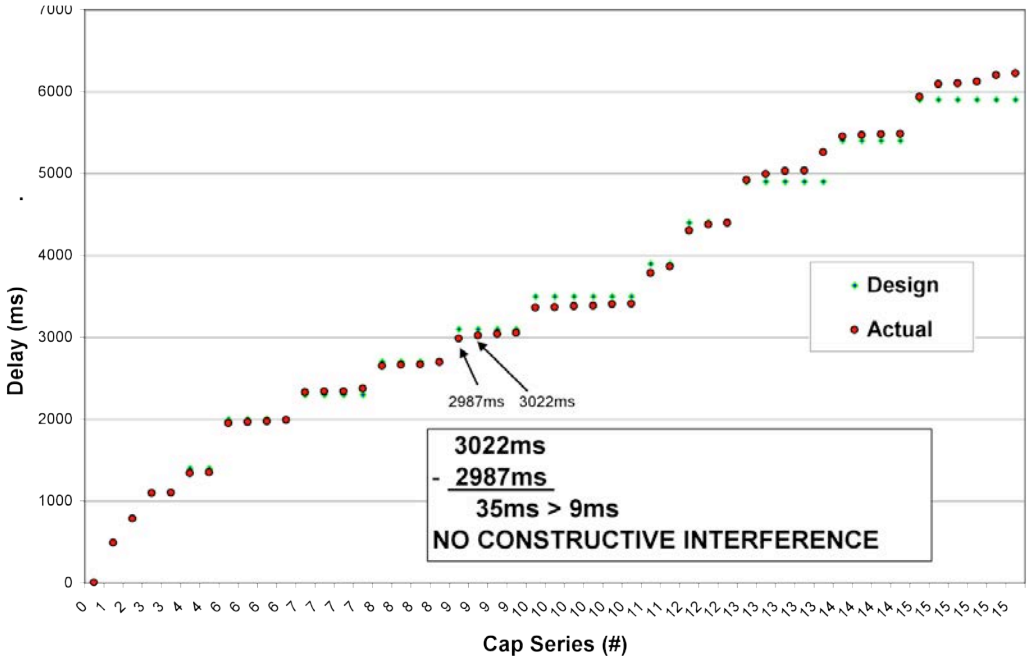

Figure 3.26 Long period cap delay scatter

Figure 3.27 shows a set of *PPV* versus *SD* measurements (D/Q^½), for one blasting round at the Turquoise Ridge JV mine. Geophones were installed at 3.5m, 6.0m, and 15.0m from the face. The different explosives used for production holes (Dyno AP®) and perimeter back holes (Trimtex®) were then standardized with the relative weight strength to that of *ANFO*. From the *PPV* versus *SD* cloud of data points, graphed in Figure 3.27, the best-fit curve is obtained and the constants *K* and *n* are determined.

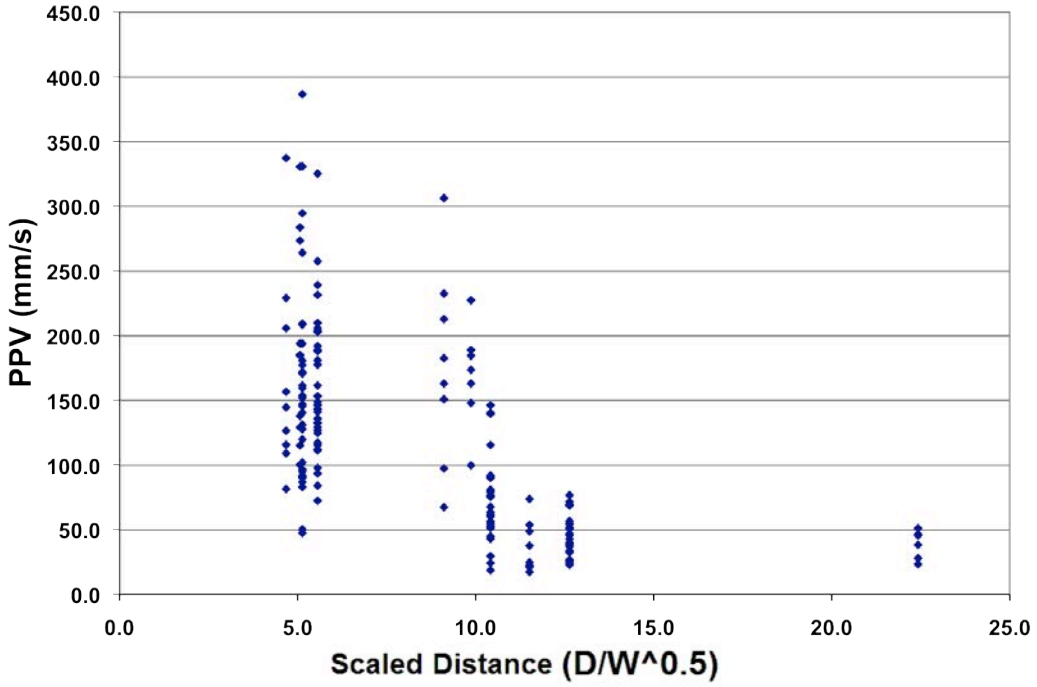

Figure 3.27 *PPV* versus *SD*

The large scatter of the cloud of data points is due to the fact that a single average distance, from the blasthole to the geophone, is used for all blastholes pertaining to the round, irrespective of their location to the different geophones installed. In the following chapters a different treatment will be used to calculate an approximate distance to each and every blasthole of the round, in an attempt to reduce this large scatter.

3.5 Limitations and Advantages of the Presented Empirical Data

There are a number of limitations in relation to the empirical data presented that are noteworthy. It is important though to highlight the fact that the data was obtained from measurements made at real underground operations and under real production conditions, that is, not from laboratory experiments (which can be repeated any number of times). The reader must understand that working with experiments as performed in a laboratory differs greatly from the process of taking measurements at the site. Also, due to the nature of the given rock mass, there could be huge variability in its behavior, making the analysis of the data thus gathered a much more complex procedure.

Due to cost constraints, a limited number of overbreak measurements were gathered from the four mine sites in question. From these, a strong correspondence among overbreak values, rock mass qualities, and *PPV* measurements was established. More measurements should naturally confirm this to a higher degree of certainty. As it stands, the finding is that the higher the rock mass quality, the higher the *PPV* recorded, and at the same time, the lower the measured overbreak.

For two of the four sites, a handheld laser distance meter was used when the *LIDAR* was not available which would have produced much greater accuracy of overbreak measurements.

The high frequency geophones used cover only the intermediate to high frequency range (28Hz – 1000Hz) leaving out the low frequency range (<28Hz), where a portion of the overall *PPV* would be expected to be encountered. Future research should, if possible, utilize two geophones installed in the same location to record a much wider range of frequencies.

The *RMR* and *Q* values were provided using the original versions of these rock mass classification systems (that is, not the updated versions). The reason for this is that they are simpler than current versions of these systems which makes comparison with other classification systems easier, provided that not just the ratings are given but a detailed description of the rock mass is included.

Rock damage and overbreak occurs relatively close to the explosive charge, normally at distances much closer than the nearest geophone is usually installed. Extrapolation of the recorded *PPV* versus *SD* curve, in order to obtain the potentially damage-inducing *PPV* levels, is therefore typically performed. In an effort to overcome this particular and very common limitation, geophones were installed very close to the explosive charge, which reduced the amount of extrapolation needed for the best-fit curve, thus limiting the error of the estimated *PPV*.

4 CASE STUDIES

4.1 Introduction

A total of five underground mines located in North America were investigated and development round blasts were monitored and assessed as previously specified.

The purpose of the field investigation was to monitor the blast rounds, characterize the rock mass quality (using *RMR* and *Q* geomechanical classification systems) and assess blast induced overbreak (using laser scanning profiles or handheld laser distance meter measurements).

Table 4.1 shows the mines site visited as part of the data gathering process.

Table 4.1 Mine site case studies

Mine	Location	Company	Dates
Stillwater	Montana, USA	Stillwater Mining Co.	July 16 – 21, 2006
Stillwater	Montana, USA	Stillwater Mining Co.	Sep 10 – 15, 2006
Steer	Nevada, USA	Queenstake Resources Ltd.	Nov 5 – 11, 2006
Turquoise Ridge JV	Nevada, USA	Barrick - Gold Corp.	Mar 26 – 29, 2007
East Boulder	Montana, USA	Stillwater Mining Co.	Sep 18 – 21, 2007
Musselwhite	Ontario, Canada	Goldcorp Inc.	May 14 – 16, 2008

Table 4.2 shows the total number of *PPV* measurements available in each case, to derive the *PPV* versus *SD* relation and associated overbreak. The author would like to highlight the fact that in the East Boulder Mine investigation no useful data was gathered as mucking equipment destroyed one datalogger – with two geophones connected – and on the second datalogger, one of the connecting cables to the geophone was torn up by fly rock.

Table 4.2 Number of *PPV* measurements and average *RMR*

Mine	No. of *PPV* Measurements	Average *RMR*
Stillwater	350	65
Steer	189	35
Turquoise Ridge JV	109	55
East Boulder	0	60
Musselwhite	190	90
TOTAL	838	

Details of the geotechnical mapping done at each of the mine sites investigated can be found in Appendix A – Rock Mass Quality Logs.

4.2 Stillwater Mine – Montana USA

The J-M Reef ore deposit stretches 28 miles underground in southern Montana's Beartooth Mountain Range, USA. At the beginning of the 1970s the J-M Reef ore deposit was discovered. It is a 45 kilometer-long reef that belongs to the Stillwater Complex. The reef deposit consists of successive layers of ultramafic to mafic rocks, silicate minerals, and rocks rich in magnesium and iron. Platinum group metals (PGMs) such as platinum, palladium, and other precious metals are contained in the ore body.

Mining methods employed include sub level open stoping, captive cut and fill, and ramp accessed mechanized cut and fill methods.

Figure 4.1 shows a plan view of the 4400ft level heading monitored.

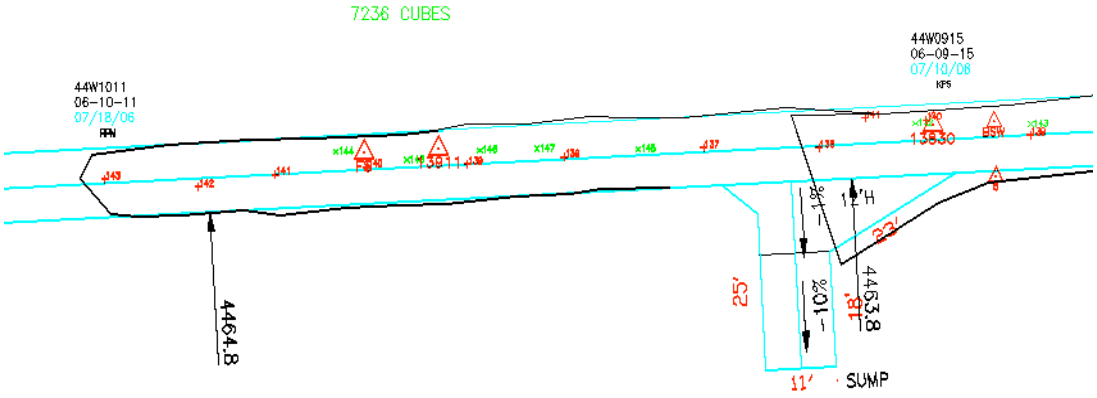

Figure 4.1 4400ft level heading – plan view – Stillwater Mine

4.2.1 Rock Mass Quality

The rock types at the Stillwater mine, considered to be medium to hard with average compressive strength in the order of 100MPa, consist principally of anorthosites, gabbros, norites and dunites.

The rock mass present in the monitored areas and the ground support (wire mesh and straps bolted with 0.9 m friction bolts with face plates for the upper corners of both walls and back) are shown in Figure 4.2, Figure 4.3, and Figure 4.4.

Figure 4.2 Typical 4400ft and 4700ft level headings – support installed – Stillwater Mine

Figure 4.3 4400ft level heading – blocky ground with support – Stillwater Mine

Figure 4.4 4400ft level headings – after-blast picture – Stillwater Mine

The average rock mass quality determined from the 4400ft and 4700ft drift levels (*Q* and *RMR*) is presented in Table 4.3 and Table 4.4, respectively. Similar rock characteristics were found at both levels. Rock mass tends to be very blocky where the excavation contour typically begins at a joint set face. Overbreak/underbreak is likely to be higher in this case. There are usually slight signs of stress build-up in the upper corners. Where the ground is less blocky, more massive and silicified, the blasted contour follows the planned profile more closely.

Table 4.3 Barton's *Q* index components – Stillwater Mine

Rock strength	100MPa
Block size (*RQD/Jn*)	7.60
Joint strength (*Jr/Ja*)	0.63
Jw/*SRF* (dry/low stress)	1.00
TOTAL	≈ 4.79

Table 4.4 Bieniawski's *RMR* ratings – Stillwater Mine

Rock Strength	R4	12
RQD	80%	15
Spacing	5cm-30cm	13
Joint condition	Tight-slightly open	15
Ground water	Dry	10
	RATING	≈ 65

The size of the 4400ft and 4700ft level drifts monitored were 3.0m wide by 3.5m tall with an arched back. The average length of each blasthole was 4.0m, of which 3.75m was loaded with explosives; no material was used as stemming. The total number of blastholes loaded was 42 with 6 relief holes, as depicted in Figure 4.5. Table 4.5 displays the explosive employed for the different blastholes used throughout the blast pattern and its weight relative to *ANFO*. The approximate blast efficiency (pull) is 92%, that is, blast depth advancement with respect to original planned blasthole depth.

Average overbreak was estimated to be about 0.20m.

Table 4.5 Summary of blasthole ID, explosive types and relative weights per blasthole – Stillwater Mine

Blasthole ID	Explosive Type	Weight Relative to *ANFO* (kg)
Lifters	Dyno AP	4.69
Back	Dynosplit D (22mm x 400mm)	3.72
Production	*ANFO*	6.00
Perimeter	*ANFO*	6.00

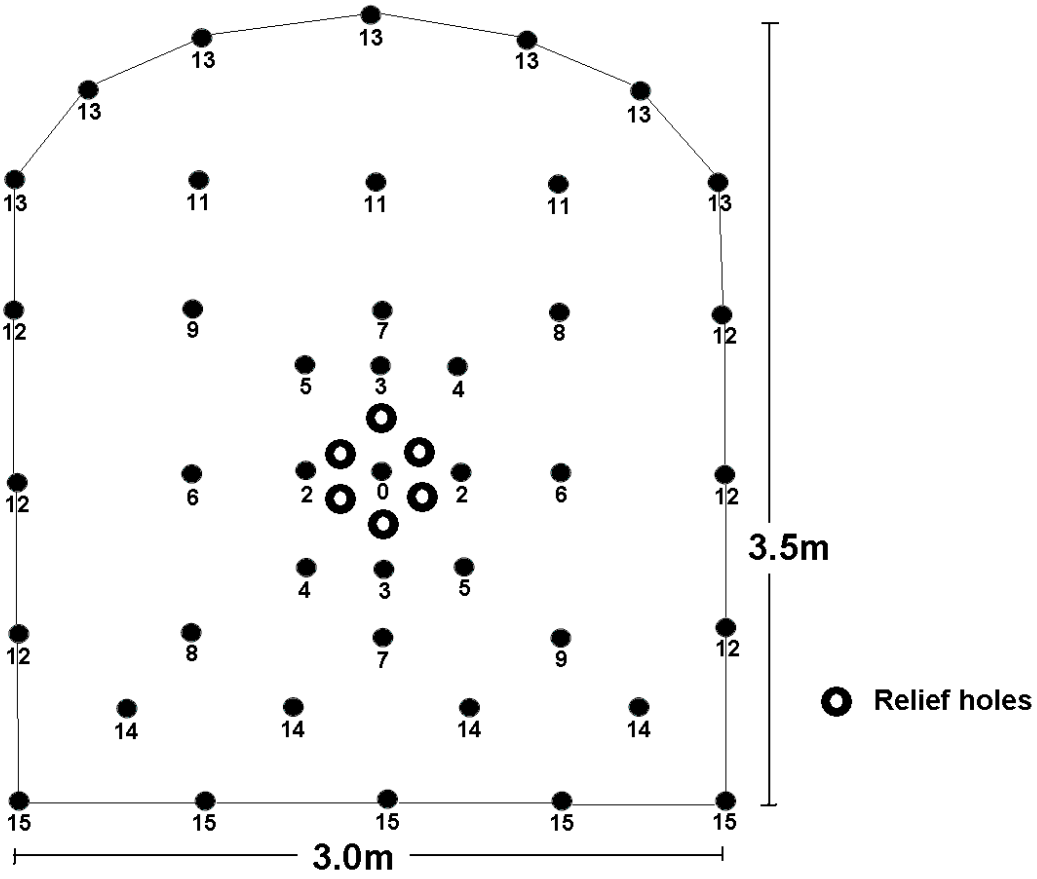

Figure 4.5 Typical 4400ft and 4700ft level headings – blast pattern – Stillwater Mine

Figure 4.6 shows the 3D profile of the excavation and blasthole projection at the 4400ft level.

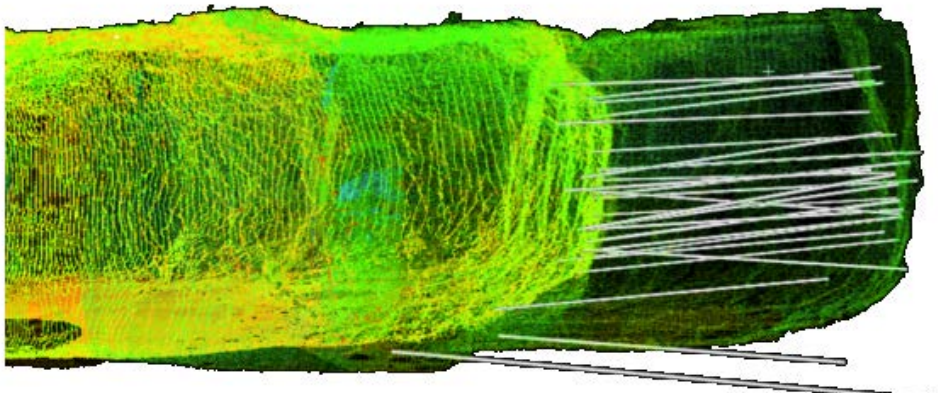

Figure 4.6 4400ft elevation heading – Laser scanned side view – SSX Mine

4.2.2 Vector Sum *PPV* and Frequency Content

A representative particle velocity record for the Stillwater Mine is presented in Figure 4.7.

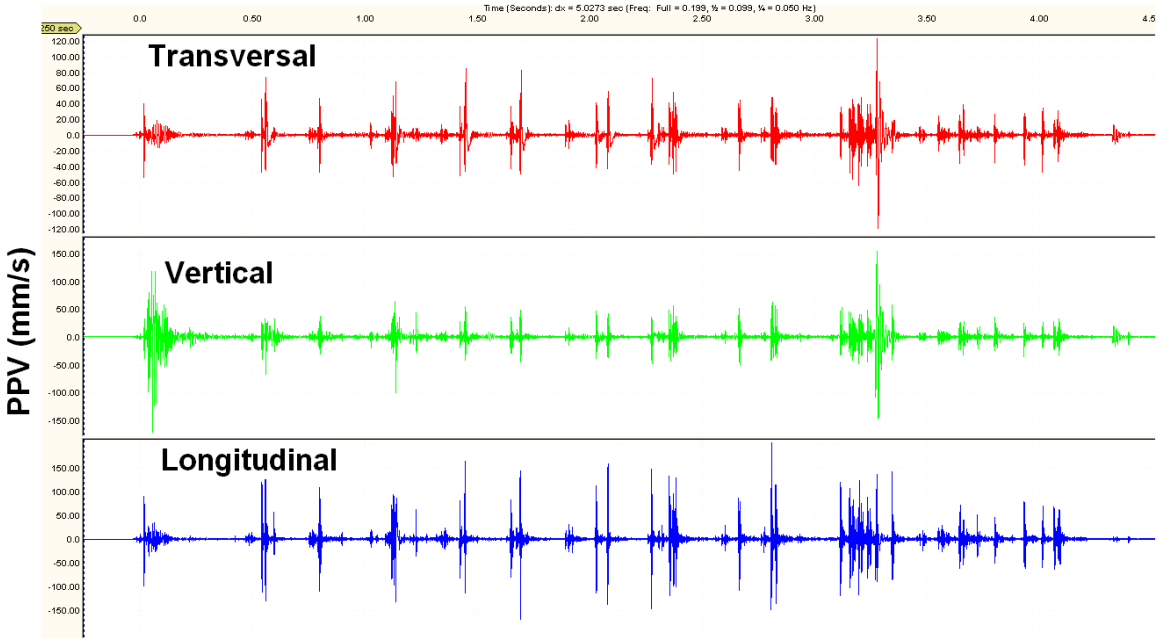

Figure 4.7 *PPV* versus time – Stillwater Mine

Figure 4.8 shows the vector sum of the *PPV* for multiple numbers of blasted rounds recorded on geophones installed in the 4400ft and 4700ft level drifts. The *PPV* values were recorded at *SD* values as low as 4.2m/kg^0.5 for all heading's blastholes and 1.1m/kg^0.5 for the nearest signature blasthole. The highest *PPV* value recorded was 450mm/s corresponding to a burn cut blasthole, and 930mm/s for a signature blasthole.

The seismic record used to determine frequency content was recorded at a sampling rate of 8192 records per second (this rate was a compromise between higher data recording versus memory available on the equipment).

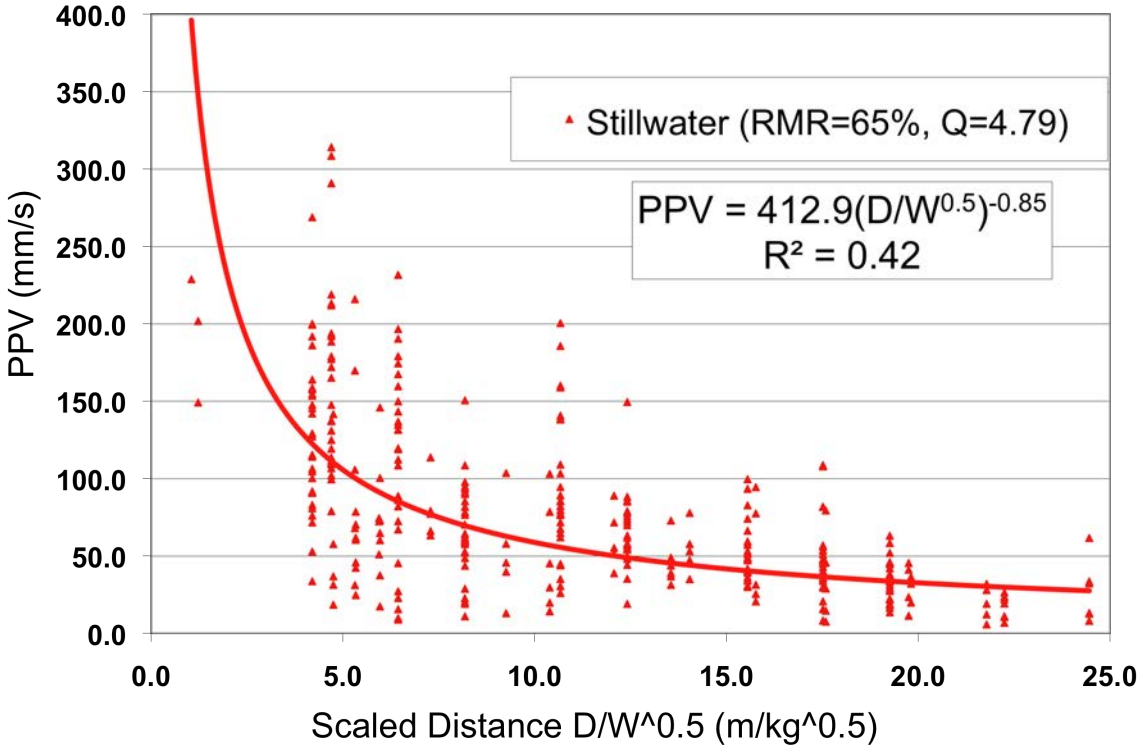

Figure 4.8 *PPV* versus *SD* values – Stillwater Mine

The *PPV* versus *SD* power law best-fit curve is estimated from 350 records:

$$PPV = 412.9 \cdot \left(\frac{D}{\sqrt{W}} \right)^{-0.85} \qquad \text{Eq. 37}$$

The 95% confidence line is shown in Figure 4.9. This additional curve includes at least 95% of the data points, which fall within or below this boundary. The additional boundary is obtained through the use of the standard error of the estimates applied to the provided data, subjected to a 95% confidence level.

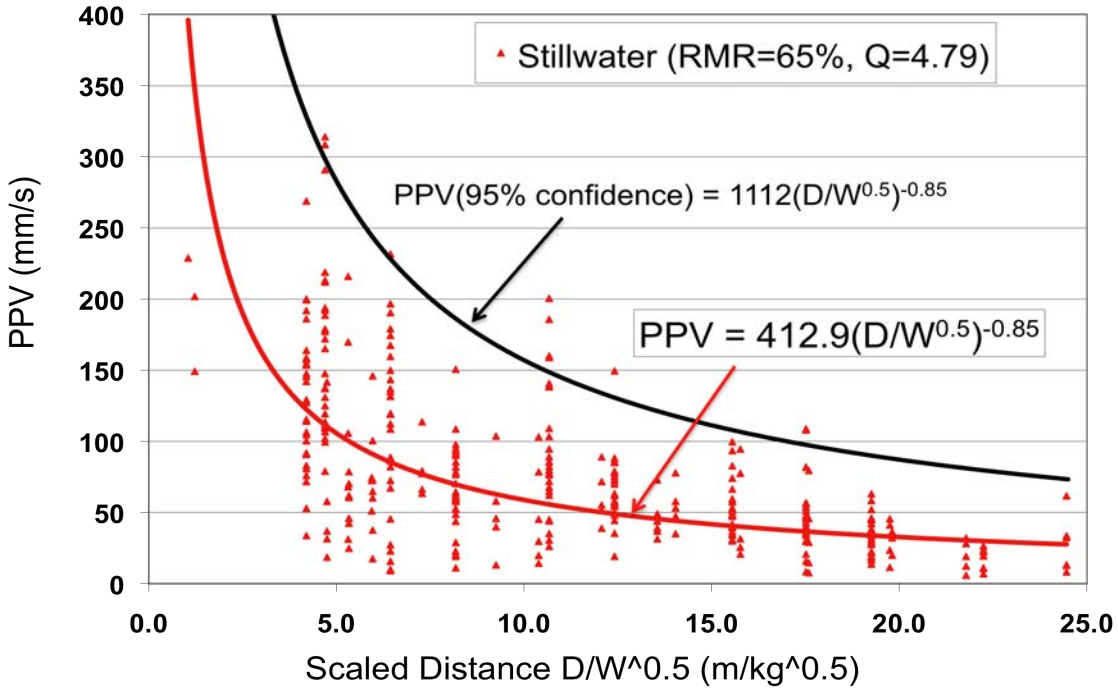

Figure 4.9 *PPV* versus *SD* boundary – 95% confidence level – Stillwater Mine

Figure 4.10 shows a characteristic frequency spectrum for a single burn cut blasthole where peak frequencies are close to 150Hz and nearly all predominant frequencies' decay occurred around 1100Hz.

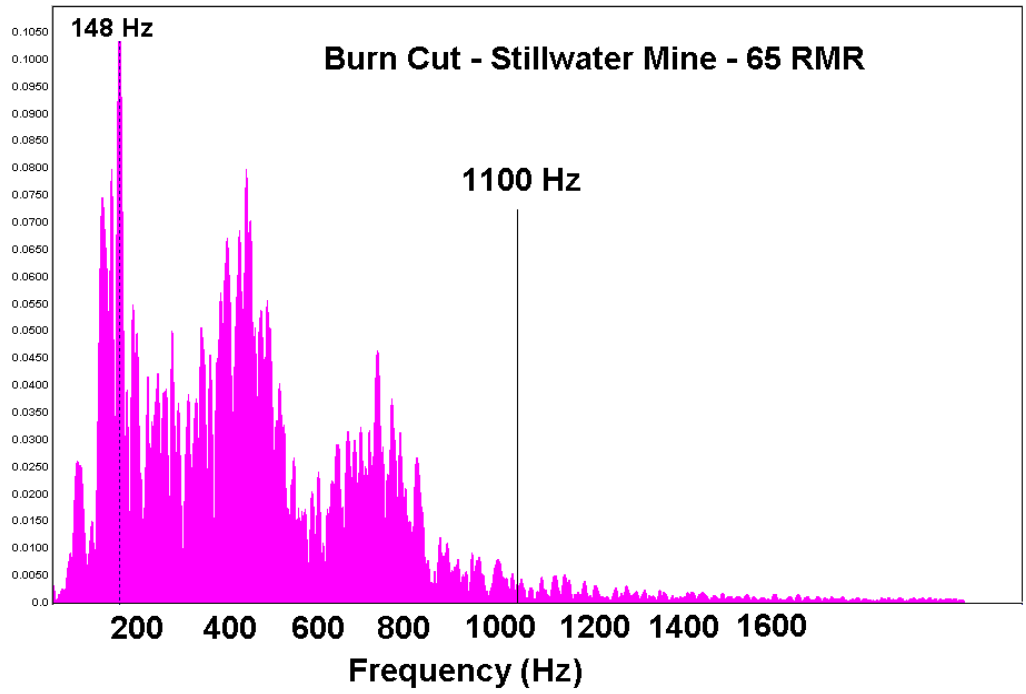

Figure 4.10 Frequency content – Stillwater Mine

4.3 SSX-Steer Mine – Nevada USA

Gold was discovered at the Jerritt Canyon District, Nevada, USA in 1972. Underground mining commenced in 1993 with the SSX-Steer Complex and the Smith mine. Since mining began, Jerritt Canyon has produced over 7 million ounces of gold. The Jerritt Canyon deposits are typical of the Carlin-type deposit of micron to submicron-sized gold particles hosted primarily by carbonaceous, Paleozoic calcareous, and sulfidic sedimentary rocks, and in intermediate to mafic intrusive rock. The SSX deposit formation is controlled by a network of structures running northwest and northeast.

Mining methods employed include conventional sublevel stoping, blind bench stoping, ramp bench stoping, and blind uphole stoping. Ground support typically uses friction rock bolts, welded mesh, and shotcrete, with cemented back-fill in mined-out areas.

4.3.1 Rock Mass Quality

The average rock mass quality *Q* and *RMR* determined from the studied area, zone 7-7170 cross-cut XC11 (see plan view in Figure 4.11), consisting of in-situ rock for the

right wall and face and cemented backfill for the left wall, are given in Table 4.6 and Table 4.7, respectively. The rock consists of black, fine-grained, carbonaceous limestone (Muntean and Henry, 2006). This limestone commonly comprises thin, wavy laminations and contains pods and lenses of black chert (silica mineral); Brecciation and veinlets, and stringers of white calcite, realgar (arsenic sulfide), and orpiment (arsenic sulfide) are typical. It is essentially a black mud, highly foliated, and weathered sedimentary rock (see Figure 4.12 and Figure 4.13). Ground support consists of 2.1m friction bolts with mesh.

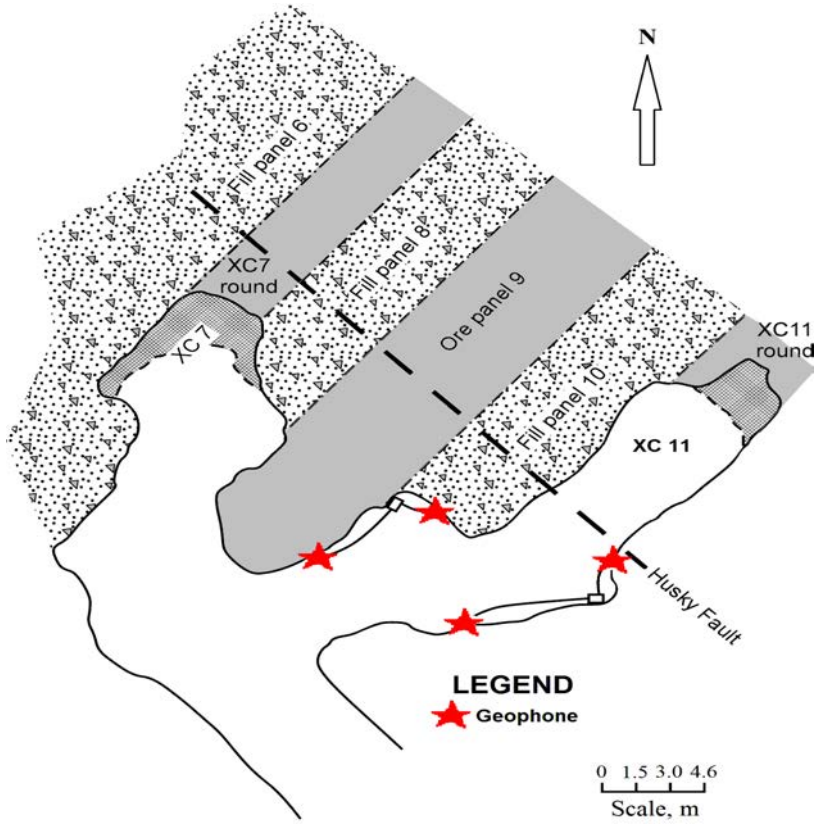

Figure 4.11 7170 cross cut XC11 level heading – plan view – SSX Mine

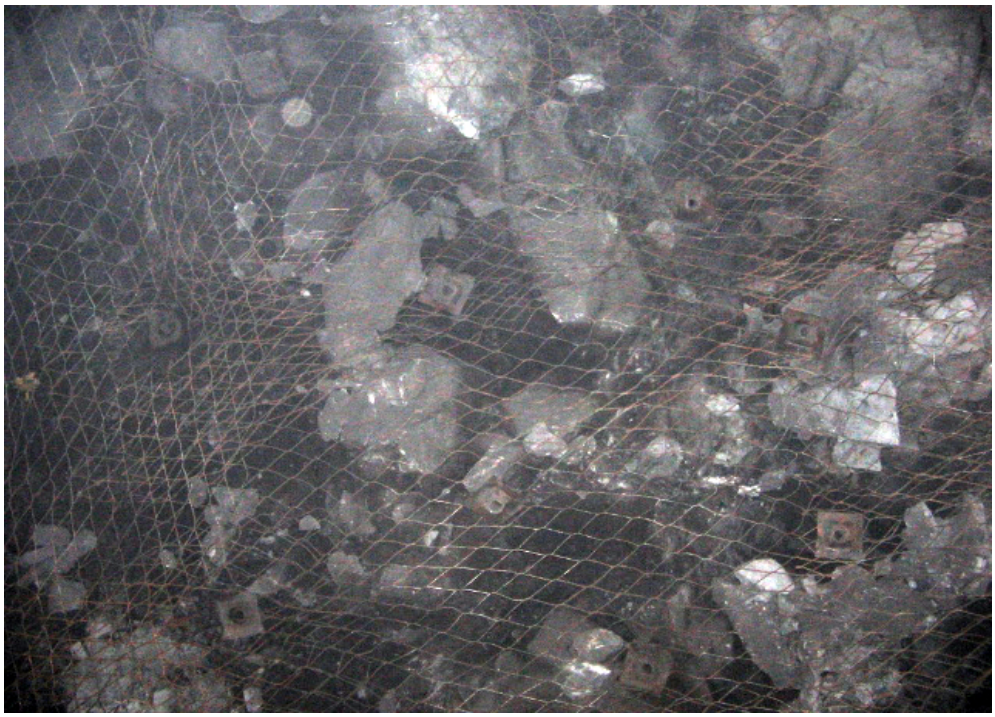

Figure 4.12 Rock mass appearance & support installed of right wall – SSX Mine

Figure 4.13 Rock mass appearance adjacent to zone under study – SSX Mine

Table 4.6 Barton's Q index components – SSX Mine

Rock strength	30-50MPa
Block size (*RQD/Jn*)	1.90
Joint strength (*Jr/Ja*)	0.16
Jw/*SRF* (dry/low stress)	1.00
TOTAL	0.30

Table 4.7 Bieniawski's *RMR* ratings – SSX Mine

Rock Strength	R2	5
RQD	20%-40%	8
Spacing	0.5-1.5cm+	5
Joint condition	Slightly open	9-6
Ground water	Dry	10
	RATING	37-33

The size of zone 7-7170 cross-cut XC11 drifts monitored was 4.3m wide by 4.3m tall. The average length of each blasthole was 3.7m, of which 3.4m was loaded with explosives; no material was used as stemming. The total number of blastholes loaded was 28 with 2 relief holes, and 15 unloaded holes, as depicted in Figure 4.14. Based on driller's experience, blast contour tends to finish within the unloaded holes (line drilling).

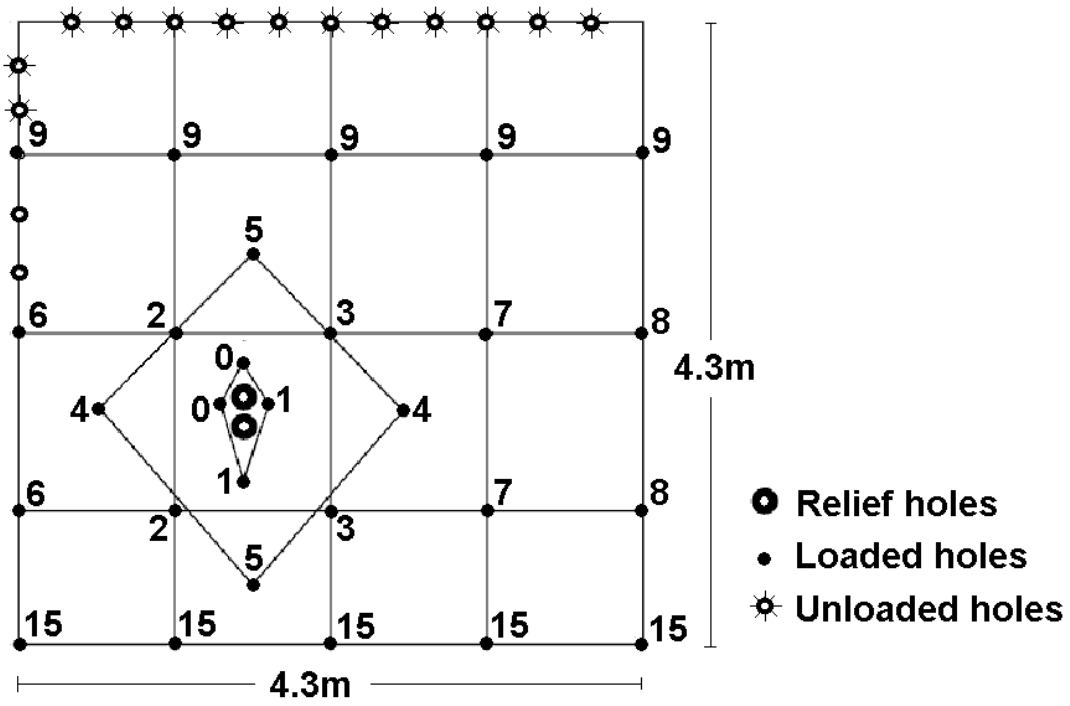

Figure 4.14 XC11 heading – blast pattern – SSX Mine

Blasted heading round resulted in overbreak of up to 1.5m deep on the upper right corner and an overbreak across the entire back of approximately 0.8m. Average overbreak was estimated to be in the order of 0.8m for the back and 0.35m for the walls. Figure 4.15 shows the 3D scanned contours of the XC11 heading viewed from the top (plan view).

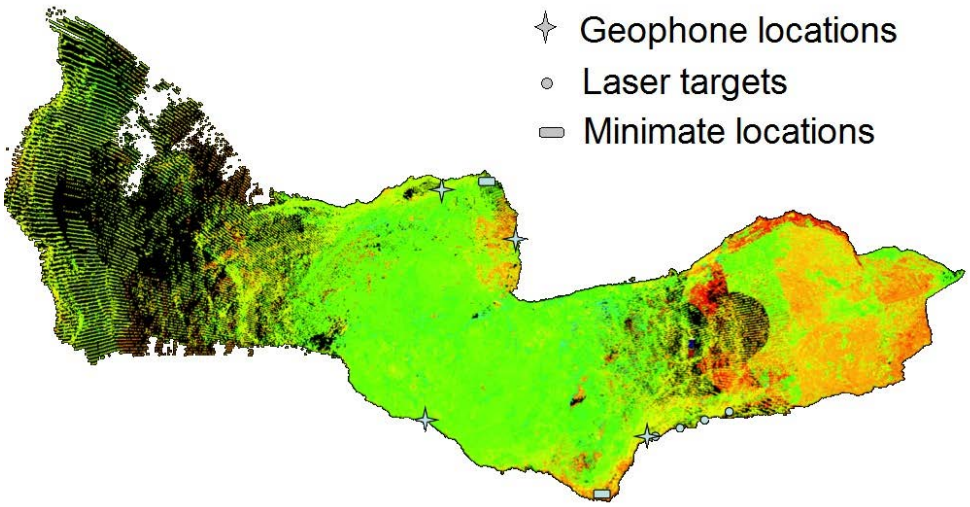

Figure 4.15 XC11 heading – Laser scanned view – SSX Mine

Table 4.8 displays the explosive employed for the different blastholes utilized throughout the blast pattern and its weight relative to *ANFO*. The approximate blast efficiency is in the order of 90%.

The diameters of the blast holes were 48mm, and the relief holes were 76mm. Holes in the back and left rib were line-drilled on 0.3m centers and were not loaded, as they were intended to limit the extent of the break. Dyno Nobel Unigel sticks were loaded into the lifters, while the remaining holes were loaded with *ANFO*.

Table 4.8 Summary of explosive ID, types and relative weights per blasthole – SSX Mine

Blasthole ID	Explosive Type	Weight Relative to *ANFO* (kg)
Lifters	Dyno Unigel (2.4m total)	3.56
Back	Unloaded	N/A
Production	*ANFO*	3.65
Perimeter	*ANFO*	3.65

The total number of blastholes loaded was 27 including 2 relief holes.

4.3.2 Vector Sum *PPV* and Frequency Content

A representative particle velocity record for the SSX Mine is presented in Figure 4.16.

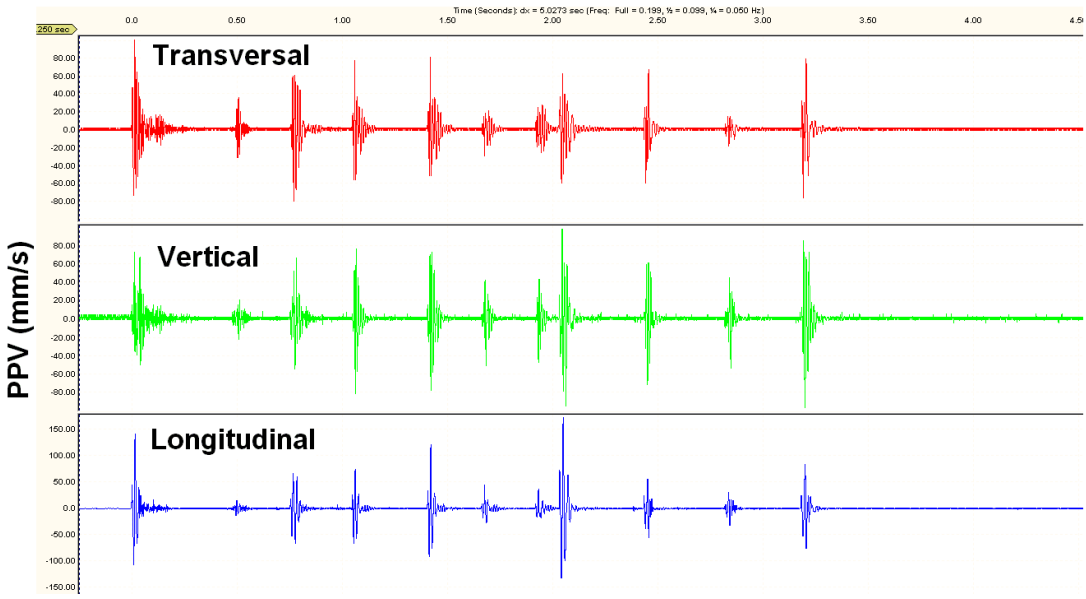

Figure 4.16 *PPV* versus time – SSX Mine

The graph in Figure 4.17 shows the vector sum of the *PPV* obtained only from geophones anchored on rock; data from geophones anchored on cemented backfill was not included in the analysis. The *PPV* values were recorded at *SD* values as low as 4.2m/kg^0.5. The highest value of *PPV* recorded was 185mm/s for a stoping blasthole.

The data loggers were set to record at a sampling rate of 8192 records per second.

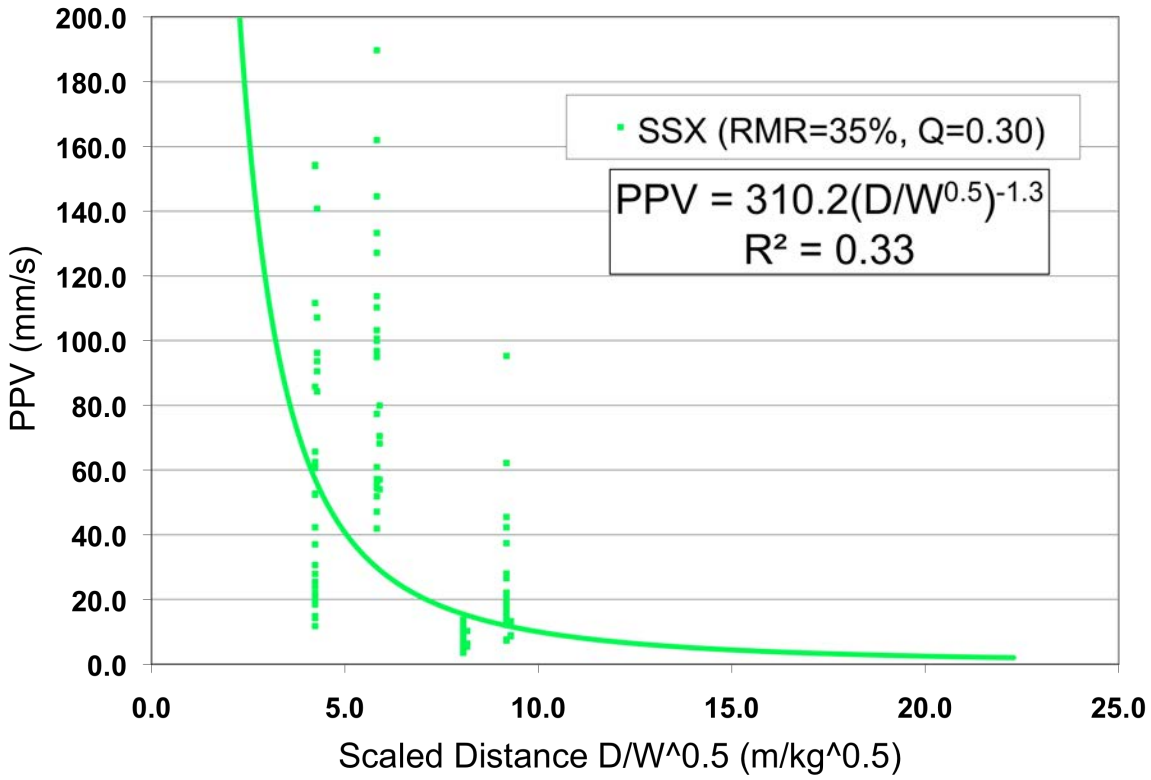

Figure 4.17 *PPV* versus *SD* values – SSX Mine

The *PPV* versus *SD* power law best-fit curve is estimated from 155 records:

$$PPV = 310.2 \cdot \left(\frac{D}{\sqrt{W}} \right)^{-1.3} \qquad \text{Eq. 38}$$

The 95% confidence line is shown in Figure 4.18.

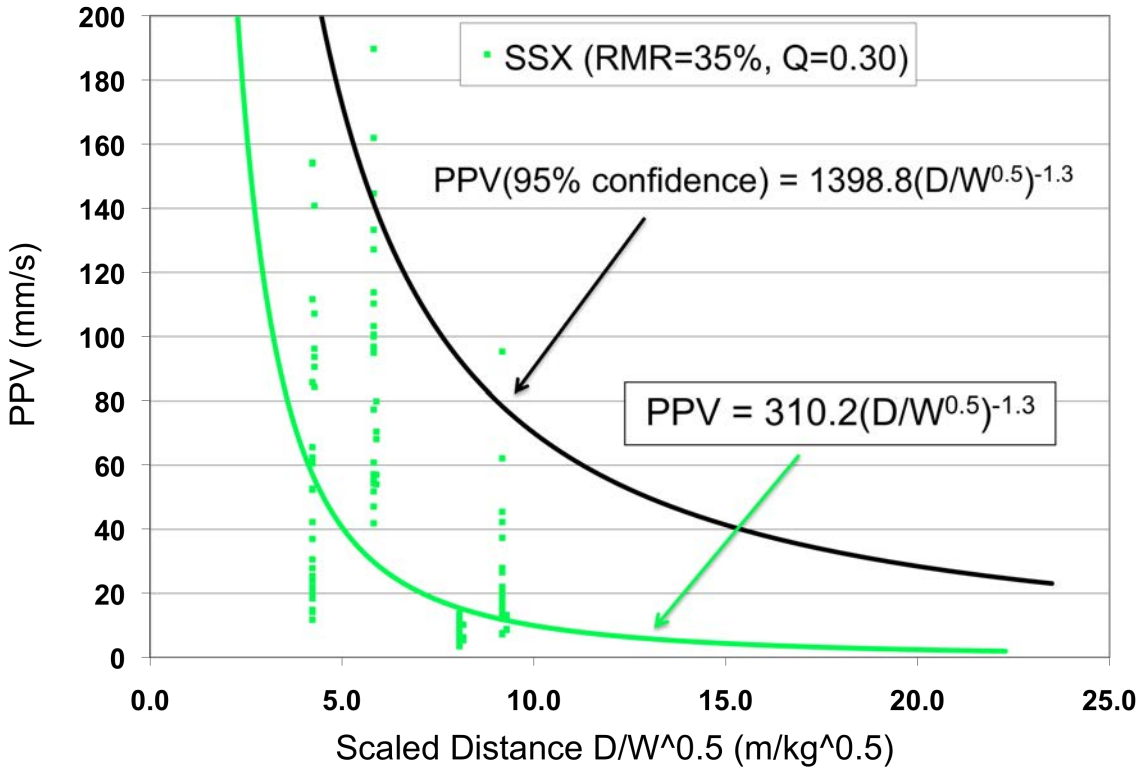

Figure 4.18 *PPV* versus *SD* boundary – 95% confidence level – SSX Mine

Figure 4.19 shows a distinct frequency spectrum for a single burn cut blasthole, where peak frequency is near 110Hz and nearly all predominant frequencies' decay occurred around 600Hz.

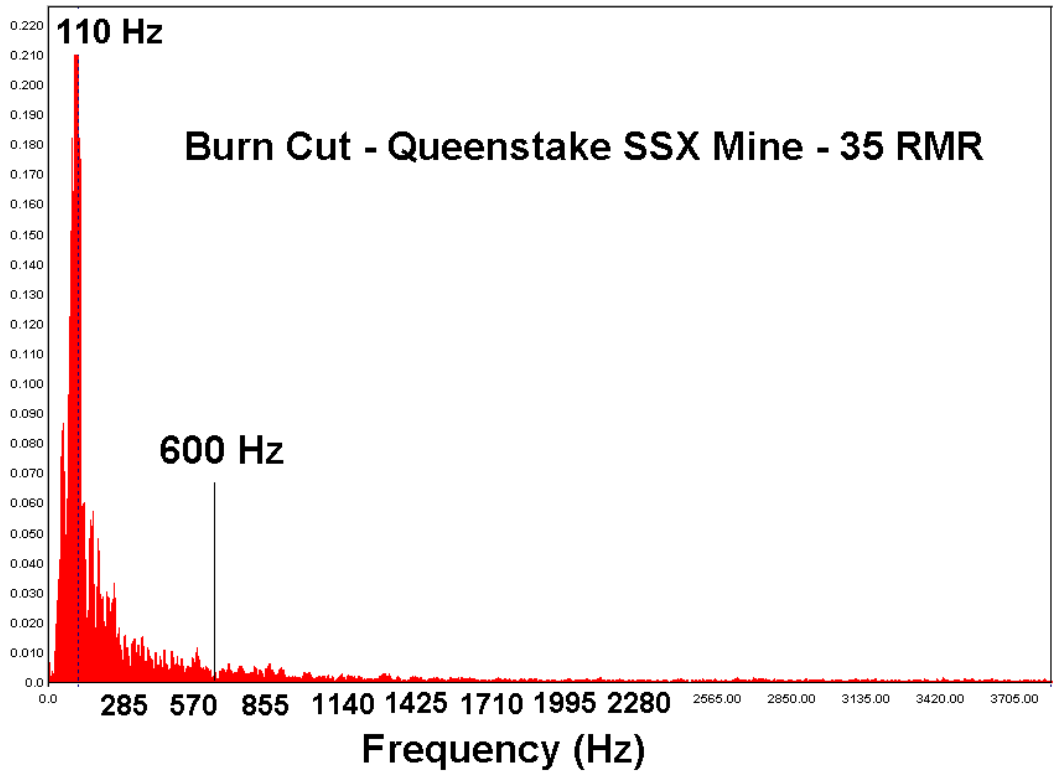

Figure 4.19 Frequency content – SSX Mine

4.4 Turquoise Ridge JV Mine – Nevada USA

The Turquoise Ridge joint venture Mine is located in Golconda, Humboldt County, Nevada, USA. Operations consist of an underground gold mine owned by Barrick. The Turquoise Ridge ore body was discovered in 1993 and mining began in 1998. The ore deposit is hosted in limy sediments with veinlets of graphite minerals intertwined with the host rock. Gold mineralization is found in the intersection of regional structural fabric and systematic regional structures.

The mining method employed at the Turquoise Ridge Mine is underhand cut and fill, due to the generally poor rock mass conditions. Ground support includes friction bolts with face plates, wire mesh, and shotcrete throughout the whole perimeter of the excavation.

4.4.1 Rock Mass Quality

The rock mass quality present at the 3471 development panel was only assessed at the face since previous round blasts were shotcreted. The *Q* and *RMR* values for the face and subsequently blasted round are shown in Table 4.9 and

Table 4.10, respectively. Figure 4.20 shows the plan view of the 3471 development panel.

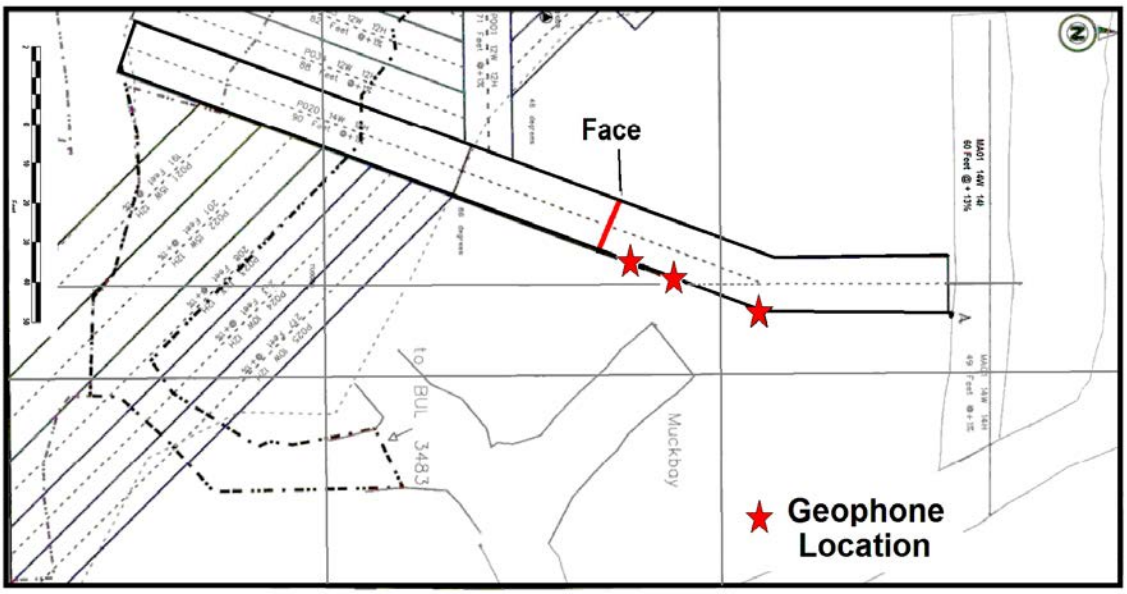

Figure 4.20 3471 development panel – plan view – Turquoise Ridge JV Mine

Figure 4.21 to Figure 4.23 show the characteristics of the rock and the support employed.

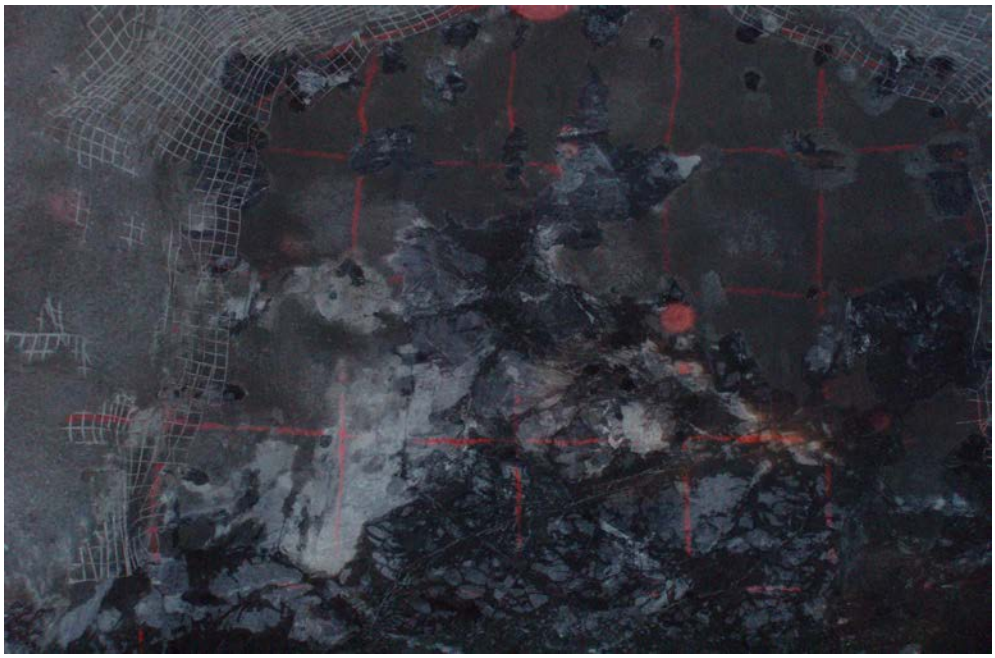

Figure 4.21 Rock mass at face and support – Turquoise Ridge JV Mine

Figure 4.22 Rock mass at upper corner – After-blast picture – Turquoise Ridge JV Mine

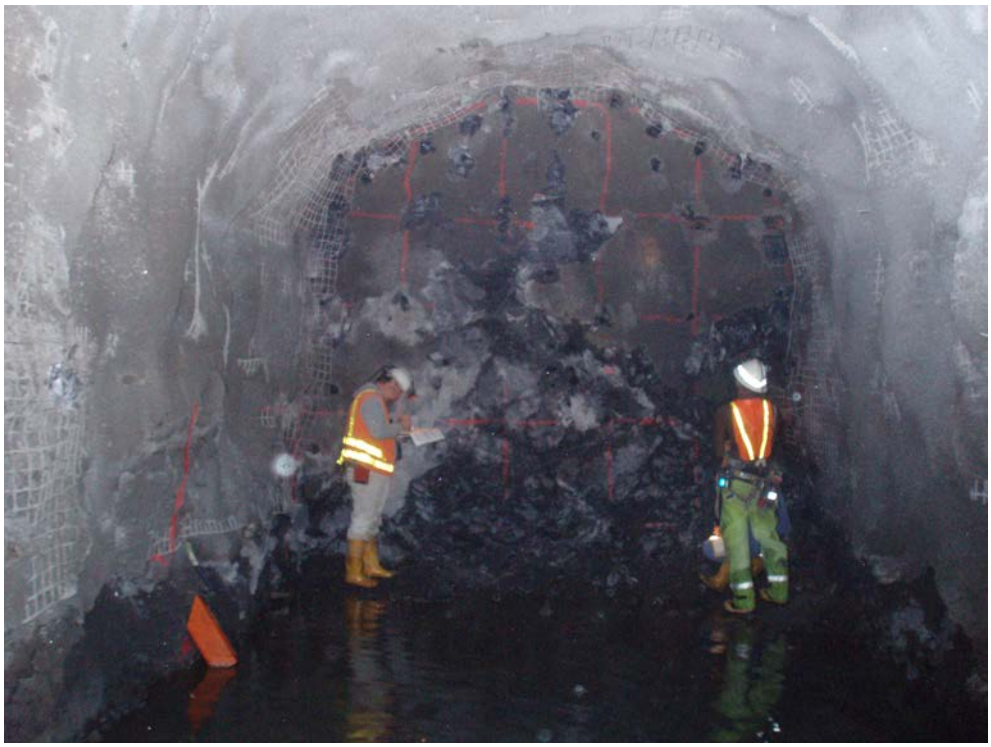

Figure 4.23 Shotcreted walls – Pre-blast picture – Turquoise Ridge JV Mine

Table 4.9 Barton's Q index components – Turquoise Ridge JV Mine

Rock strength	80-100MPa
Block size (*RQD/Jn*)	6.25
Joint strength (*Jr/Ja*)	0.50
Jw/SRF (dry/low stress)	1.00
TOTAL	3.13

Table 4.10 Bieniawski's *RMR* ratings – Turquoise Ridge JV Mine

Rock Strength	R3+	7
RQD	75+	13
Spacing	5-10cm+	10
Joint condition	Tight/slightly open	15
Ground water	Dry	10
	RATING	55

The size of the 3471 development panel monitored was 4.3m wide by 4.3m tall with arched back. The average length of each blasthole was 2.8m, of which approximately 2.5m was loaded with explosives; no material was used as stemming. Table 4.11 displays the explosive employed for the different blastholes utilized throughout the blast pattern and its weight relative to *ANFO*. The approximate blast efficiency is on the order of 93%.

Blasted heading round resulted in an estimated average overbreak of 0.25m.

Table 4.11 Summary of explosive ID, types and relative weights per blasthole – Turquoise Ridge JV Mine

Blasthole ID	Explosive Type	Weight Relative to *ANFO* (kg)
Lifters	Dyno AP™ (6 sticks)	3.05
Back	Trimtex (2 sticks) + Dyno AP (2 sticks)	1.42
Production	Dyno AP™ (6 sticks)	3.05
Perimeter	Dyno AP™ (6 sticks)	3.05

The total number of blastholes loaded was 49, including 2 relief holes for the burn cut. No stemming was used and only 35cm were left of unloaded blasthole length.

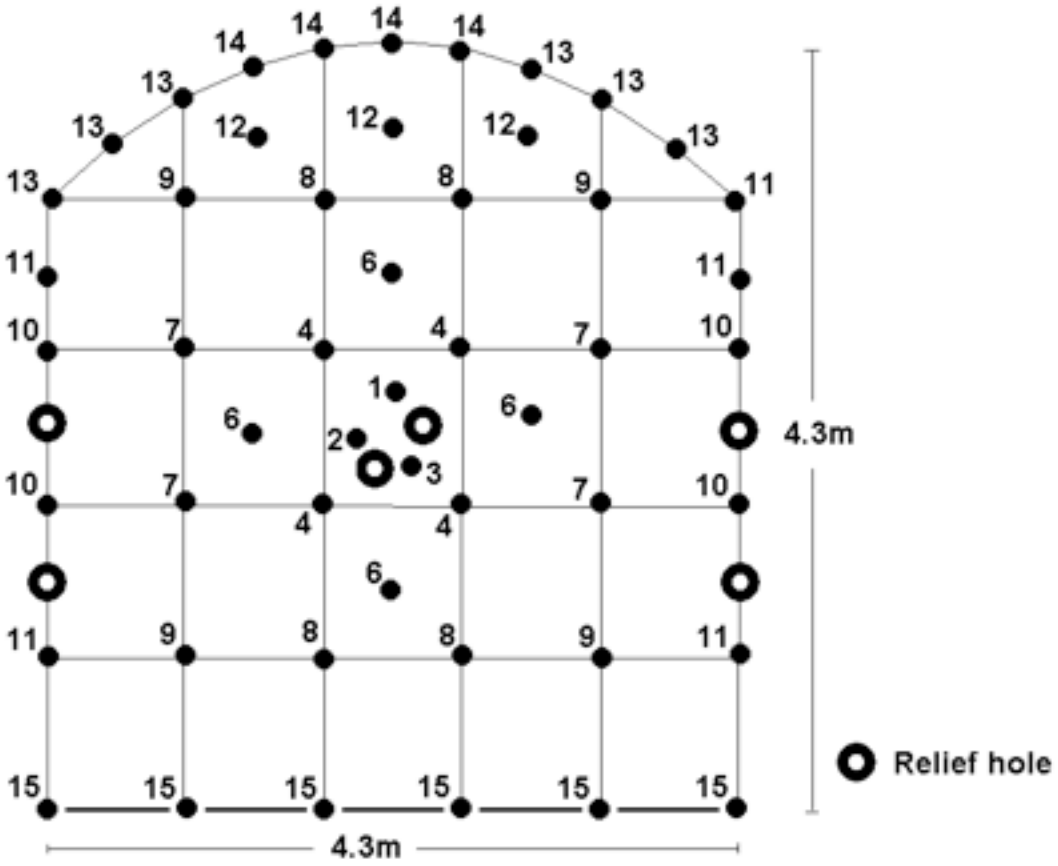

Figure 4.24 3471 development heading – blast pattern – Turquoise Ridge JV Mine

4.4.2 Vector Sum *PPV* and Frequency Content

A representative particle velocity record for the Turquoise Ridge JV Mine is presented in Figure 4.25.

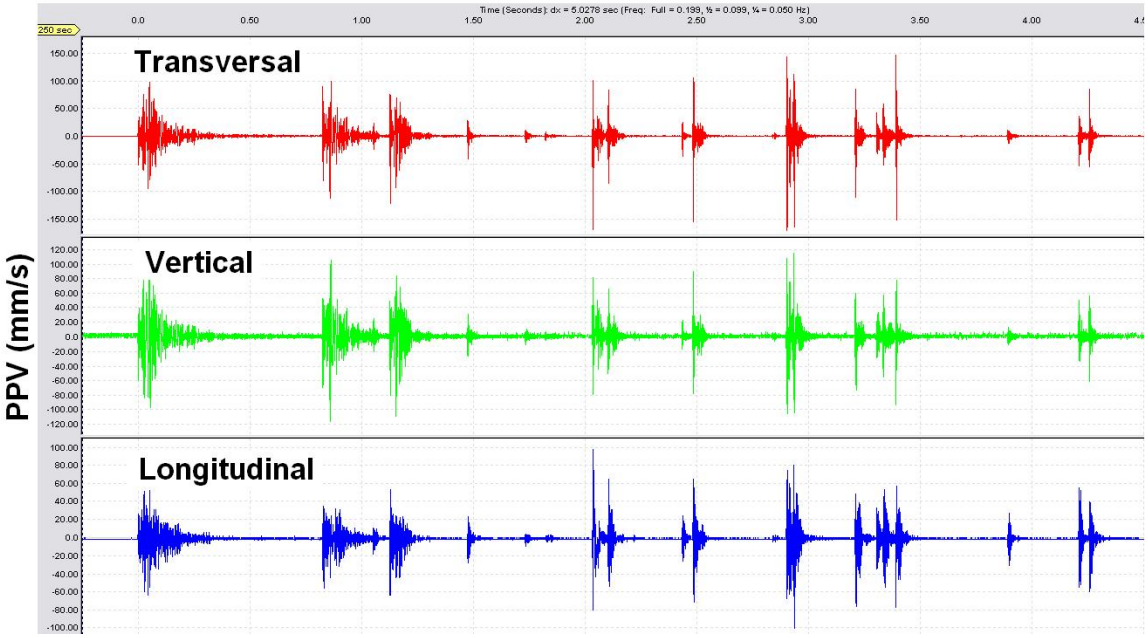

Figure 4.25 *PPV* versus time – Turquoise Ridge JV Mine

The graph in Figure 4.26 shows the vector sum of the *PPV* for one blasted round monitored with 3 geophones, installed on the ribs of the 3471 development panel. The *PPV* values were recorded at *SD* values as low as 2.8m/kg^½. The highest *PPV* recorded was 190mm/s, corresponding to a rib contour blasthole. Geophones were anchored at 3.5m, 8.0m, and 15.0m from the face, on shotcreted walls.

The data loggers were set to record at a sampling rate of 16384 records per second.

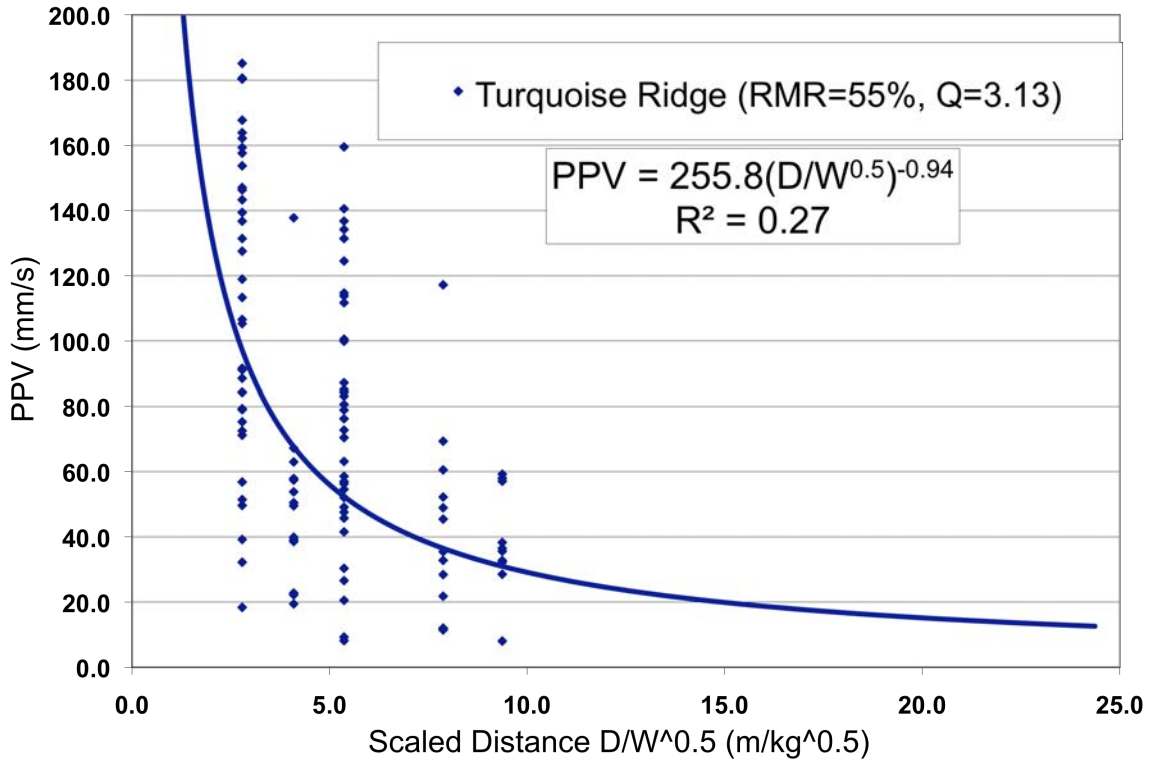

Figure 4.26 *PPV* versus *SD* values – Turquoise Ridge JV Mine

The *PPV* versus *SD* power law best-fit curve is estimated from 109 records:

$$PPV = 255.8 \cdot \left(\frac{D}{\sqrt{W}} \right)^{-0.94} \qquad \text{Eq. 39}$$

The 95% confidence line is shown in Figure 4.27.

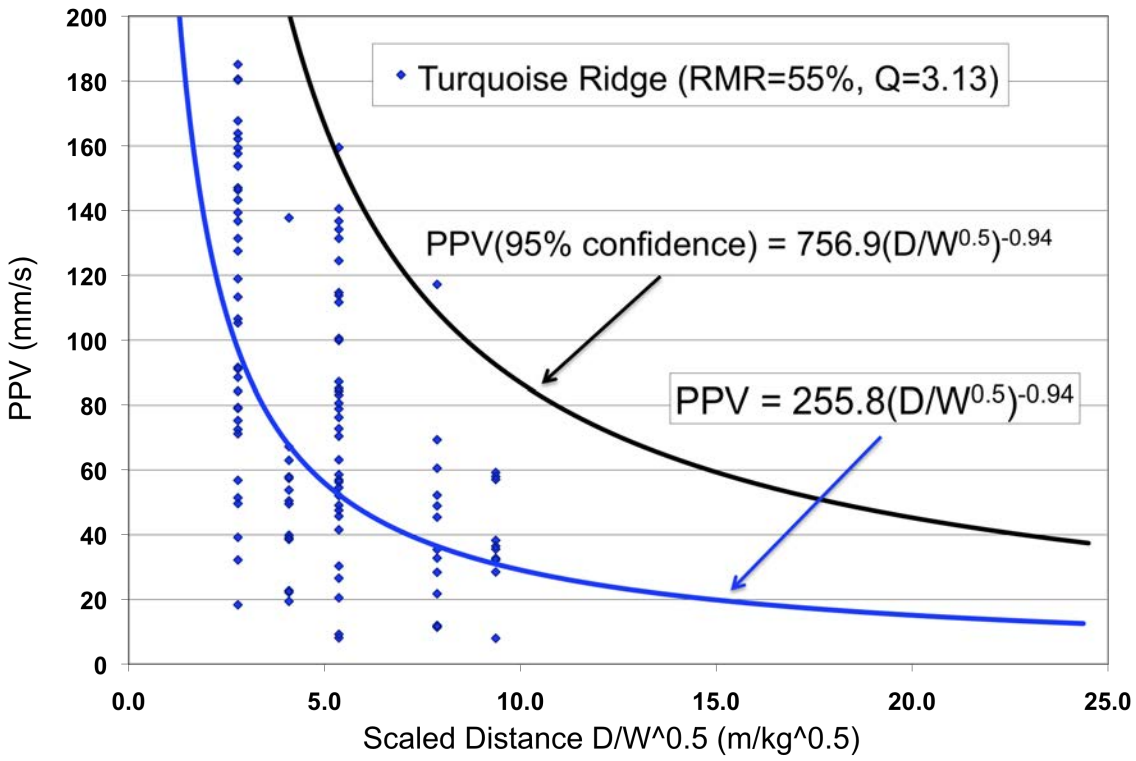

Figure 4.27 *PPV* versus *SD* boundary – 95% confidence level – Turquoise Ridge JV Mine

Figure 4.28 shows a distinct frequency spectrum for a single burn cut blasthole, recorded from the nearest geophone at 3.5m from the face, where frequency peaks near 370Hz, and nearly all predominant frequencies' decay occurred around 1250Hz.

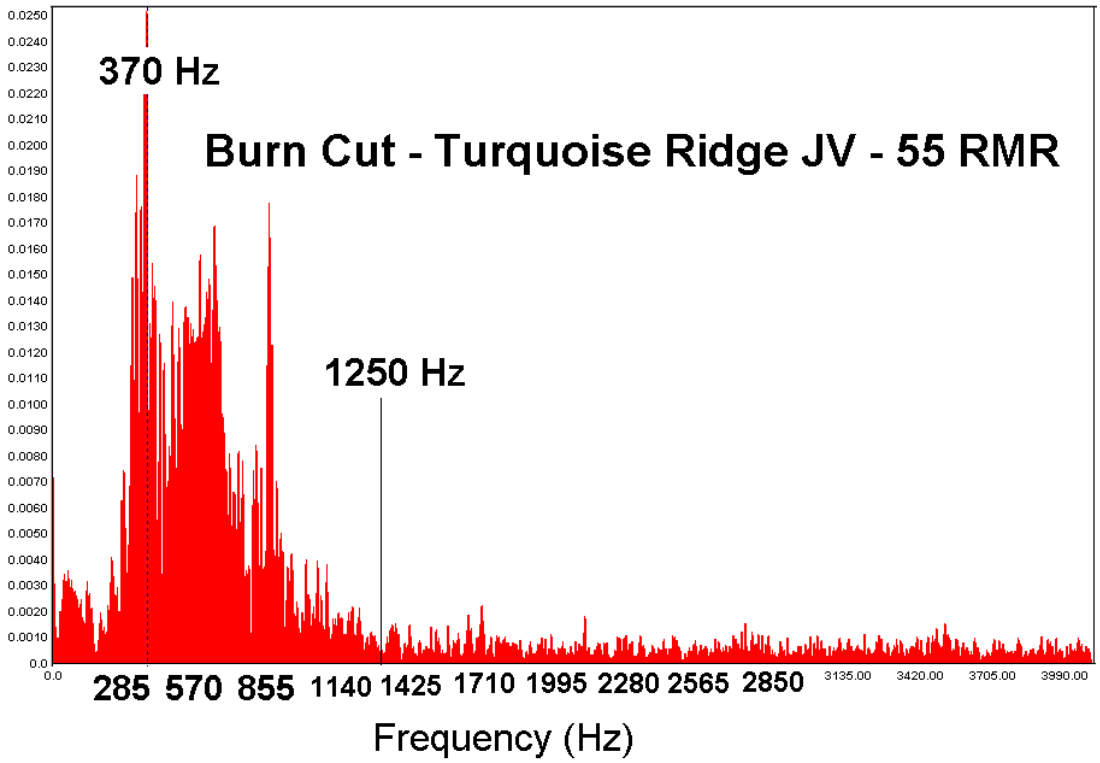

Figure 4.28 Frequency content – Turquoise Ridge JV Mine

4.5 Musselwhite Mine – Ontario Canada

Musselwhite Mine is a fly-in fly-out, 4,000 tons per day underground gold producer. The mine is located in Northwestern Ontario, Canada and is owned and operated by Goldcorp Canada Ltd. Gold mineralization is typically hosted in highly foliated – small scale – and folded metamorphic rock masses – larger scale – within oxide-silicates contained in banded iron formations.

Musselwhite utilizes sub level open stoping with delayed backfill, in particular the Avoca and transverse (primary/secondary) stoping methods. The area studied corresponds to 720L C Block East, 720 meters below surface.

4.5.1 Rock Mass Quality

Figure 4.29 shows the plan view of 720L C Block East and the geophone locations. By far, this is the best rock mass encountered during the field investigations (see Figure 4.30, Figure 4.31 and Figure 4.32). Table 4.12 and Table 4.13 show the average *Q* and *RMR*

values respectively for the back and walls of the area under study. Ground support consisted of 2.4m resin rebar rock bolts with mesh placed at the back and upper corners of both walls, as shown on Figure 4.32.

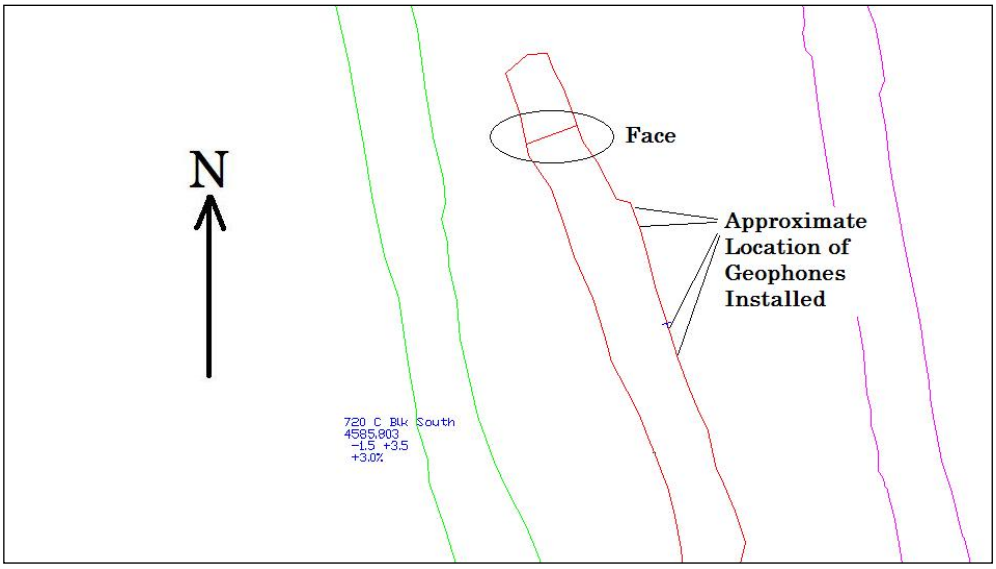

Figure 4.29 720L C Block East plan view – Musselwhite Mine

Figure 4.30 720L C Block East face and drill pattern – Musselwhite Mine

Figure 4.31 720L C Block East rock mass and rebar bolts pattern – Musselwhite Mine

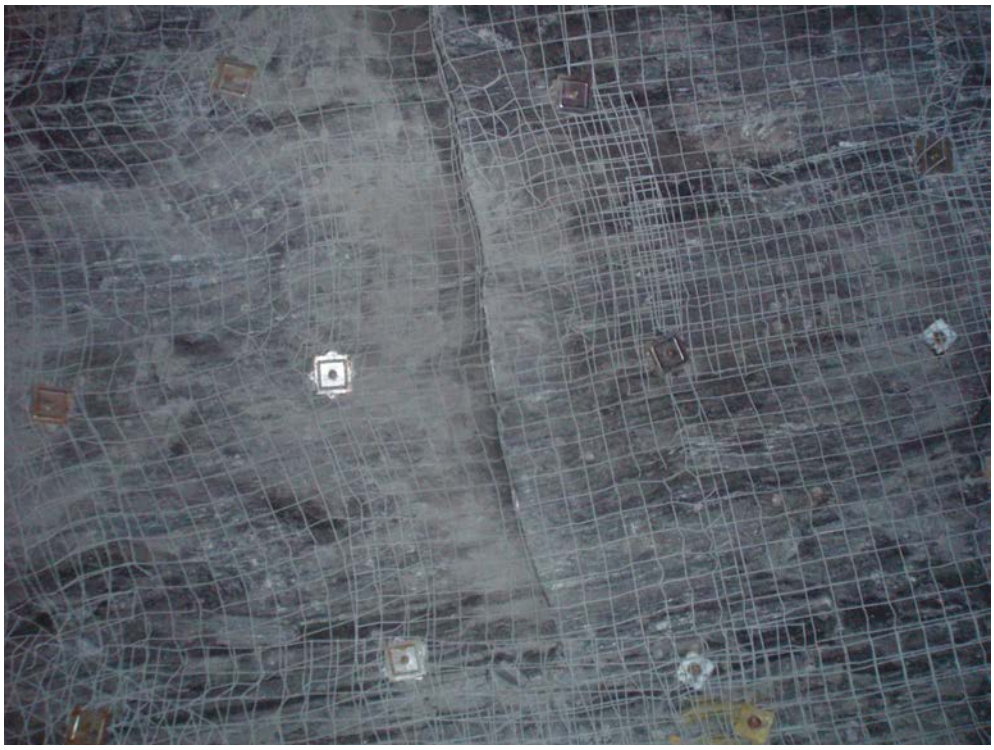

Figure 4.32 720L C Block East back support with rebar and mesh – Musselwhite Mine

Table 4.12 Barton's Q index components – Musselwhite Mine

Rock strength	100-150MPa
Block size (*RQD*/*Jn*)	45.00
Joint strength (*Jr*/*Ja*)	4.00
Jw/*SRF* (dry/low stress)	1.00
TOTAL	180.00

Table 4.13 Bieniawski's *RMR* ratings – Musselwhite Mine

Rock Strength	R4+	13
RQD	90+	20
Spacing	2m+	28
Joint condition	Tight	20
Ground water	Dry	10
	RATING	≈ 90

Manual measurements of overbreak were taken using a handheld laser distance meter and they approximately average 3.0cm, where the bulk of overbreak occurred in the upper corners of both walls. Five (5) complete half-barrels were present on the back of the drift (where the strong vertical foliation reduced the likelihood of half-barrels on the walls).

Table 4.14 shows the explosive used for each group of blastholes, its quantities in kilograms for each blasthole, and the equivalent quantities relative to *ANFO*. Values are based on a blasthole diameter of 1¾in (4.45cm) by 4.3m long, with 0.3m of unloaded blasthole at the collar.

Table 4.14 Summary of explosive ID, types and relative weights per blasthole – Musselwhite Mine

Blasthole ID	Explosive Type	Weight Relative to *ANFO* (kg)
Lifters	Dyno AP™ (4.0m total)	6.22
Back	SEC Detagel Presplit (22mm x 400mm)	1.64
Production	*ANFO*	5.17
Perimeter	*ANFO*	5.17

The total number of blastholes loaded was 59, including 5 relief holes.

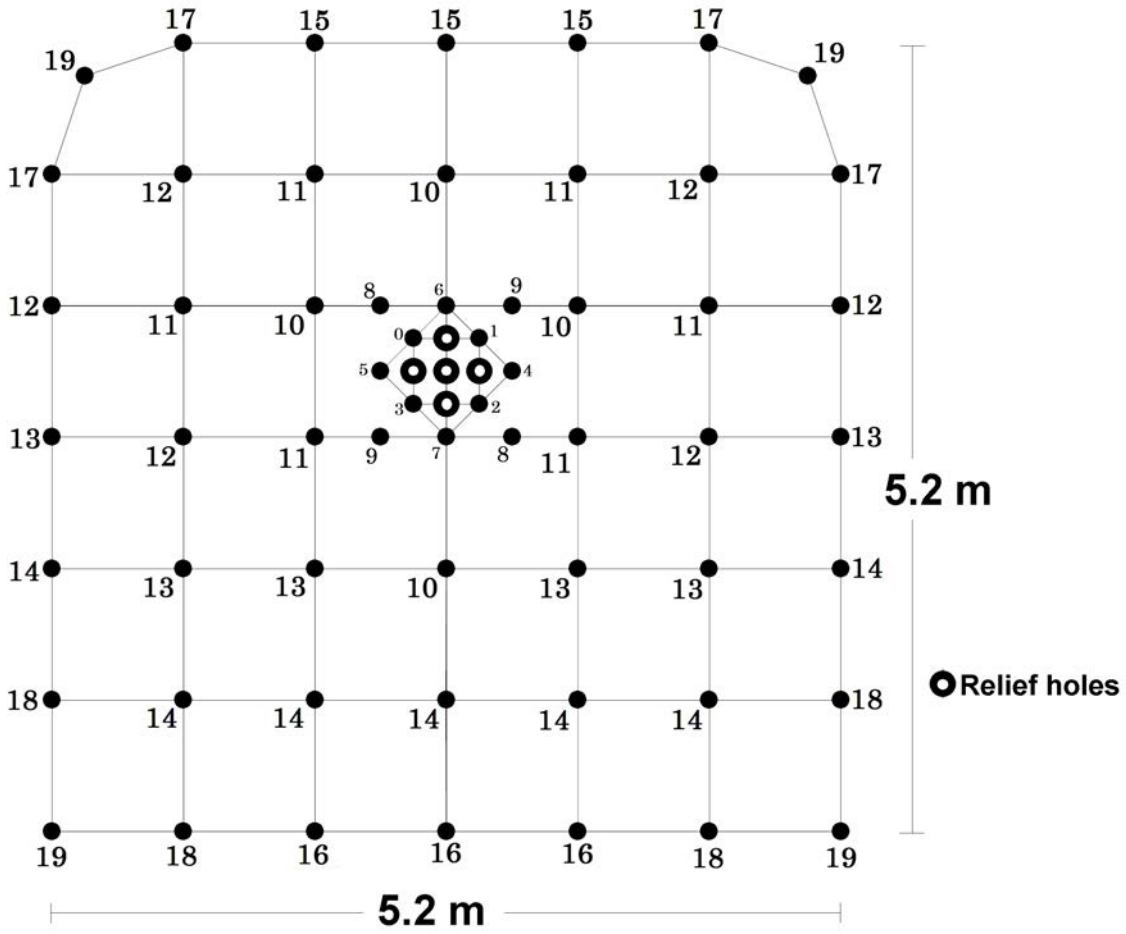

Figure 4.33 720L C Block East heading – blast pattern – Musselwhite Mine

4.5.2 Vector Sum *PPV* and Frequency Content

Figure 4.34 shows the particle velocity versus time record and the graph in Figure 4.35 shows the vector sum of *PPV* for one of the geophones (of 6 geophones installed) recording the blasted round as monitored at the ribs of the 720L C Block East drift, where 2 geophones were damaged by the blasted rock. The *PPV* values were recorded at *SD* values as low as 4.7m/kg^0.5. The highest *PPV* recorded was 390mm/s, corresponding to a rib contour blasthole. Figure 4.37 shows a distinct frequency spectrum for a single burn cut blasthole, recorded from the nearest geophone installed approximately 9.5 m away from the face. The rest of the geophones were located at 10.5m, 21.5m, and 26.6m. In this

case, frequency peaks were near 1050Hz and nearly all predominant frequencies' decay occurred around 2600Hz (Figure 4.37).

The data loggers were set to record at a sampling rate of 8192 records per second.

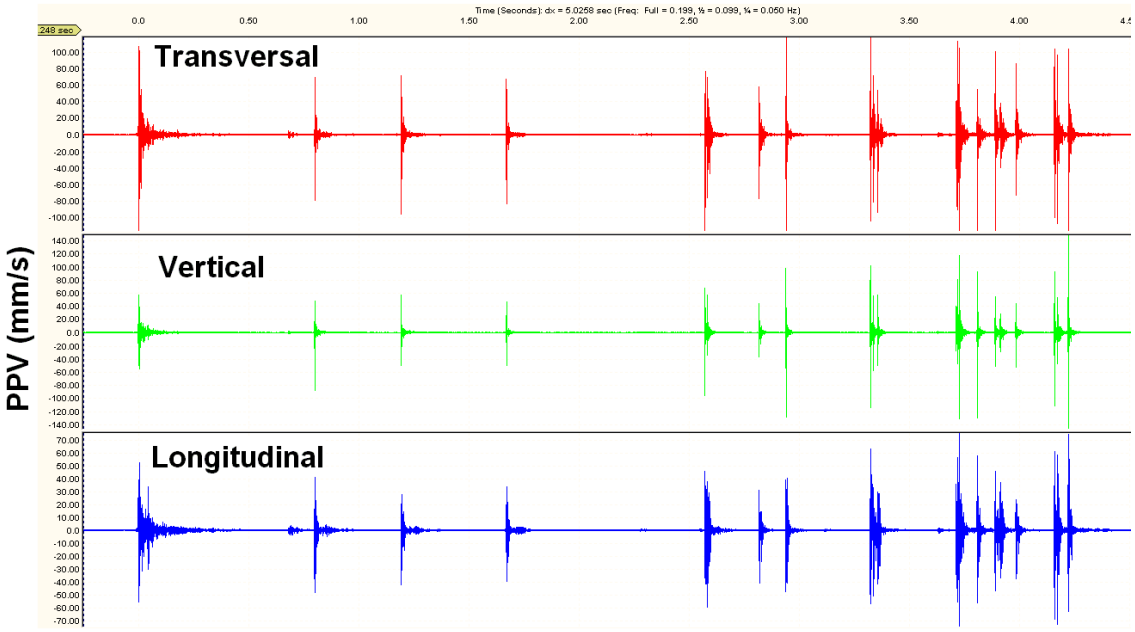

Figure 4.34 *PPV* versus time — Musselwhite Mine

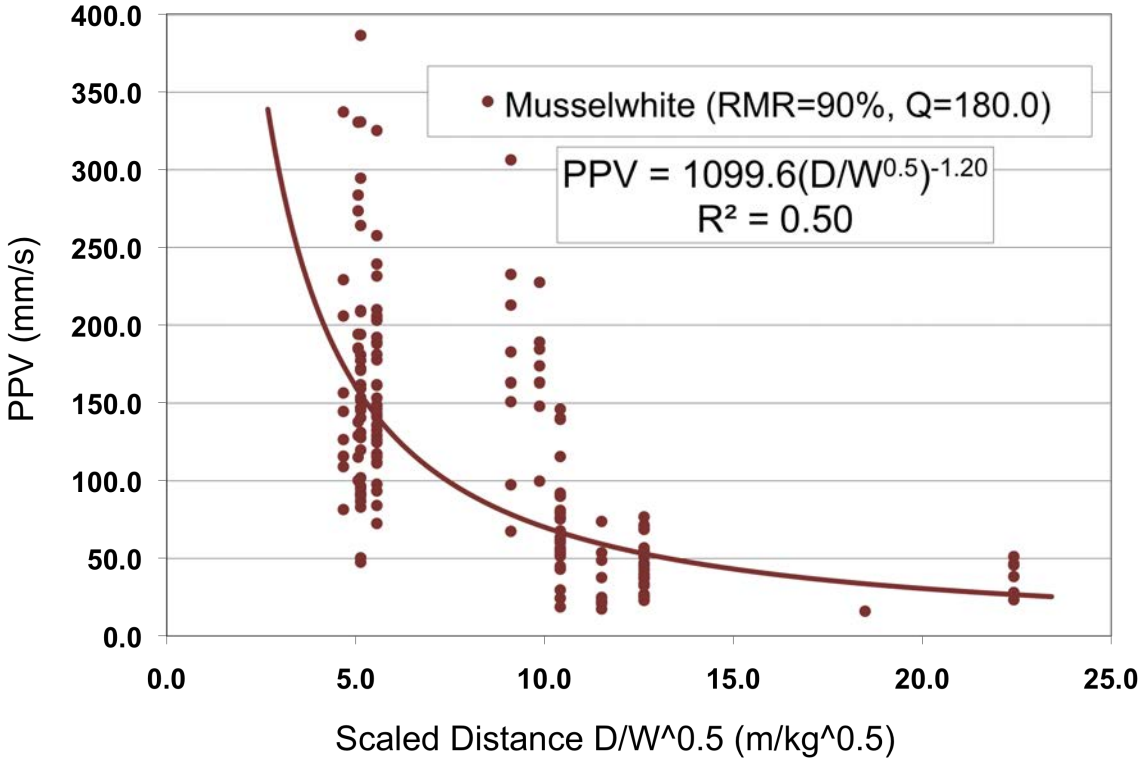

Figure 4.35 *PPV* versus *SD* values – Musselwhite Mine

The *PPV* versus *SD* power law best-fit curve is estimated from 167 records:

$$PPV = 1099.6 \cdot \left(\frac{D}{\sqrt{W}} \right)^{-1.2} \qquad \text{Eq. 40}$$

The 95% confidence line is shown in Figure 4.36.

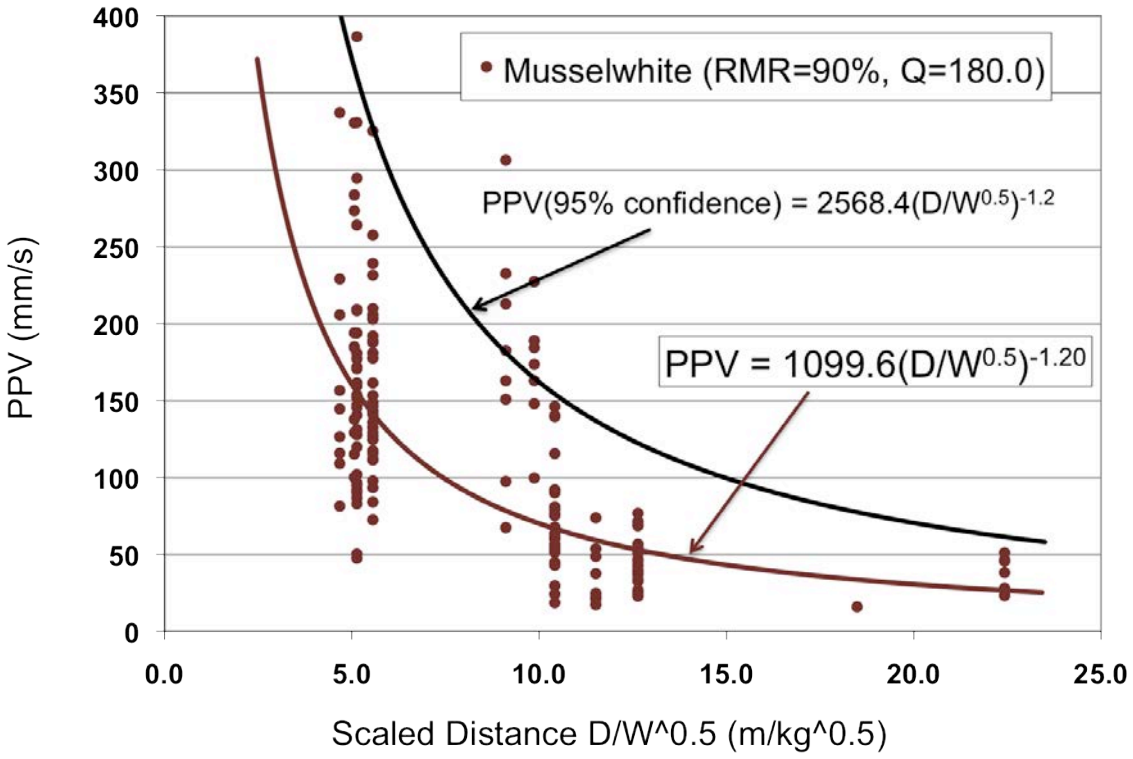

Figure 4.36 *PPV* versus *SD* boundary – 95% confidence level – Musselwhite Mine

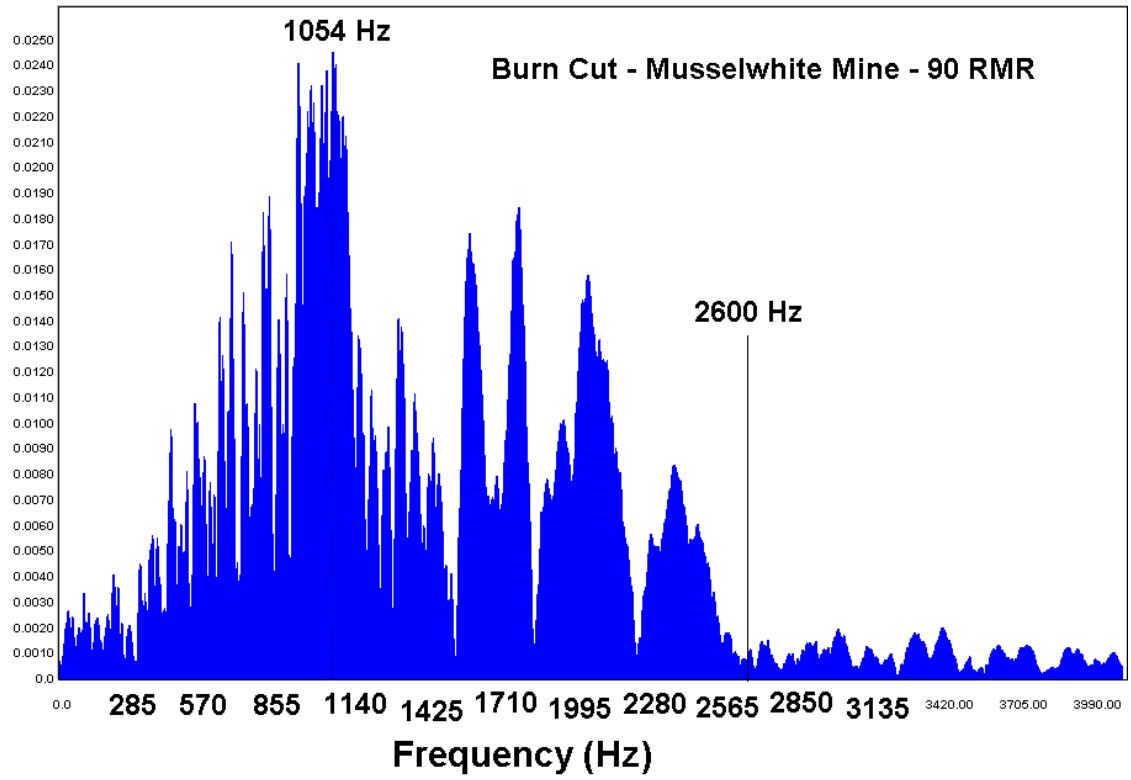

Figure 4.37 Frequency content – Musselwhite Mine

4.6 Analysis of Results

The following are the most relevant results obtained from these field investigations:

4.6.1 *PPV* versus *SD* for a Wide Range of Rock Mass Qualities

The relation between *PPV* and *SD* as a function of rock mass quality was obtained from multiple records of particle velocity versus time, in which the highest velocity recorded for each blasthole or set of blastholes is the measurement of the *PPV* value. Each blasthole or set of blastholes determines a single point on the *PPV* versus *SD* graph. Various best-fit exponential curves were established for the various sets of *PPV* versus *SD* points obtained at the mine sites investigated. These best-fit curves represent the site-specific characteristic curves shown in Figure 4.38, and the logarithmic scale graph is shown in Figure 4.40. The 95% confidence lines are shown in Figure 4.39.

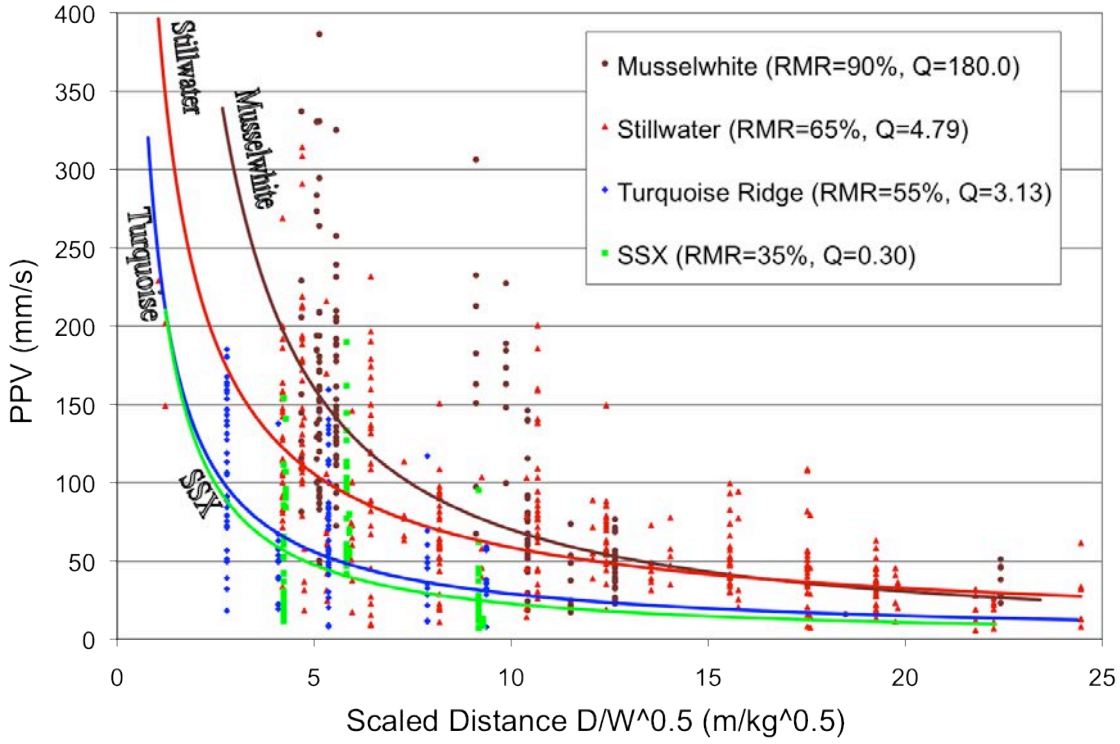

Figure 4.38 *PPV* versus *SD* for a range of rock mass qualities

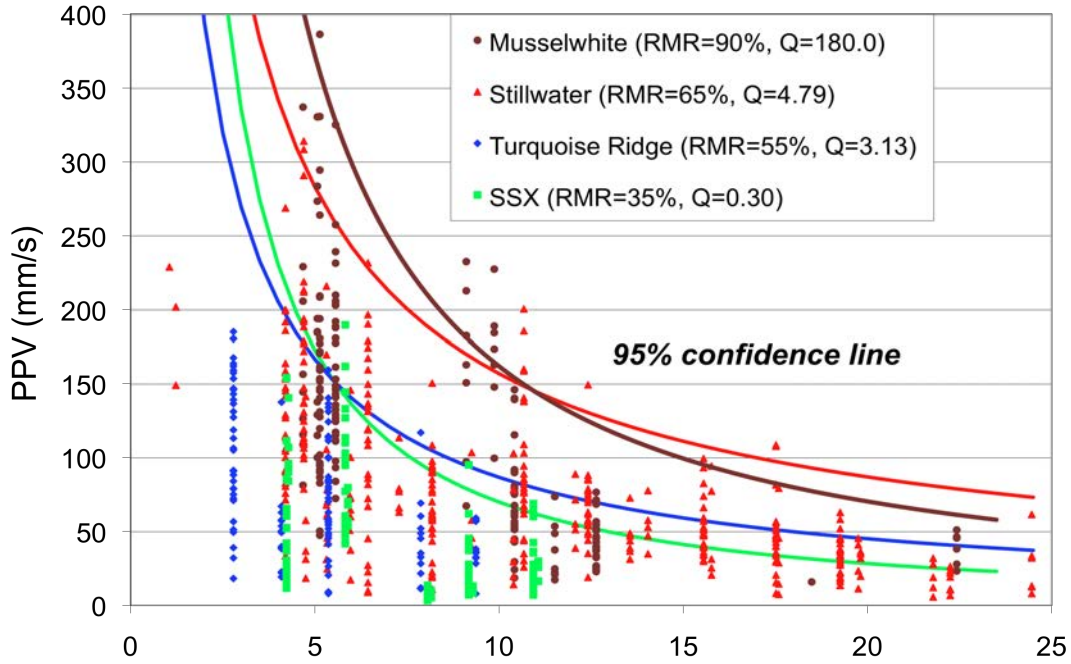

Figure 4.39 *PPV* versus *SD*. Solid lines represents 95% confidence level

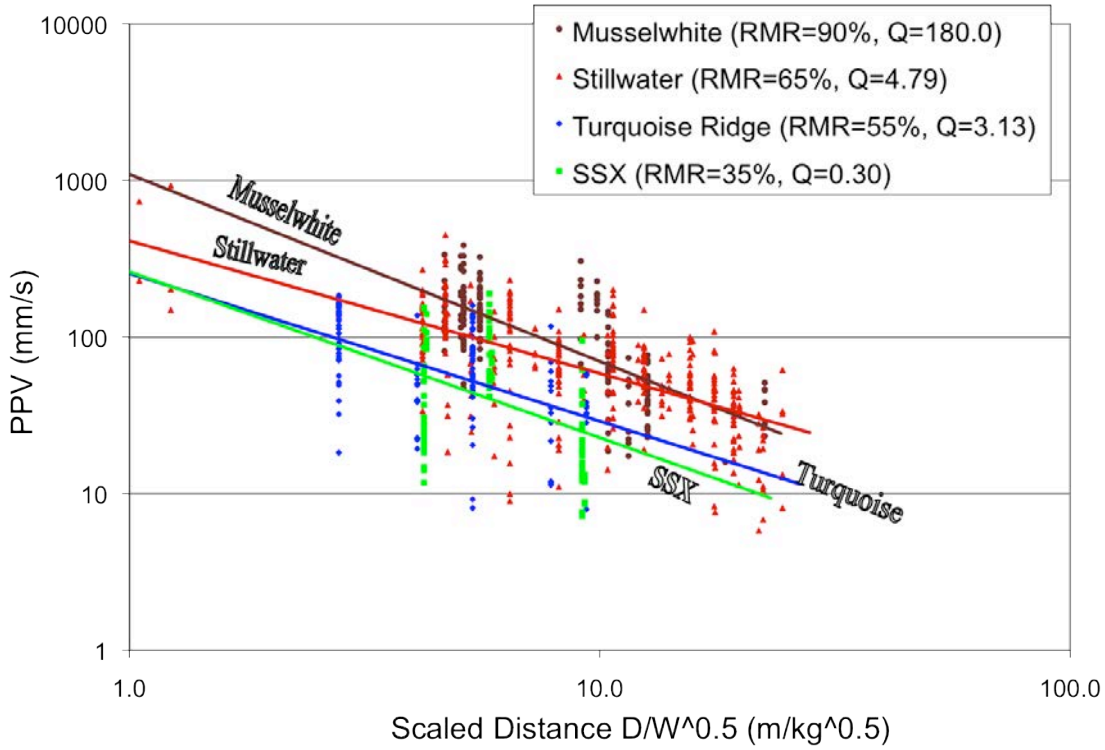

Figure 4.40 *PPV* versus *SD* – Log scale – for a range of rock mass qualities

In Figure 4.41, the logarithmic function is applied to the *PPV* and *SD* pair and the best-fit Log(*PPV*) versus Log(*SD*) line is plotted.

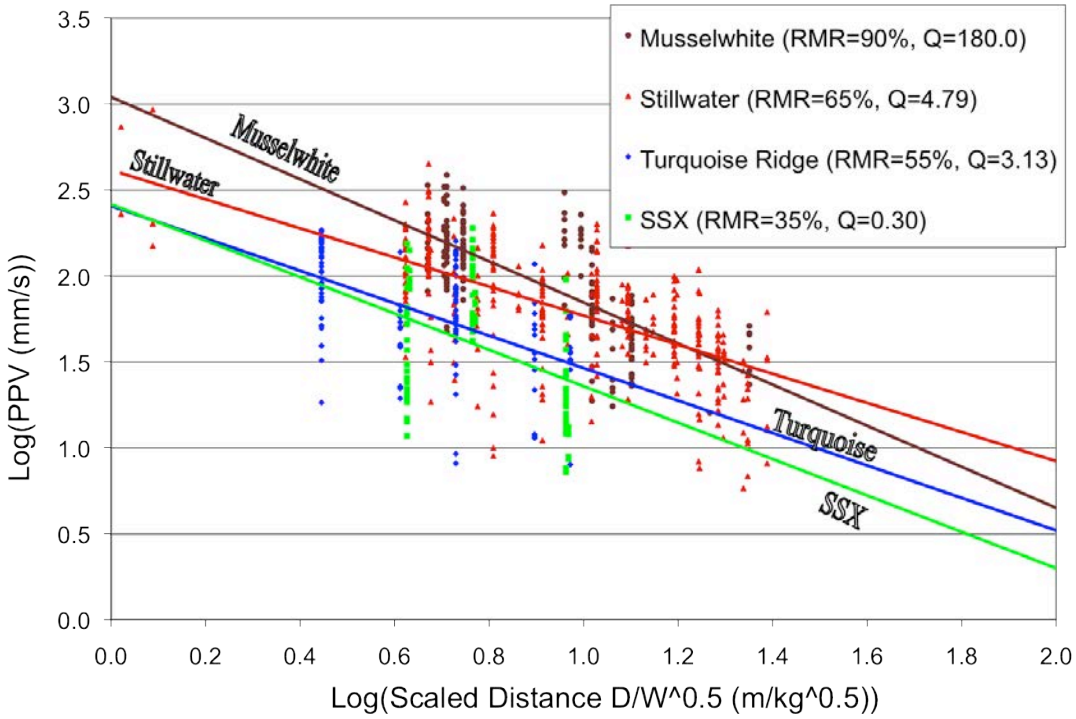

Figure 4.41 Log(*PPV*) versus Log(*SD*) – for a range of rock mass qualities

The best-fit linear equations obtained from the data points of each of the mine sites investigated and presented in the form of equation 24, is as follows:

Musselwhite Mine: $\text{Log}(PPV) = -1.19 \times \text{Log}(SD) + 3.04$

Stillwater Mine: $\text{Log}(PPV) = -0.85 \times \text{Log}(SD) + 2.62$

Turquoise Ridge JV Mine: $\text{Log}(PPV) = -0.94 \times \text{Log}(SD) + 2.41$

SSX Mine: $\text{Log}(PPV) = -1.06 \times \text{Log}(SD) + 2.42$

4.6.2 Charge Weight per Delay

At the mine sites investigated it is apparent that the time scatter in long period pyrotechnic blasting detonators (which were used at all four sites), rarely produced constructive interference. This is either due to the time scatter itself, which is greater than the minimum required to produce constructive interference, or due to the spatial location of the blastholes detonated on the same delay. This implies that the total weight of explosive fired per delay should not be numerically summed. The great majority of the data points plotted on the *PPV* versus *SD* graph, shown in previous figures, are the result

of a single independently recorded waveform. In all of the monitored rounds, there were up to 5 blastholes detonated with the same nominal delay, but from the analysis of the waveforms, the great majority did not present constructive interference. As an example, the following particle velocity versus time record shows the time scatter present in these long period pyrotechnic blasting caps with same nominal delay number. In this particular case, Figure 4.42 shows that there are four clearly identifiable independent seismic waveforms from the four blastholes fired using the same nominal delay number. Given the location of the installed geophones, no constructive interference was found, and therefore, the weights of explosives for individual blastholes should be treated independently of one another.

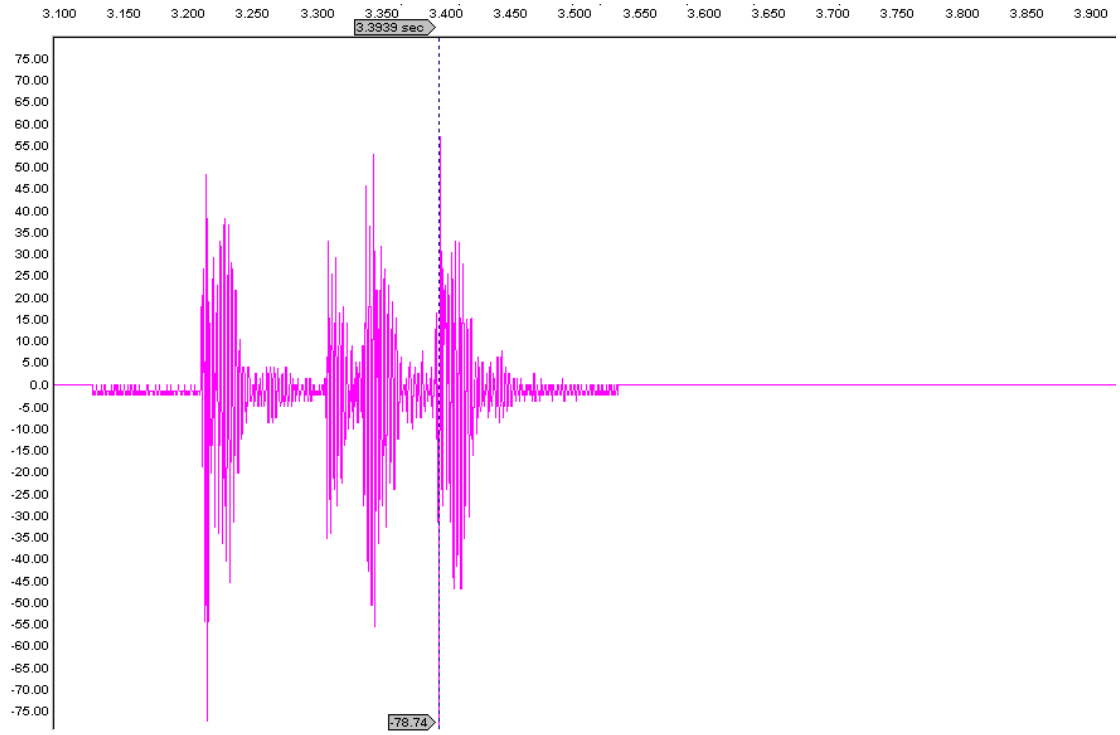

Figure 4.42 Delay time scatter – Pyrotechnic blasting caps

5 *PPV* MODELING – THE PROPOSED METHODOLOGY

5.1 Introduction

The model reviewed here was originally developed with the objective of finding a way to reduce the substantial scatter of the actual data recorded from the mine sites investigated. In these cases, a single distance from all the blastholes to every geophone installed was used, independent of their individual locations within the round. The resultant *PPV* versus *SD* analysis presented a large number of *PPV* values for a single *SD* factor, resulting in the large scatter of the data. The existing near-field Hustrulid-Lu equation (Eq. 29) was modified, and evolved into one that could integrate the physical properties of the rock and the explosives used. The incorporation of these properties made possible the analysis of a variety of geometrical and physical conditions, considered fundamental toward the objective of explaining the behavior of seismic waves generated by an explosive charge. A detailed explanation of the nature of the model, assumptions made, testing, and results, is given throughout this chapter.

The proposed (semi-empirical) modeling tool is intended for use in determining the *PPV* of a blasthole located within the round, at any particular location either on the face of the blasted round itself or within the walls of the drift. If *PPV* is determined right at the face, this could be considered to be the near field case. The latter (walls) is likely to be the most appropriate location for the installation of instrumentation, such as geophones, and could be considered to be the intermediate- or far-field cases.

The model incorporates geophysical principles, analytical equations, and user-defined parameters, which provide the basis for the analysis of the physical data gathered, and are presented in the previous chapter.

The analysis uses a modification of the Hustrulid-Lu equation (Eq. 29) to derive the final *PPV* by adding up the contributions of small incremental charges within the blasthole, but differs from the Hustrulid-Lu method, in that it incorporates individual incremental charges as waveforms. This generates various particle velocity waveforms for each individual packet, and it incorporates the arrival times of all packets, thus allowing for the superposition of the generated waveforms.

The model is highly accessible since it runs on Microsoft™ Excel® or any compatible spreadsheet software.

5.2 The Semi Empirical Modeling Tool

5.2.1 Background

In an attempt to reduce the large scatter of the recorded *PPV* versus *SD* data obtained from the mine sites investigated, the semi-empirical model (or "model") was developed. This model modifies the Hustrulid-Lu equation (Eq. 29) by incorporating measurable, physical properties of the rock mass, and the explosives in use. In addition, it uses a waveform seed generator, from which particle velocity waveforms are constructed, thus allowing for the use of the estimated arrival times of every individual packet pertaining to a blasthole of the round, to estimate the final *PPV*. The *PPV* for each blasthole is then determined from the linear superposition of all individual packet waveforms whose phases are shifted by their respective arrival time differences (i.e., as they arrive at the geophone or location of interest).

It assumes that the travelled path of the seismic wave is unique, and is determined from the shortest possible distance starting at the packet location and ending at the geophone location. Due to the geometry of the blasting round, the seismic wave cannot travel directly to the geophone. It first, must pass through a point located at the edge of the face of the round and the walls of the drift, and from that point travel to the geophone.

The physical and geophysical features employed in the model include: the location, length, and diameter of each blasthole with respect to the position of the geophone; the explosive's linear charge density and *VOD*; the rock mass medium's body and surface wave velocities and its main resonant frequency or frequencies; and the travelled length for each individual packet from which the associated travel time is determined.

Figure 5.1 depicts a section of a blast pattern in the vicinity of each blasthole, which produces a three-dimensional representation of that section (Figure 5.2), where the strike of the drift is visualized vertically, and the blastholes are projected in space in the vertical direction.

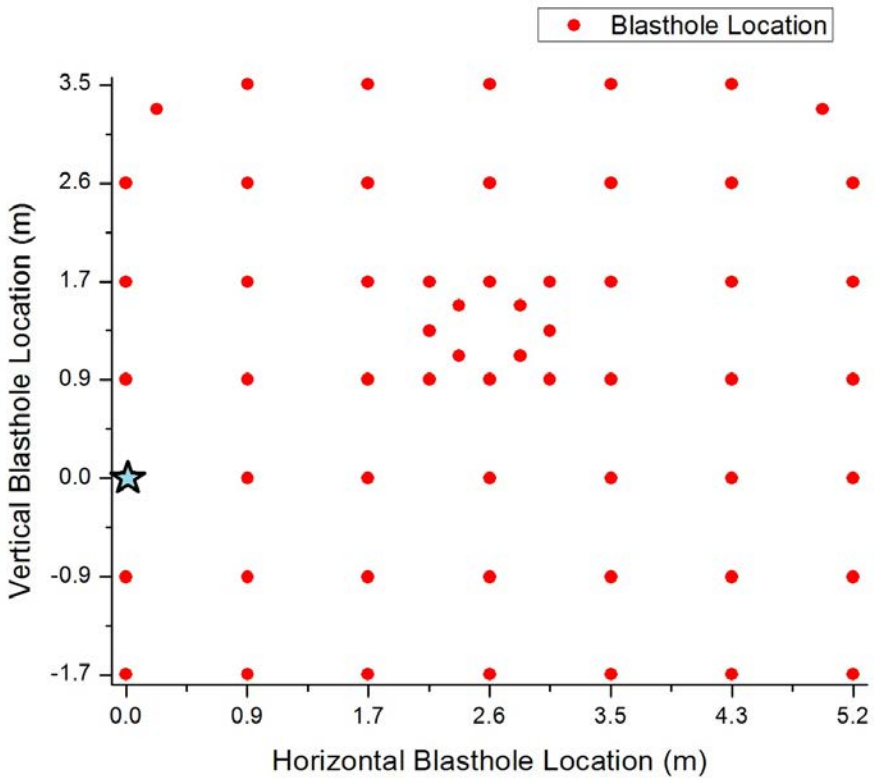

Figure 5.1 2D representation of a blast pattern

The star in Figure 5.1 represents the location of the geophone or the point of interest, either immediately at the face-wall contact or some distance away from the face, where from the analysis, the *PPV* is to be determined.

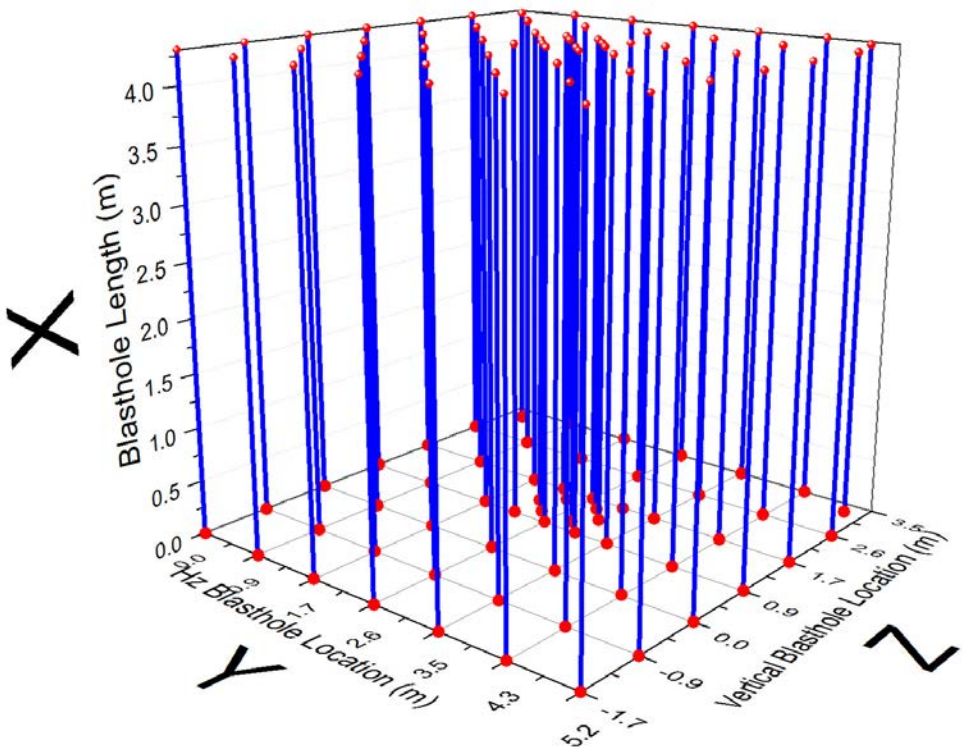

Figure 5.2 Three dimensional projection of the blasthole locations

5.2.2 Model Set-Up

The model subdivides the total length of a blasthole into "*n*" packets of equal charge length, and then determines the contribution of each of those packets to the final *PPV*. As a compromise between full data manipulation and the correspondent model becoming unmanageable, the number of packets "*n*" was arbitrarily chosen to be 17, as this yields a reasonably good estimation of *PPV* while maintaining a relatively fast processing time. At present, the model calculates *PPVs* for 60 different blastholes in about 10-15 seconds using an i7 Intel core processor. The number of packets and/or blastholes can be increased to any value, as deemed necessary in any given situation, assuming a correspondent increase in processing time. A greater number of divisions (i.e., a higher number of packets) would not contribute significantly to the overall accuracy of the modeled results. Increasing the number of packets greatly increases the processing time involved.

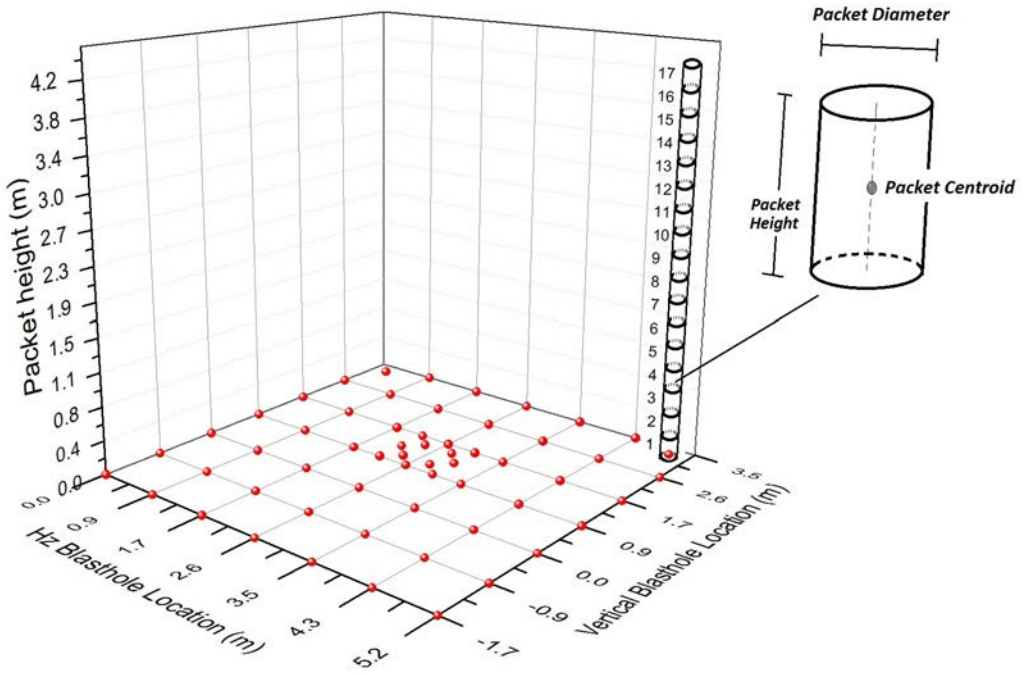

Figure 5.3 Packet representation and location of a centroid

Figure 5.3 is a three-dimensional representation of a single packet located within a particular blasthole, including its centroid and its dimensions, which are used to determine the packet's explosive charge and location.

5.2.3 Point of Diffraction (*POD*)

The model was constructed with attention to the fact that the trajectory of the seismic wavefront must pass through a point of diffraction (*POD*) at the face-wall contact of the blasting round, and then travel through the surface of the drift wall, ultimately arriving at the geophone location (as depicted in Figure 5.4).

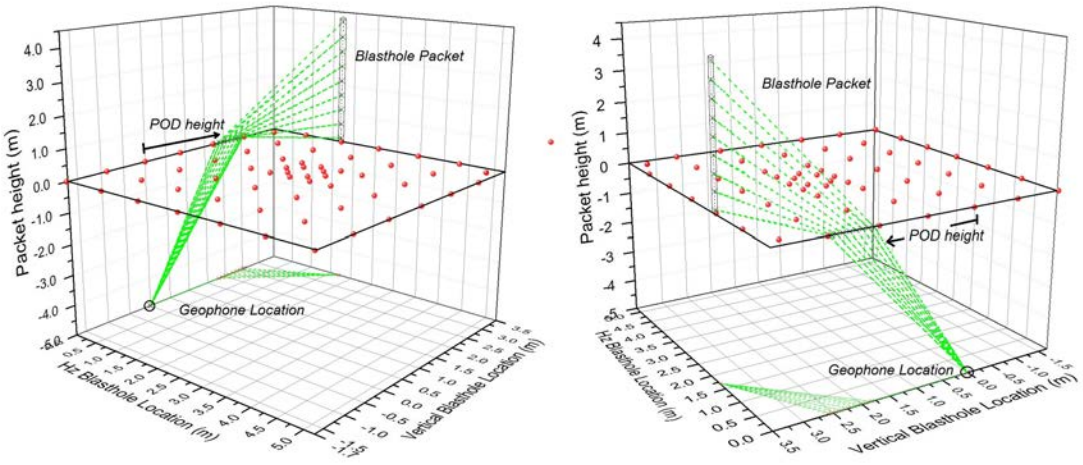

Figure 5.4 Point of diffraction height Z_{POD} of multiple packets

In the event that an elastic stress wave encounters a boundary demanding a sharp turn of 90 degrees or more, only a portion of the total incidence energy of this elastic stress wave will continue through the rock face as refracted and diffracted energy, whereas the remaining portion would be reflected (Figure 5.5).

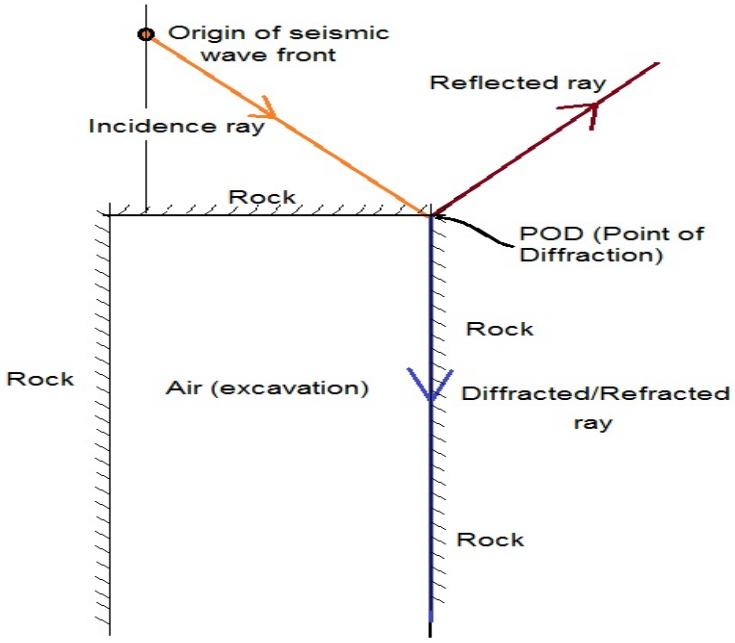

Figure 5.5 Incidence, reflected and diffracted/refracted rays

The contribution of the refracted and diffracted portion of the incident seismic wave is determined by factoring the length of each packet ray (taken from the packet's origin

location to the face-wall contact point, the *POD*), by the ratio of the depth to the packet's origin, versus the length from the packet's origin to the *POD*. This ratio yields the projection of the velocity vector parallel to the drift orientation.

5.2.4 Assumptions

A fundamental aspect of this model is its simplicity, and therefore, results should be based on calibration of recorded data whenever possible. This simplicity is imperative, since, in order to be rigorous, many parameters must be included to account for the aggregate of influences on the physical behavior of a rock-explosive interaction.

The model makes the assumption that only the shortest path would generate the peak of the particle velocity and that any other path would add merely to the residual portion of the particle velocity. This assumption is fully consistent with the physics of wave propagation, and it will be used to determine the unique path of travel from the origin of the seismic wave to the point of interest, and from this length and the velocities involved, the total travel time of the seismic wave will be determined.

It is assumed that blastholes are bottom initiated (base-primed), which is the most common method of initiating a drift blasthole. In this case, the first initiated packet corresponds to packet 17 and the last packet to be initiated corresponds to packet 1. The explosive column is initiated at the bottom of the cylindrical charge from where the seismic wavefront expands in a spherical manner. As this happens, the explosive in the column charge, which propagates at a finite velocity (i.e., the *VOD* of the explosive utilized), and reaches the subsequent packet centroid at a certain time. When the detonation front has reached the next packet, a new seismic wavefront begins to propagate in a fashion similar the previous one. This continues as the whole column charge detonates, as depicted in the four images of Figure 5.6.

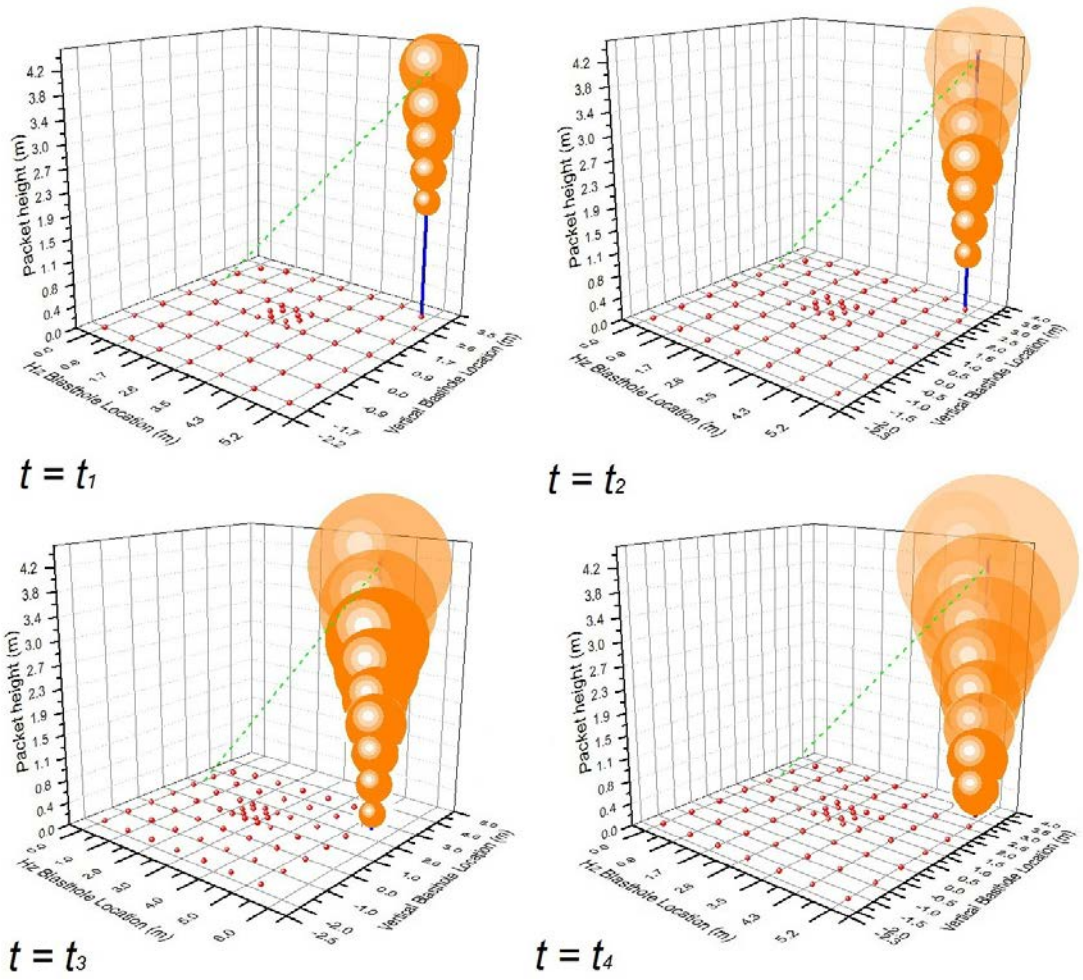

Figure 5.6 Packet initiation sequence – Expanding seismic wavefront and ray path

Blastholes are considered to be straight lines, perpendicular to the face and parallel to the walls of the drift. No blasthole deviation was assumed.

Notably, a more comprehensive analysis would include particle velocity as determined from the combination of a wide range of frequencies generated from a single blasthole, as indicated in the frequency spectrum analysis of the seismic wave velocity records given in Chapters 3 and 4. However, for ease, all of the analyses performed for the research herein were based on a single predominant resonance frequency.

Two assumptions in this case are, that the seismic wave produced by the blasthole packets takes the shortest route to the geophone, and, that it passes through that wall upon which the geophone is located. Although this might not always be the case, given that examples could be found where the shortest path does not pass necessarily through the

wall on which the geophone is installed, nevertheless, this assumption likely yields the highest particle velocity measurement as compared with the shortest path, owing to the fact that more points of diffraction will be encountered and the energy will dissipate more rapidly. This could happen, for example, when blastholes are located at the contour of the excavation, where the seismic wave will travel through the surface of the roof or back of the excavation, and then along the wall to the geophone location.

As the blastholes detonate and fragment the rock, and as this volume of fragmented rock is displaced, the transitory volume defined by the blasthole sequence becomes empty, which in turn prevents the seismic waves from travelling through the opened space. The actual trajectory of the seismic wave should go around this momentarily emptied space. In this case, the assumption is that the seismic wave travels in a straight line, from the origin of the packet to the *POD*, and then to the geophone, avoiding any other, more complicated path.

5.2.5 Analytical Background

In order to determine the shortest travelled distance from the point of origin to the arrival point (geophone), necessarily passing through the face-wall contact, the height of that unique point (Z_{POD}), at the face-wall contact must be found, such that the total travelled distance is minimized. Figure 5.7 and Figure 5.8 depict two different points of origin, for the n_{th} and the i_{th} packets, where the seismic wave originating at these points should pass through Z_{PODnth} and Z_{PODith} at the face-wall contact, yielding the total shortest distance. The vertical reference location of the geophone is always assumed to be at 0m elevation but could be set at any distance from the face.

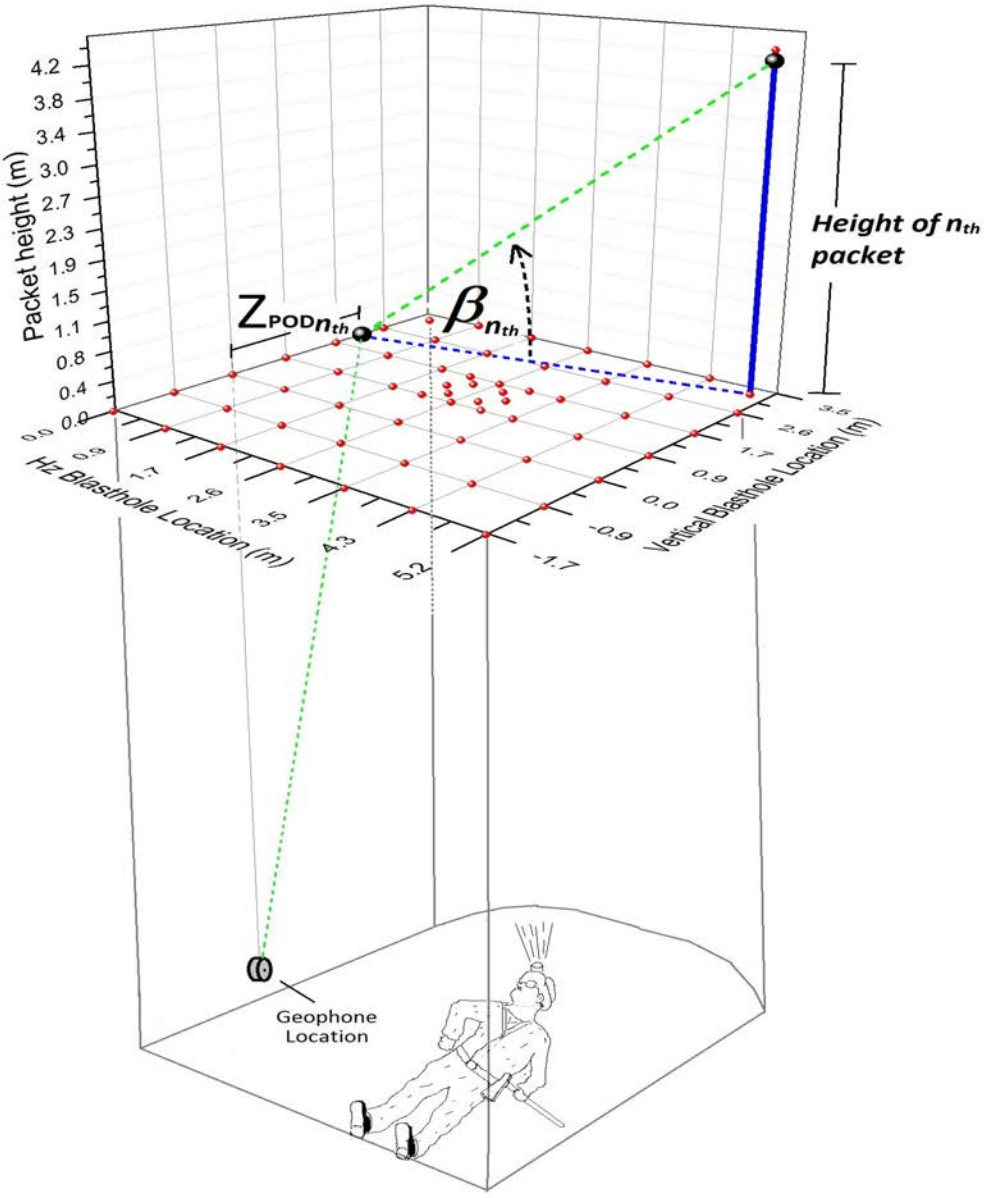

Figure 5.7 Point of diffraction height $Z_{POD\ nth}$ and angle of incidence β_{nth} of n_{th} packet

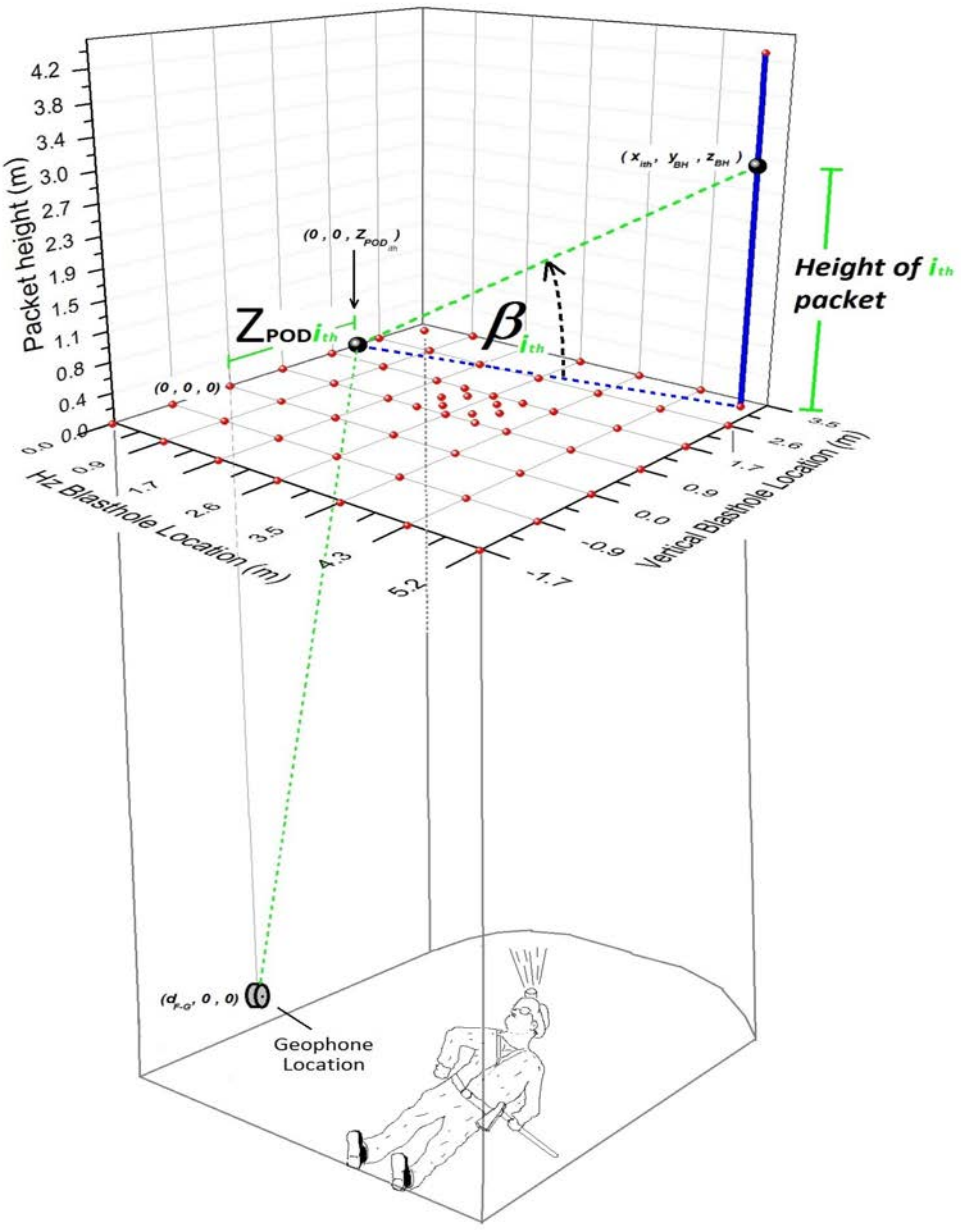

Figure 5.8 Point of diffraction height $Z_{POD\,ith}$ and angle of incidence β_{ith} of i_{th} packet

The total travelled distance is determined by summation of the distance from the origin of a particular packet, passing through the Z_{POD} at the face-wall contact, and continuing to the location of interest, in this case a geophone. The total travelled distance of the seismic wave starting from the i_{th} packet is given by:

$$D_{TOTAL\,ith} = \sqrt{x_{ith}^2 + y_{BH}^2 + (z_{BH} + Z_{POD_{ith}})^2} + \sqrt{d_{F-G}^2 + Z_{POD_{ith}}^2} \qquad \text{Eq. 41}$$

Where:

- y_{BH} is the horizontal blasthole location with respect to the geophone,
- z_{BH} is the vertical blasthole elevation with respect to the geophone,
- x_{ith} is the depth of the i_{th} packet with respect to the geophone,
- Z_{PODith} is the vertical elevation of the point of diffraction for the i_{th} packet, and
- $d_{F\text{-}G}$ is the horizontal distance from the face of the round to the geophone.

To determine the Z_{PODith} that minimizes the total travelled distance ($D_{TOTALith}$) of the i_{th} packet the following calculations are required:

$$\frac{\partial D_{TOTAL_{ith}}}{\partial Z_{POD_{ith}}} = 0 \qquad \text{Eq. 42}$$

then,

$$Z_{POD_{ith}} = \frac{z_{BH} \cdot d_{F-G} \cdot (-d_{F-G} \pm \sqrt{x_{ith}^2 + y_{BH}^2})}{(x_{ith}^2 + y_{BH}^2 - d_{F-G}^2)} \qquad \text{Eq. 43}$$

The total arrival time for the i_{th} packet is composed of the time that it takes for the detonation front to reach the i_{th} packet centroid from the bottom of the charge, (travelling at the *VOD* of the given explosive), the travelled time from the i_{th} packet centroid to the point of diffraction Z_{PODith} at the face-wall contact (travelling at the body wave velocity), and the travelled time from Z_{PODith} to the geophone location at the surface wave velocity. In this case, the arrival time of the i_{th} packet is given by the following equation:

$$t_{ith} = \frac{h_{BH} - x_{ith}}{VOD_{\text{exp}losive}} + \frac{\sqrt{x_{ith}^2 + y_{BH}^2 + (z_{BH} - Z_{POD_{ith}})^2}}{V_{M\_BodyWave}} + \frac{\sqrt{d_{F-G}^2 + Z_{POD_{ith}}^2}}{V_{M\_SurfaceWave}} \qquad \text{Eq. 44}$$

Where,

- t_{ith} is the arrival time of the i_{th} packet,
- h_{BH} is the total length of the blasthole
- $VOD_{explosive}$ is the velocity of detonation of the explosive,
- $V_{M\_BodyWave}$ is the body wave velocity of the medium, and

- $V_{M\_SurfaceWave}$ is the surface wave velocity of the medium.

5.3 Arrival Time Analysis

5.3.1 General

The most general case for determining *PPV* of a blasthole from the contribution of its individual incremental charges is by considering that each and every one of these individual incremental charges arrive simultaneously, that is, there is no time delay associated with their arrival time. This is probably the most significant disadvantage of the Holmberg-Persson and Hustrulid-Lu methods, since both only consider simultaneous arrival of all individual incremental charges. In a sense, there is no actual consideration whatsoever of arrival time. Moreover, even if these methods were to incorporate time delay, there can be no solution possible, unless the incremental charges are treated as a waveform, as opposed to an independent numeric value. As will be shown, there could be substantial variation in the final *PPV* as determined when the arrival time of each incremental charge is considered, i.e., where incremental changes are treated as a waveform, versus final *PPV* as determined without consideration for arrival times.

Given that the explosive charges are bottom initiated (base-primed blastholes), there are many different possible alternatives to the sequence of the arrival of the seismic wave at the geophone location. This of course will depend on the location of the blasthole with respect to the geophone, as well as the *VOD* of the explosive used, and the propagation velocity of the seismic wave. Among the possible forms of the curve of arrival times with respect to the packet location, several are depicted in Figure 5.9 through Figure 5.13.

In all of these examples, the point or points that are lowest with respect to the rest of the points indicates the first to arrive at the geophone location, as opposed to the point or points located at the top.

In Figure 5.10, the first stress wave to arrive pertains to the collar of the blasthole. In this case, the detonation velocity of the explosive is much larger than the seismic wave velocity. In Figure 5.9, just the opposite occurs, that is, the seismic wave velocity is greater than the detonation velocity.

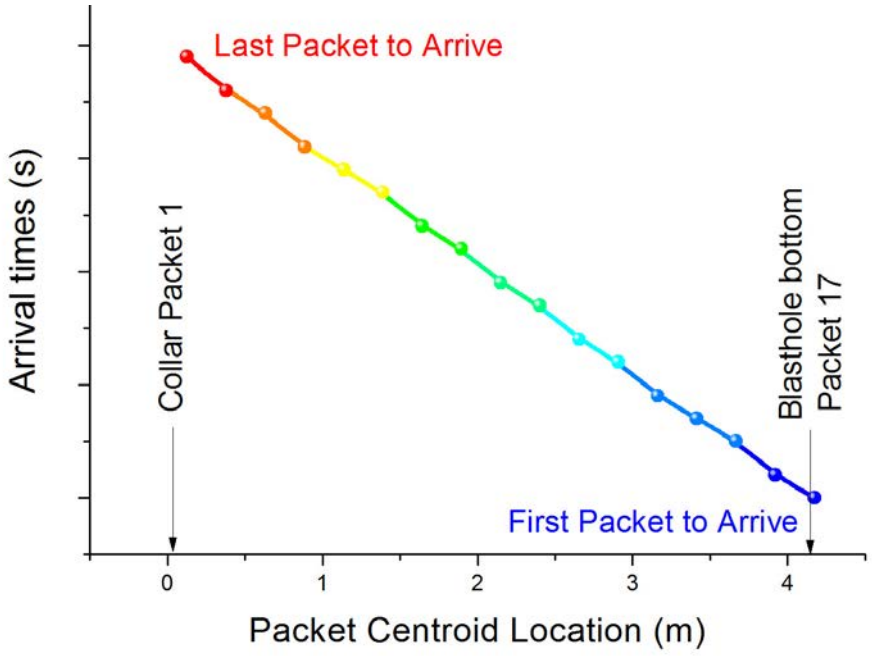

Figure 5.9 Ascending arrival times from the initiation point (Packet 17)

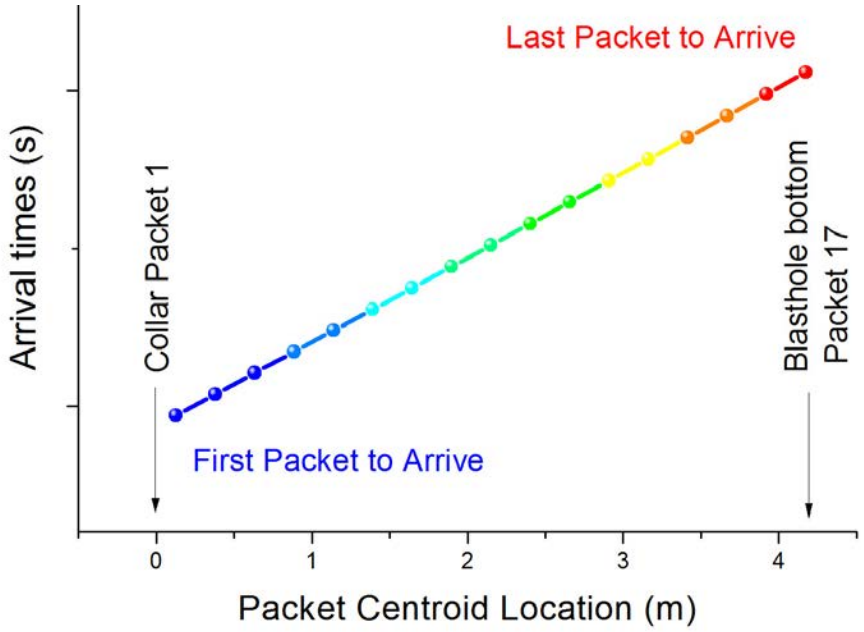

Figure 5.10 Descending arrival times from the initiation point (Packet 17)

Figure 5.11 and Figure 5.12 portray parabolic curves of the arrival time with respect to the packet location. In both cases, there is more than one packet location whose stress waves arrive simultaneously with another.

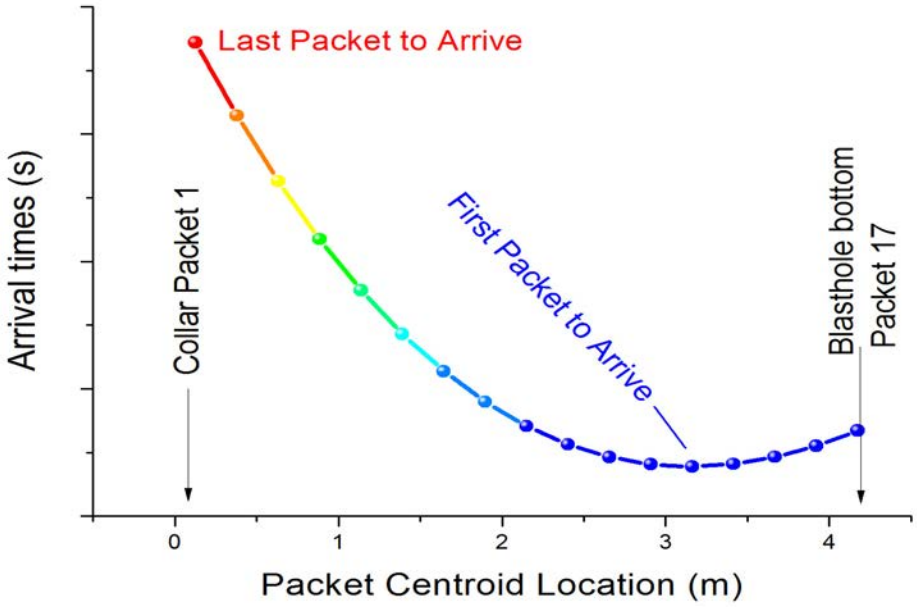

Figure 5.11 Parabolic ascending arrival times from the initiation point (Packet 17)

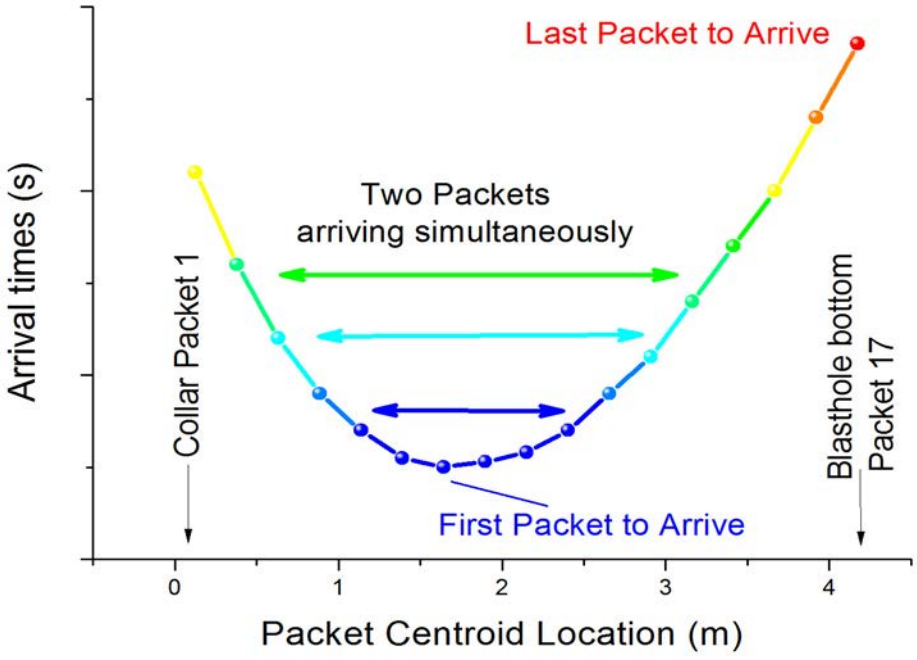

Figure 5.12 Parabolic arrival times. Central packets of the wavefront arrives first

Figure 5.13 would be an extreme case where all the stress waves arrive simultaneously. This form of arrival time curve is representative of the current state of methods, as employed in the Holmberg-Persson (Eq. 26) and Hustrulid-Lu (Eq. 29) equations.

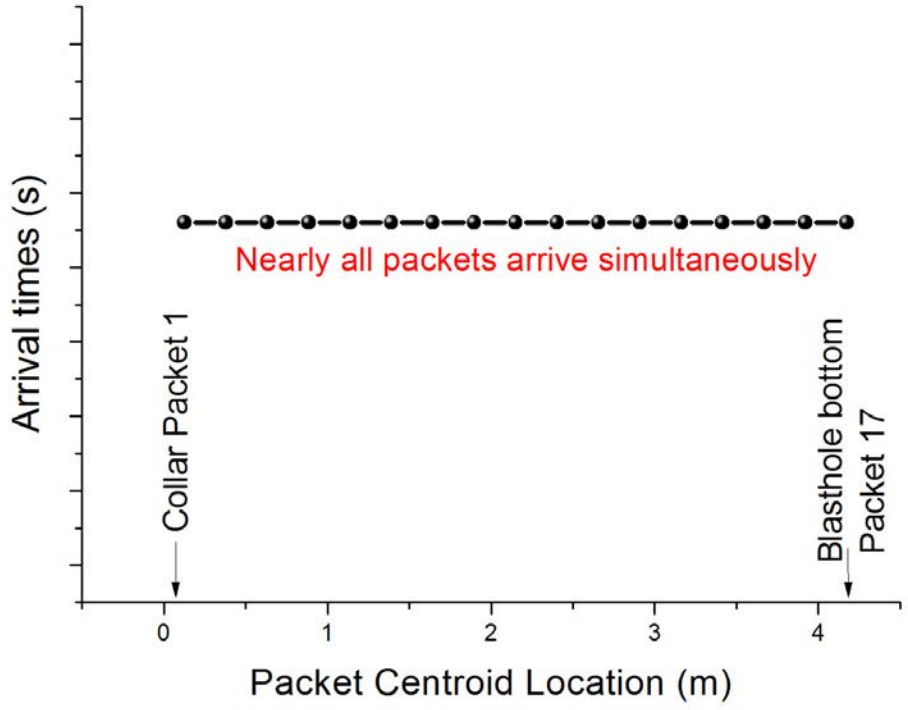

Figure 5.13 Simultaneous arrival times for all packets

5.3.2 Stress Wave Propagation Velocity – Rock Mass Quality Dependence

It is commonly accepted that a relation exists between the types of rock and the sound velocity of a stress wave propagating in that medium, where stronger rocks or better defined, more competent rock masses will present higher propagation velocities, as compared to softer rocks or less competent rock masses. It is clear that the weaker the rock mass, in terms of its quality, the slower the propagation velocity. The presence of more features within the rock mass such as cracks, joint sets, faults, etc., imposes obstacles to the propagation of the stress wave, reducing its energy and velocity.

Table 5.1 shows propagation velocities for different mediums. Rock types classified from weak, such as sandstone, to competent, such as metamorphosed hard rock, are relevant to the research conducted herein.

Table 5.1 Table of propagation velocities for different mediums (source: Pavlovic, 1998)

MEDIUM	Velocity (m/s) min	Velocity (m/s) max
Air (temperature dependence)	310	360
Gravel, dry sand	100	500
Wet sand (with water)	200	1,800
Clay	1,200	2,500
Water (temperature dependence)	1,430	1590
Sandstone friable	1,500	2,500
Sandstone dense	1,800	4,000
Chalk	1,800	3,500
Limestone	2,500	6,000
Gypsum	4,500	6,500
Ice	3,100	4,200
Granite	4,000	5,700
Metamorphosed	4,500	6,800

Figure 5.14 shows a representation of the primary P-wave velocity propagating in different rock types.

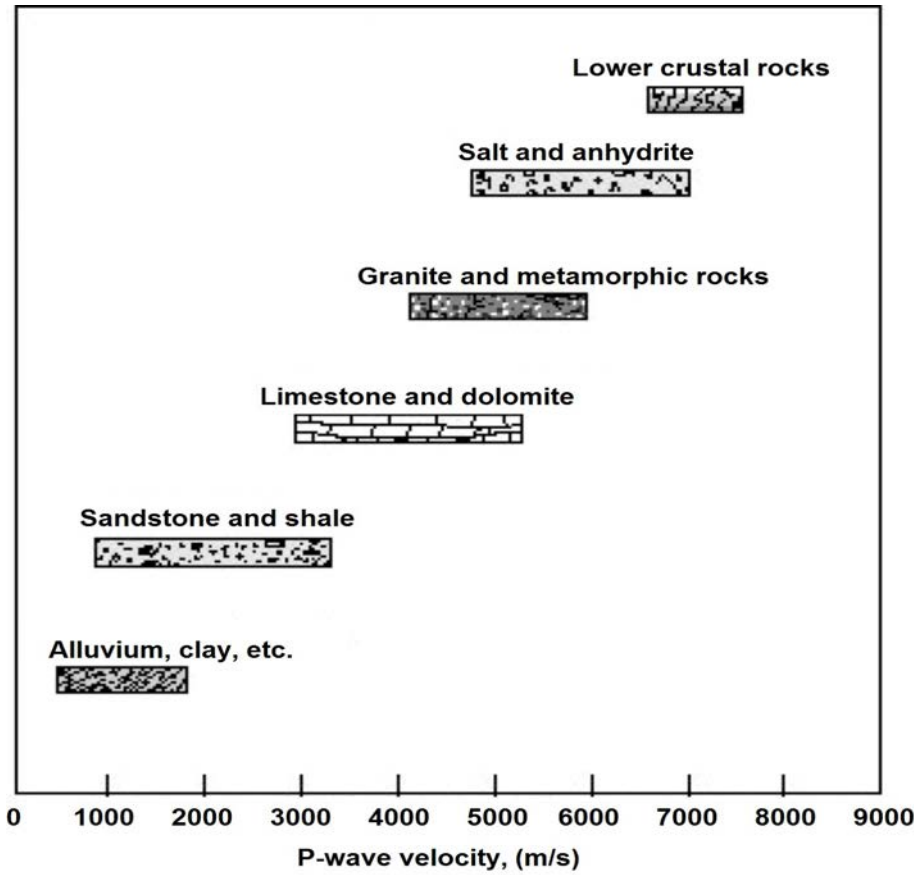

Figure 5.14 P-wave velocity (m/s) for various rock types (modified from source: http://science.jrank.org/pages/48110/seismic-properties-rocks.html, January 2011)

5.3.3 Arrival Time – Rock Mass Sound Velocity Dependence

There are different forms of arrival time curves and actual time differences for a stress wave originating at a particular packet location within the blasthole. Those differences depend on the location of the blasthole within the round with respect to the location of the geophone and also depend on the *VOD* of the explosive, and on the body and surface sound velocities of the rock medium.

The green triangles in Figure 5.15 mark the locations of the blastholes within the round as they are analyzed in relation to their arrival times at the geophone location. In this case, the geophone was located 10.5m from the face. For convenience, the reference location coordinate of the geophone is always (0.0m, 0.0m). The arrival times for the following blasthole's collar location coordinates were analyzed: (0.9m, 0.0m), (0.0m, 0.0m), (2.6m, 3.5m), (5.0m, 3.3m), and (0.2m, 3.3m).

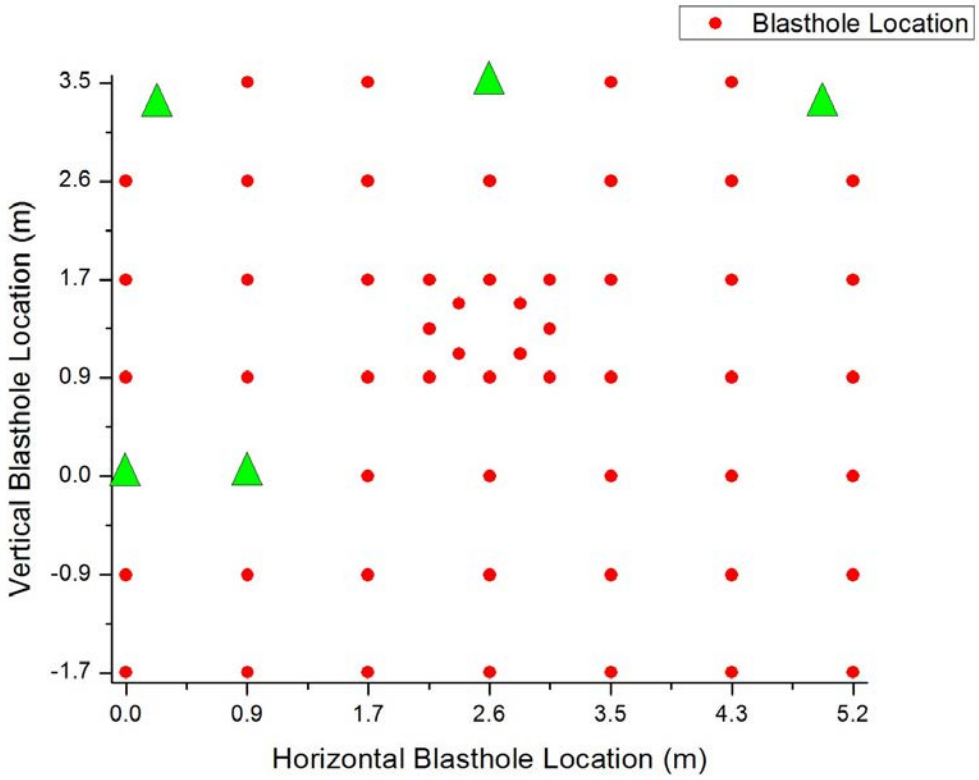

Figure 5.15 Arrival times for highlighted blasthole location

Arrival time analysis takes into consideration the different detonation velocity ranges for different types of commercial explosives, as well as some hypothetical detonation velocities above and below these ranges (for the purpose of testing the model). Table 5.2 illustrates a wide range of explosive types and their associated detonation velocity.

Table 5.2 Table of explosive detonation velocities

Explosive Name	Abbreviation	Detonation Velocity (m/s)	Density (g/cm³)
Triazido-trinitrobenzene	TATNB	7,300	1.71
Trinitrobenzene	TNB	7,450	1.6
Dinitro-diazenofuroxan	DDF	10,000	2.02
Acetone Peroxide	AP	5,300	1.18
Aliphatic explosives			
Ammonium Nitrate	AN	5,270	1.3
Aromatic explosives			
Cyclotetramethylene Tetranitramine	HMX	9,100	1.91

Explosive Name	Abbreviation	Detonation Velocity (m/s)	Density (g/cm³)
Cyclotrimethylenetrinitramine	RDX	8,750	1.76
Dunnite		7,150	1.6
Ethyl Picrate		6,500	1.55
Ethylenedinitramine	EDNA	7,570	1.65
Hexanitrohexaazaisowurtzitane	HNIW or CL-20	9,400	2.04
Inorganic explosives			
Lead azide		4,630	3.0
Lead styphnate		5,200	2.9
Mannitol hexanitrate	MHN	8,260	1.73
Mercury Fulminate		4,250	3.0
Methyl nitrate		8,000	1.21
Methyl Picrate		6,800	1.57
Nitrocellulose	NC	7,300	1.2
Nitroglycerine	NG	7,700	1.59
Nitroglycol	EGDN	8,000	1.48
Nitroguanidine	NQ	8,200	1.7
Octanitrocubane	ONC	10,100	2.0
Organic Explosives			
Pentaerythritol Tetranitrate	PETN	8,400	1.7
Picric Acid	TNP	7,350	1.7
Picryl Chloride		7,200	1.74
Silver azide		4,000	4.0
Tetranitroglycoluril	Sorguyl	9,150	1.95
Tetryl		7,570	1.71
Triaminotrinitrobenzene	TATB	7,350	1.80
Trinitroaniline	TNA	7,300	1.72
Trinitrocresol		6,850	1.62
Trinitrotoluene	TNT	6,900	1.6
Urea nitrate	UN	4,700	1.59

Reference Cooper, Paul W., Explosives Engineering, New York: Wiley-VCH, 1996. ISBN 0-471-18636-8

Figure 5.16 through Figure 5.20 show the arrival time versus the blasthole's packet depth for each blasthole location as represented by the triangles in Figure 5.15, for a rock with

body wave velocity of 6,500m/s, which corresponds to a good, competent rock mass, such as the one studied at the Musselwhite Mine site. At the other extreme, Figure 5.21 through Figure 5.25 show the arrival times for a rock with body wave velocity of 2,000m/s, corresponding to rock with poor to fair rock mass quality, such as the one present at the SSX mine. The different curves represent the ratio between the *VOD* of the explosive, and the body (*Vbw*) and surface (*Vsw*) wave velocity of the rock mass.

Note from the following graphs that the arrival times of packet 17, i.e., the one closest to the bottom of the blasthole (at approximately 4.3m into the rock face), turn out to be nearly all equal (Figure 5.16 - Figure 5.25). This happens because packet 17 is the shortest distance into the blasthole column and therefore travels the shortest distance at the explosive's detonation velocity, i.e., the one varied for this analysis. The great majority of the travelling time occurs in the rock mass medium, in which the body and surface wave velocities were set constant throughout this portion of the analysis.

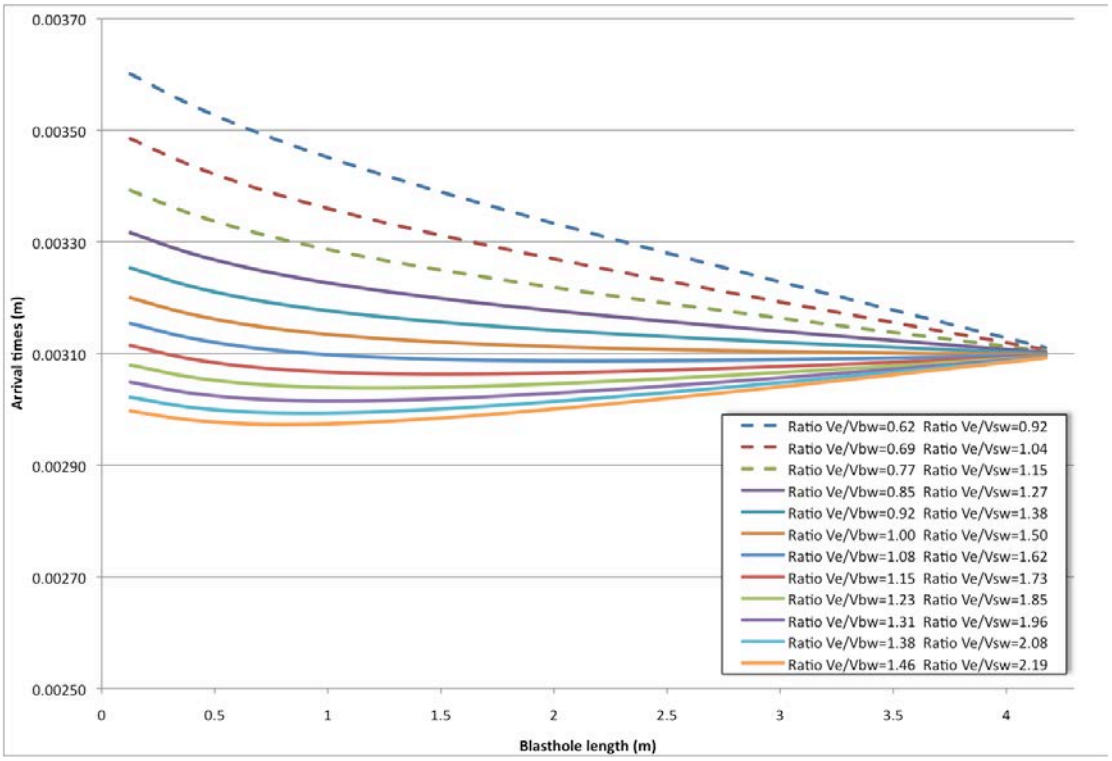

Figure 5.16 Arrival times – *Vbw*=6500m/s – Good rock quality – Y=0.9m Z=0.0m

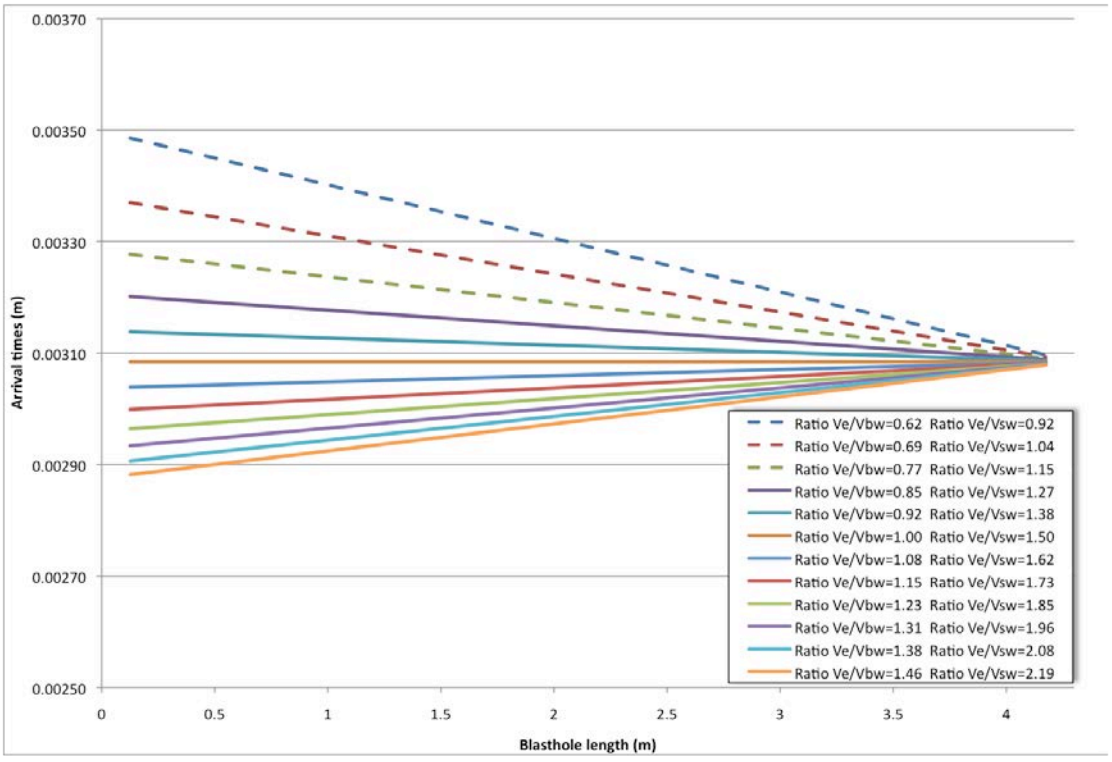

Figure 5.17 Arrival times – *Vbw*=6500m/s – Good rock quality – Y=0.0m Z=0.0m

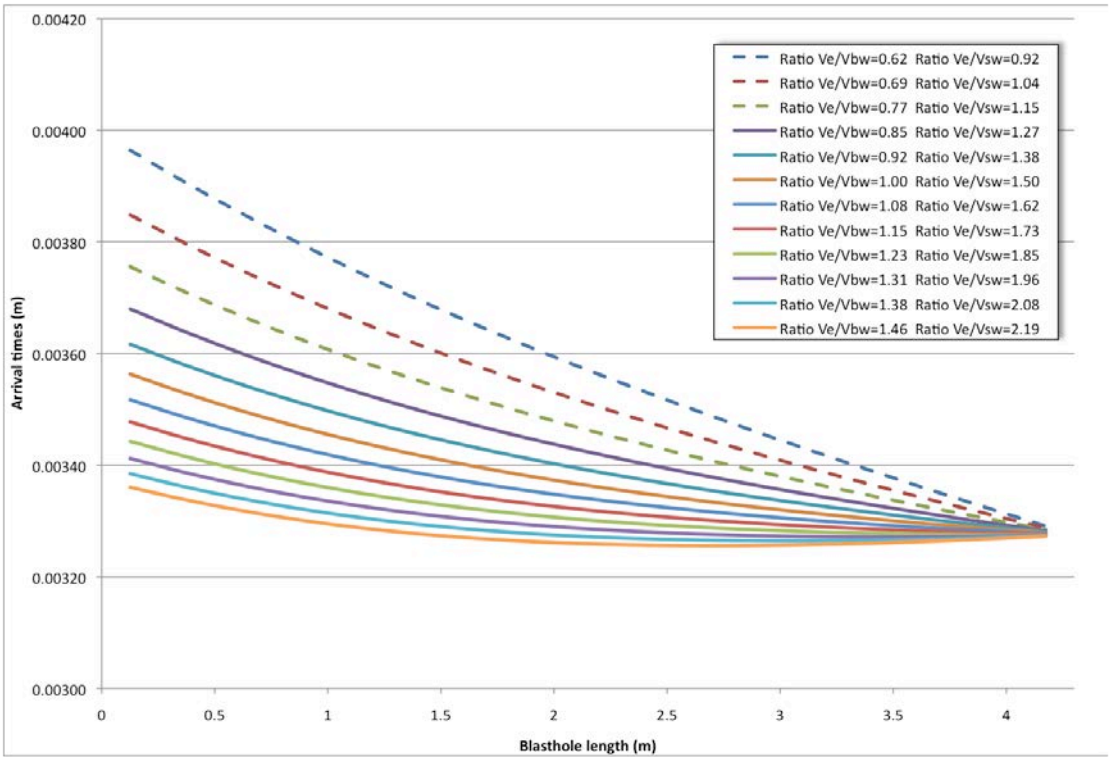

Figure 5.18 Arrival times – *Vbw*=6500m/s – Good rock quality – Y=2.6m Z=3.5m

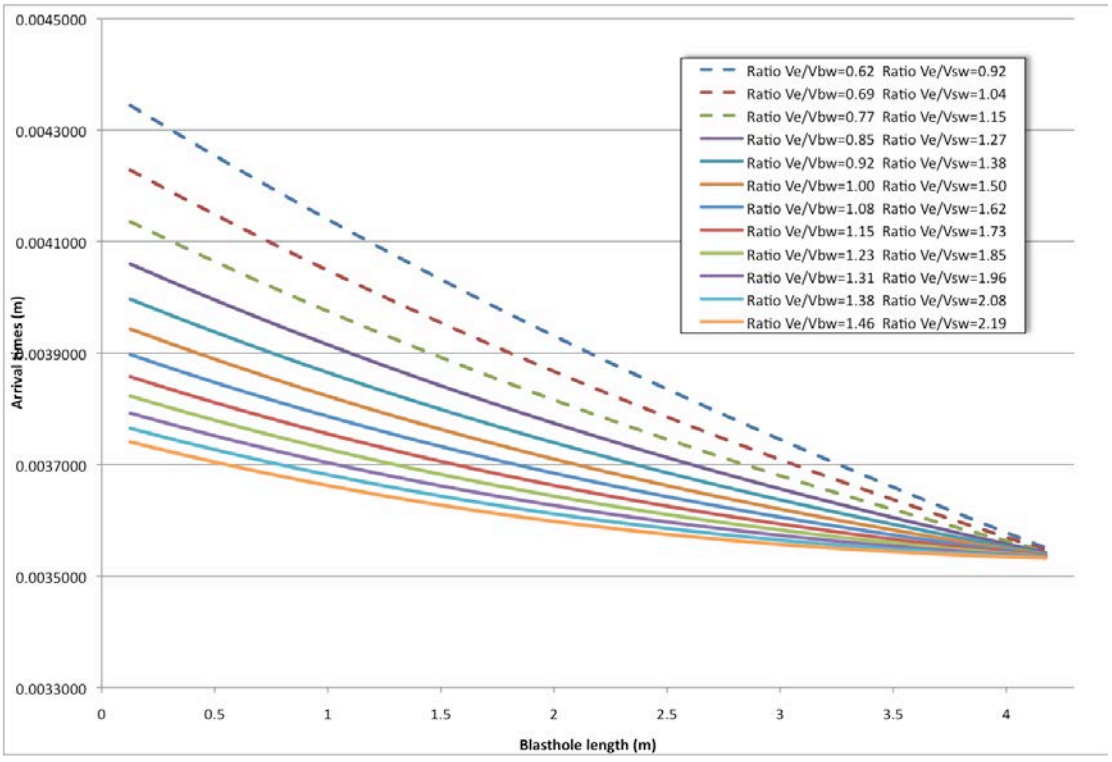

Figure 5.19 Arrival times – *Vbw*=6500m/s – Good rock quality – Y=5.0m Z=3.3m

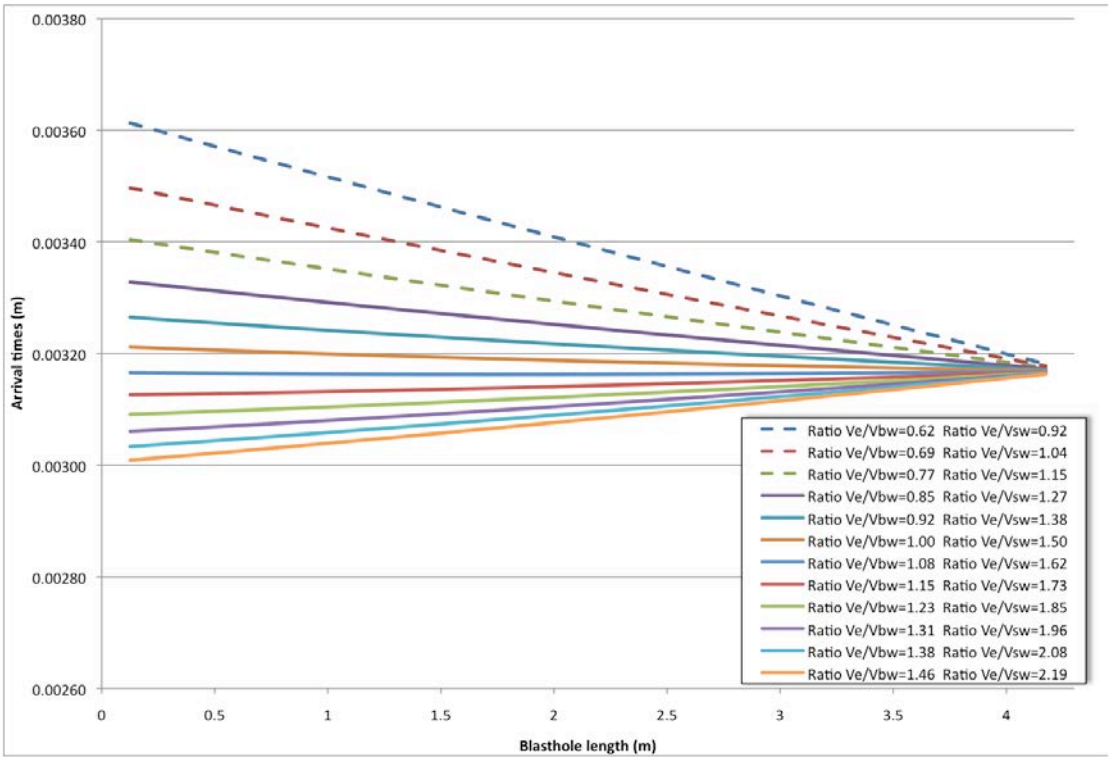

Figure 5.20 Arrival times – *Vbw*=6500m/s – Good rock quality – Y=0.2m Z=3.3m

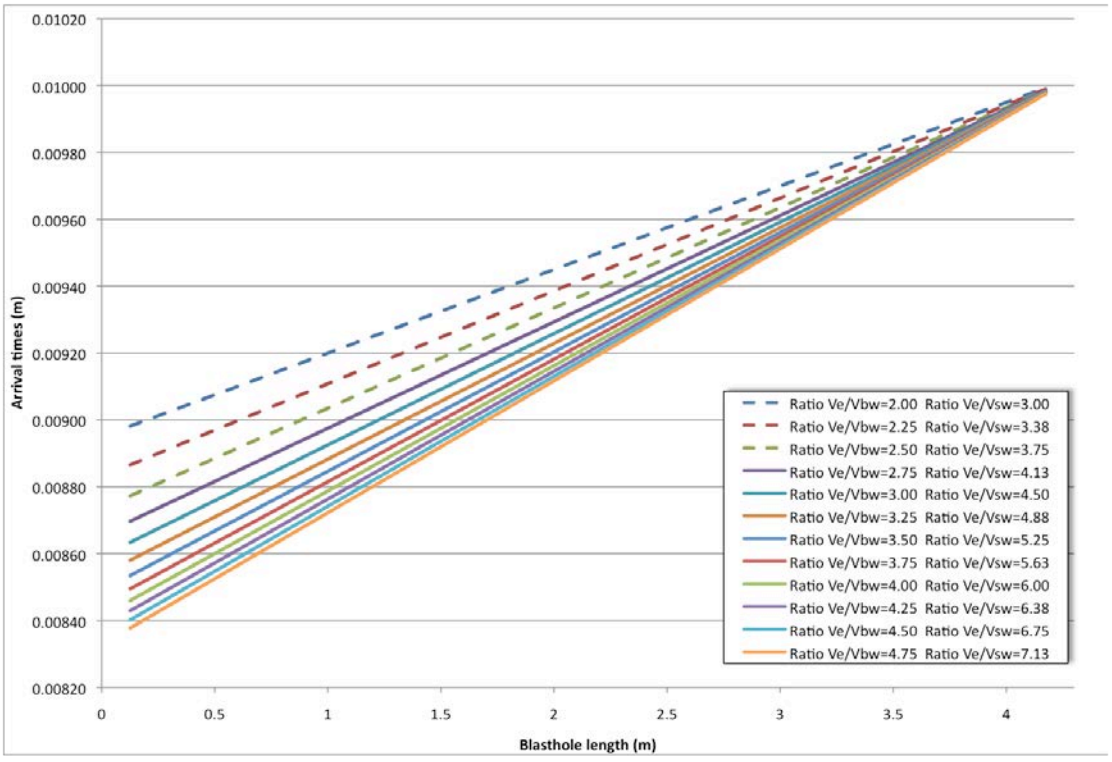

Figure 5.21 Arrival times – *Vbw*=2000m/s – Poor/Fair rock quality – Y=0.9m Z=0.0m

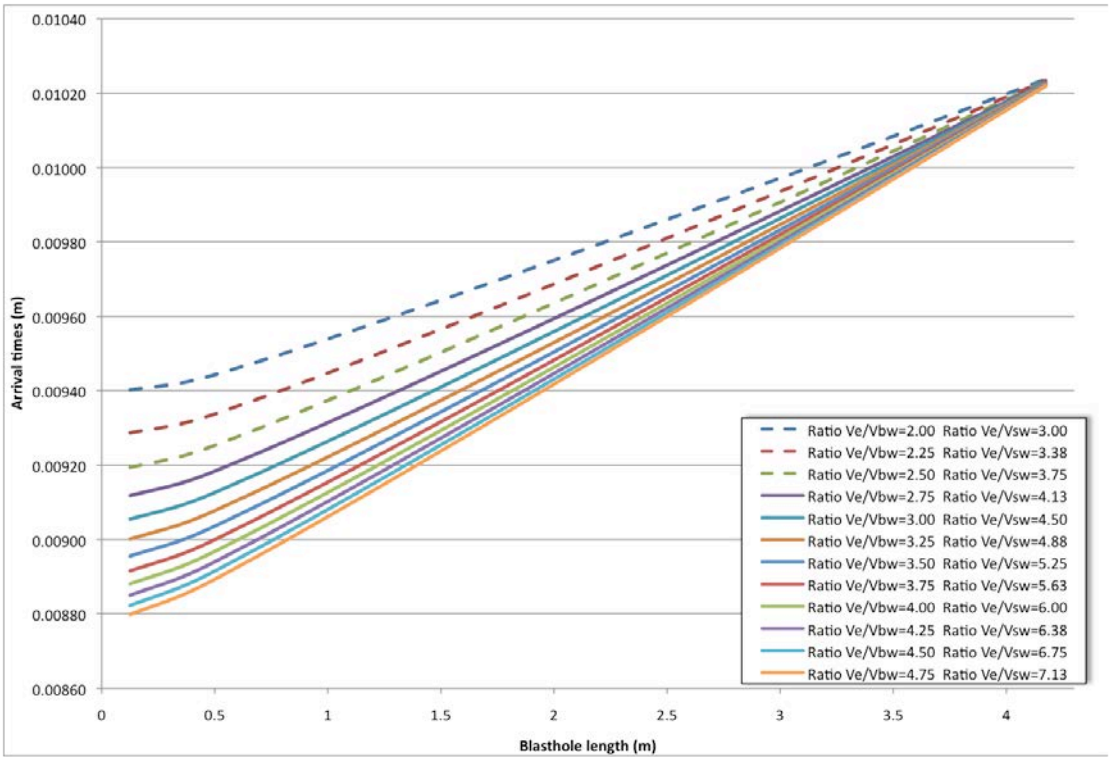

Figure 5.22 Arrival times – *Vbw*=2000m/s – Poor/Fair rock quality – Y=0.0m Z=0.0m

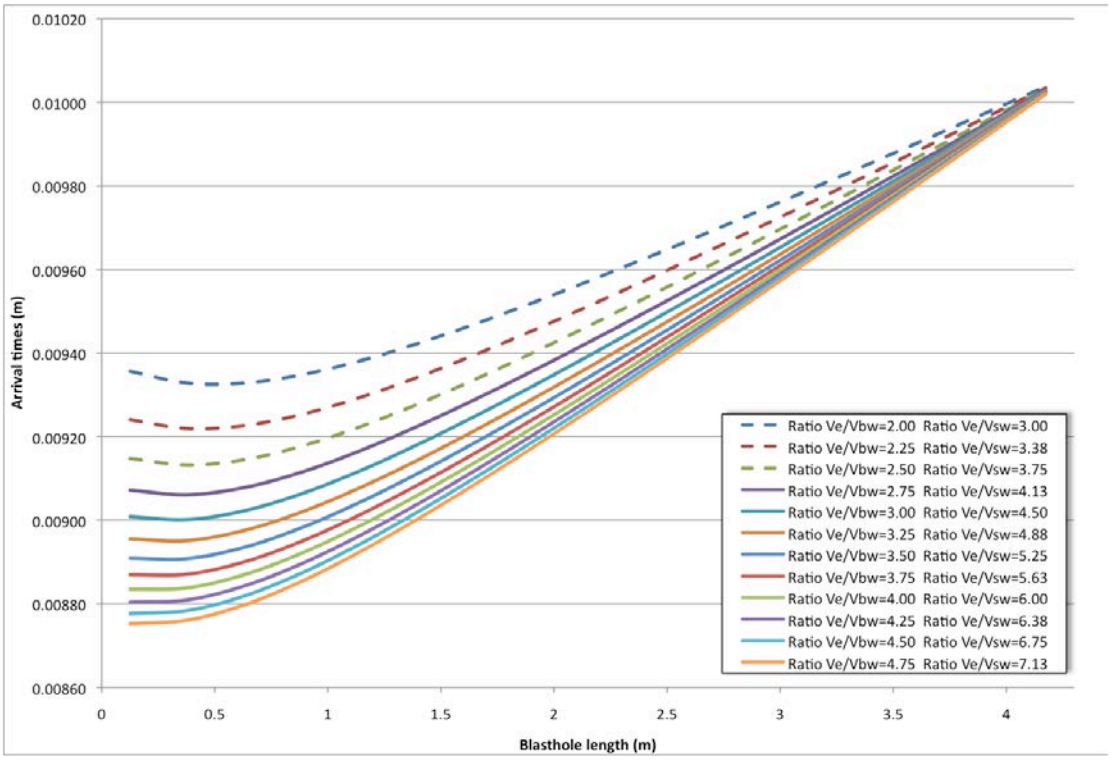

Figure 5.23 Arrival times – *Vbw*=2000m/s – Poor/Fair rock quality – Y=2.6m Z=3.5m

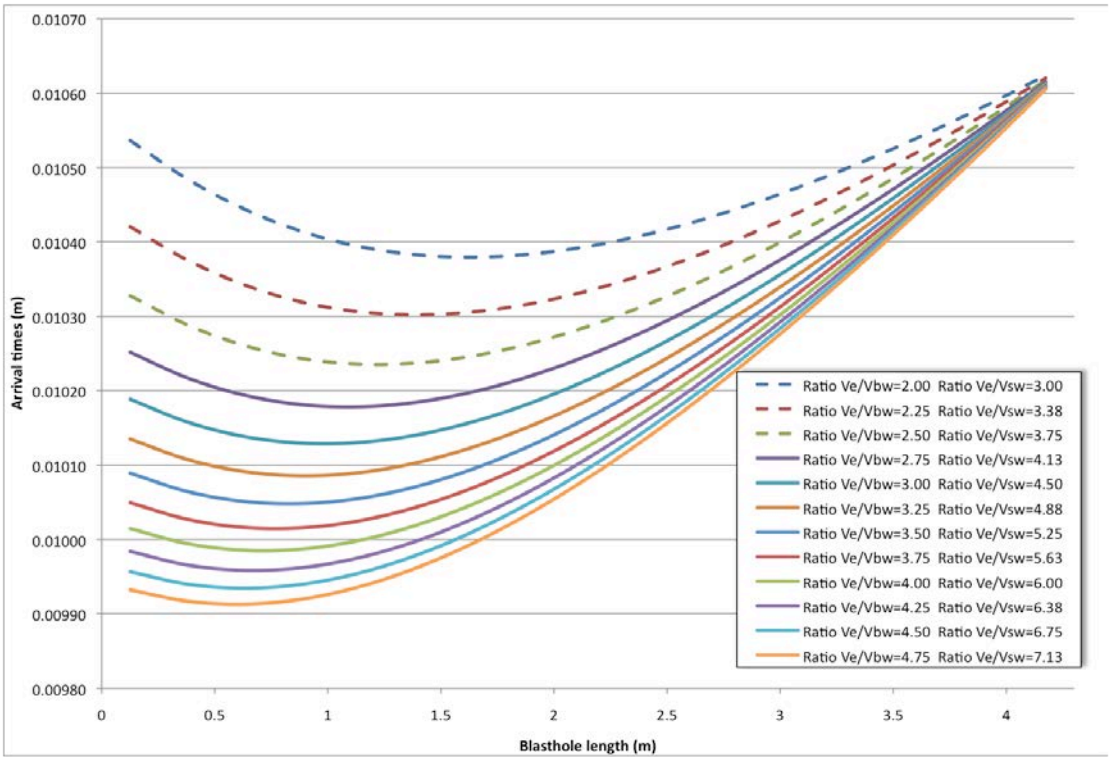

Figure 5.24 Arrival times – *Vbw*=2000m/s – Poor/Fair rock quality – Y=5.0m Z=3.3m

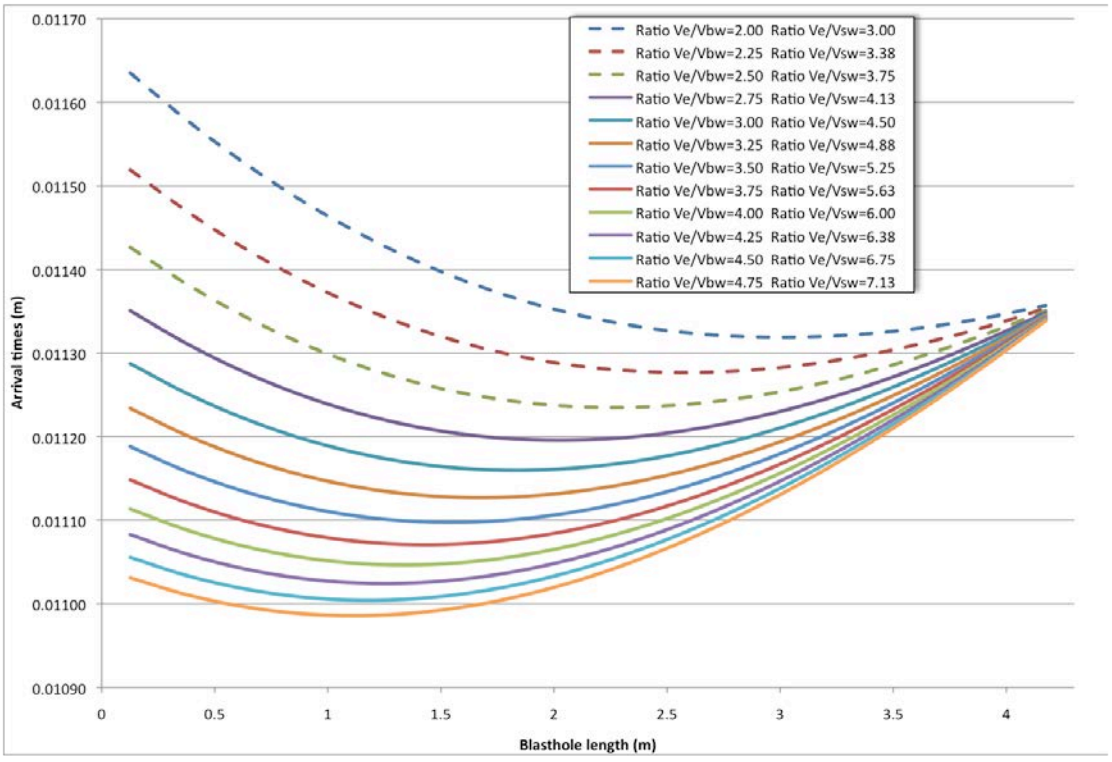

Figure 5.25 Arrival times – *Vbw*=2000m/s – Poor/Fair rock quality – Y=0.2m Z=3.3m

5.4 Particle Velocity Analysis – Drifting Case

5.4.1 Proposed *PPV* Equation – Analytical Background

The new proposed model quantifies *PPV* via the linear superposition of a number of waveforms generated for each of the packets or elements of the original blasthole column based on a scaled distance equation component (equation 29, in Section 2.2.10), a simplified particle velocity wave equation component (equation 7, in Section 2.2.3) and a simplified inelastic attenuation component (equation 13, in Section 2.2.4). The waveform of each packet is generated using a waveform generator, including the travelled distance to the point of interest (equations 41 and 43), the main predominant frequency of vibration, a pre-peak inelastic attack component and a post-peak inelastic attenuation component of the waveform, the standardized linear charge density, and a series of constants associated with these terms. Also, the arrival time delay of every packet is indirectly accounted for, via a phase shift of the waveform peaks by their respective arrival time based on equation 44. This new proposed linear superposition scaled distance general analytical equation (45), has been specifically designed for a drifting situation. The new proposed equation that is used to determine the *PPV* at any given time is presented as follows:

$$PPV(t) = K' \cdot \omega \cdot l^{\alpha} \cdot \sum_{ith=1}^{N} \frac{\Delta x^{\alpha}}{\left[\frac{\left(\sqrt{x_{ith}^2 + y_{BH}^2 + (z_{BH} - Z_{POD_{ith}})^2} \right)^{f1}}{Sin^{f3}(\beta_{ith})} + \left(\sqrt{d_{F-G}^2 + Z_{POD_{ith}}^2} \right)^{f2} \right]^{n}} \cdot Cos\left(\omega \cdot t + \phi_{ith}\right) \cdot e^{-(\delta_1, \delta_2)\omega \cdot t}$$

Eq. 45

Where,

- *K', α, n, f1, f2, and f3* are site specific constants (*f1=f2=f3*=1, most general case),
- ω is the angular frequency of the waveform,
- Δx is the packet height,
- ϕ_{ith} is the phase shift,
- δ_1 or δ_2 are the pre-peak attack or post-peak decay constants,
- *t* is the time at which *PPV* is determined,

- N is the number of packets, and
- β_{ith} is the angle between the ray formed from the i_{th} packet to the $PODi_{th}$ with the horizontal.

The sinusoidal waveform term of equation 45 is a simplified form of equation 7, in which the position x is considered fixed. Equation 45 incorporates the distance of every packet within the blasthole such that there is no need to define a unique distance value such as in the case of the *SD* factor, even for the far-field case. The delay in the arrival of every seismic waveform originating at each of the packets in the blasthole is accounted for, identical to the near-field case. In essence, the proposed linear scaled distance equation can incorporate into a single formulation the near- and intermediate/far-field components as a combined body (i.e., distance between packet centroid and *POD*) and surface (i.e., distance between *POD* and geophone) component of equation 45.

The flowcharts in Figure 5.26 - Figure 5.29 reflect the steps needed to determine *PPV* at a given distance from the blasthole location.

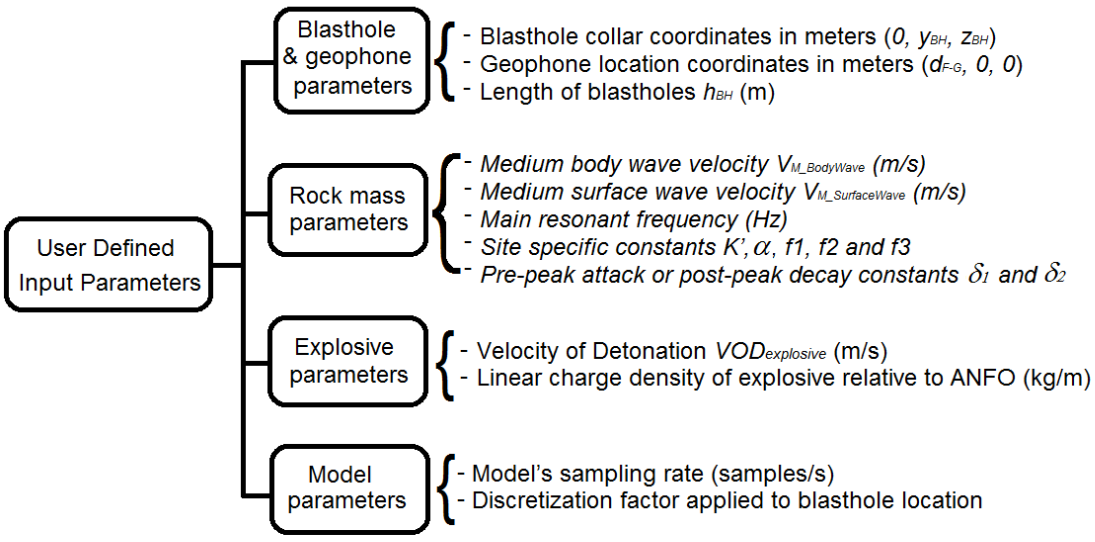

Figure 5.26 User defined modeling parameters flowchart

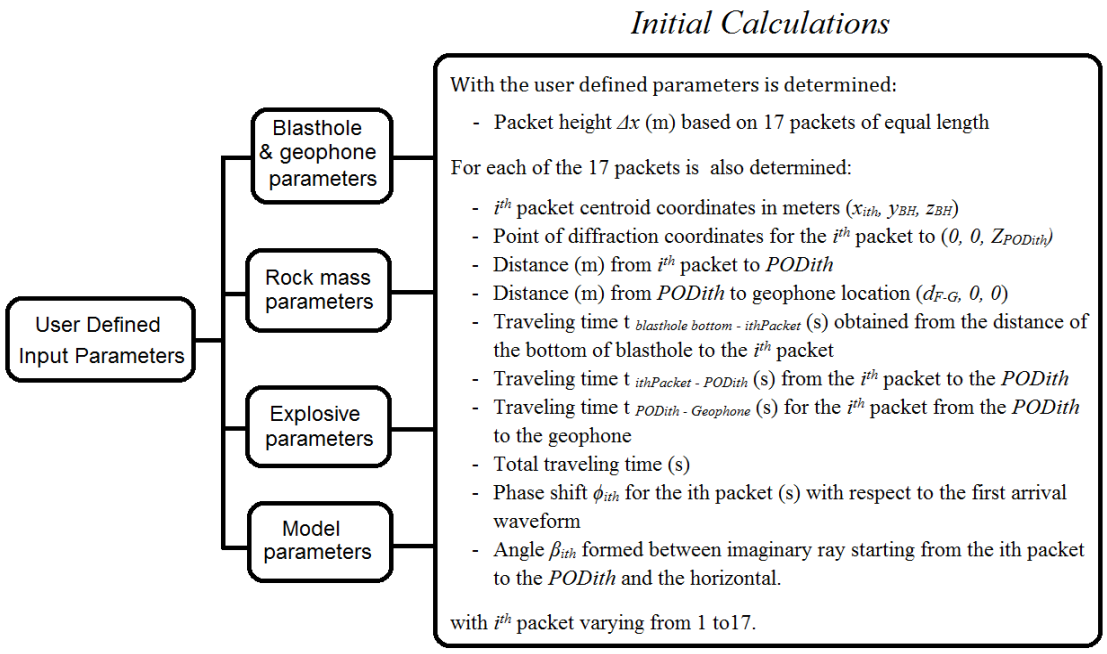

Figure 5.27 Initial calculations flowchart

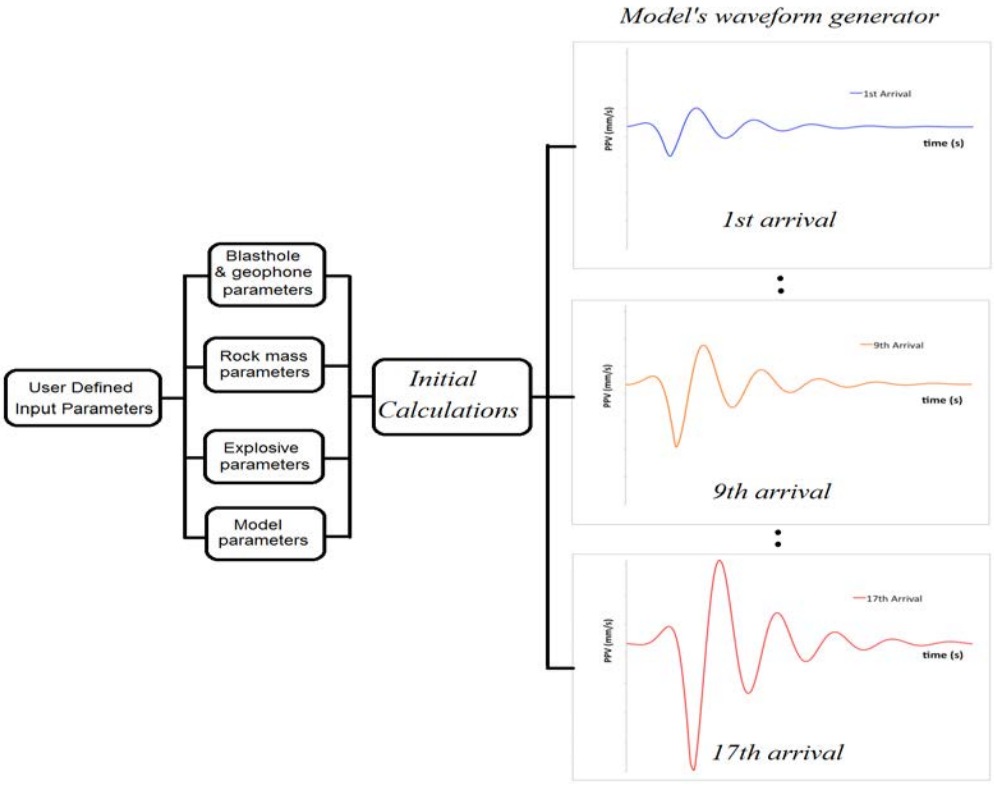

Figure 5.28 Model waveform generation

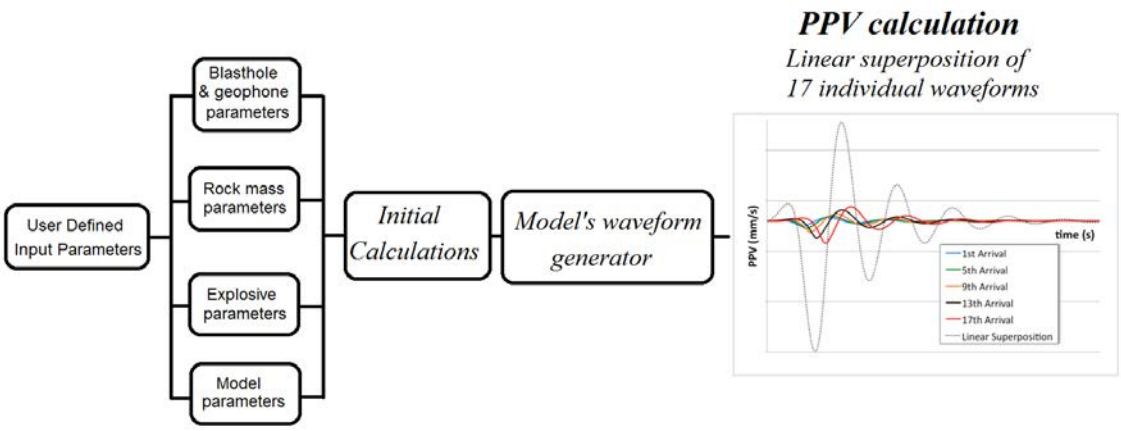

Figure 5.29 Model *PPV* determination from linear superposition of multiple waveforms

5.4.2 Determination of Constants

The model makes use of various constants necessary for accurate *PPV* prediction, which must be determined through a calibration process involving a number of blast rounds monitored using geophones. Various tests of signature blastholes (or blastholes without a free-face) should be done to establish the value of the constant *f1* (Eq. 45), owing to the fact that the far-field term is zero. The *f3* constants could be determined from, for example, detonation of packet size explosive charges (e.g., one cartridge of dynamite) located at different depths within the blasthole (where the geophone is installed on the drift wall). This enables the determination of the effect of the angle formed between the packet centroid and the point of diffraction at the face-wall intersection, on *PPV*. In the absence of data, the *Sin(β)* term could be ignored by defining *f3* as equal to zero (0). From records obtained for a number of geophones located at various distances from the blast, and once the *f1* and *f3* constants have been determined, the *K'*, α, and *f2* constants could be resolved.

Angular frequency, ω, is directly determined from the frequency content of the particle velocity versus time records. Similarly, the constants δ_1 and δ_2 are directly determined from the pre- and post-*PPV* versus time records.

The model calculates the phase shift term ϕ_{ith}, based on travelled distance, *VOD* of the explosive and body and surface wave propagation velocities, which can be experimentally determined.

5.4.3 Waveform Generation – Frequency Dependence

The following two figures show the results of generating two waveforms for two dissimilar frequencies, that is, dissimilar in terms of their representation of the rock mass quality. One is a high frequency waveform (1000Hz) corresponding to an extremely competent rock mass -- such as the Musselwhite Mine case -- and the other a low frequency (150Hz) waveform corresponding to a fair-poor rock mass quality -- such as the SSX Mine case. Figure 5.30 shows only 5 of the 17 waveforms corresponding to 5 of the 17 packets of a single blasthole generated at a frequency of 1000Hz, and Figure 5.31 shows those waveforms generated at a frequency of 150Hz. The scale of the horizontal time axis (x-axis) is equal for both examples. In these particular cases, there is no phase shift among the peaks of the waveforms, meaning that all the waveform peaks are coincident with the same time value. It is important to note that the peak velocity values of individual packets corresponding to the same location in the explosive column are exactly the same, irrespective of what frequency is used.

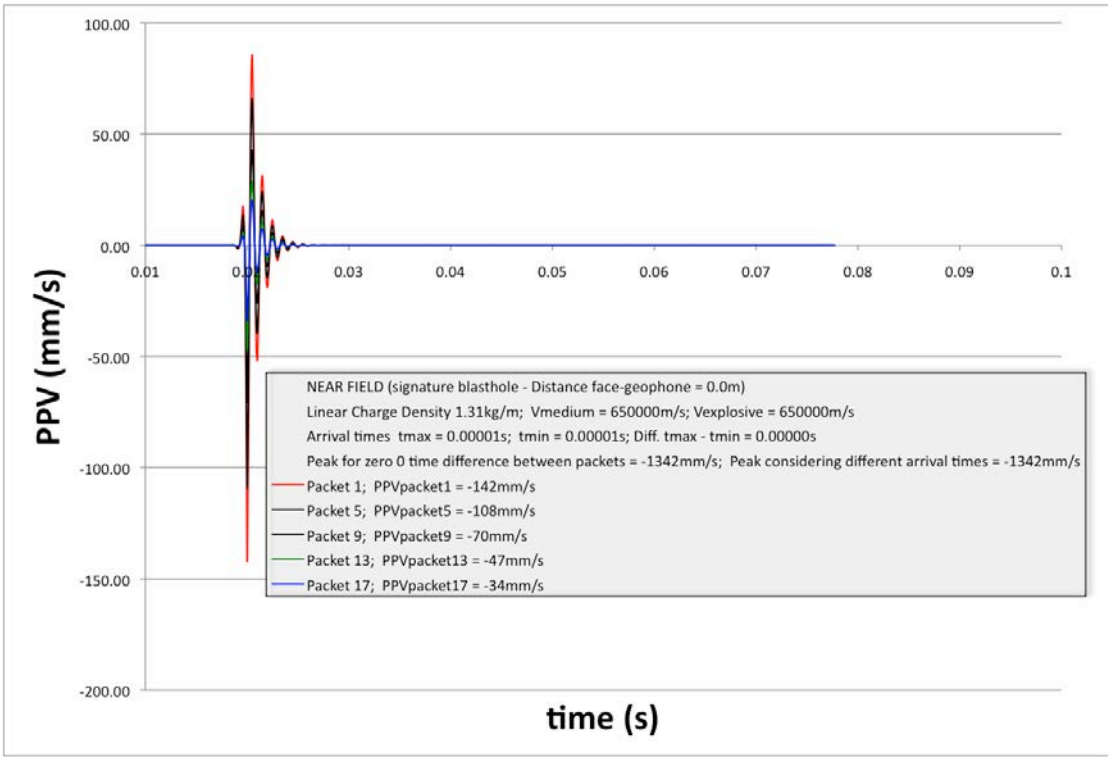

Figure 5.30 High frequency; Packets arrive simultaneously – Zero phase shift

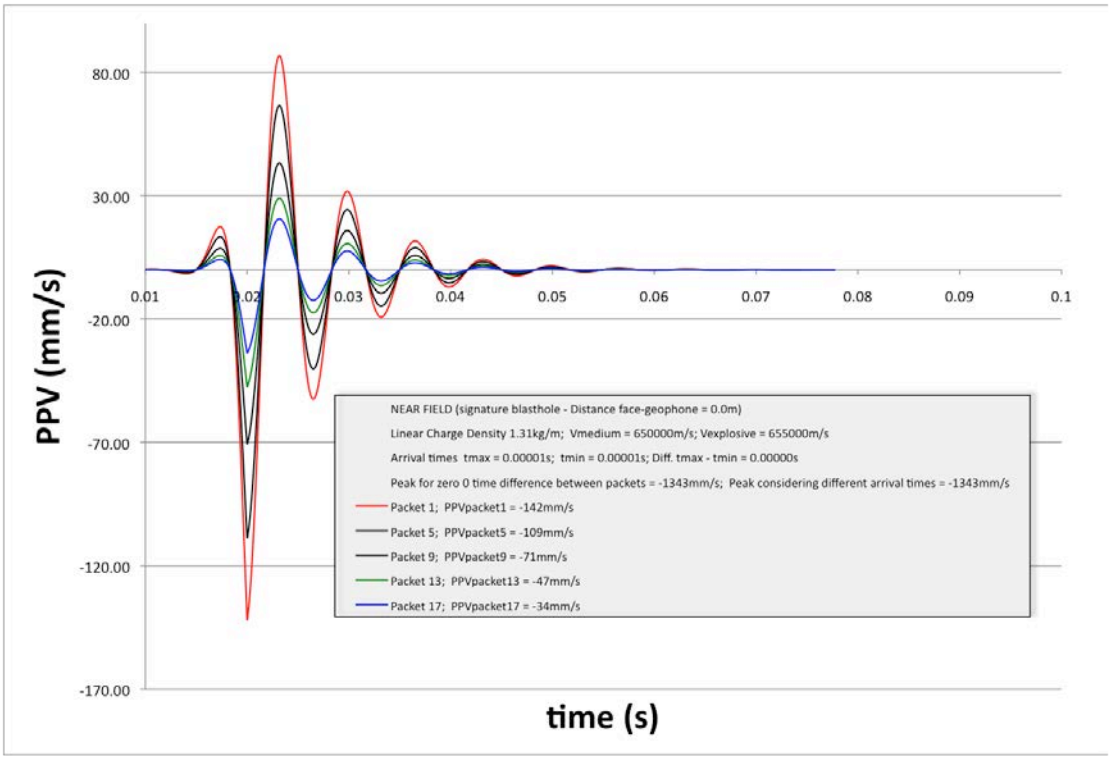

Figure 5.31 Low frequency; Packets arrive simultaneously – Zero phase shift

5.4.4 Phase Shift - Delayed Arrival Times of Peak Velocities

When an analysis to determine the *PPV* is done using the approximate physical values for the detonation velocity of an explosive and the velocity of propagation of the seismic wave in a rock mass medium, the value of taking into consideration the arrival times for each different packet in a given blasthole becomes clear. Figure 5.32 shows two waveforms that, due to excavation geometry, rock mass properties, and the explosive's properties, have arrived with a time delay (or shift).

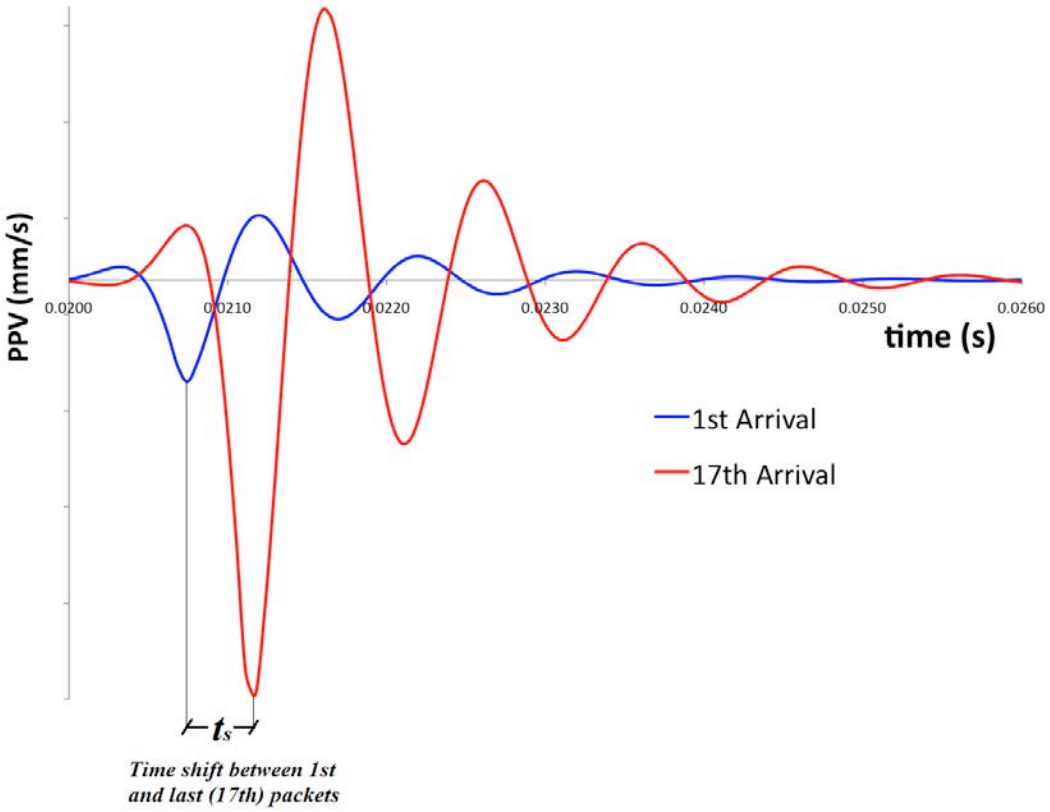

Figure 5.32 Waveform time shift between two packets

The model can be validated by examining results, in the near-field, using the Hustrulid-Lu equation, comparing them with the results obtained from the model. The Hustrulid-Lu equation is restricted to the near-field and assumes zero delay in the arrival times of the incremental charges. This can be emulated by assigning in the model extremely high velocities of detonation to the explosive and propagation velocities to the rock medium,

yielding zero time delay. To emulate this in the near-field, the model may be set to consider the location of the geophone as being at the face of the blasted round. As a result of this, the phase shift between the peaks of the individual packets becomes negligible, and both the Hustrulid-Lu equation (Eq. 29) and the model give equal values, packet by packet (Figure 5.33), in the calculation of particle velocity when of course, the same equivalent set of constants is used. Figure 5.33 shows 5 of the 17 waveforms that form part of the total number of waveforms pertaining to a single blasthole. The circles indicate the equivalent discrete value determined using the Hu-Lu equation. In this case, both the Hu-Lu values and the peaks of the waveforms give exactly same value, although the peaks of the waveforms are shifted in time. The effect is only noticeable when the linear superposition of all individual waveforms is applied.

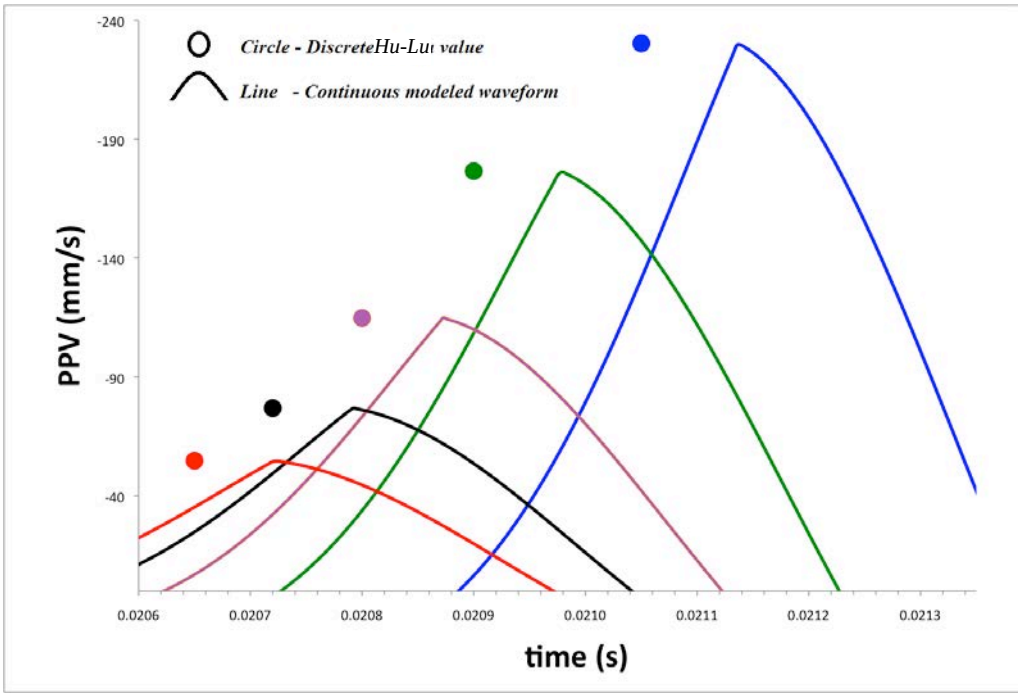

Figure 5.33 Discrete Hustrulid-Lu values and continuous modeled waveforms

The values of every single peak waveform generated for each packet comprising the final *PPV* value for a given blasthole will be identical to those obtained using the Hustrulid-Lu equation (Eq. 29). On the other hand, if the time shifts are taken into account, the final linear superposition of the set of waveforms pertaining to a single blasthole would yield *PPV* values that are always lower than those using the Hustrulid-Lu equation (Eq. 29).

The *PPV* values generated via Hustrulid-Lu will always be the maximum obtainable values.

Note that at the peak of each waveform in Figure 5.33, the shape is not smooth but rather sharp. The reason for this is the use of different attack and decay constants in order to adjust the model's pre- and post-peak waveform shape to the recorded waveform shape.

Figure 5.34 and Figure 5.35 compare *PPV* obtained using both methods, where the model applies frequencies of 1000Hz and 150Hz with zero phase shifts.

The results obtained using the Hustrulid-Lu equation (Eq. 29) are plotted with a green circle, whereas the model results are plotted by means of a waveform indicated by a red circle, symbolizing their peaks. As can be seen, both methods yield the same results.

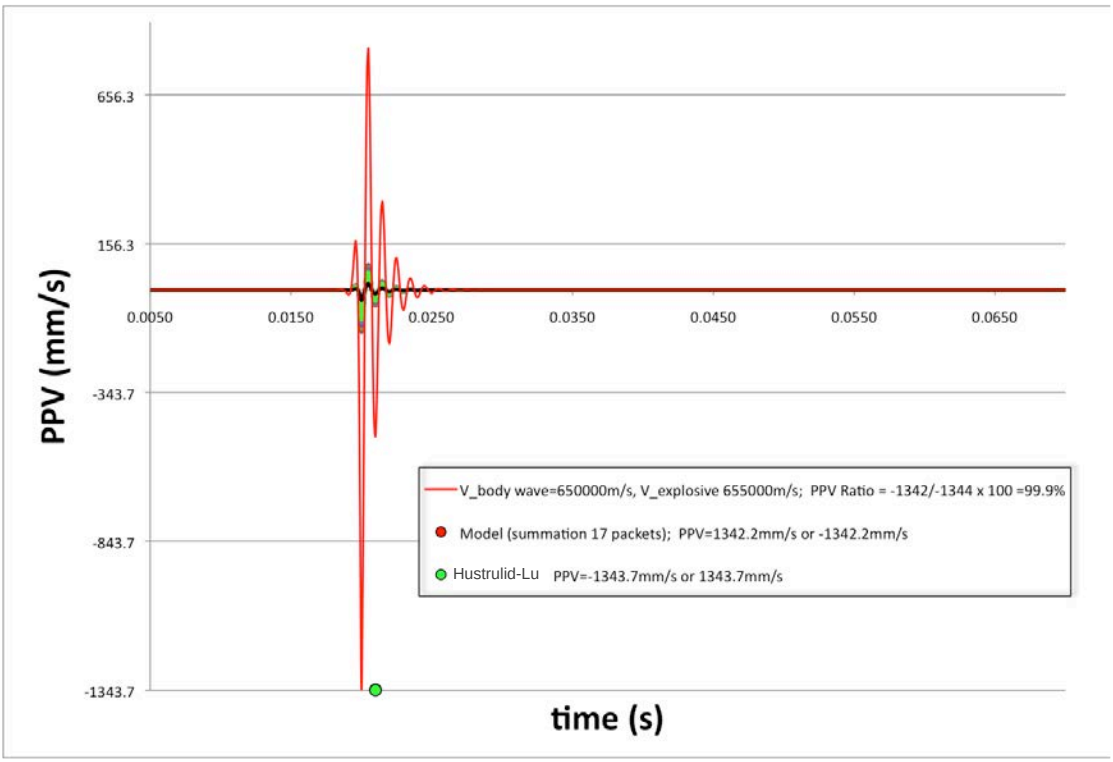

Figure 5.34 High frequency waveform; *PPV* modeled versus *PPV* from Hustrulid-Lu equation (2000) – Zero phase shift

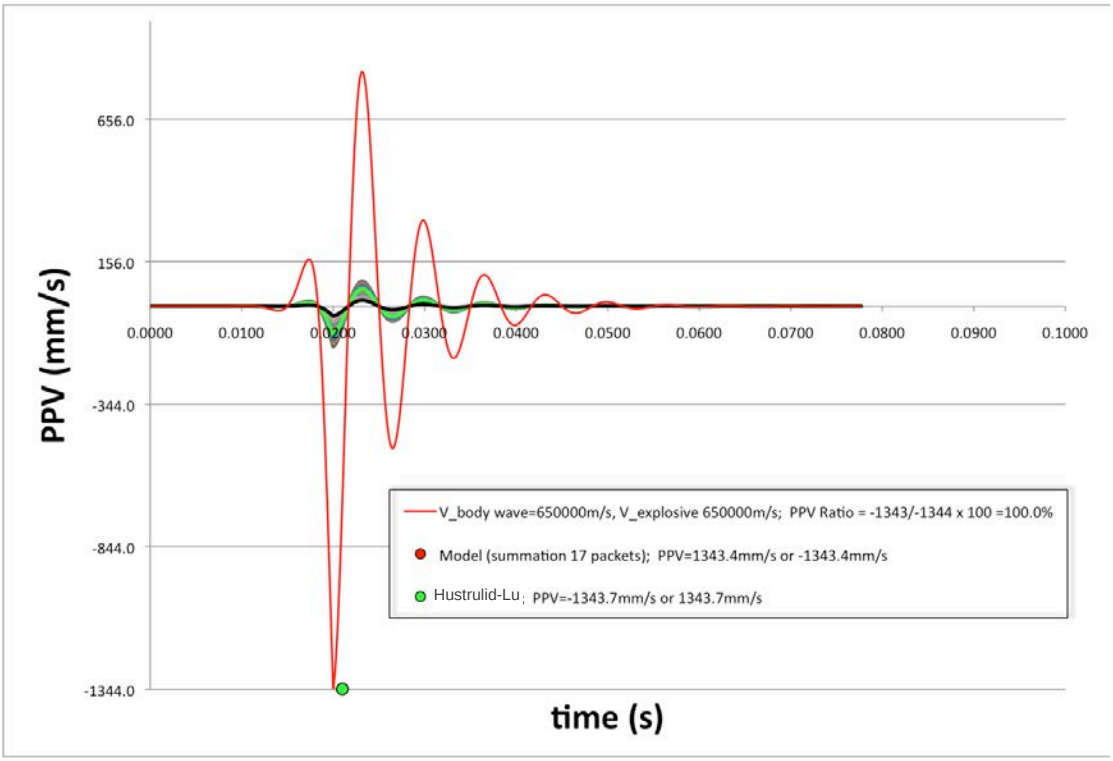

Figure 5.35 Low frequency waveform; *PPV* modeled versus *PPV* from Hustrulid-Lu equation (2000) – Zero phase shift

Similarly, Figure 5.36 through Figure 5.47 compare *PPV* obtained using both methods, for the same set of frequencies, but in this case, the phase shift has been varied from zero, and set according to the time delay associated with the packet's arrival time. Reasonable values for the *VOD* of the explosive and the rock's sound velocity have been employed. A series of *VOD* values ranging from 10,000m/s down to 3,200m/s, corresponding to different explosives types, densities, and confinement conditions were tested. The propagation velocities of the seismic wave for a high velocity (6500m/s), high frequency (1000Hz) good rock mass quality and a slow velocity (2000m/s), low frequency (150Hz) fair/poor rock mass quality, were also part of these modeling experiments.

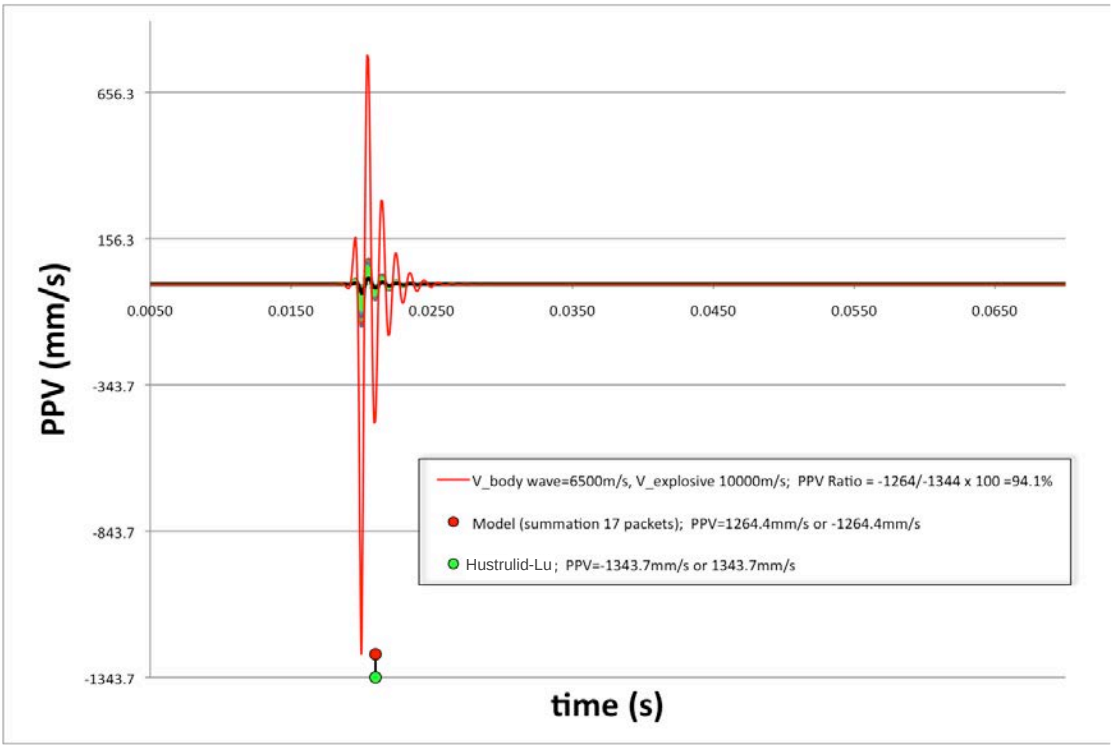

Figure 5.36 High Velocity and Frequency; *PPV* modeled vs. *PPV* from Hustrulid-Lu equation Vexplosive=10,000m/s

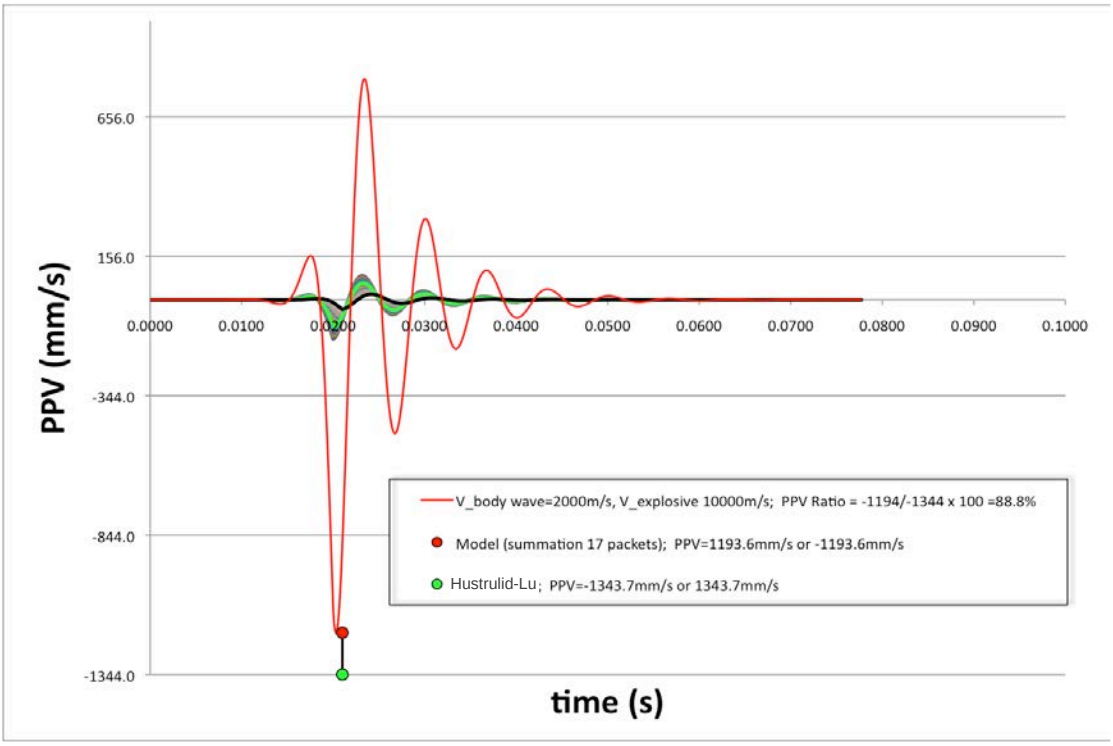

Figure 5.37 Low Velocity and Frequency; *PPV* modeled vs. *PPV* from Hustrulid-Lu equation Vexplosive=10,000m/s

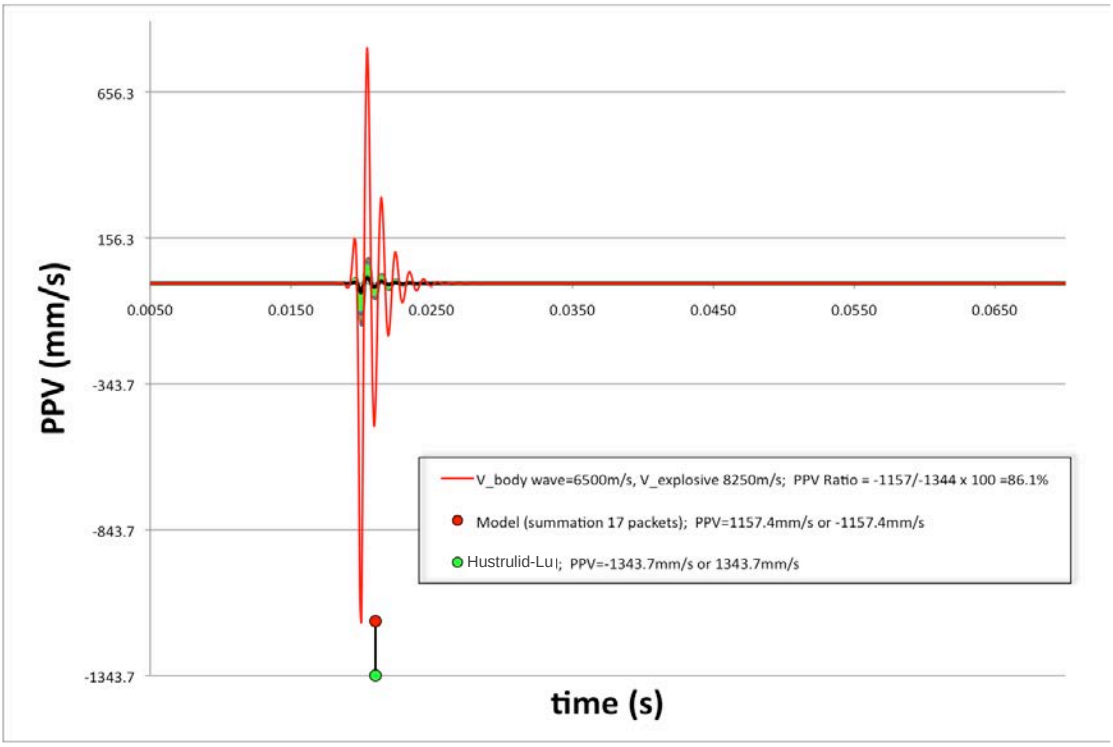

Figure 5.38 High Velocity and Frequency; *PPV* modeled vs. *PPV* from Hustrulid-Lu equation Vexplosive=8,250m/s

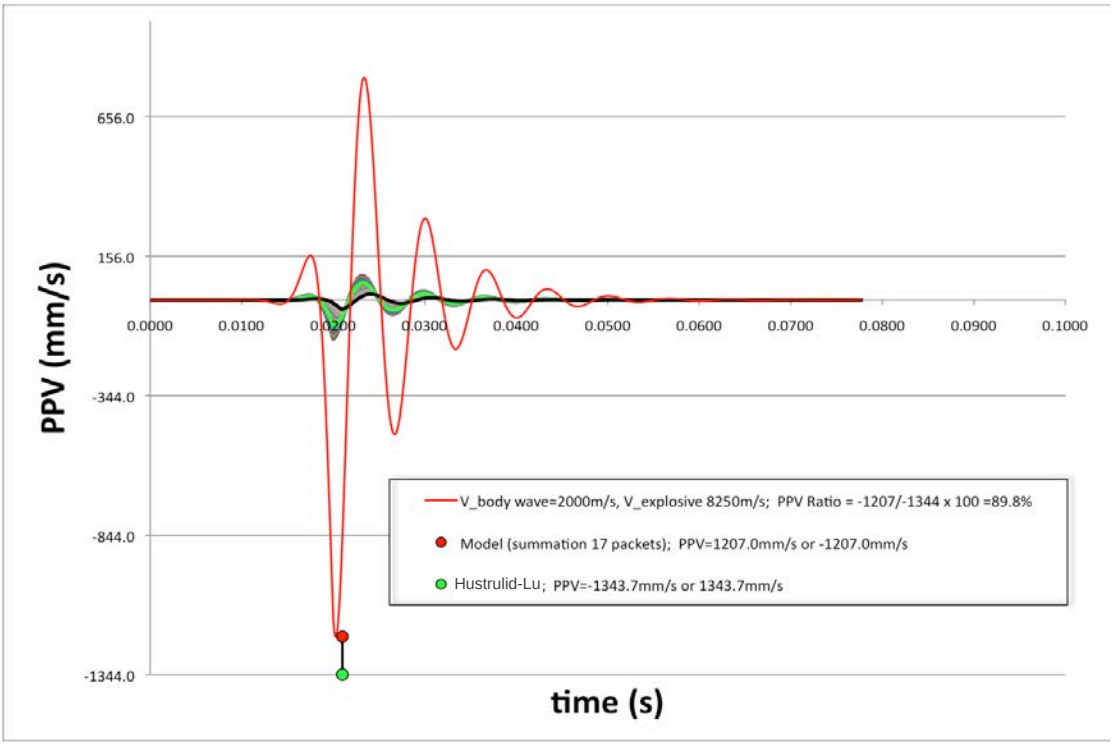

Figure 5.39 Low Velocity and Frequency; *PPV* modeled vs. *PPV* from Hustrulid-Lu equation Vexplosive=8,250m/s

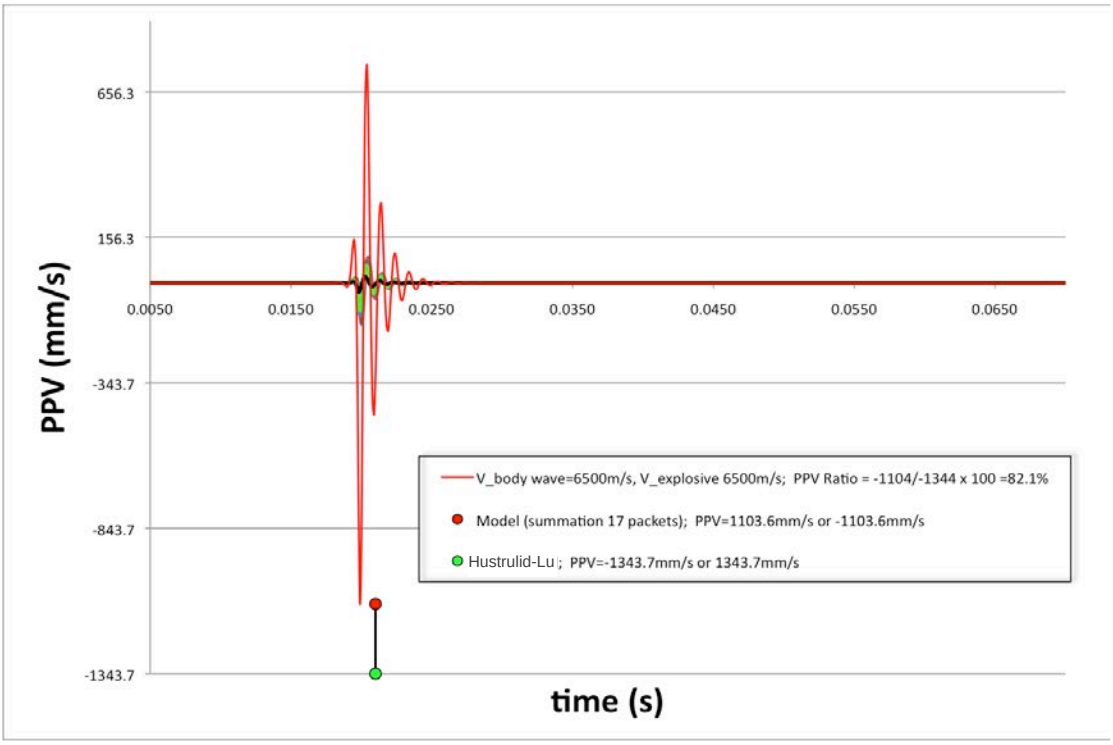

Figure 5.40 High Velocity and Frequency; *PPV* modeled vs. *PPV* from Hustrulid-Lu equation Vexplosive=6,500m/s

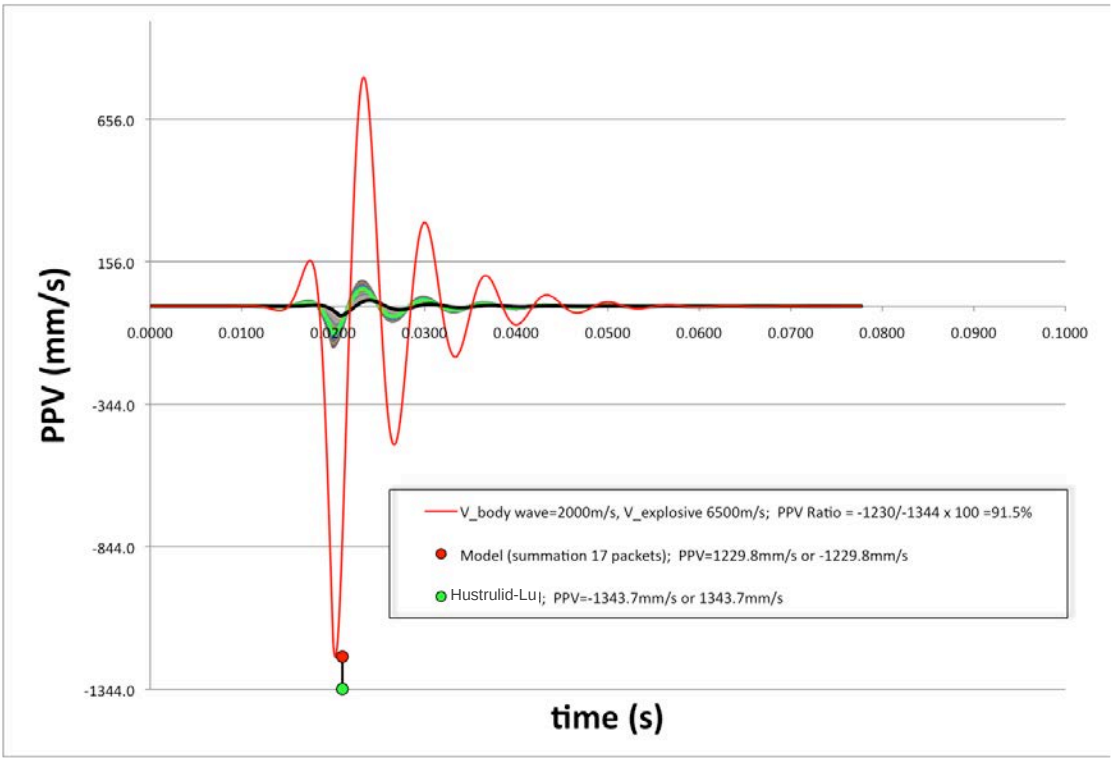

Figure 5.41 Low Velocity and Frequency; *PPV* modeled vs. *PPV* from Hustrulid-Lu equation Vexplosive=6,500m/s

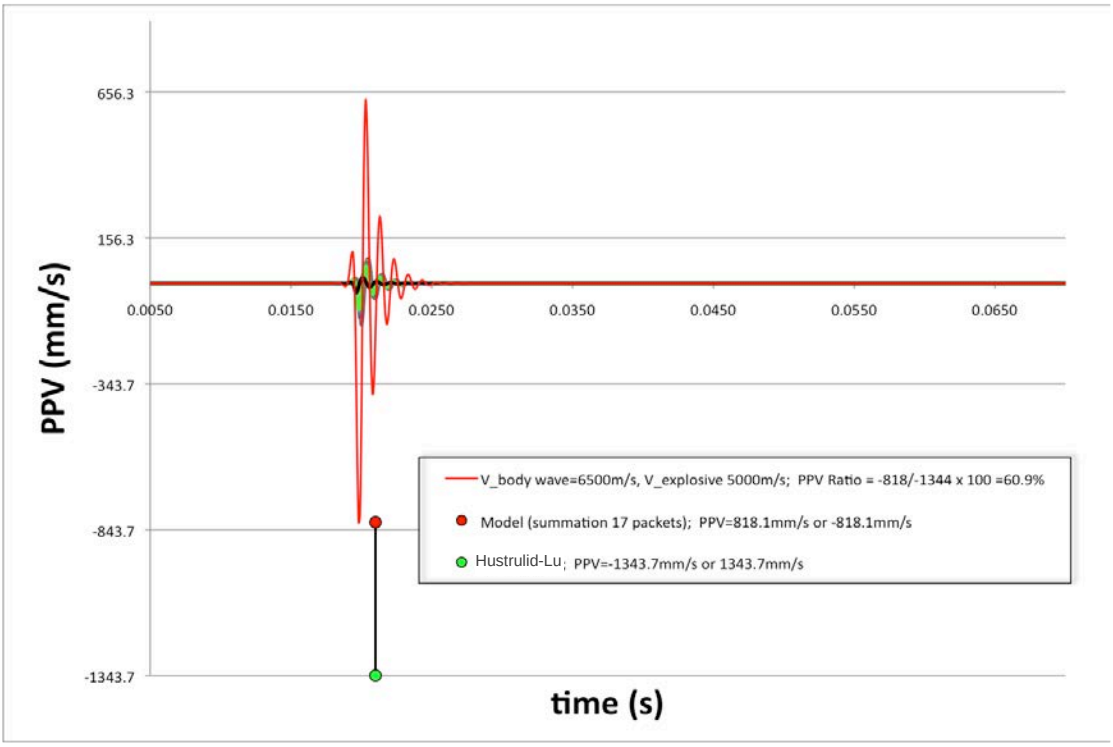

Figure 5.42 High Velocity and Frequency; *PPV* modeled vs. *PPV* from Hustrulid-Lu equation Vexplosive=5,000m/s

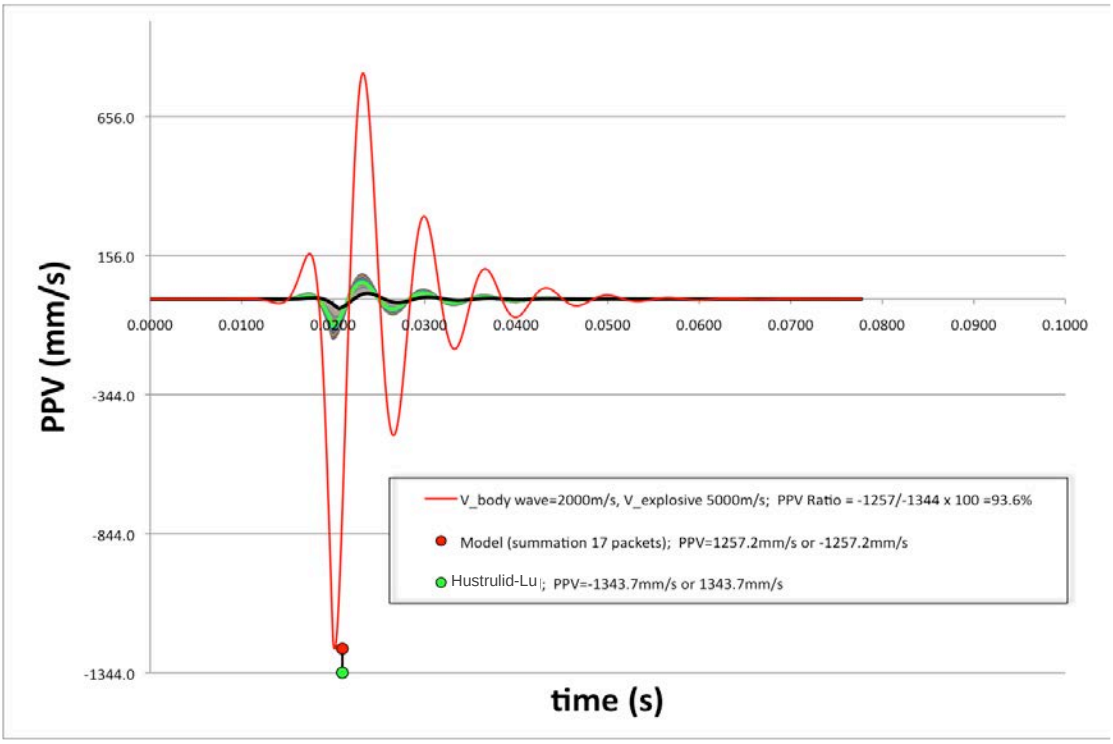

Figure 5.43 Low Velocity and Frequency; *PPV* modeled vs. *PPV* from Hustrulid-Lu equation Vexplosive=5,000m/s

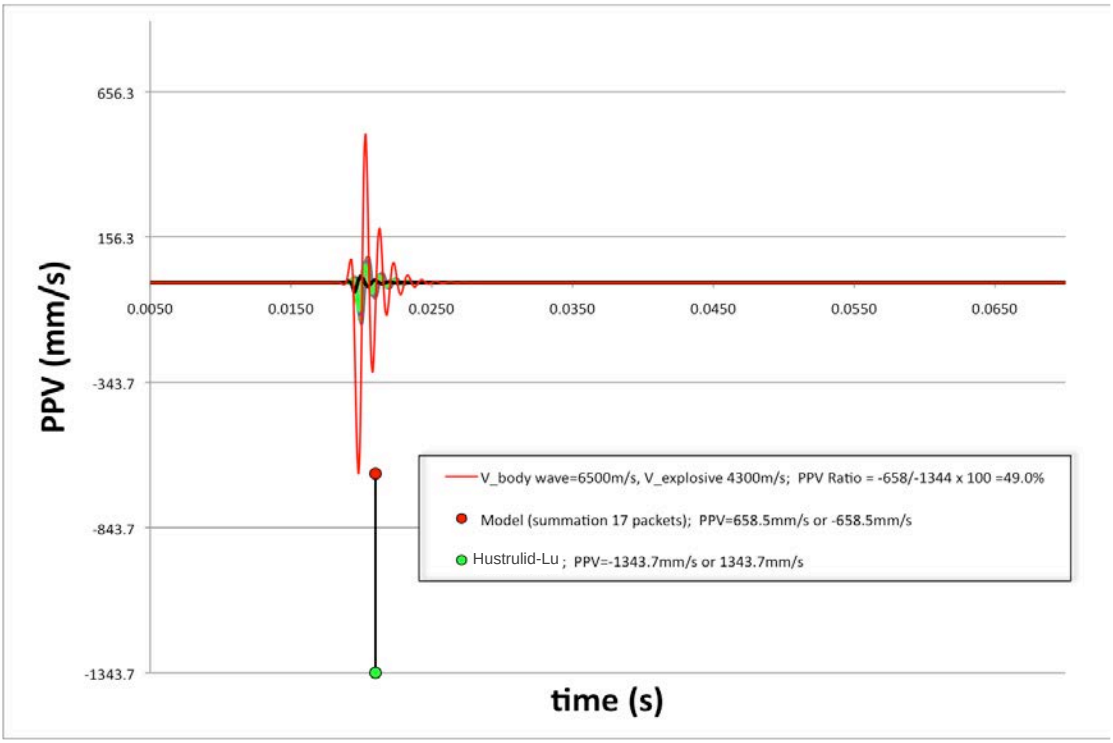

Figure 5.44 High Velocity and Frequency; *PPV* modeled vs. *PPV* from Hustrulid-Lu equation Vexplosive=4,300m/s

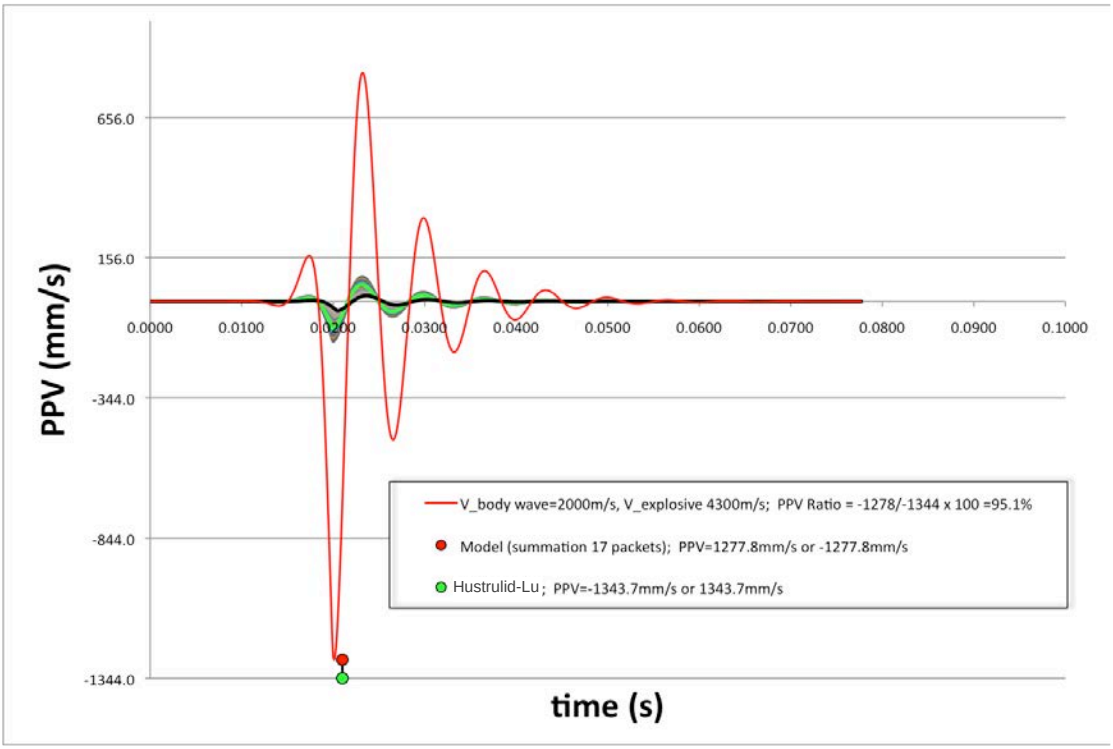

Figure 5.45 Low Velocity and Frequency; *PPV* modeled vs. *PPV* from Hustrulid-Lu equation Vexplosive=4,300m/s

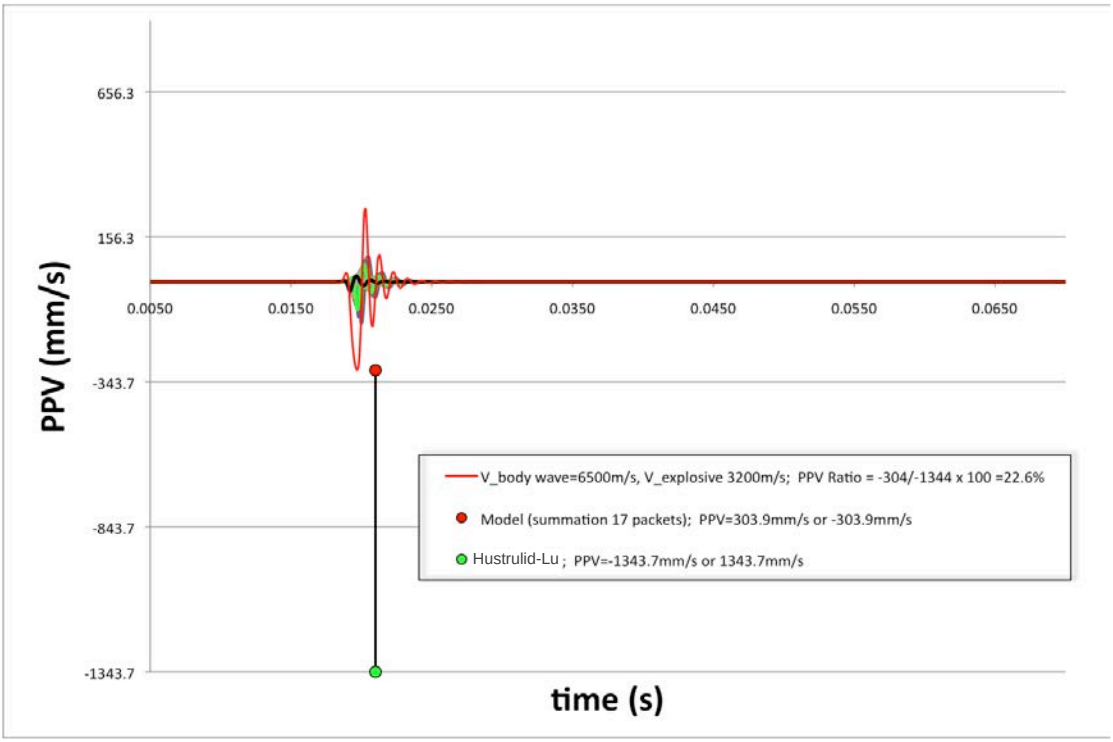

Figure 5.46 High Velocity and Frequency; *PPV* modeled vs. *PPV* from Hustrulid-Lu equation Vexplosive=3,200m/s

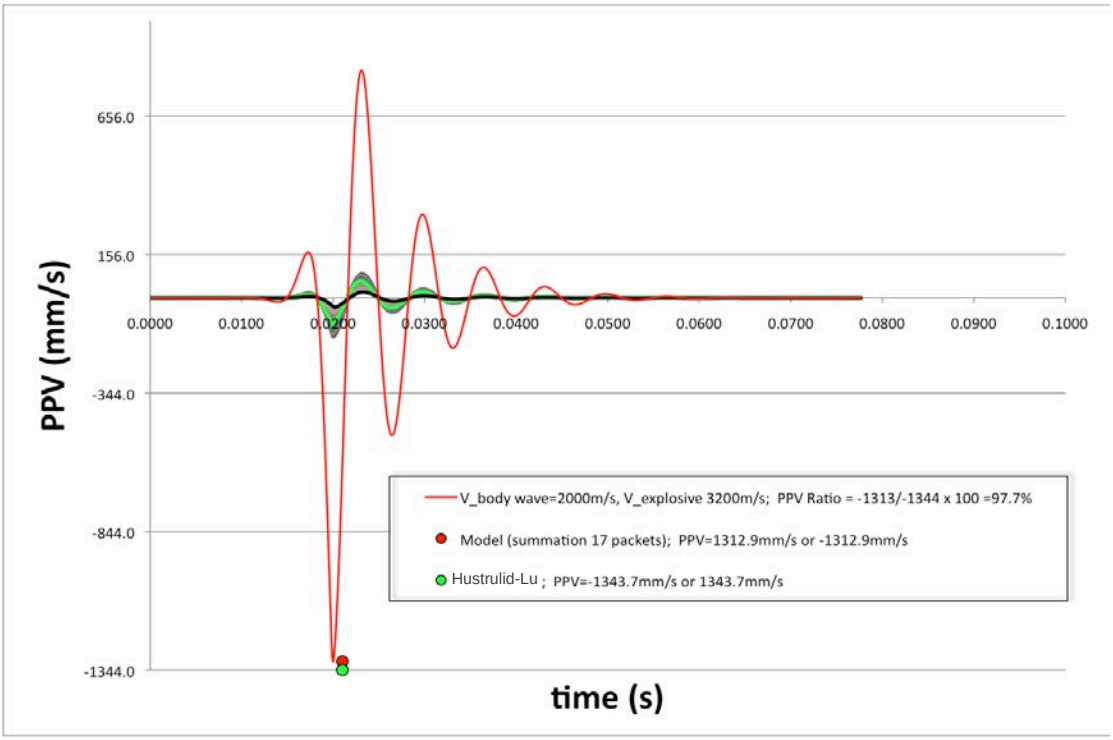

Figure 5.47 Low Velocity and Frequency; *PPV* modeled vs. *PPV* from Hustrulid-Lu equation Vexplosive=3,200m/s

From the previous results, the significance of arrival times in the determination of the *PPV* sustained by the rock at a specific location from the blast, becomes clear. The greater the differences in arrival time of individual packet waveforms, the greater the decrease in final *PPV* value. Final *PPV* value is determined by the linear superposition of individual packet waveforms while the peak value of each individual packet remains unchanged.

5.4.5 Resonance Vibration Frequency Range of a Rock Mass Medium

So far the model has been used to determine *PPV* for a unique dominant frequency from a broader range of natural frequencies at which the rock mass vibrates. This section is intended to provide proof that the model can be used to analyze *PPV* obtained from a range of frequencies that could be generated from a single blasthole. Multi-frequency analysis is beyond the scope of this research and its relevance could be determined through continuation of this research in future investigations.

Figure 5.48 shows the *PPV* of individual waveforms, for a single blasthole location, each generated at a different frequency of oscillation. Each of the waveforms plotted is obtained from the linear superposition of each of the 17 waveforms generated at a single frequency of oscillation.

An appropriate multi-frequency analysis should determine the amplitude of the waveform (*PPV*) obtained within a short range of frequencies, and the propagation velocity for this frequency range. The procedure would be repeated successively, to account for the entire spectrum of frequencies propagating through the rock mass. This is done in the same way as was the case in Chapter 3, shown in Figure 3.12 through Figure 3.15, in which the recorded waveform was filtered on a pre-established frequency range, where the amplitude of the waveform is then determined for that specific frequency range. The procedure would then be repeated for each subsequent frequency range, in turn, until the whole spectrum of frequencies for the given rock mass is covered.

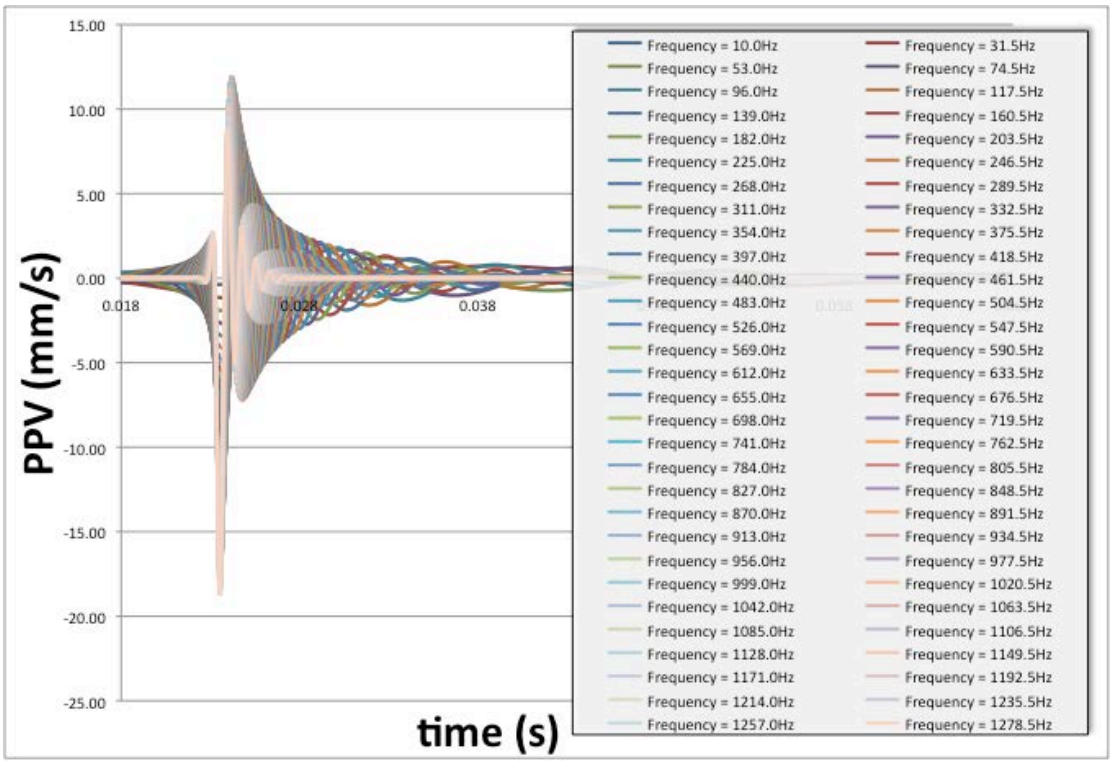

Figure 5.48 Waveforms generated at various frequency ranges

Figure 5.49 displays the linear superposition of the combined waveforms obtained for each individual frequency tested and displayed in Figure 5.48. It is important to note that there could be a delay in arrival time for each of the waveforms generated at any particular frequency. Kolsky (Kolsky, 1953) addressed this issue where velocity dispersion caused high-frequency plane waves to travel faster than the low frequency waves. In this particular example, no considerations were made with respect to propagation velocities for a particular frequency value tested, which could have potentially yielded differences in their arrival times, and thus their *PPV* results.

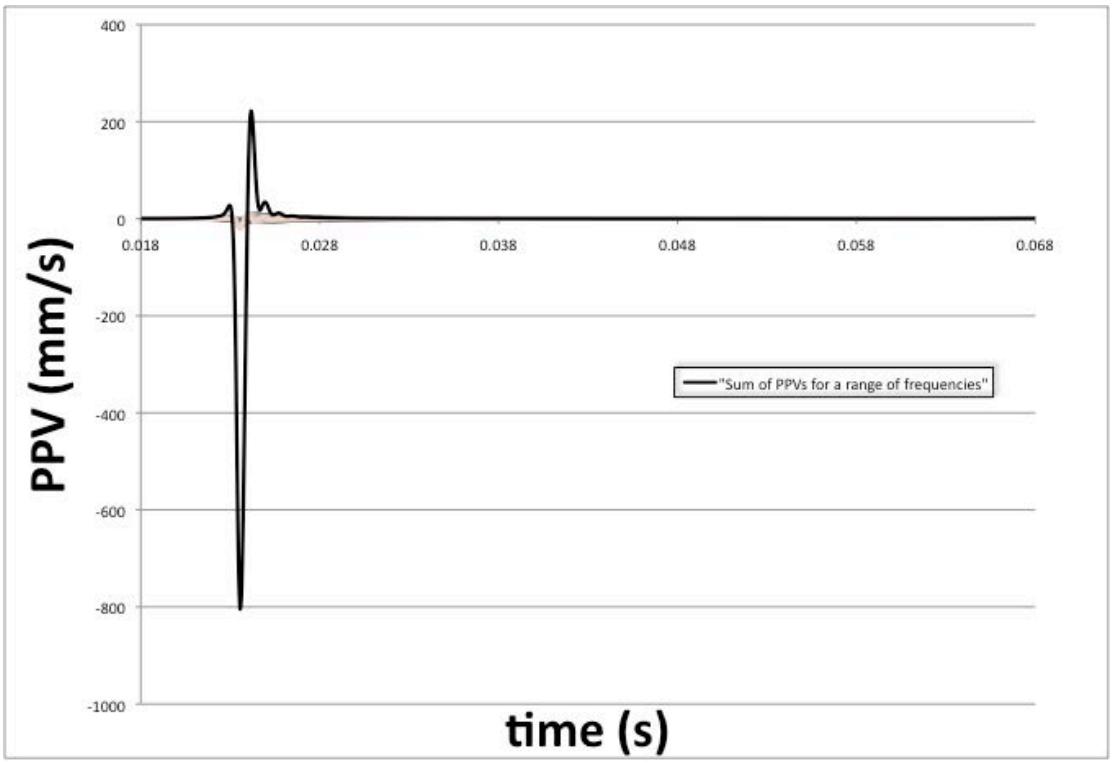

Figure 5.49 Linear superposition of waveforms generated at various frequency ranges

5.4.6 Model Sampling Rate

Different sampling rates can also be accounted for in the model. The sampling rate is the number of samples per second. This is also a parameter selectable on the dataloggers and can be set up at fixed rates of 1024, 2048, 4096, 8192, and 16384 samples per second. Naturally, the higher the sampling rate, the larger the memory consumption. This is particularly relevant when a limited amount of memory is available, as is the case with Minimate Plus® datalogger, because, for example, an unintentional triggering of the datalogger recording process, as when machinery is operating nearby, could rapidly cause the memory to fill up, and thereby prevent monitoring of the actual blasting event.

Another important issue to consider regarding the sampling rate is that lower sampling rates cannot record the peak as accurately as is the case at higher sampling rates. As an illustration, the sampling rate of the model was varied from an extremely high value of 500,000Hz down to 4,096Hz. *PPV* obtained at a sampling rate of 500,000Hz is 660mm/s (Figure 5.50), whereas *PPV* obtained at a sampling rate of 16,384Hz is 655mm/s (Figure

5.51), which represents a 0.8% error. *PPV* obtained at a sampling rate of 4,096Hz is 601mm/s (Figure 5.53), or an 8.9% error.

Figure 5.50 through Figure 5.54 show the resulting *PPV* waveform values obtained using different sampling rates.

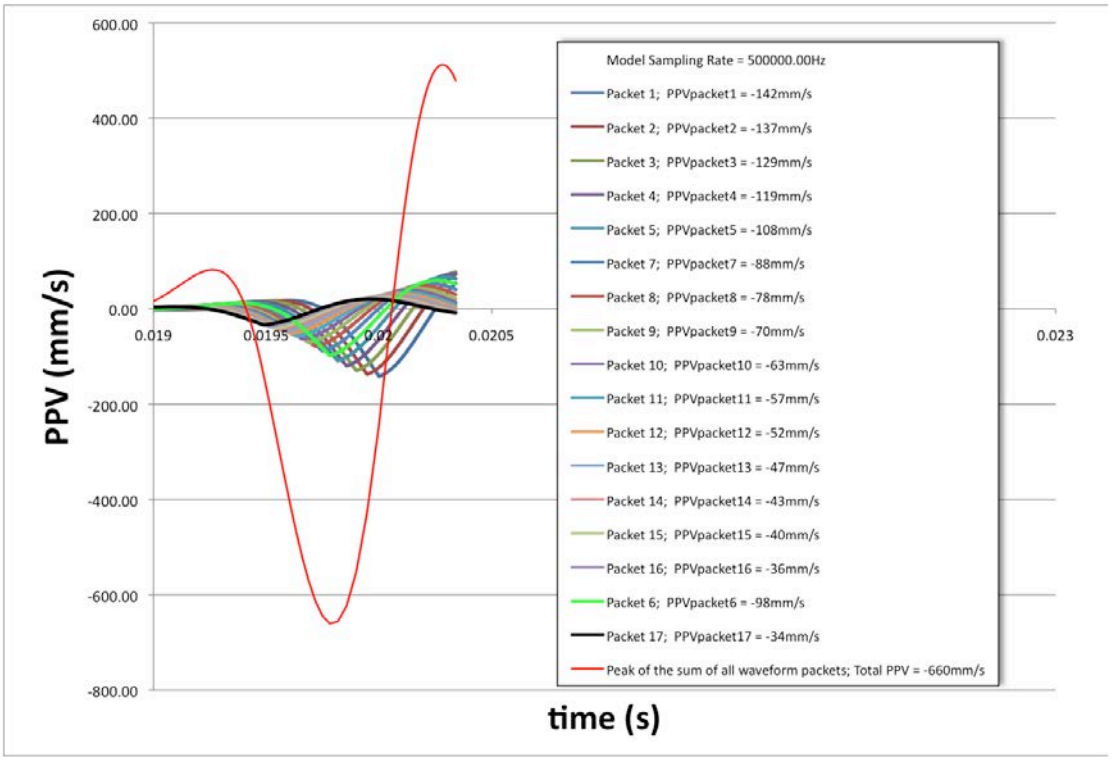

Figure 5.50 Model sampling rate = 500,000Hz

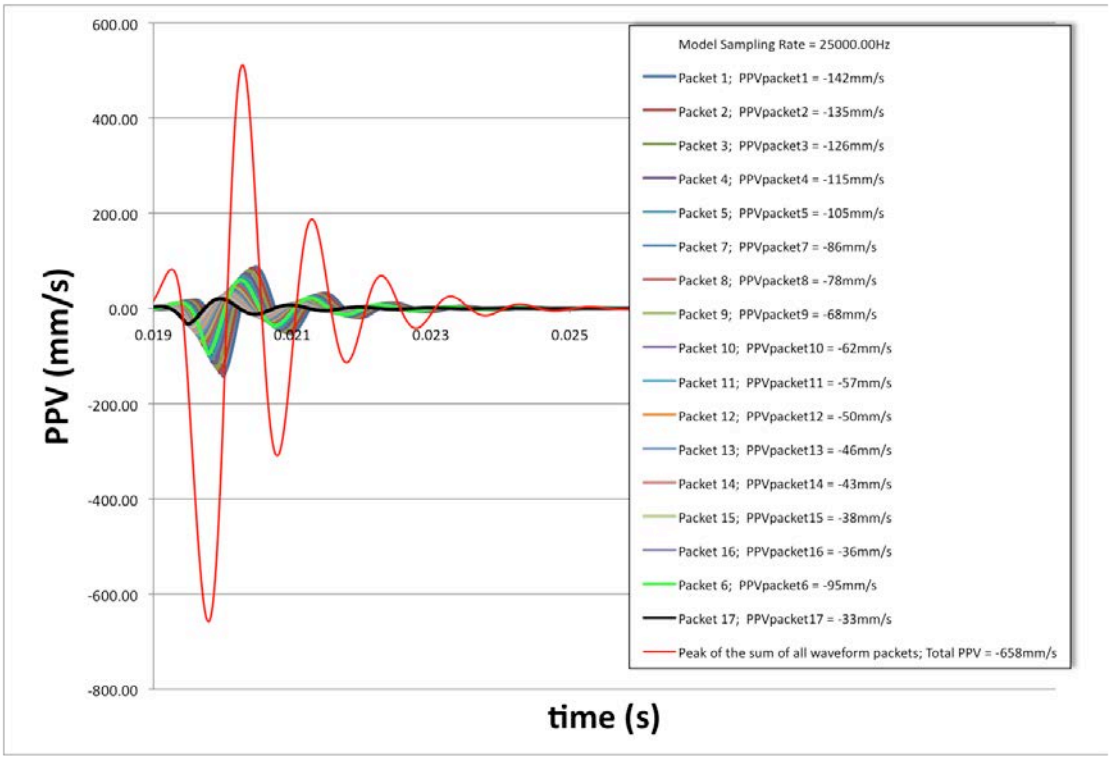

Figure 5.51 Model sampling rate = 25,000Hz

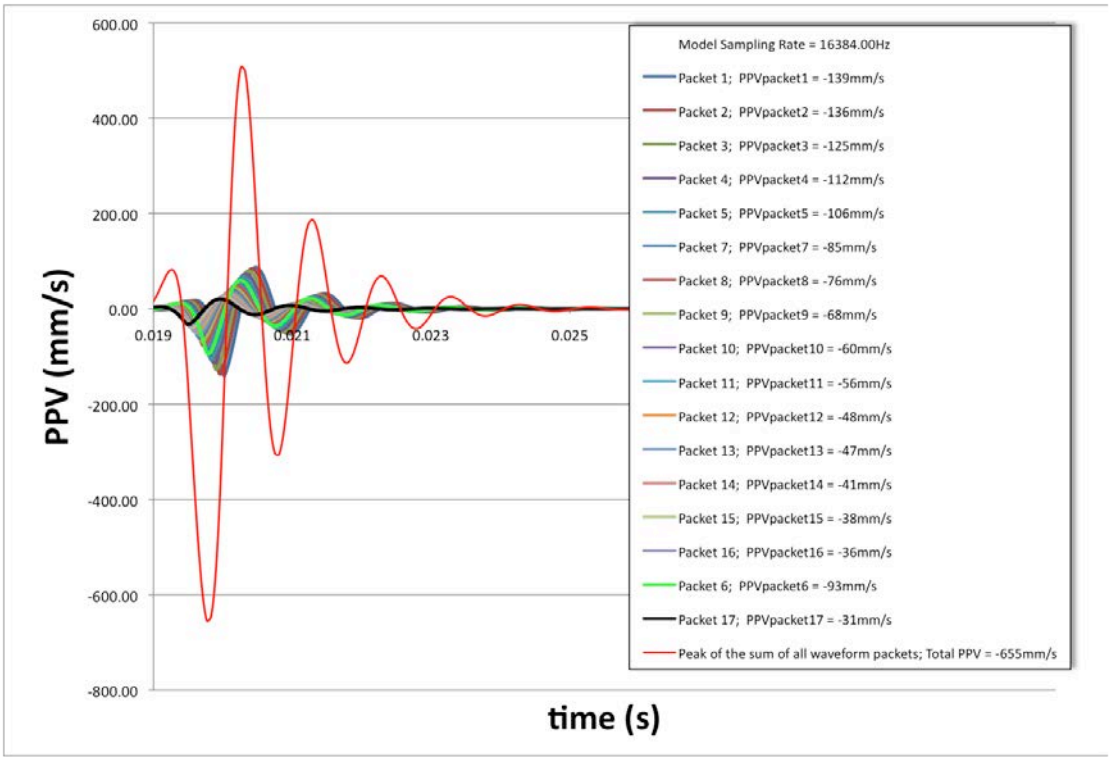

Figure 5.52 Model sampling rate = 16,384Hz

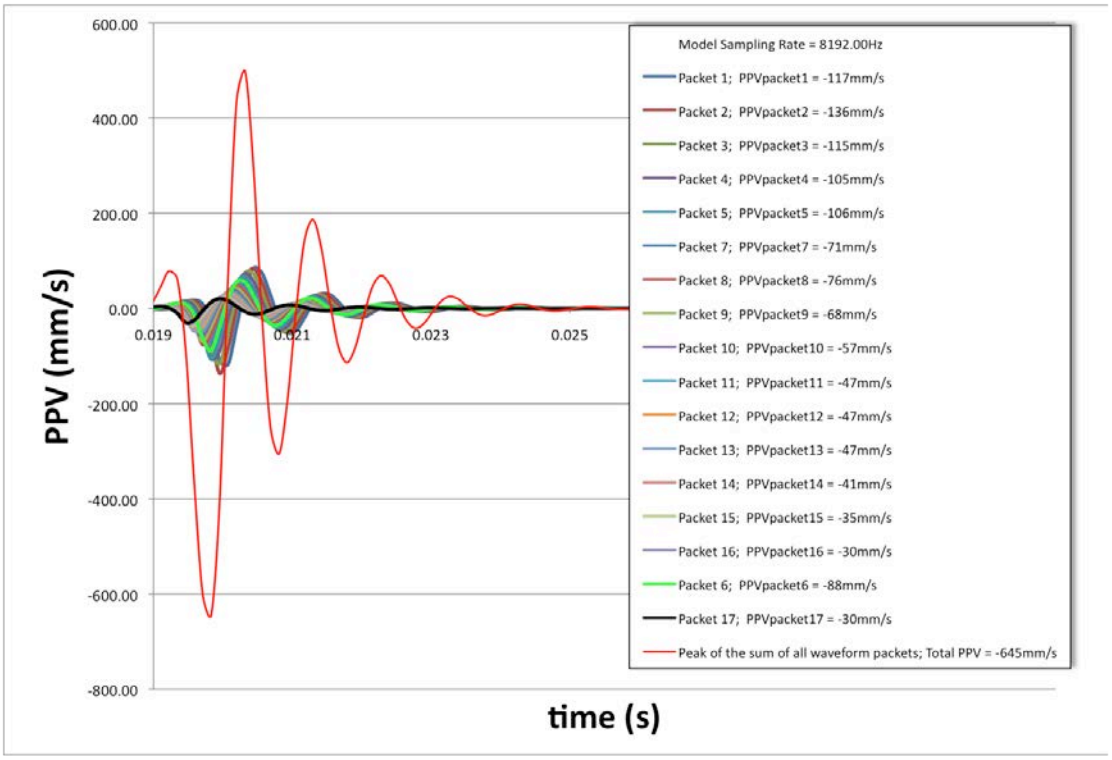

Figure 5.53 Model sampling rate = 8,192Hz

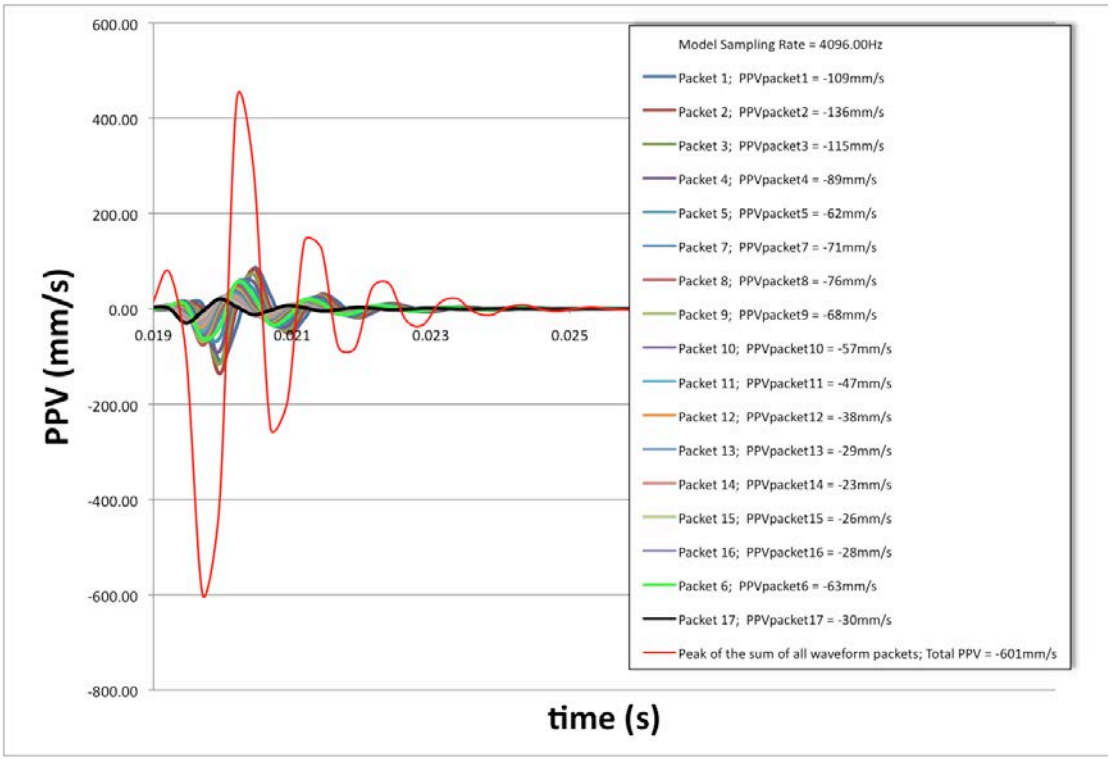

Figure 5.54 Model sampling rate = 4,096Hz

5.5 *PPV* – Diffraction Case

5.5.1 General

So far, the model has only been used to determine the *PPV* in the near-field instance, where the travelled distance to the point of interest is relatively short, only a few meters away, and each packet travels in a straight line toward the point of interest (i.e., signature blasthole). Note that the equations prescribed by the Holmberg-Persson and Hustrulid-Lu methods were presented solely for illustration in this simple case scenario.

The model determines the distances from each and every packet in the blasthole, passing through a point of diffraction Z_{POD} or $(0,0,Z_{POD})$ at the face-wall contact, to the geophone location or point of interest. Note that for each packet there is a different Z_{POD} that yields the shortest packet-geophone distance. The model assumes that the vibration travels from the packet centroid to the Z_{POD} through the body of rock at its body wave velocity. From this point onward the wave travels on the surface of the wall excavation to the geophone at the surface wave velocity. As a consequence of such unfavorable geometry, where an open volume prohibits a direct path of propagation, the vibrational energy experiences a

sharp loss at this Z_{POD} location, which, in the worst case corresponds to a turn angle of nearly 90^{o}. The assumption here is that only a portion of the original packet velocity magnitude continues to propagate parallel to the wall, while the remainder vanishes into the medium, and consequently does not get recorded by the datalogger.

In practice, this situation has been incorporated in the model by assuming that only the vertical projection of the original magnitude of the packet's particle velocity parallel to the wall reaches the geophone. In addition, the user can apply a power factor to the vertical projection, to increase or decrease the weight that the point of diffraction has on the vertical *PPV* projection. This happens since not all of the seismic energy that makes a turning angle toward the point of interest at the face-wall contact will dissipate, some of the energy diffracts. At this stage, for simplification, the model does not incorporate other constants or variables. Another solution, not being explored as part of this research, is that the original waveforms could have been decomposed as the projection of the magnitude parallel and perpendicular to the wall using the $Sin(\beta_{ith})$ and $Cos(\beta_{ith})$ factors respectively (times a constant for each projection), and not just using the one parallel to the wall, as is used for the model. It is of course implied that the vector summation of both components should not generate amplitudes greater than the original.

The following two examples illustrate both cases: one in which there are solely straight path lines from the packets to the geophone – signature blastholes case; the other such that the geophone is located on the surface of the excavation and the seismic rays originating in each packet must pass through points of diffraction. In both cases, the propagation velocity of the medium, the *VOD* of the explosive, the vibrational frequency, and the site constants were all set to be the same values.

Figure 5.55 shows the arrival time results for a blasthole located 5.2m from the geophone, the signature blasthole case, whose distance is measured along the surface of the excavation, from the collar of the blasthole to the point of interest. Figure 5.56 shows the particle velocity waveforms for a selected number of packets (1, 5, 9, 13, 17) and Figure 5.57 shows the particle velocity waveforms for all 17 packets of the array, where the red-dashed short-spaced line is the waveform corresponding to packet 1, i.e., the packet closet

to the geophone, yielding the highest *PPV* value. Figure 5.58 shows the linear superposition waveform of all 17 packets.

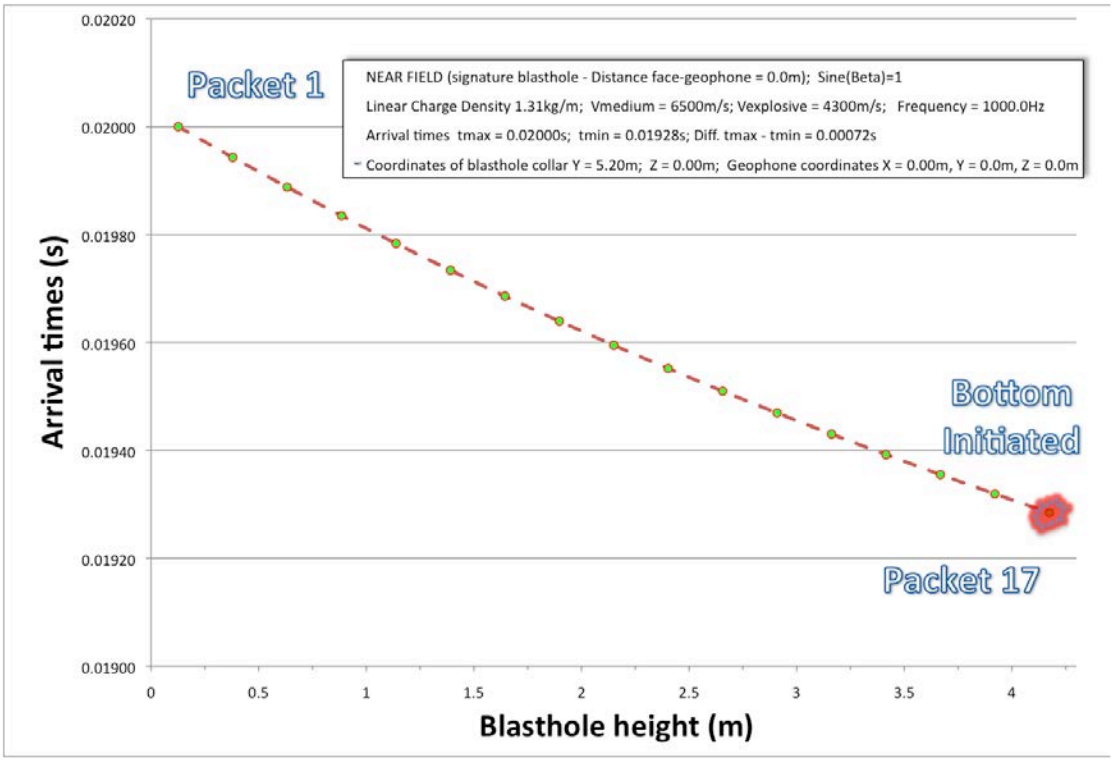

Figure 5.55 Arrival times – Signature blasthole case

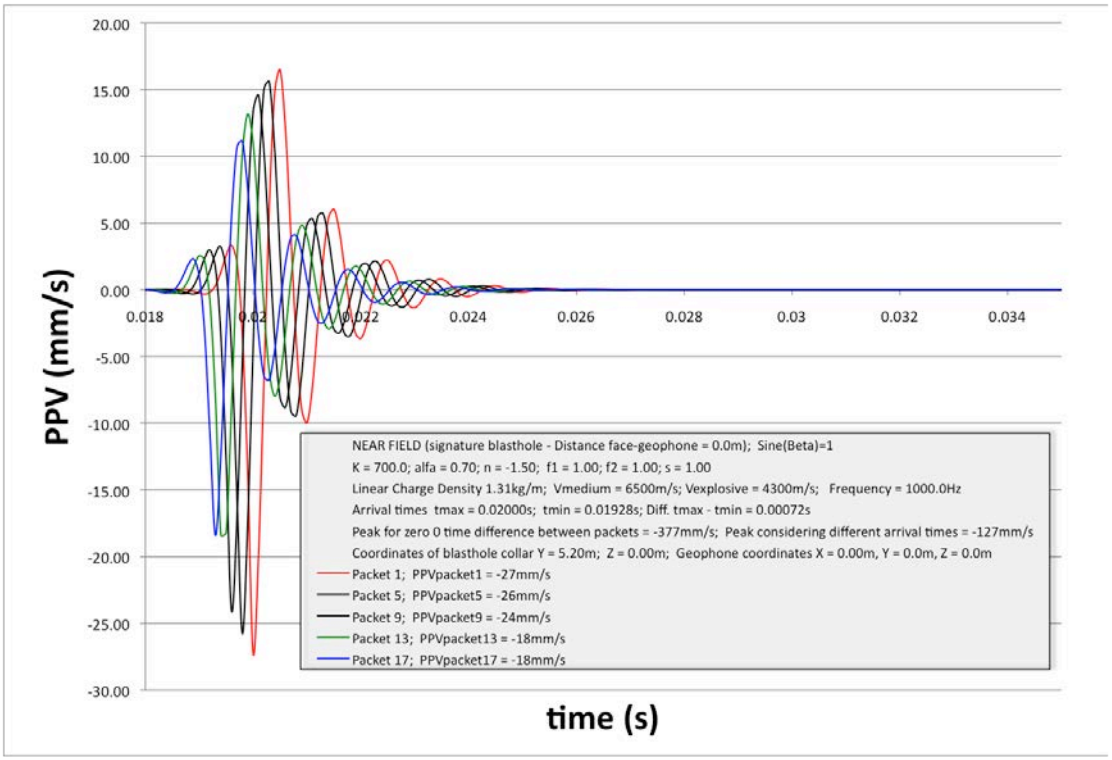

Figure 5.56 *PPV* waveforms for selected packets – Signature blasthole case

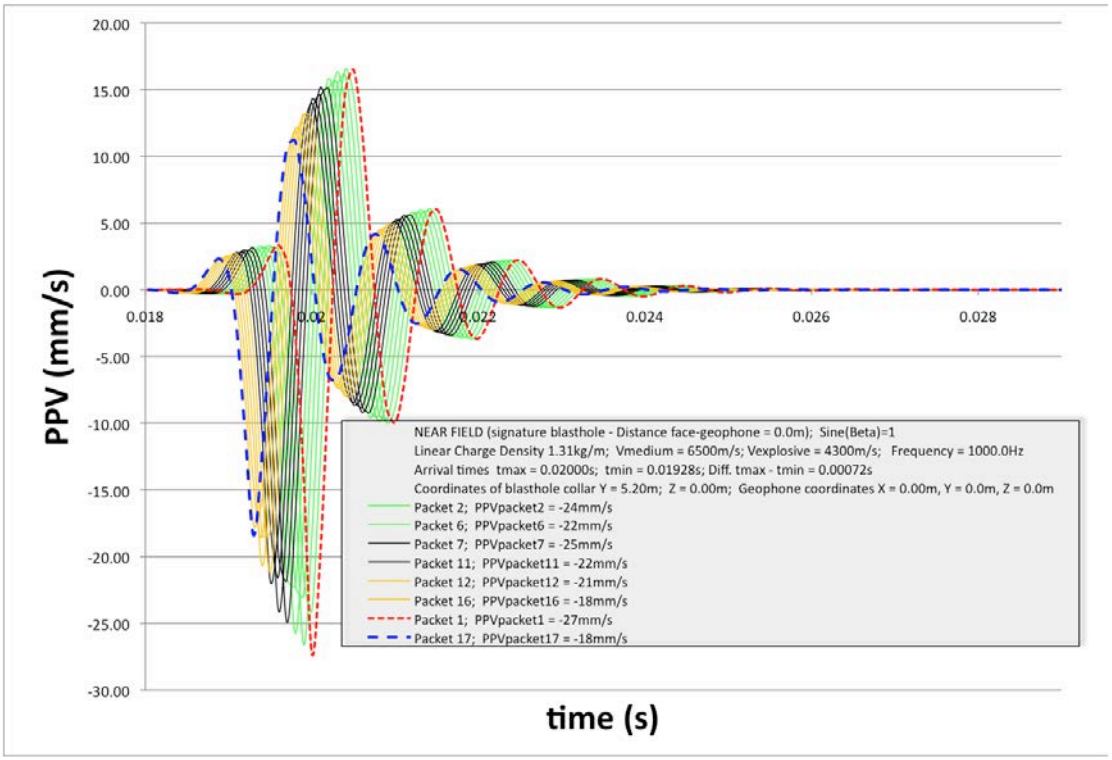

Figure 5.57 *PPV* waveforms for all 17 packets – Signature hole case

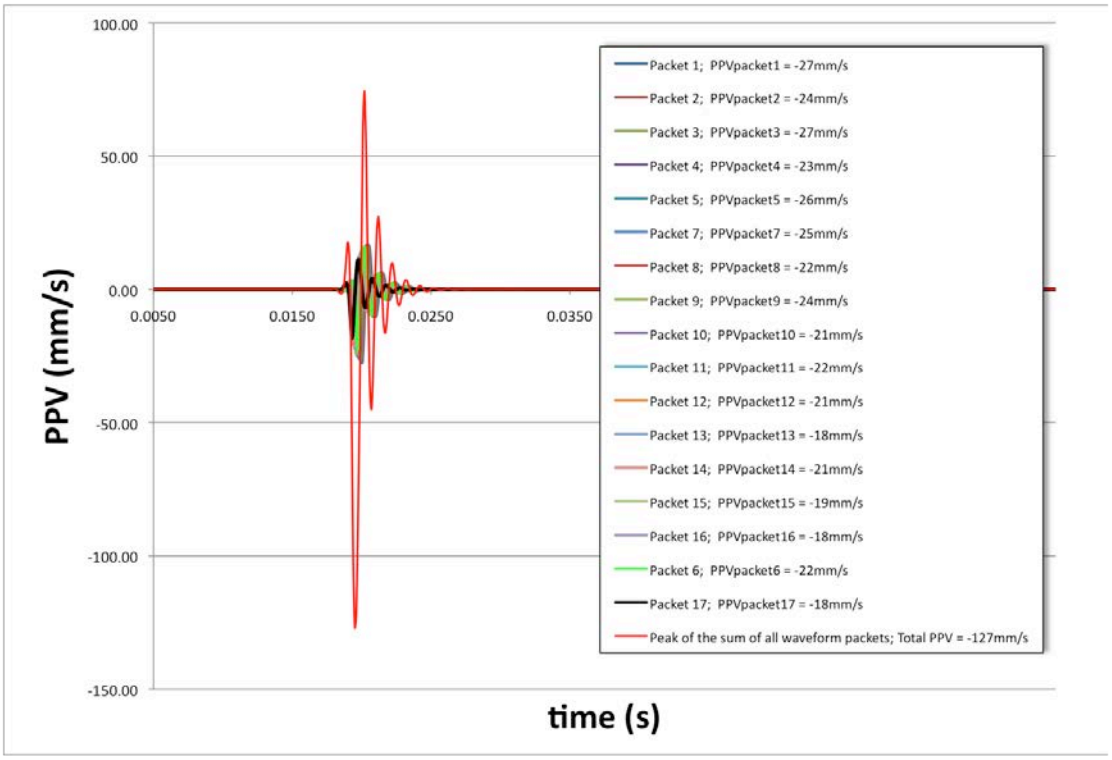

Figure 5.58 Linear superposition of individual *PPV* waveforms – Signature blasthole case

Figure 5.59 shows the arrival time results of a blasthole located 5.2m from the geophone, where the distance is also measured along the surface of the excavation. The distance is 2.6m from the collar of the blasthole to the point of diffraction at the face-wall contact, and 2.6m from the point of diffraction to the geophone, in the diffraction case. Figure 5.60 shows the particle velocity waveforms for the same selected number of packets (1, 5, 9, 13, 17) and Figure 5.61 shows the particle velocity waveforms for all 17 packets of the array. As in the previous example, the red-dashed short-spaced line represents the waveform corresponding to packet 1 (i.e., closest to the geophone.) In this case, however, it yields the lowest *PPV* value. Figure 5.62 shows the linear superposition waveform of all 17 packets. In this example, the packets that are closest to the face, even though their distances to the geophone are the shortest, have the greatest reduction in their *PPV* values due to the sharp (90^{o}) turn at the point of diffraction.

Note that with respect to the previous examples, it would not be possible to match all 17 distances for every packet in the array.

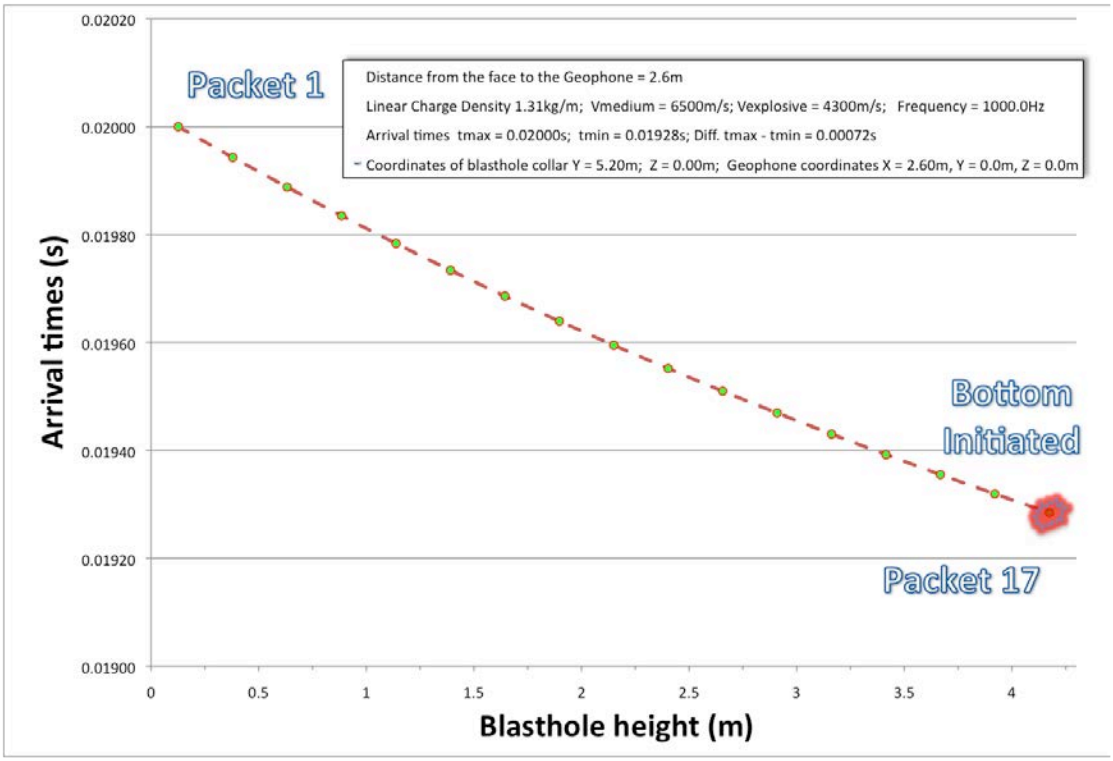

Figure 5.59 Arrival times – Diffraction case

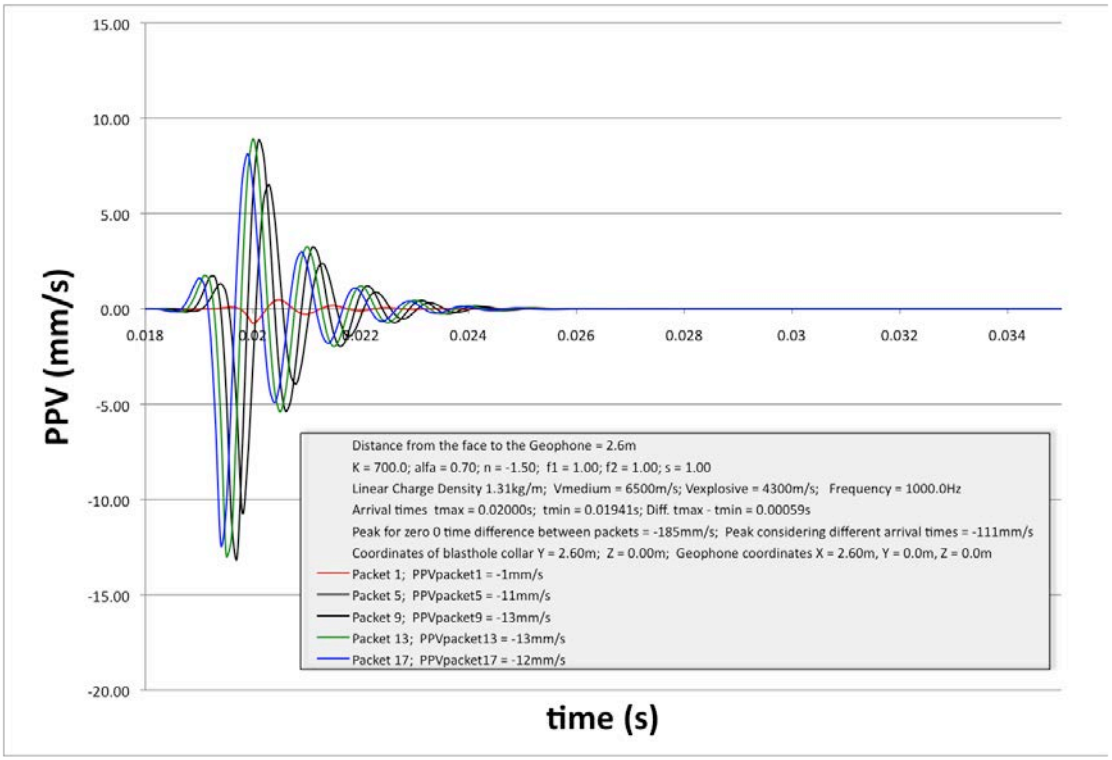

Figure 5.60 *PPV* waveforms for selected packets – Diffraction case

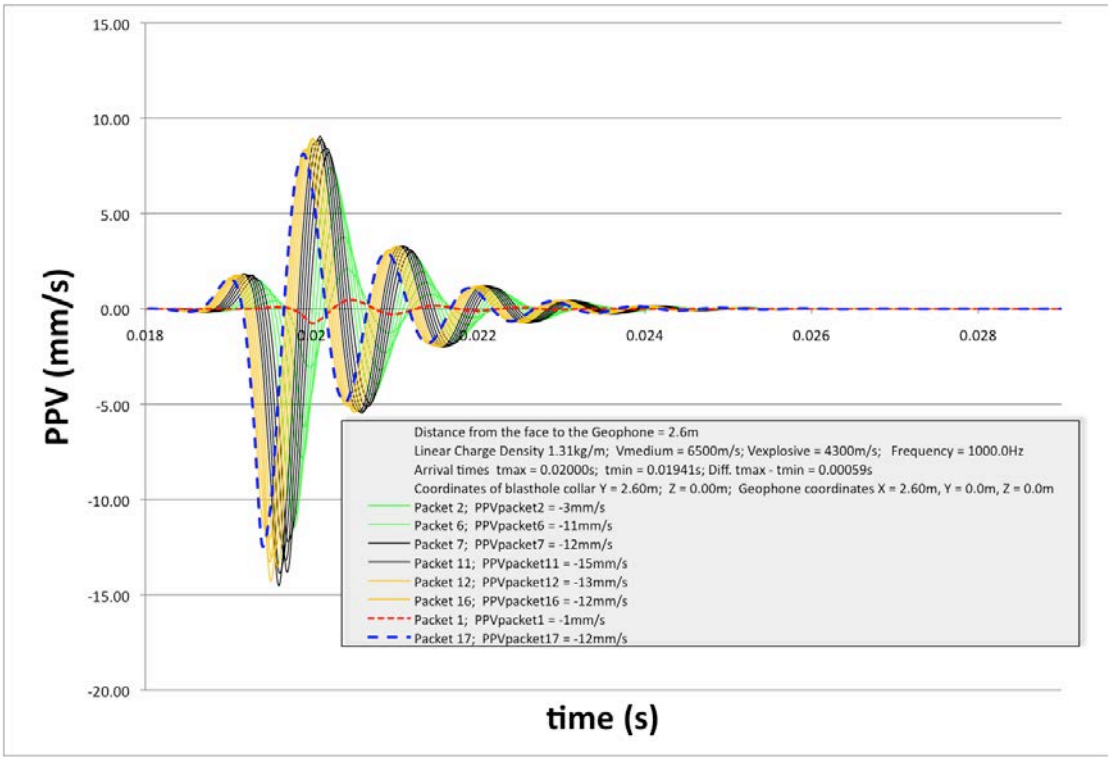

Figure 5.61 *PPV* waveforms for all 17 packets – Diffraction case

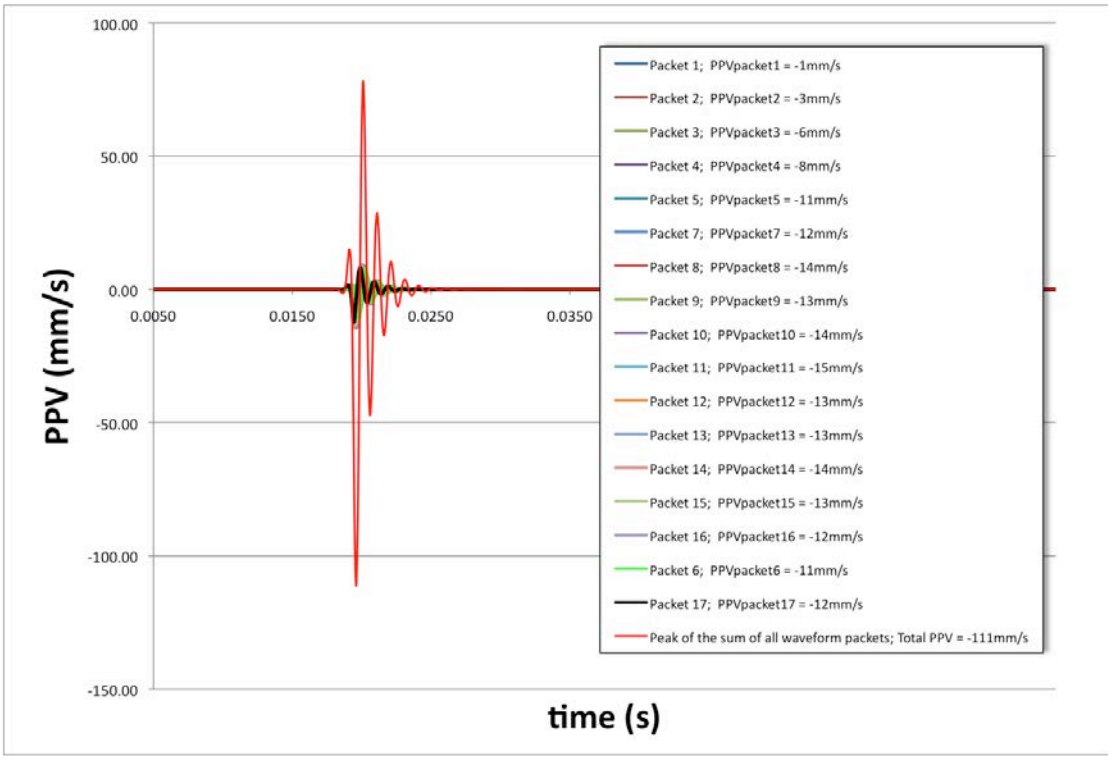

Figure 5.62 Linear superposition of individual *PPV* waveforms – Diffraction case

5.5.2 Arrival Time – Two Blastholes with identical Nominal Delay

The following example is intended to demonstrate that two blastholes with the same nominal delay number, while considering zero time delay scatter, located at a certain distance from each other, should yield no constructive interference. As a consequence, the linear superposition of the two waveforms combined could yield the same, and in some cases even smaller, final *PPV* than the original *PPV* of each waveform on its own.

Figure 5.63 shows the arrival times of two opposite bottom corner lifter blastholes. For this example, in a real case scenario, such as the Musselwhite mine, both of these lifter blastholes would be detonated with a #19 nominal delay number. No time delay scatter was considered in this example. In this figure, it is clear that the arrival time of the peak of the waveform of one blasthole never intersects with the arrival time of the peak of the waveform of the second blasthole. Each dot on both curves indicates the arrival time of the peak of individual waveforms.

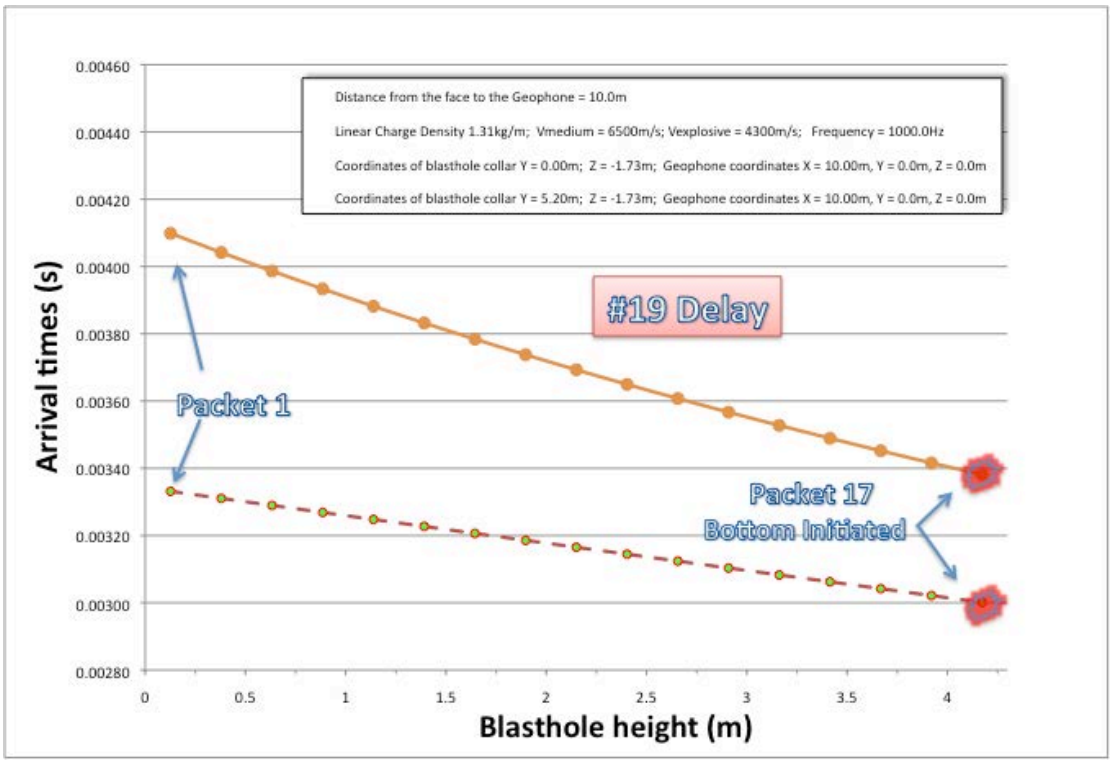

Figure 5.63 Arrival times for two blastholes at different locations – Zero time scatter

Figure 5.64 shows the two individual waveforms for each lifter blasthole, as indicated by the long-spaced red line and the short-spaced blue line. In Figure 5.64, the linear superposition of both waveforms is combined, indicated by a continuous black line. In this example, destructive rather than constructive interference occurs between both waveforms.

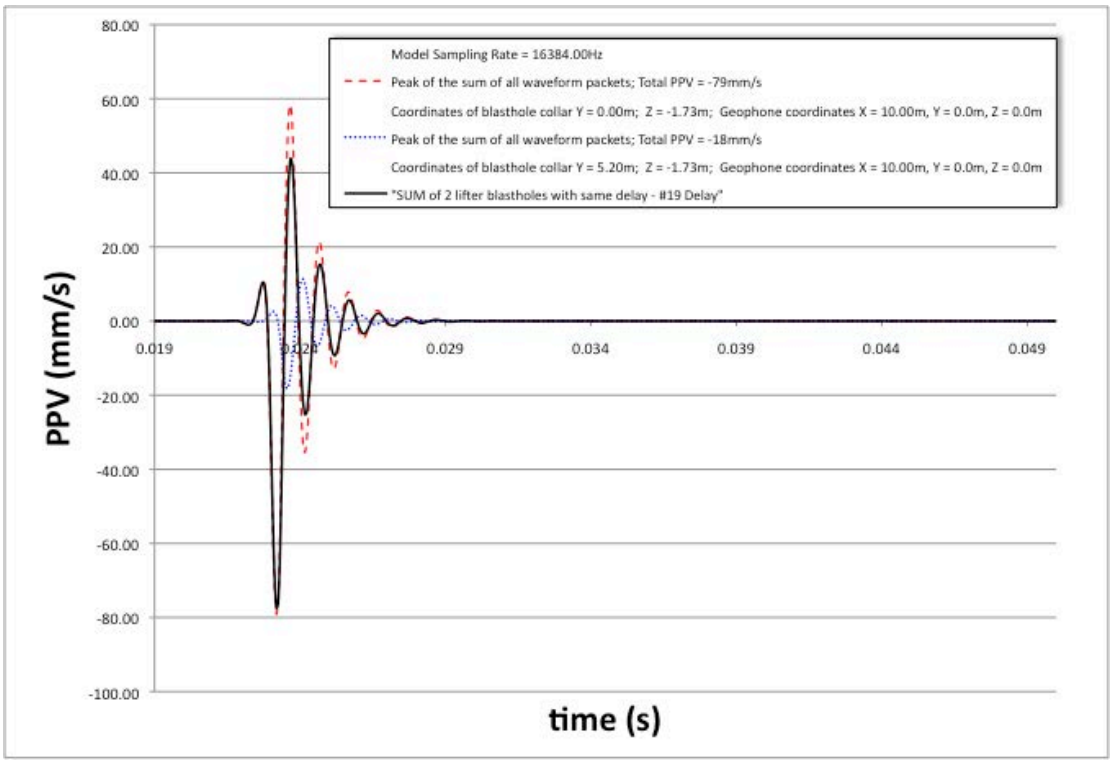

Figure 5.64 Linear superposition between 2 blastholes with same delay number

In the previous example, the explosive's *VOD*, its type and quantities, the velocities of propagation, the frequency, plus all the other constants for both samples are all assumed to have equal values.

5.6 *PPV* for Practical Cases

5.6.1 General

So far, the model has been validated against the Hustrulid-Lu equation using non-real values for the propagation velocity and the *VOD* of the explosive. In this case, the peak of every packet of a blasthole coincides at time t_{ini}, that is, there is no time shift among the arrival times of the peaks of every packet, and the model and equation yield exactly the same results. It has also been tested for the near-field and diffraction case scenarios. In this section, the model will be tested in a more realistic scenario where the *VOD* of the explosive (4,300m/s) is similar to the cartridge explosive Dyno AP^{TM}, used in the lifter blastholes. The body and surface propagation velocities of the seismic wave and the predominant frequencies tested are closer to that of a poor-fair and good rock mass

qualities. These cases are, to some extent, representative of the SSX and the Musselwhite mines, respectively.

In Figure 5.65, the blue triangles indicate the locations of two blasthole collars. The differences among *PPV* generated by each of the blastholes for both rock mass qualities will be analyzed.

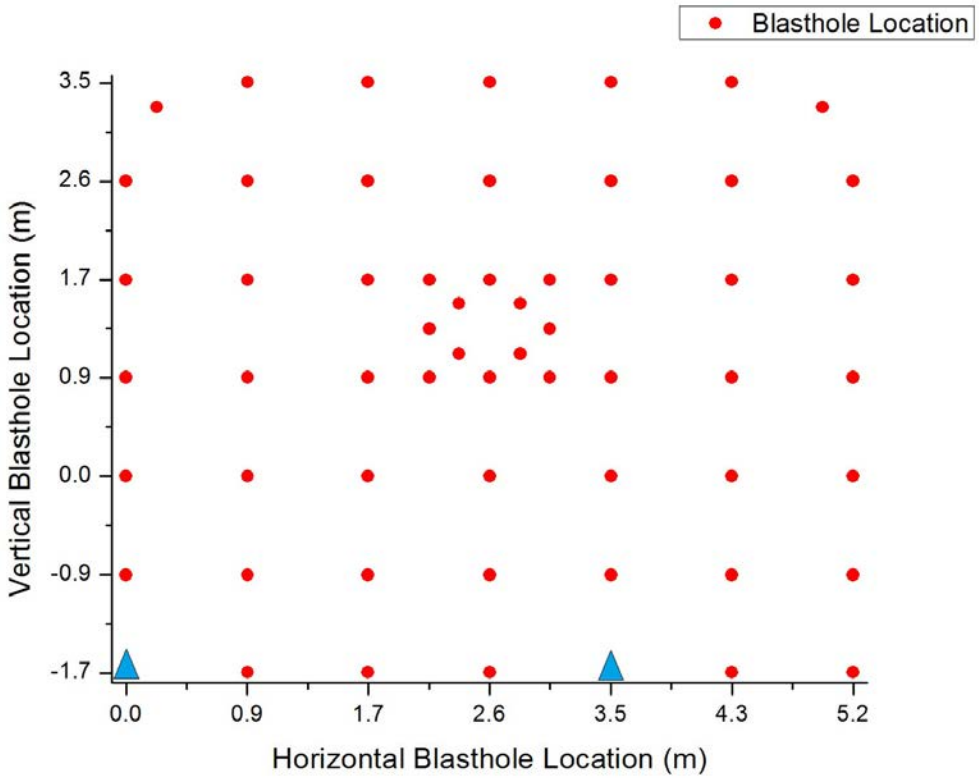

Figure 5.65 Arrival times and *PPV* for highlighted blasthole location

The analysis includes the arrival time and the individual waveforms of each packet in the array as well as the linear superposition of the combined individual waveforms. In this case, both blastholes are located at the floor level of the drift corresponding to the coordinates (0.0, -1.7) and (3.5, -1.7). The geometry of the drift and the explosive properties are identical for both of these otherwise dissimilar rock mass qualities.

5.6.2 Competent Rock Mass – Good Rock Mass Quality; *RMR* > 75

Figure 5.66 compares *PPV* versus time of a single blasthole recorded waveform against the model waveform, for the Musselwhite Mine case. The rock mass dominant vibration

frequency was set to 1000Hz and the velocity of propagation of the body wave was set to 6500m/s. The pre- and post-decay constants were varied to achieve similar waveform patterns. The use of similar waveform patterns could improve the reliability of the model's predictive capabilities as it is expected that the model will better interpret the recorded *PPV*.

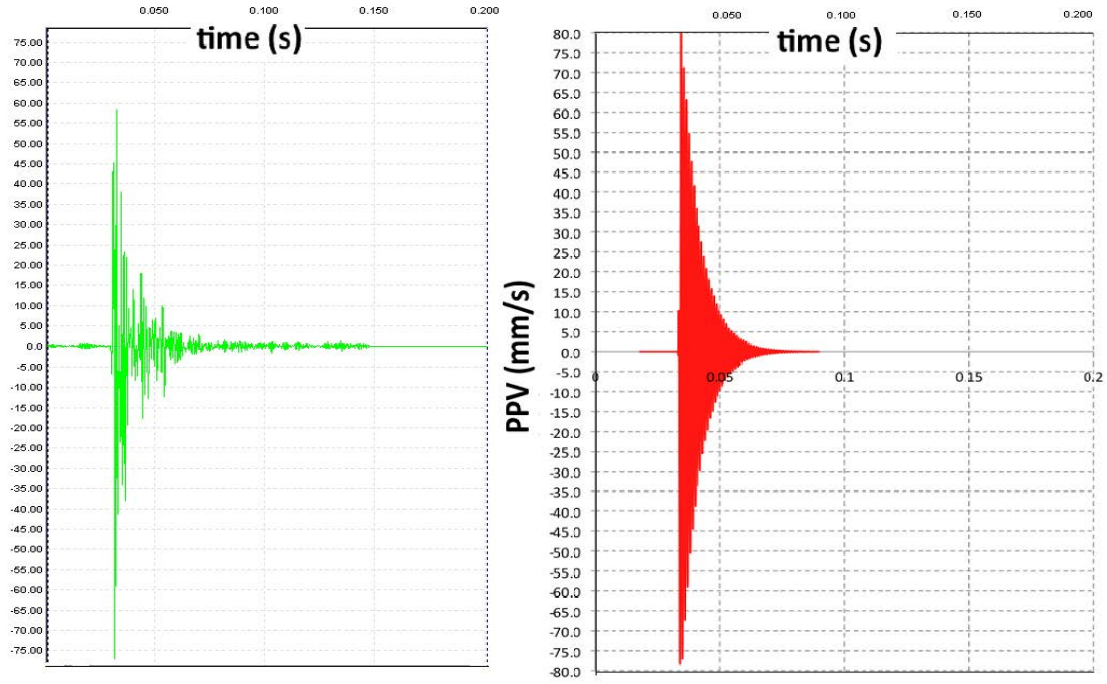

Figure 5.66 Good rock mass quality – *PPV* vs. time waveform – Record & model

The following sets of figures were obtained after adjusting the rock mass and explosive properties to represent a good rock mass quality, such as that encountered at the Musselwhite mine. In this case, constant *K* was set to 1000, *n=-1.5,* and *α=0.7*, and *f1=1*, *f2=1*, and *f3=1*. The distance from the face of the round to the geophone location was set at 5m.

Figure 5.67 shows the arrival times of each of the waveforms for every packet in the array. The first vibration waveform to arrive at the geophone corresponds to the packet located at the bottom of the blasthole. This result is expected, as the body wave velocity is faster than the *VOD* of the explosive.

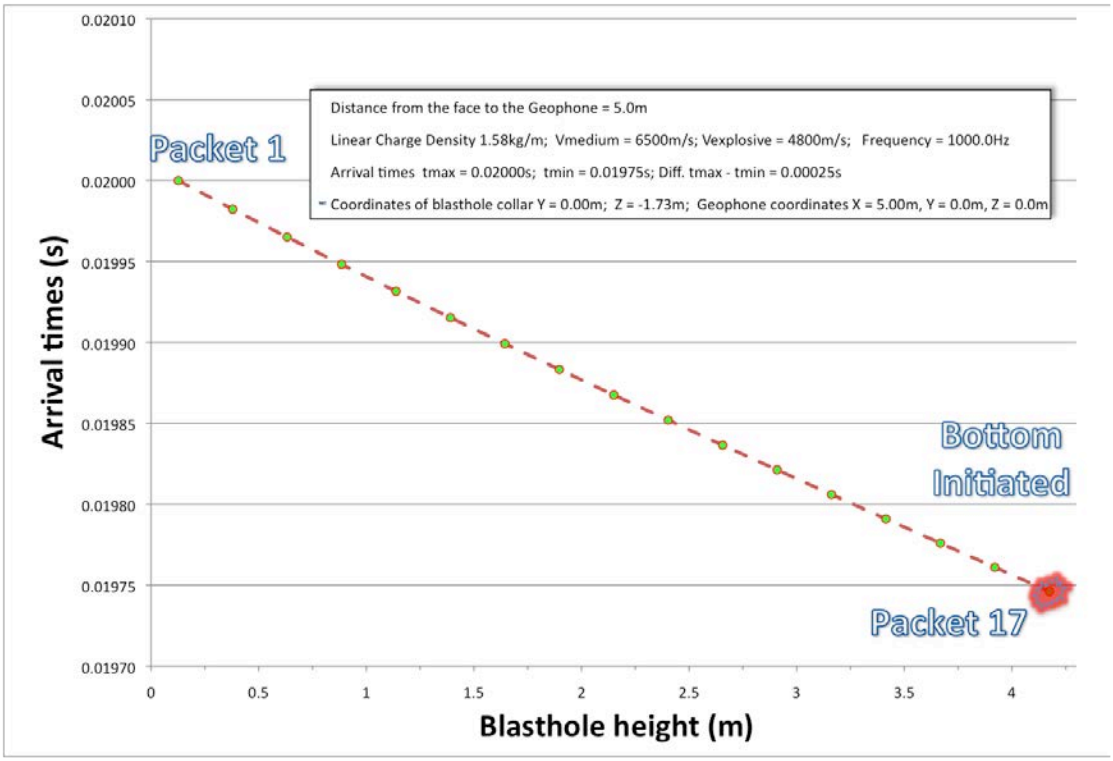

Figure 5.67 Arrival times - Good rock mass quality case - Y=0.0 Z = -1.73

Figure 5.68 shows all the waveforms generated for every packet in the array. In this case, the seismic wavefront has to pass through a point of diffraction, so that the distances are factored by $Sin(\beta_{ith})$. It is evident that those blastholes located at the perimeter, closest to the geophone, will have a factor approximately equal to one $\{Sin(\cong 90°) \cong 1\}$ in which case the factor applied has no noticeable impact on their distances. The closer the blasthole's collar is to the perimeter, the less significant this factor becomes.

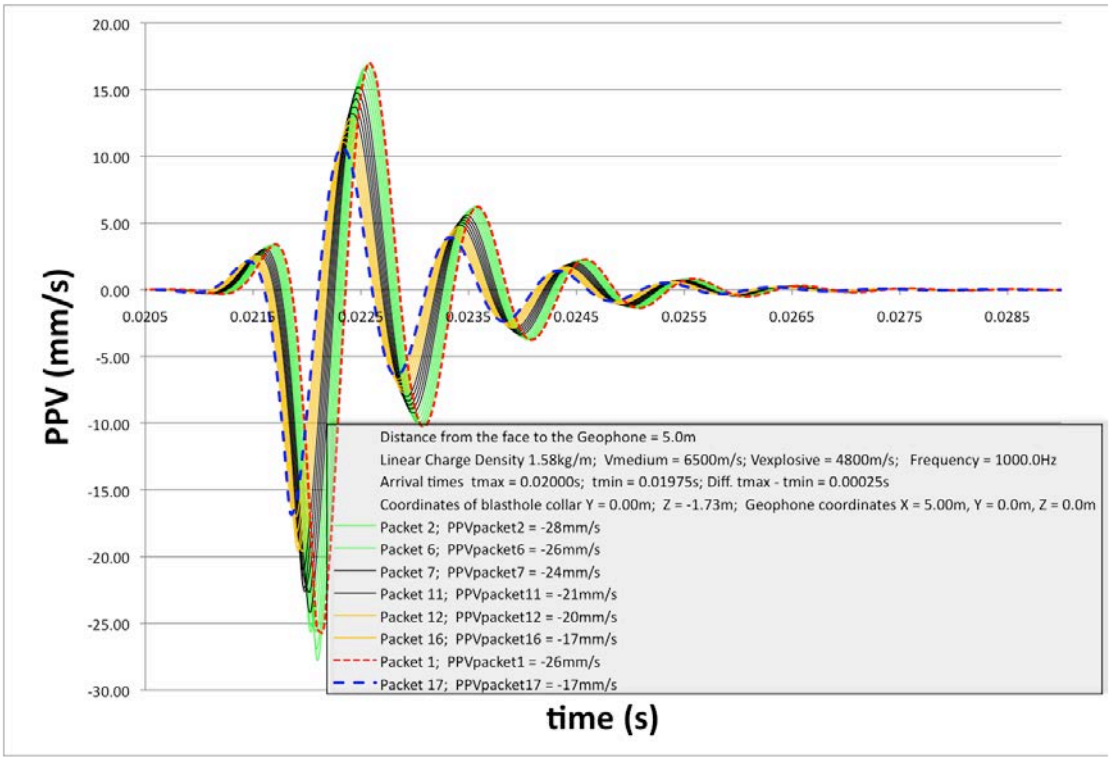

Figure 5.68 Particle velocity waveforms - Good rock mass quality case - Y=0.0 Z = -1.73

Figure 5.69 shows the linear superposition of the combined individual waveforms generated for the blasthole located at (0.0,-1.73).

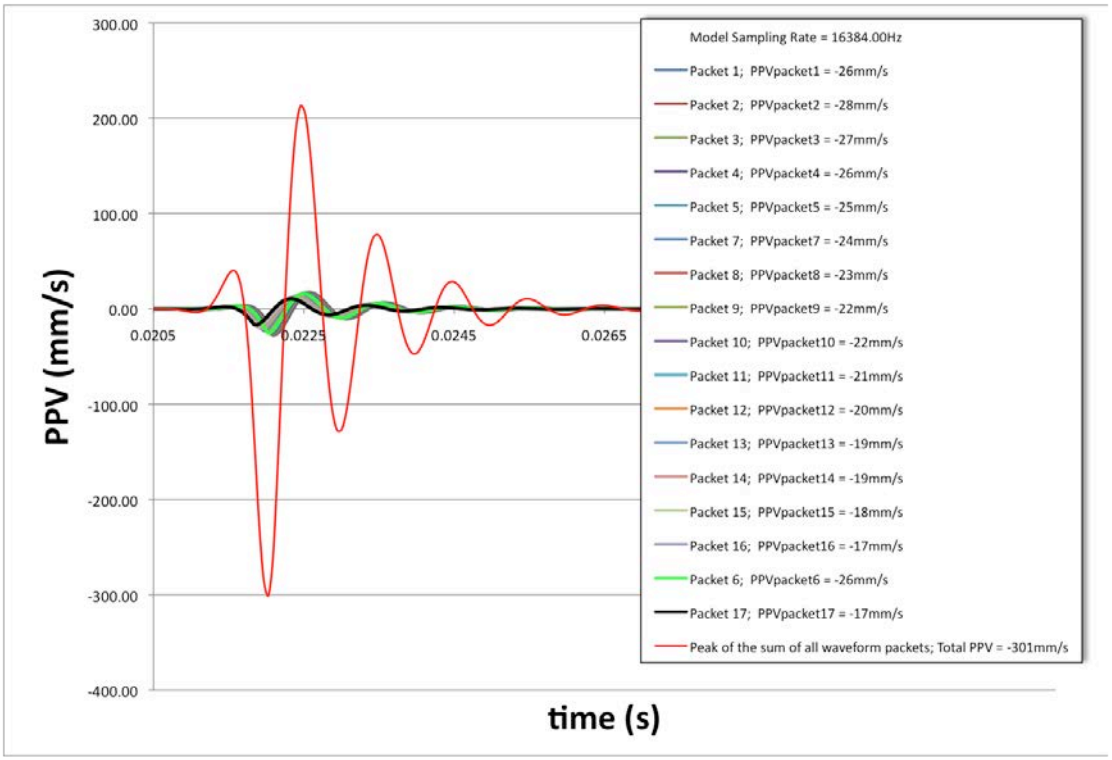

Figure 5.69 Linear superposition - Good rock mass quality case - Y=0.0 Z = -1.73

Figure 5.71, Figure 5.72, and Figure 5.74 show similar sets of figures as the previous cases, but now the collar location at (3.47m,-1.73m) is considered (i.e., farther from the perimeter). In this case, the factor applied to the portion of the distance between the packet centroid and the point of diffraction becomes more significant, as is evident by comparing the peak waveform values for packet 1, the one closest to the collar, where, in the first case, this value was nearer to maximum, and in the second case was closer to minimum (short-spaced red line).

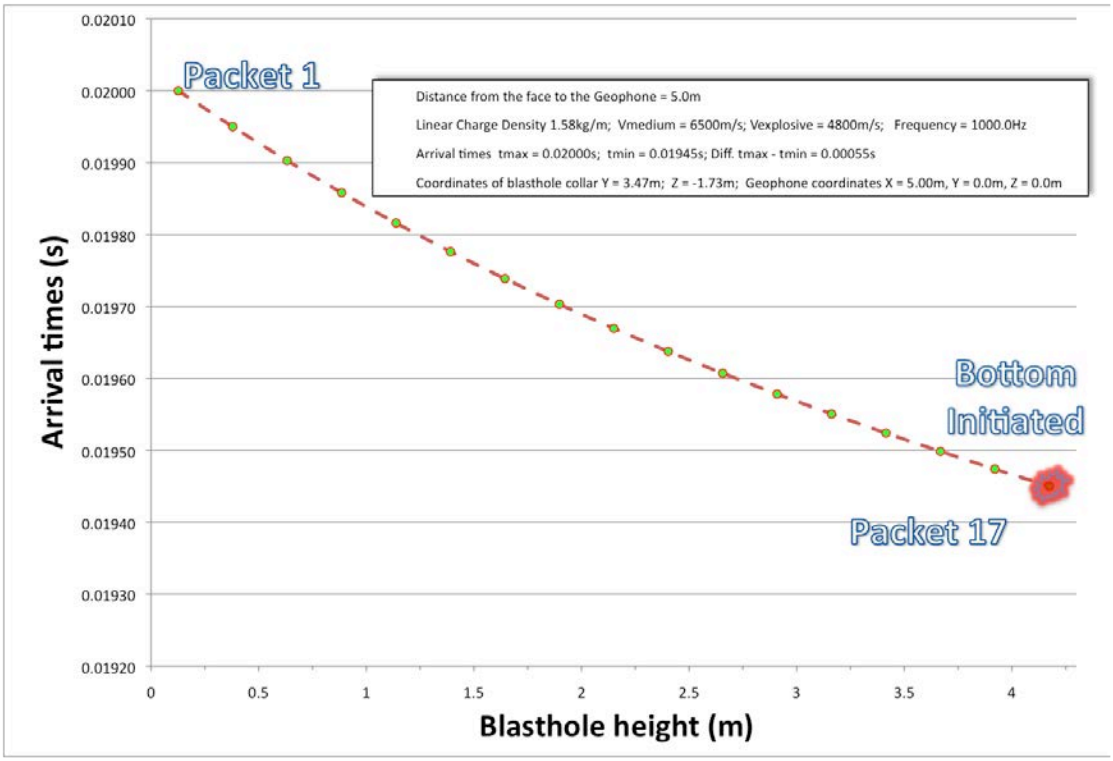

Figure 5.70 Arrival times - Good rock mass quality case - Y=3.5 Z = -1.73

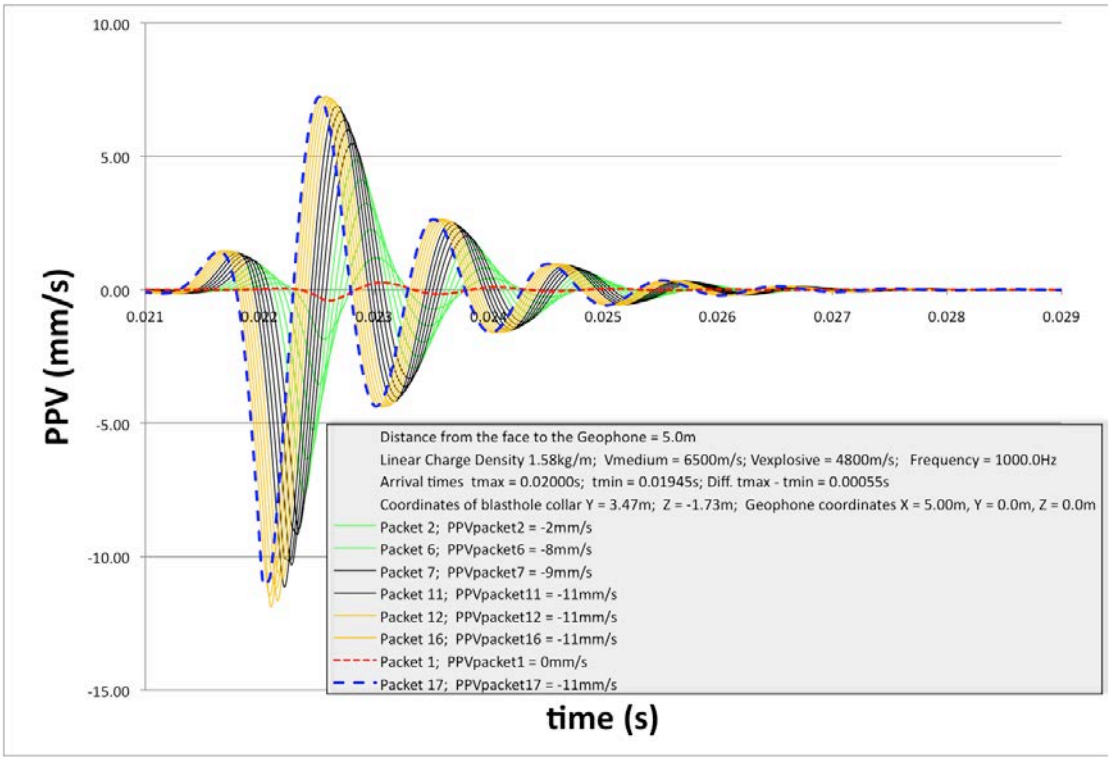

Figure 5.71 Particle velocity waveforms - Good rock mass quality case - Y=3.5 Z = -1.73

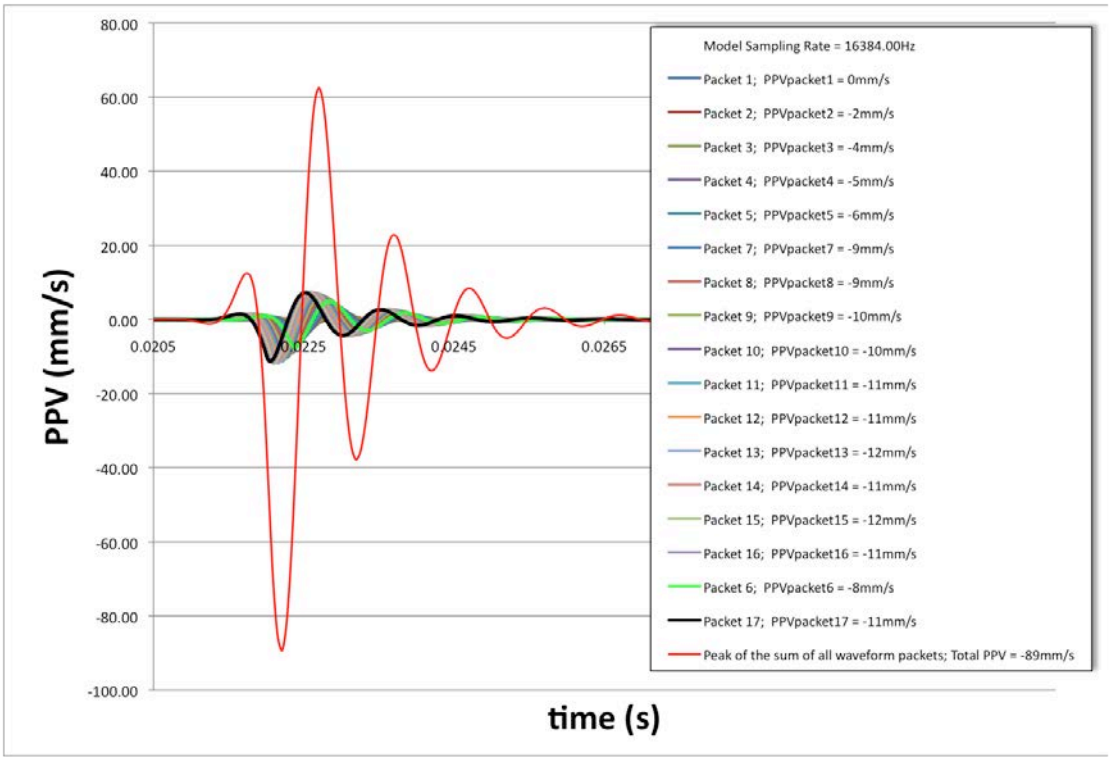

Figure 5.72 Linear superposition - Good rock mass quality case - Y=3.5 Z = -1.73

5.6.3 Weak Rock Mass – Poor/Fair Rock Mass Quality; *RMR* > 35

As in the previous example, the following sets of figures were obtained after adjusting the rock mass and explosive properties to represent a poor/fair rock mass quality, with an *RMR* on the order of 35, such as that encountered at the SSX mine. Figure 5.73 compares *PPV* versus time of a single blasthole waveform against the modeled waveform for the SSX Mine case.

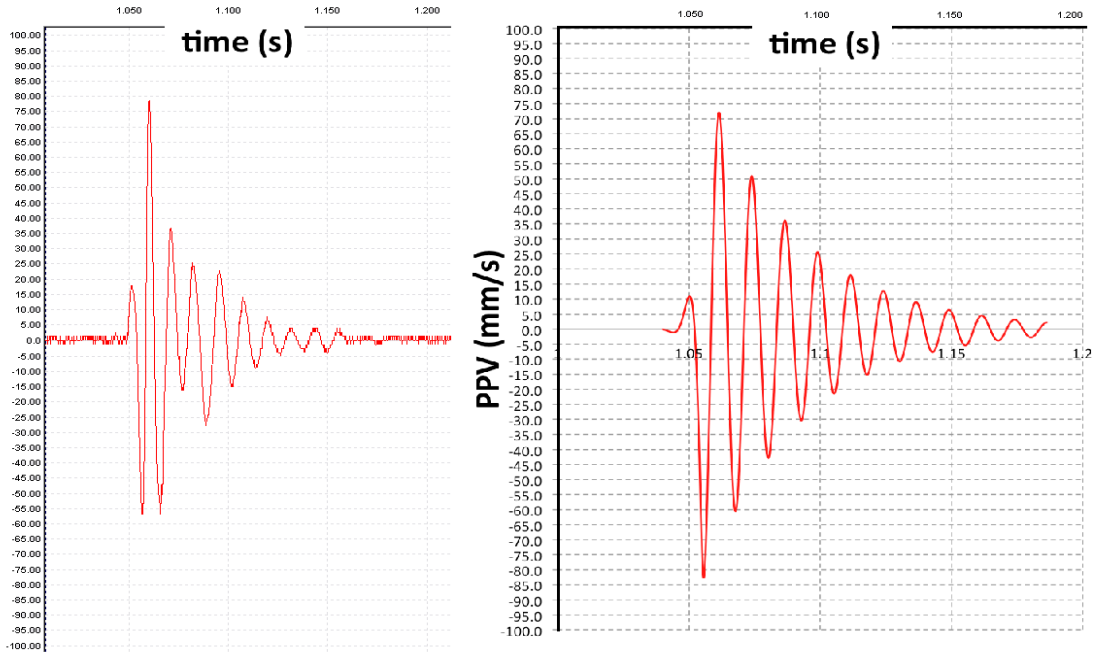

Figure 5.73 Fair/Poor rock mass quality – *PPV* vs. time waveform – Record & model

For the following case, the constant *K* was set to 150 and for comparison purposes, the constants n and α were kept the same as in the previous example, i.e., n = -1.5 and α = 0.7. The rock mass dominant vibration frequency was set to 150Hz and the velocity of propagation of the body wave was set to 2000m/s. The distance from the face of the round to the geophone location was set to 5m.

Figure 5.74 shows the arrival times of each of the waveforms for each packet in the array. In this case, the first vibration waveform to arrive at the geophone corresponds to the packet located at the collar of the blasthole. Just as before, this is an expected result, owing to the fact that the body wave velocity is much slower than the *VOD* of the explosive.

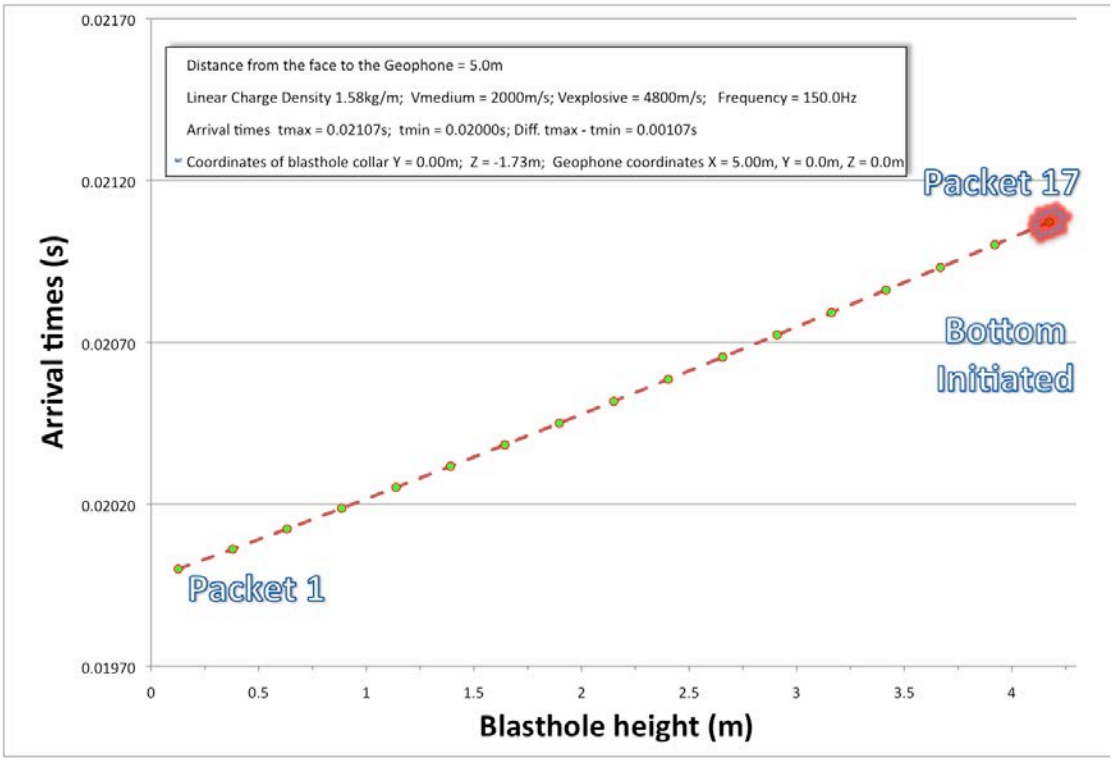

Figure 5.74 Arrival times - Poor/Fair rock mass quality case - Y=0.0 Z = -1.73

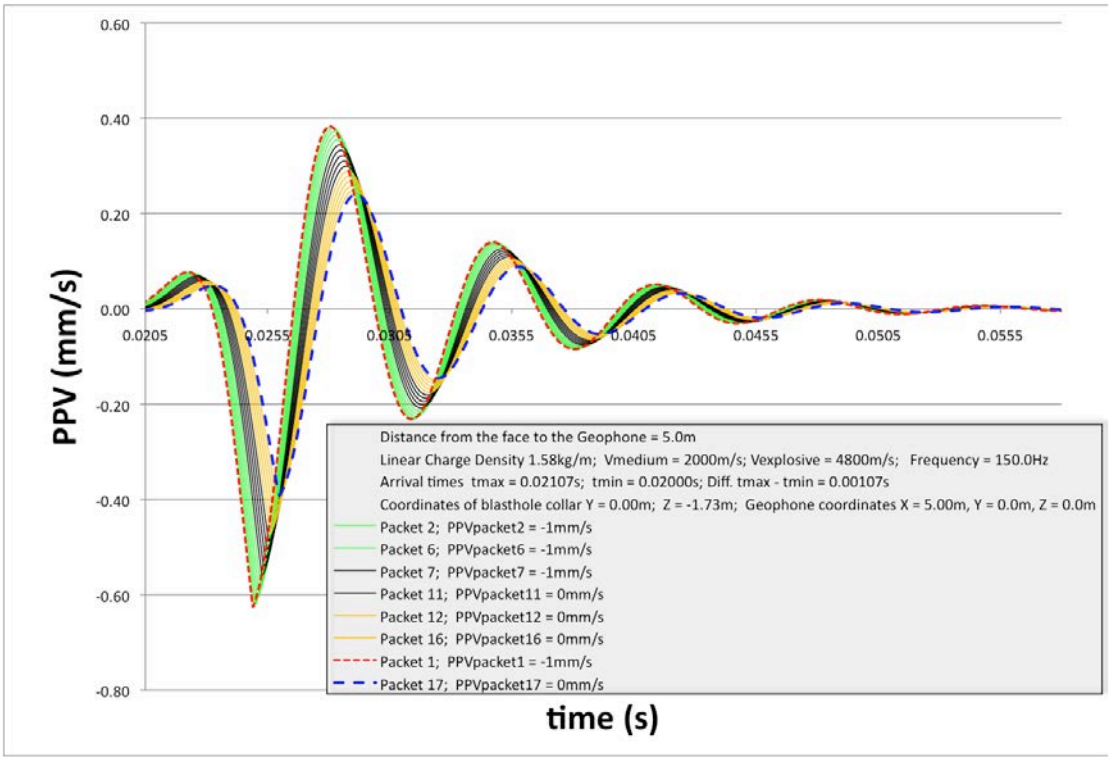

Figure 5.75 Particle velocity waveforms - Poor/Fair rock mass quality case - Y=0.0 Z = -1.73

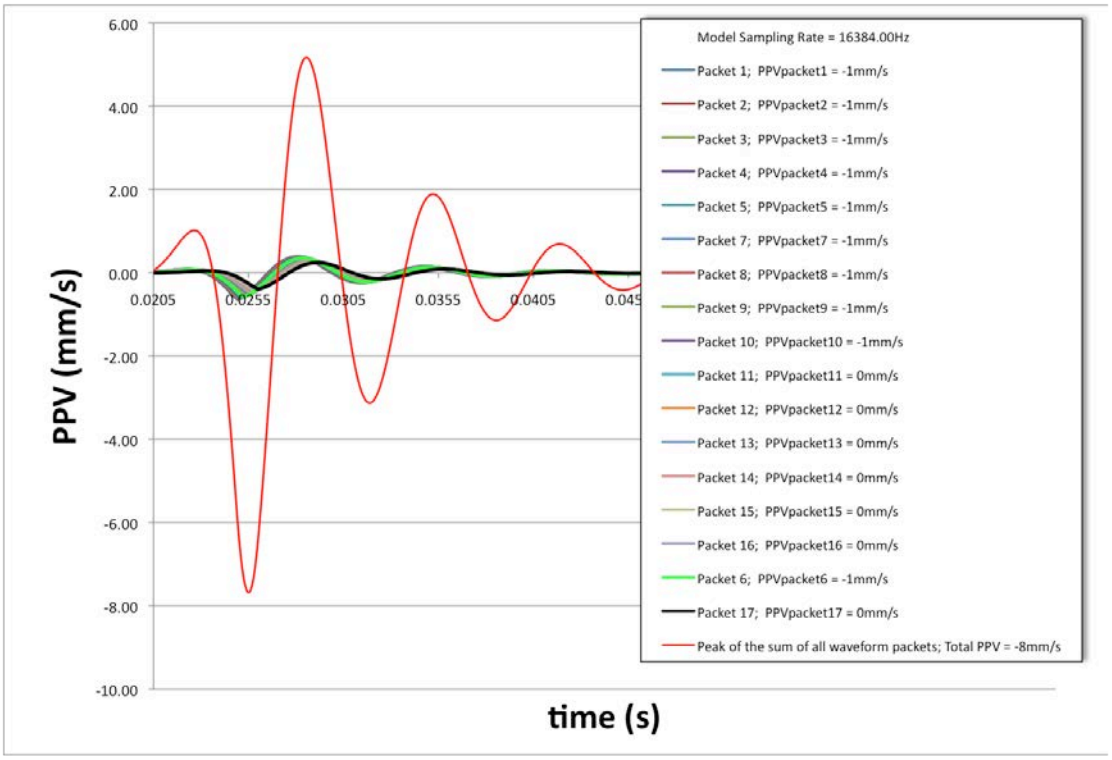

Figure 5.76 Linear superposition - Poor/Fair rock mass quality case - Y=0.0 Z = -1.73

Figure 5.77 shows the arrival times of the waveforms of each packet of the blasthole located at (3.47m,-1.73m). In this case, the first waveform to arrive is the one corresponding to packet 7. Waveforms for packets 6 and 8 arrive nearly simultaneously as do the waveforms for packets 5 and 9 and so on, up until the arrival corresponding to packets 1 and 14. In this case, the simultaneous arrival of two or more packets produces a greater peak when compared to that of individual independent arrival times.

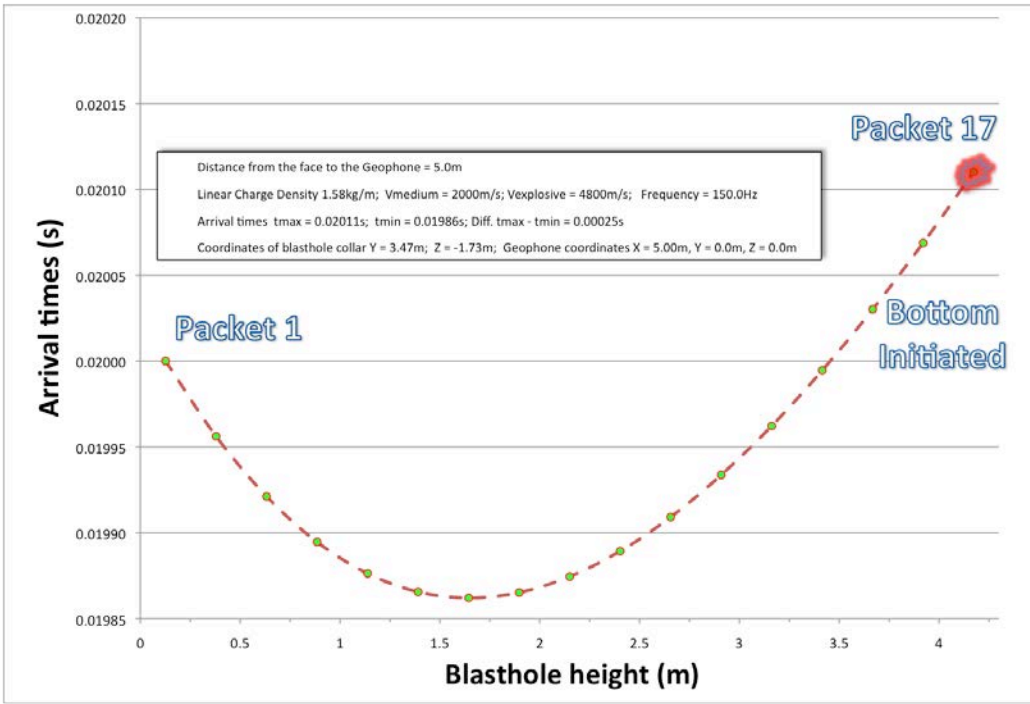

Figure 5.77 Arrival times - Poor/Fair rock mass quality case - Y=3.5 Z = -1.73

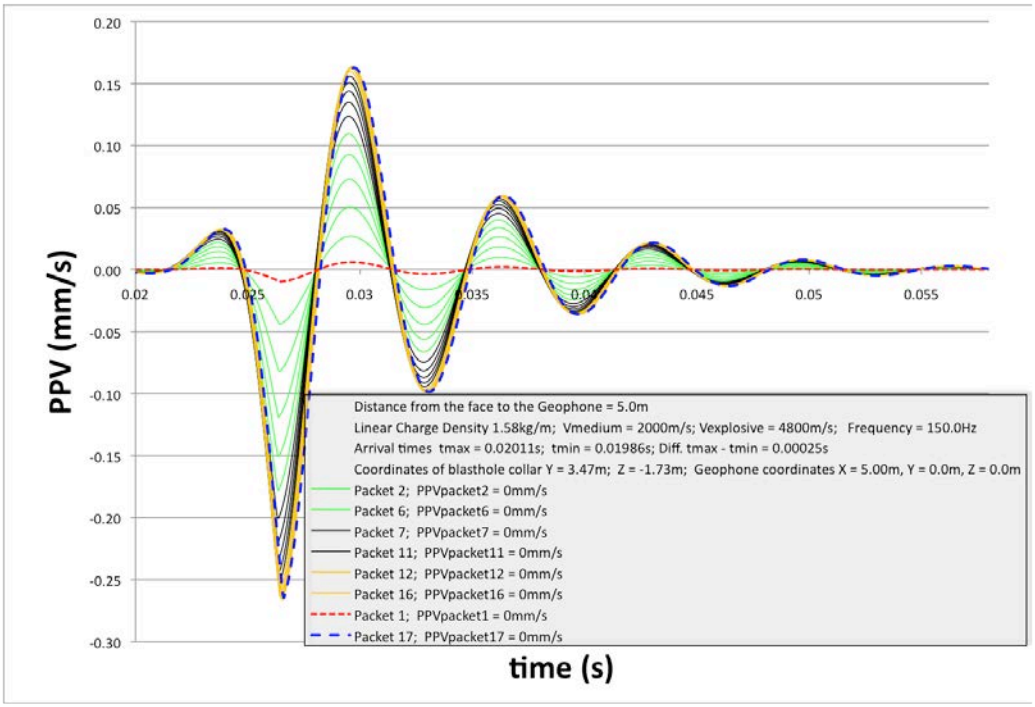

Figure 5.78 Particle velocity waveforms - Poor/Fair rock mass quality case - Y=3.5 Z = -1.73

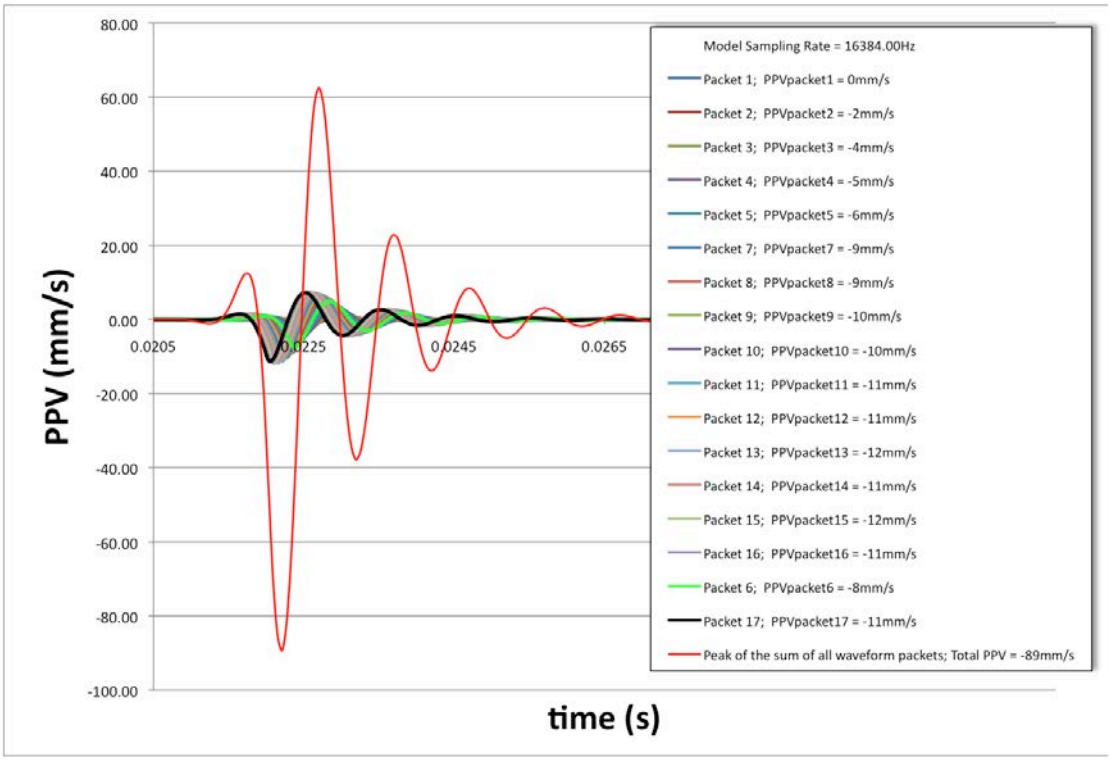

Figure 5.79 Linear superposition - Poor/Fair rock mass quality case - Y=3.5 Z = -1.73

6 MODEL TESTING

6.1 Field Data *PPV* Measurements – Musselwhite Mine Case

This chapter considers model validation using Musselwhite Mine *PPV* versus *SD* data compared with modeling results. One significant difference from current methodologies, as evident in this example, is that the modeling and recorded data points are analyzed using three axes rather than the more common *PPV* versus *SD* plotting method. In this example, the recorded *PPV* data points are plotted on the vertical axis with the magnitude corresponding to *PPV* values. Although the *PPV* values are recorded at some distance from the face, the value of the *PPV* of each blasthole in the round is assigned to its specific location. Similarly, the modeling results are plotted as a colored-surface contour indicating the range of the actual *PPV* values modeled. By plotting both the actual and the modeled surface contours, their difference enables assessment of how well the input parameters were established.

A significant drawback of the far-field *PPV* versus *SD* plot, specifically with the use of near-field data points, is the fact that it considers the explosive charge as concentrated into a point, and the distance is therefore considered a discrete quantity, and so it is unclear which value is to be used, that of the collar, the toe, or a location somewhere in between. Regarding this, the model accounts for the distance to every packet regardless if it is in the near or far-field, and the accuracy of the predictions of the *PPV* should increase accordingly.

Due to the fact that the model was developed after the actual gathering of data, that the model can provide the highest possible accuracy for prediction of *PPV* values is somewhat limited. Some of the parameters utilized to generate the model results were obtained from existing literature, whereas other parameters, such as the frequency of vibration and pre- and post-decay factors were determined by interpretation of recorded data. Among the parameters obtained from the literature are the n and α constants, the estimation of the vibrational propagation velocity of the rock mass, and the *VOD* of the explosive. It is beyond the scope of this research to determine specific values for the n and α constants that could yield optimum model prediction with the least standard deviation of error.

For the recorded data, the *PPV* values were assigned to each blasthole location based on the nominal delay number and the distance to the geophone, and when there were two or more blastholes detonated with the same nominal delay, the location in the round was assigned based on the *PPV* magnitude and their distances to the geophone. For each of the blastholes that were detonated with the same cap delay, the greater the distance of the blasthole to the geophone, the lower the *PPV* that was assigned to a given blasthole location among those possible. In principle, this method is consistent with the theory but can in practice, lead to interpretation errors.

This chapter provides *PPV* predictions, obtained post modeling process, which yielded an acceptable difference with the recorded *PPV* values. In this regard, in the validation of the model, it was not meant to determine the n, α, and other constants that yield the lowest statistical error. Given that some of the constants were not determined from empirical data but rather were obtained from literature, it should be clear that there is little benefit in performing statistical analysis. Nevertheless, this chapter demonstrates the potential of the modeling tool, featuring three-axial plots through which it is possible to present and compare the modeling results with the data records obtained from the monitoring campaigns.

Figure 6.1 shows a plot of a section of the blasthole pattern where the red dots correspond to the locations of the blastholes in the round and the number refers to the linear charge density, in kilograms per meter, for each particular blasthole location.

The graphs in this and the following chapters were created using OriginPro 8.5™ plotting software.

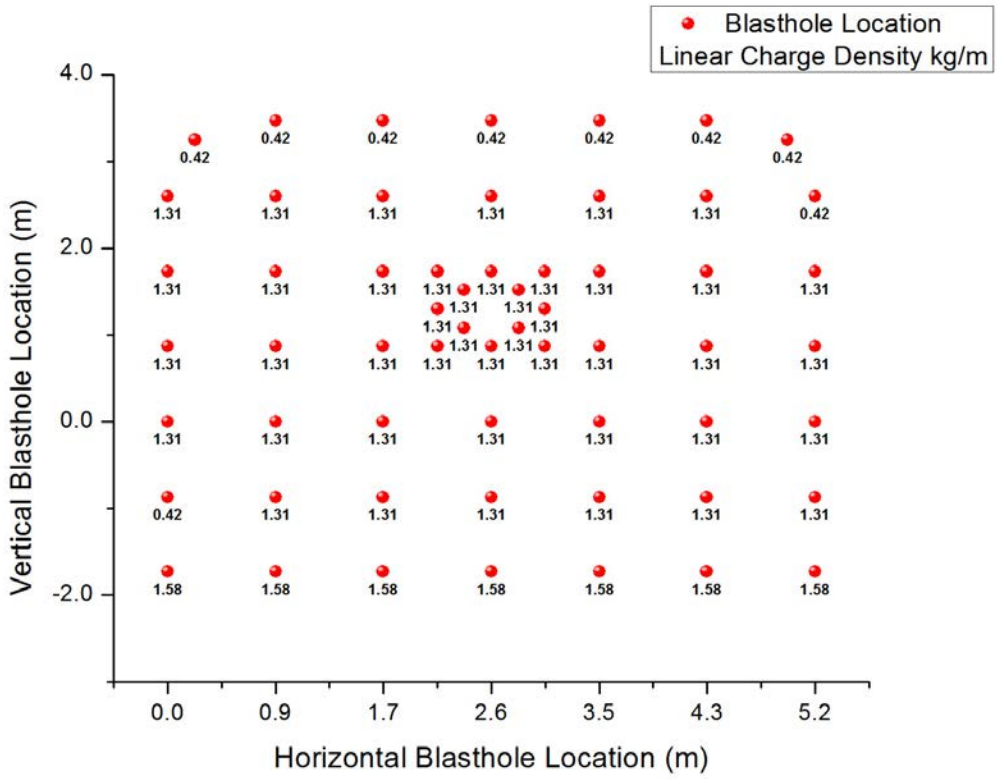

Figure 6.1 Blasthole's location and linear charge density

Figure 6.2 through Figure 6.5 show *PPV* values recorded at the geophone location and subsequently assigned to each blasthole in the round, where the *PPV* is plotted in the vertical axis for almost every location in the round, at face-geophone distances of 9.5m, 10.5m, 21.5m, and 26.6m, respectively.

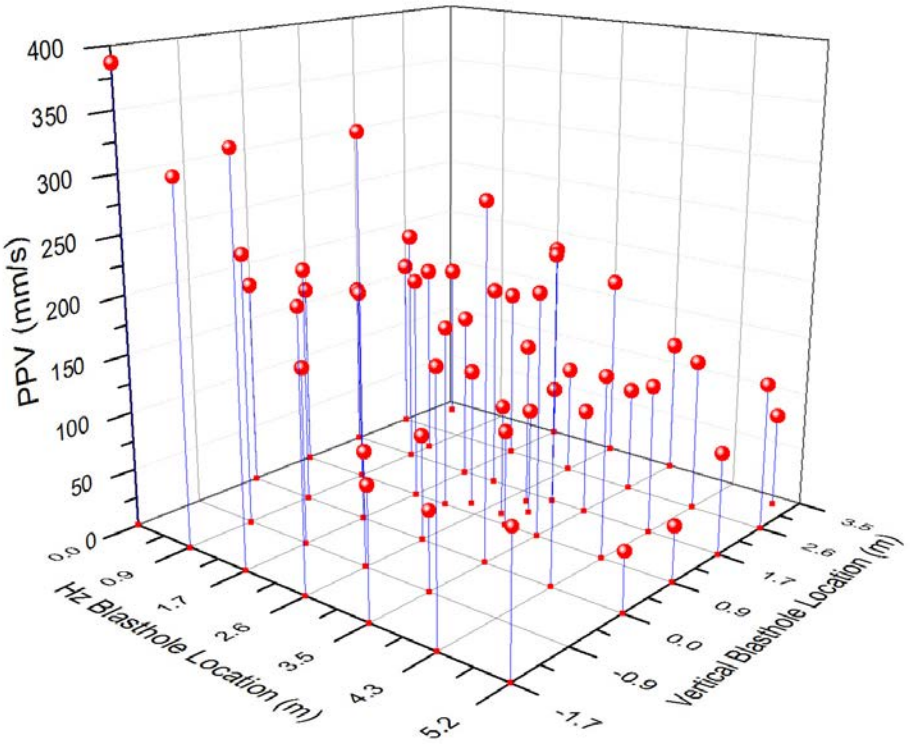

Figure 6.2 Measured *PPV* values – Musselwhite Mine – 9.5m from the face

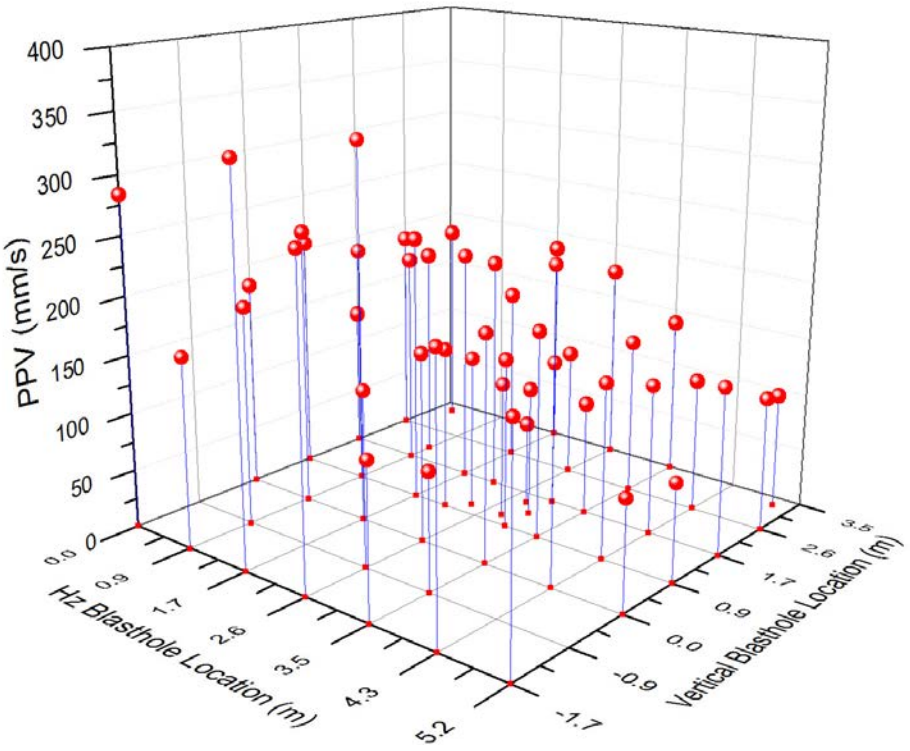

Figure 6.3 Measured *PPV* values – Musselwhite Mine – 10.5m from the face

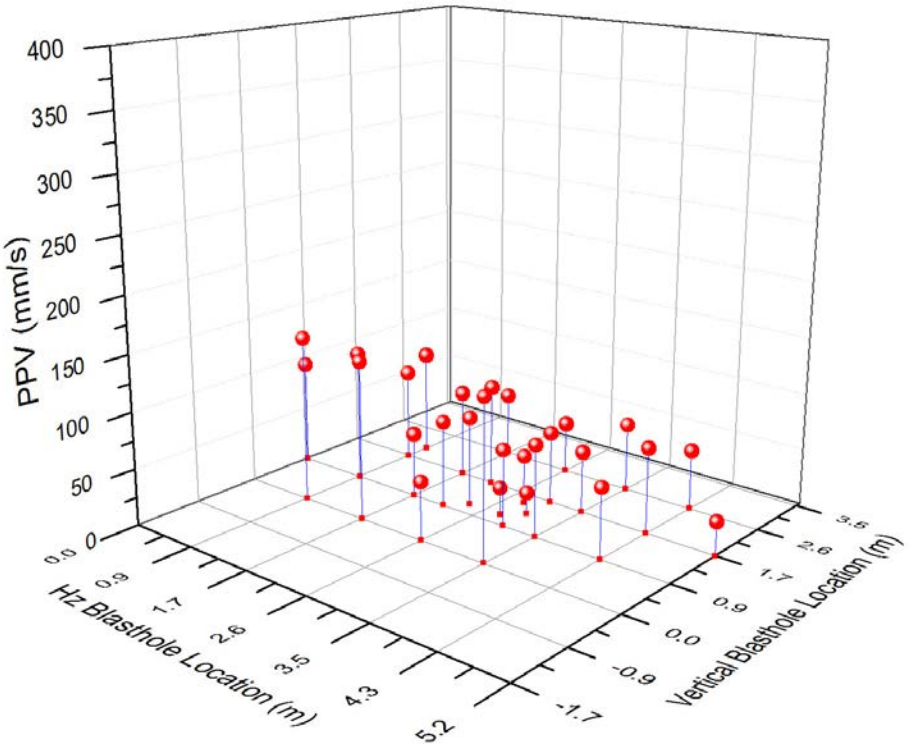

Figure 6.4 Measured *PPV* values – Musselwhite Mine – 21.5m from the face

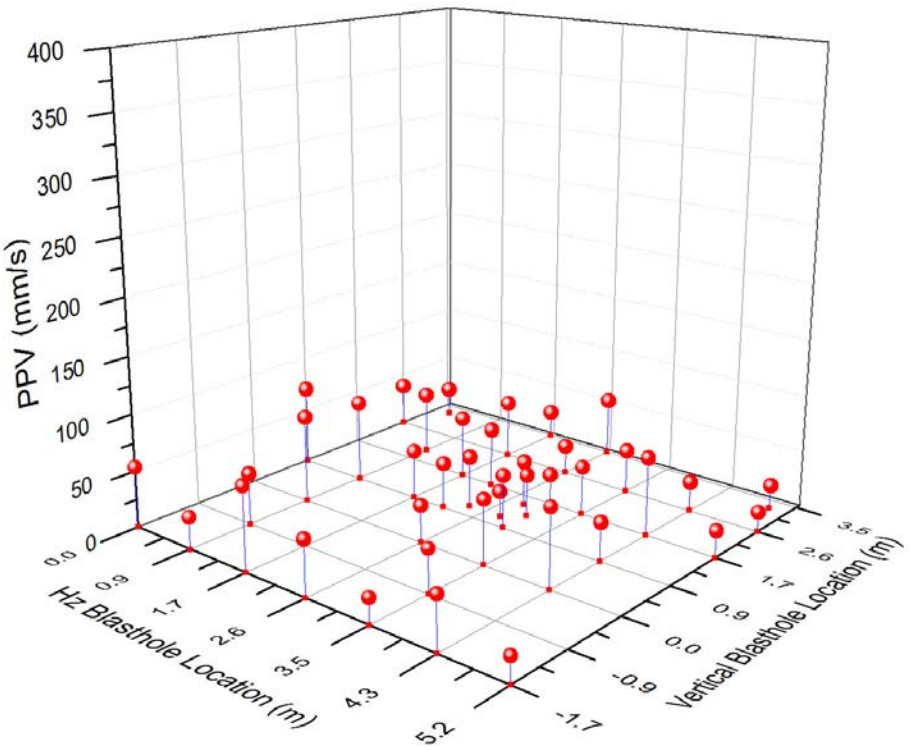

Figure 6.5 Measured *PPV* values – Musselwhite Mine – 26.6m from the face

6.2 *PPV* Data Measured versus Modeled – Musselwhite Mine Case

From the model, *PPV* values corresponding to each blasthole location were determined, and from these values a series of surface contours were plotted against recorded *PPV* values, as shown in Figure 6.6, Figure 6.8, Figure 6.10, and Figure 6.12. The surface contours indicate the magnitude range of the *PPV* modeled, in millimeters per second. The surface projections of these three-dimensional surface contours were also plotted in Figure 6.7, Figure 6.9, Figure 6.11, and Figure 6.13, as an aid to the reading of the values.

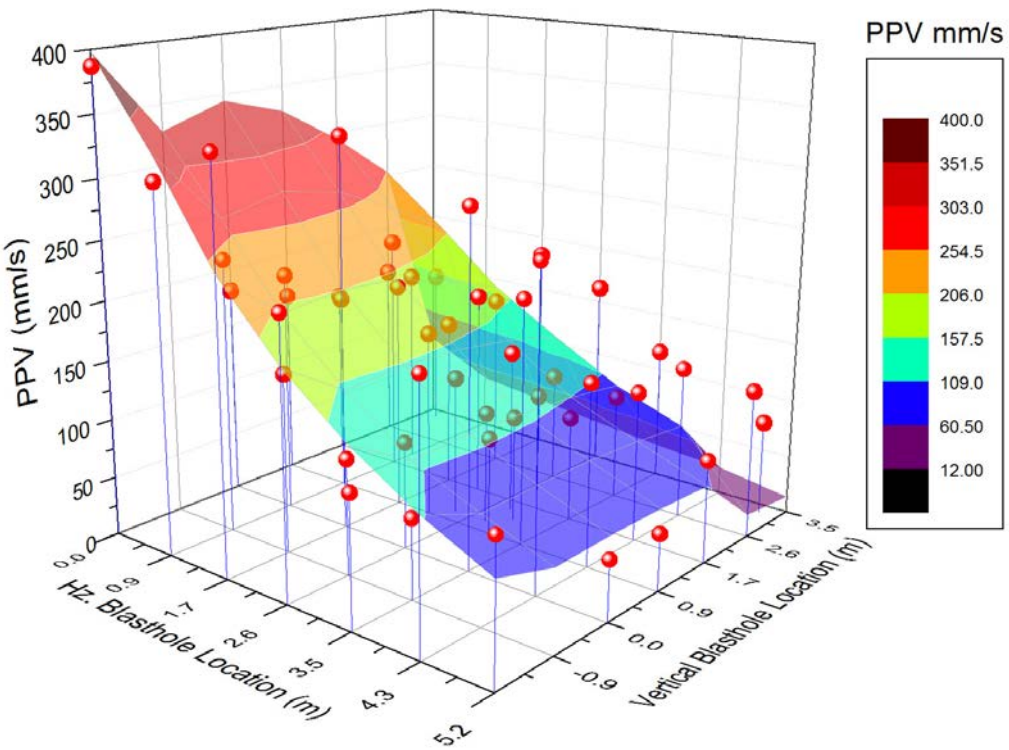

Figure 6.6 Measured versus modeled *PPV* surface contours – 9.5m from the face

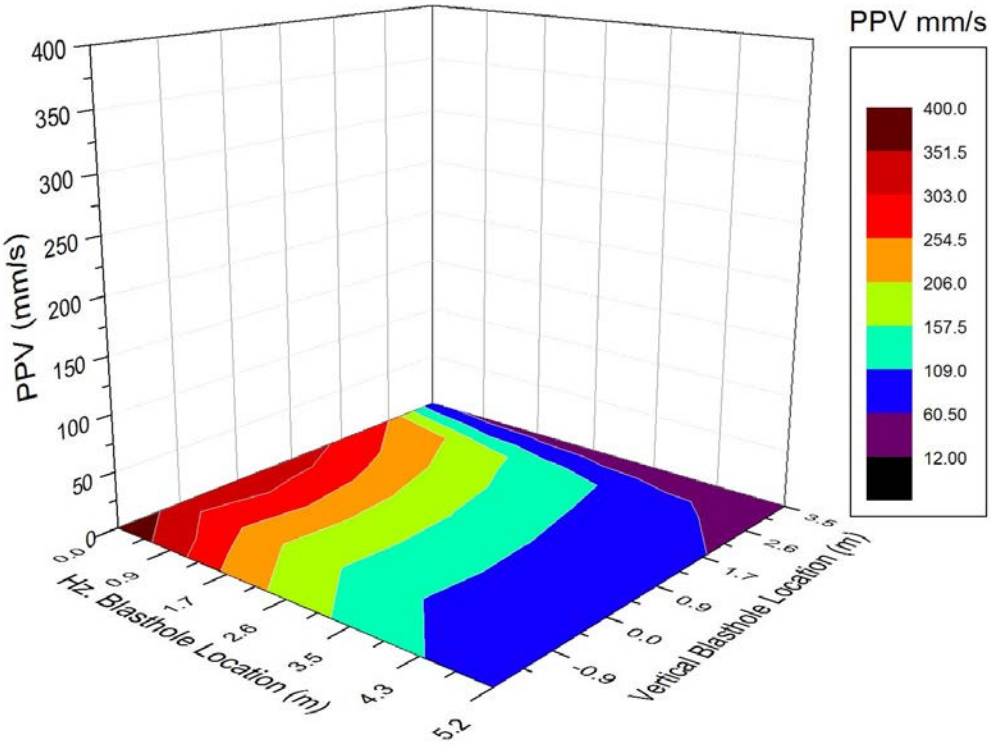

Figure 6.7 Surface projection of modeled surface contours – 9.5m from the face

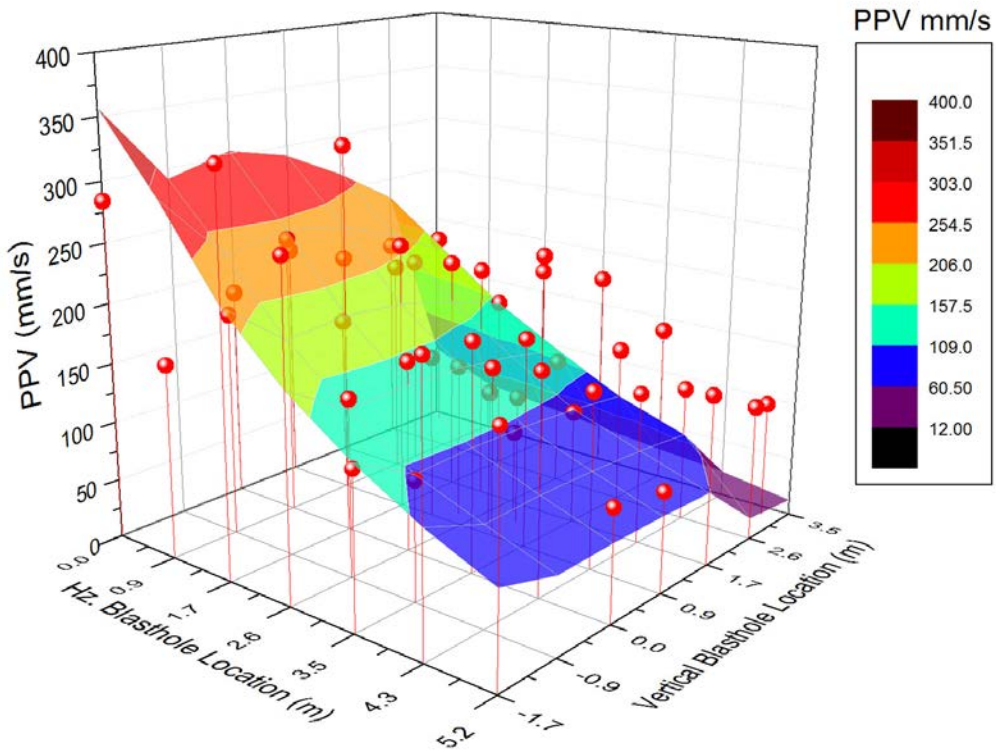

Figure 6.8 Measured versus modeled *PPV* surface contours – 10.5m from the face

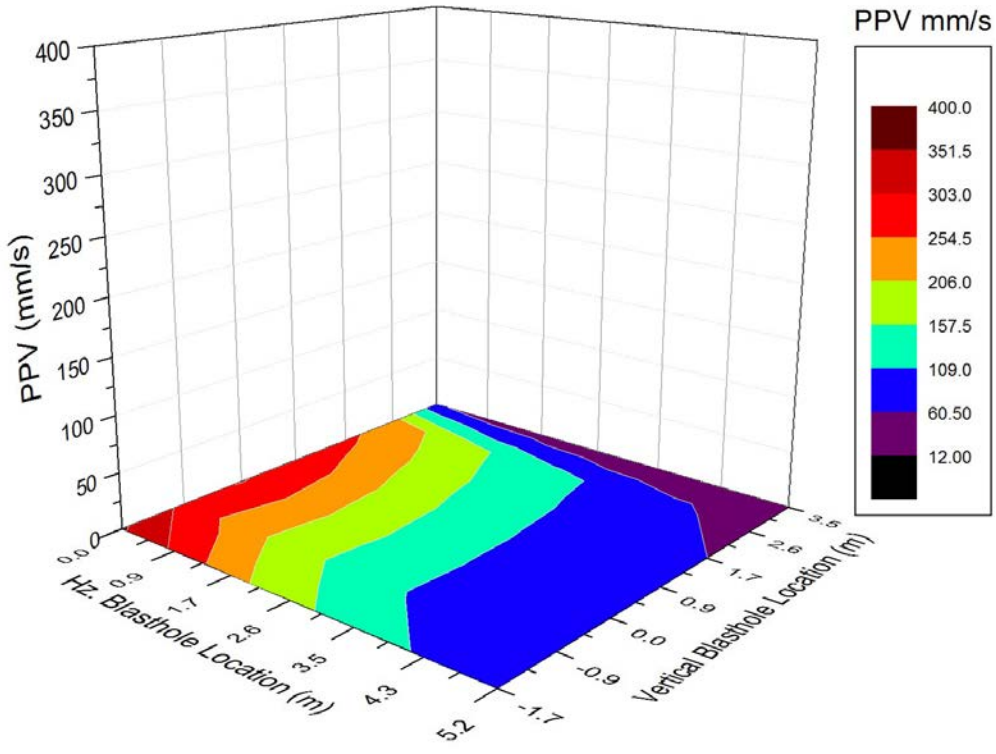

Figure 6.9 Surface projection of modeled surface contours – 10.5m from the face

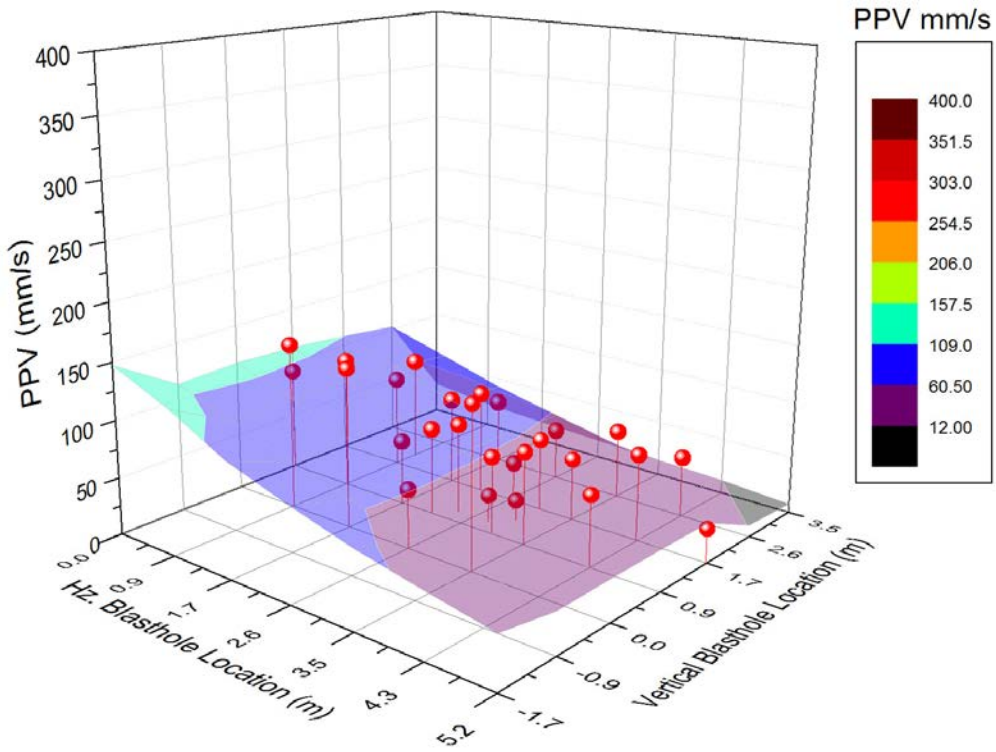

Figure 6.10 Measured versus modeled *PPV* surface contours – 21.5m from the face

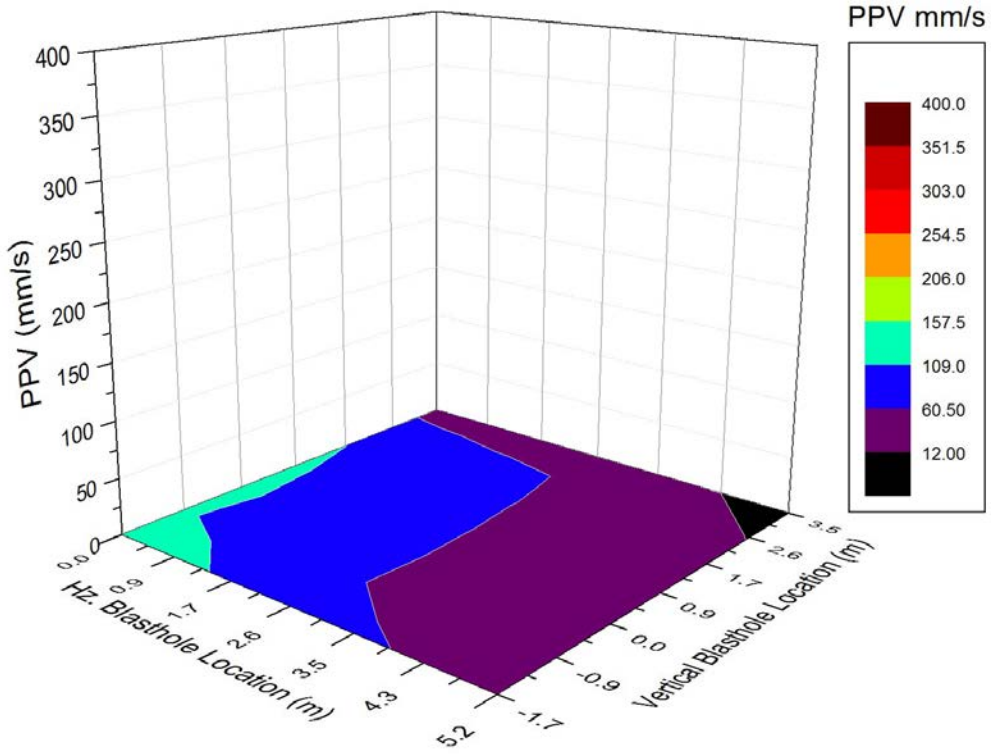

Figure 6.11 Surface projection of modeled surface contours – 21.5m from the face

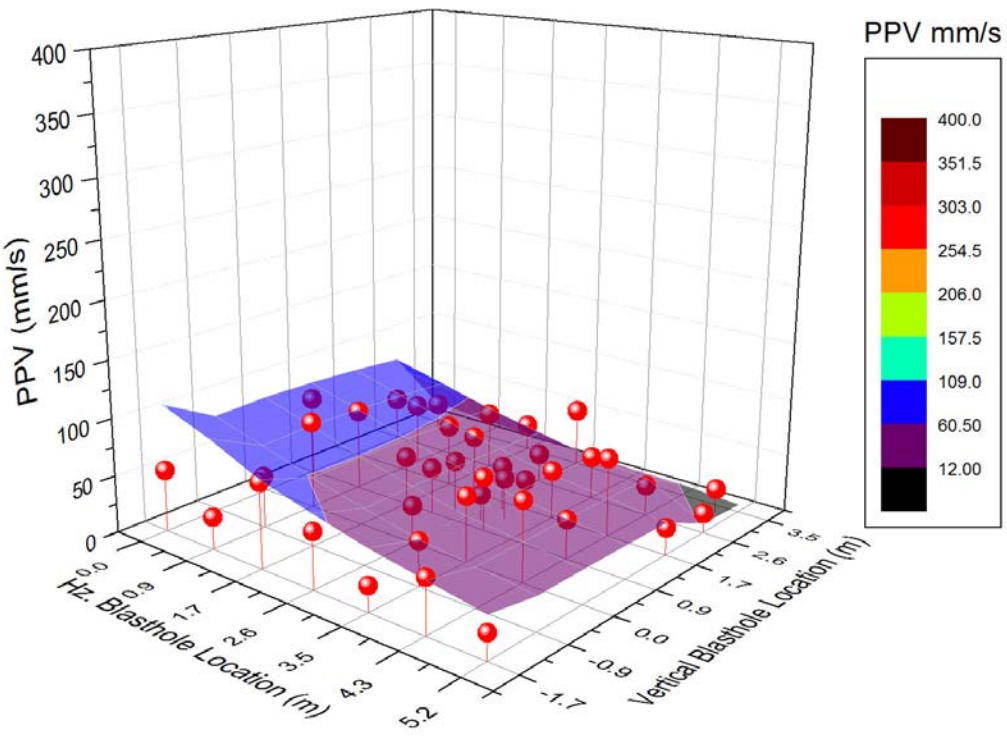

Figure 6.12 Measured versus modeled *PPV* surface contours – 26.5m from the face

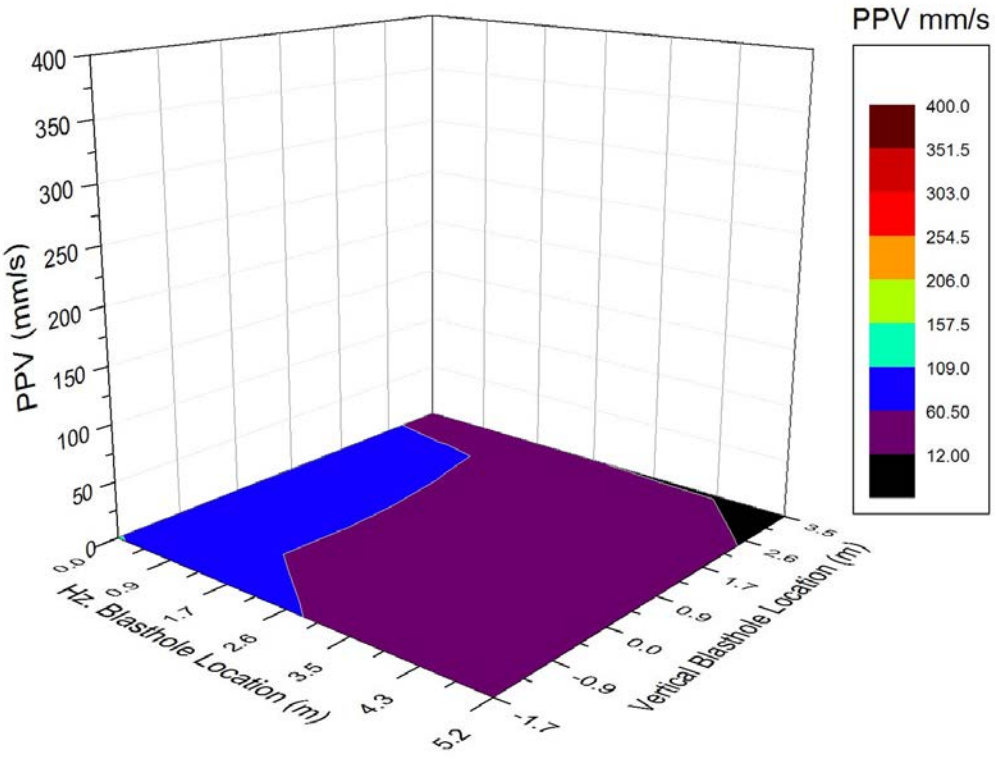

Figure 6.13 Surface projection of modeled surface contours – 26.5m from the face

Three main factors that form part of the model's architecture, which were used to obtain the *PPV* results in this chapter, are considered to enhance its potential beyond current methodologies: first, the proposed model predicts a *PPV* value in which the distance to every individual packet is accounted for, including as it is applied to a far-field case type scenario; second, the model uses linear superposition of the generated waveforms after they have been shifted by their respective arrival times; and third, it also accounts for the diffraction of the seismic waves. The combination of these factors with the right set of constants should lead to a much more precise *PPV* prediction. In contrast, current methodologies make the use of discrete values for the near-field *PPV* calculation, with its applicability being limited only to "signature blastholes" and without consideration of the time component. For the far-field (as well as the intermediate-field), current methodologies do not consider the time component and it is up to the user to choose whether to use the collar, or a mid-point, or the toe of the blasthole for the geophone-blasthole distance. Although in the far-field, the time component and the appropriate geophone-blasthole distance might not be as relevant as in the near- and intermediate-field cases, it is still valid to apply the model to the far-field situation.

7 APPLICATIONS OF THE PROPOSED MODEL

7.1 General

A broad range of blasting applications could be analyzed with the proposed modeling tool. All modeling tools, including this one, require calibration of input parameters. This model requires the input of fitting constants to yield an accurate prediction of *PPV* values, which must be established via numerous particle velocity monitoring records of near-, intermediate-, and far-field detonations.

Potential applications include explosive analysis where *PPV* in the very-near-field, i.e., within a few centimeters of the blasthole, could be estimated. As well, the determination and analysis of the appropriate explosive type and its distribution throughout the blast pattern could be made, aiming to reduce potential damage to rock excavations and structures.

The proposed model is not limited to *PPV* analysis of drifting and tunneling operations, but could also be used in underground and surface production blasting, where the geometry of the blast with respect to the point of interest is similar to that of the model's set-up, that is, in the near-field or where the seismic waves would pass through a point of diffraction before arriving at the point of interest.

7.2 Analysis of the *PPV* for different Explosive Types

The following example shows the 3-D surface contour of the distribution of the *PPV* for one blasthole loaded with *ANFO,* obtained for many location points around the face of the round (Figure 7.1). Figure 7.2 shows *PPV* results, but in this case the scale of the *PPV* was increased and discretized to a much finer degree, at a very close range to the blasthole. This greater level of discretization around the zone of interest can easily be achieved in the model by factoring the monitoring's (x,y) location point with a factor lower than one. The reader should be aware of the non-linear waveform superposition affecting the blastholes at the very close range of the explosive charge (Blair, 2007), where irreversible deformation takes place. The non-linear waveform superposition that should be used for the very-near-filed would yield a smaller or greater *PPV* calculation value – depending on the constant used – than the linear scheme used in the proposed

solution. Also, it would be necessary to make modifications to the model in order to achieve a smooth transition at the boundary of the non-linear and linear zones.

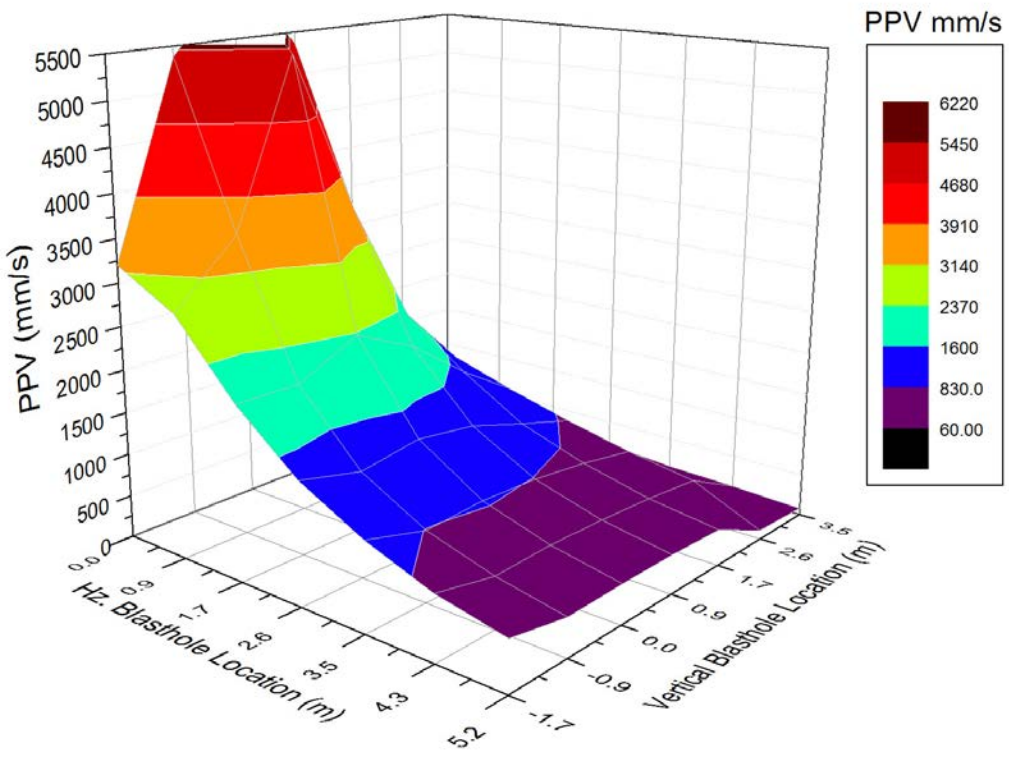

Figure 7.1 Near-field *PPV* of *ANFO*

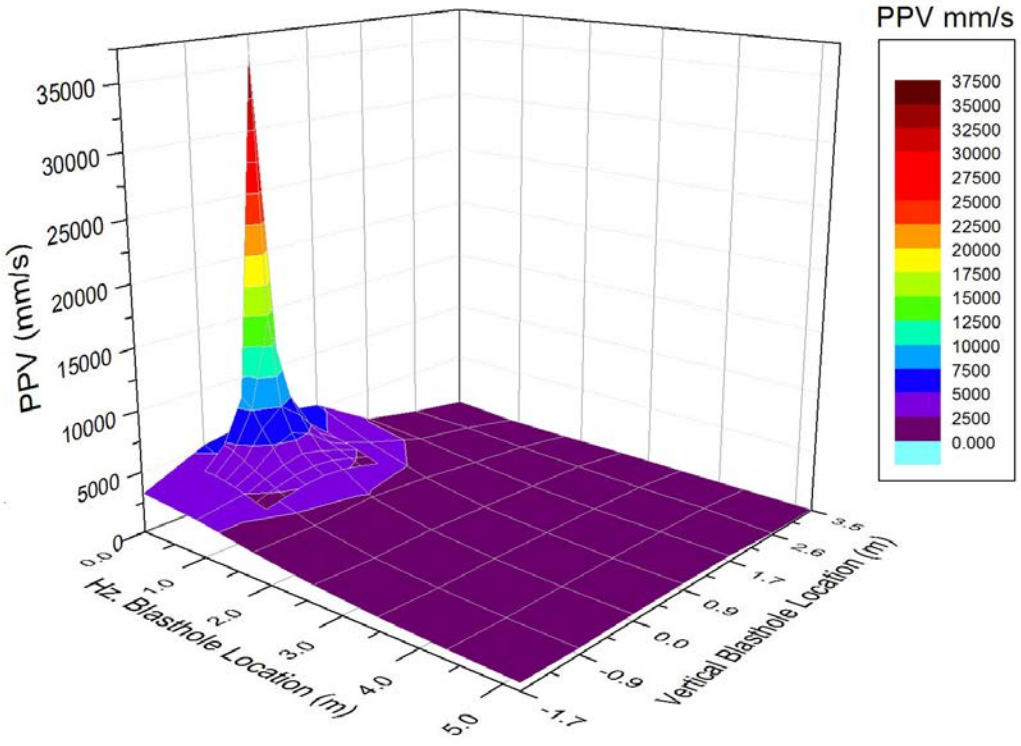

Figure 7.2 Near-field *PPV* of *ANFO* – Finer discretization around the blasthole

Another set of predicted *PPV* values, obtained in close proximity to the blasthole location, was plotted for each (x,y) location point surrounding the blasthole, but where different types of explosives, commonly employed at the mine sites investigated, were used. In this case, the maximum horizontal distances from the blasthole to the point of interest is approximately 0.6m.

Figure 7.3 through Figure 7.7, show the three-dimensional *PPV* surface contours for SEC Detagel™, *ANFO*, and Dyno AP™ explosives, respectively. These explosives are commonly employed in the perimeter, body, and lifter blastholes, respectively. Figure 7.4 through Figure 7.8, show the two-dimensional surface projection for the same explosives.

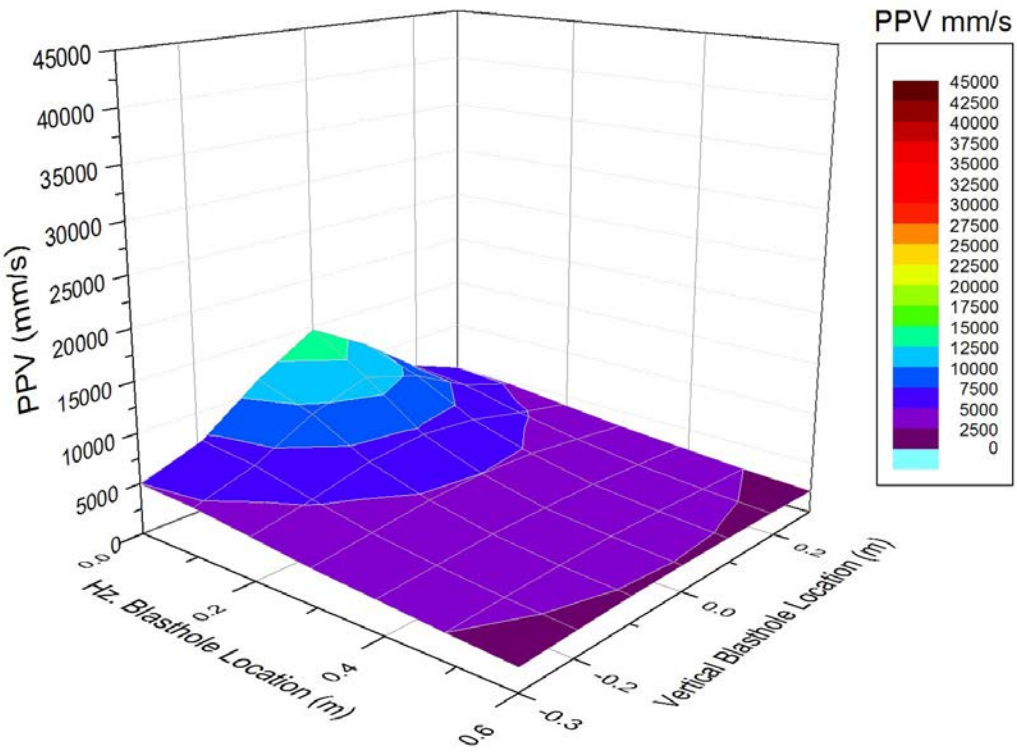

Figure 7.3 Near-field *PPV* modeled – 3D surface – SEC Detagel™

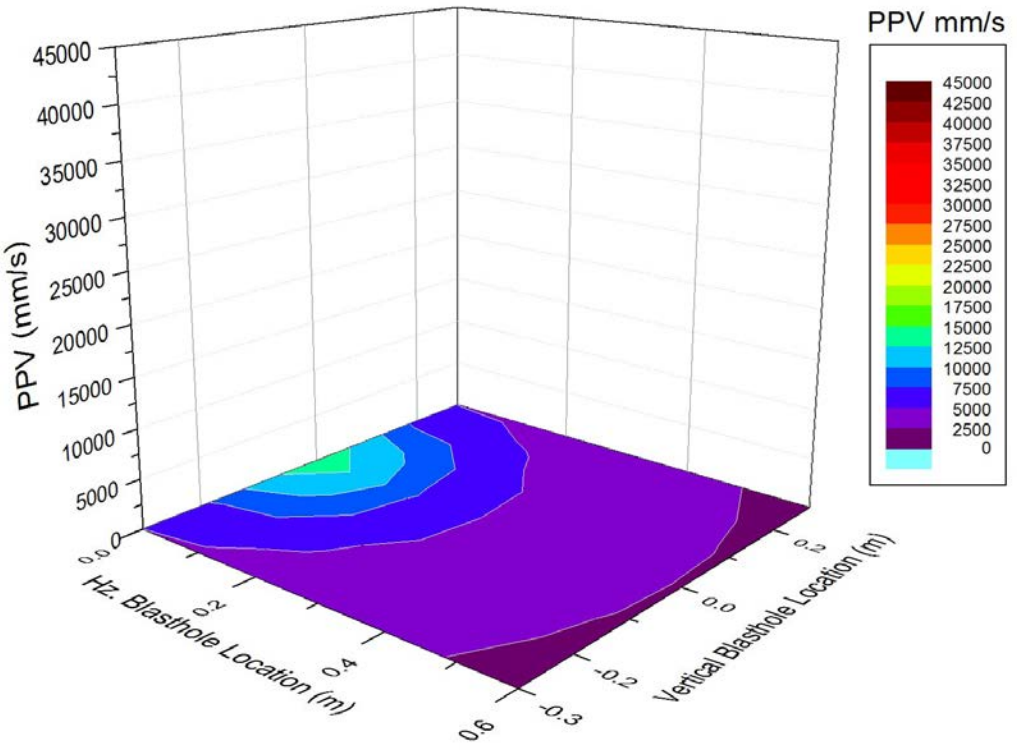

Figure 7.4 Near-field *PPV* modeled – 2D projection – SEC Detagel™

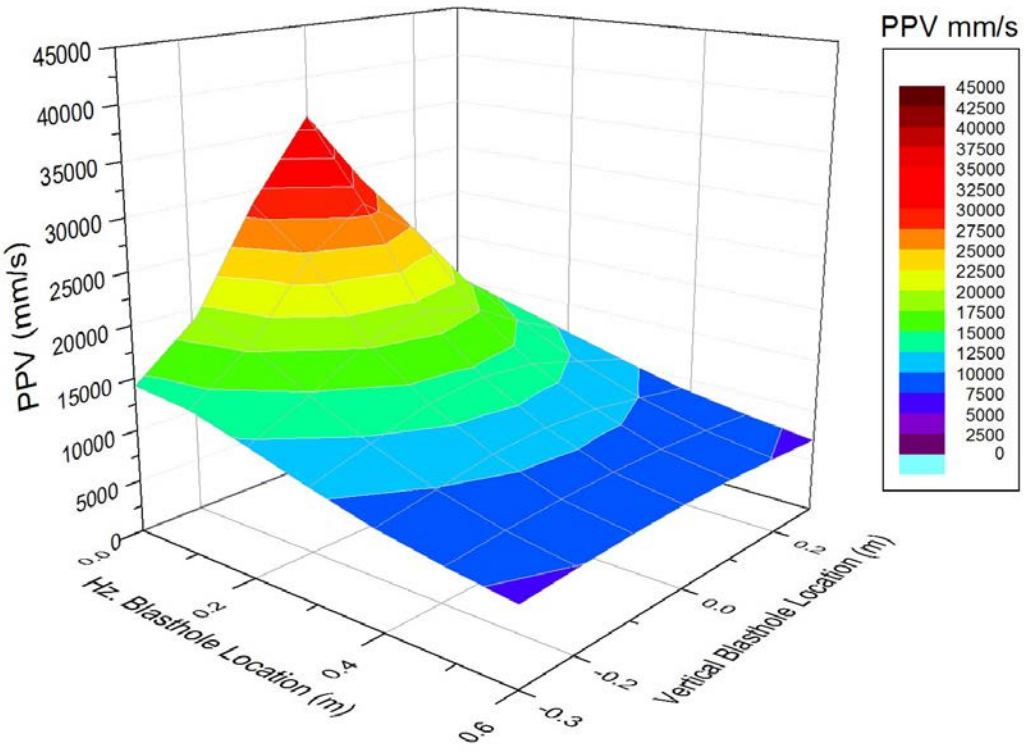

Figure 7.5 Near-field *PPV* modeled – 3D surface – *ANFO*

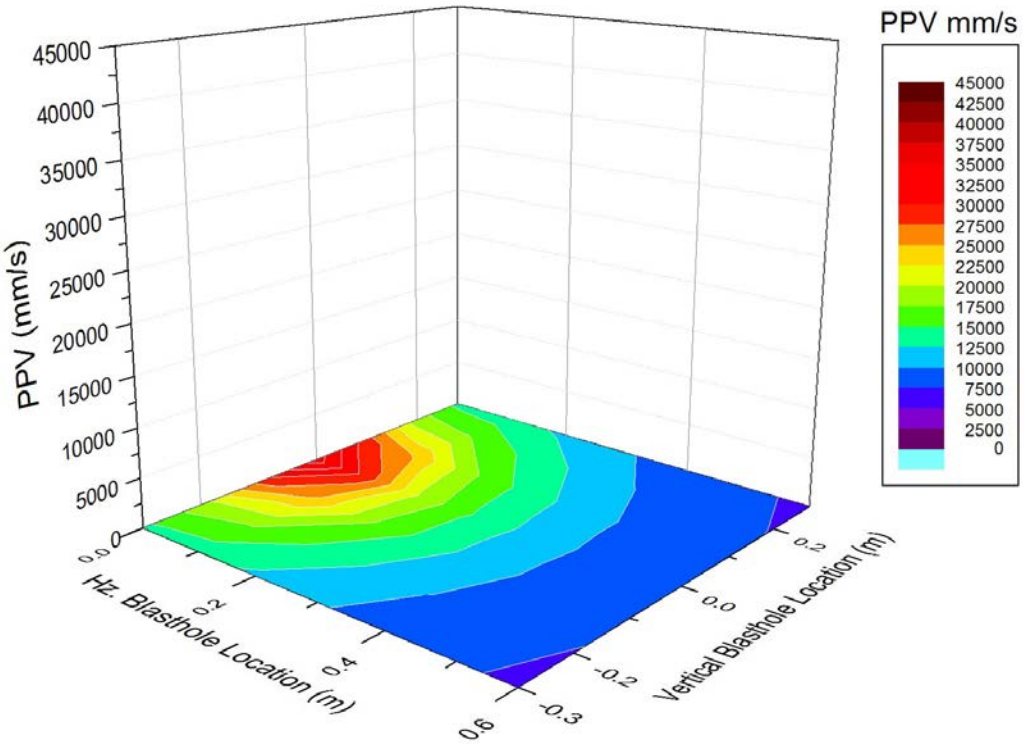

Figure 7.6 Near-field *PPV* modeled – 2D projection – *ANFO*

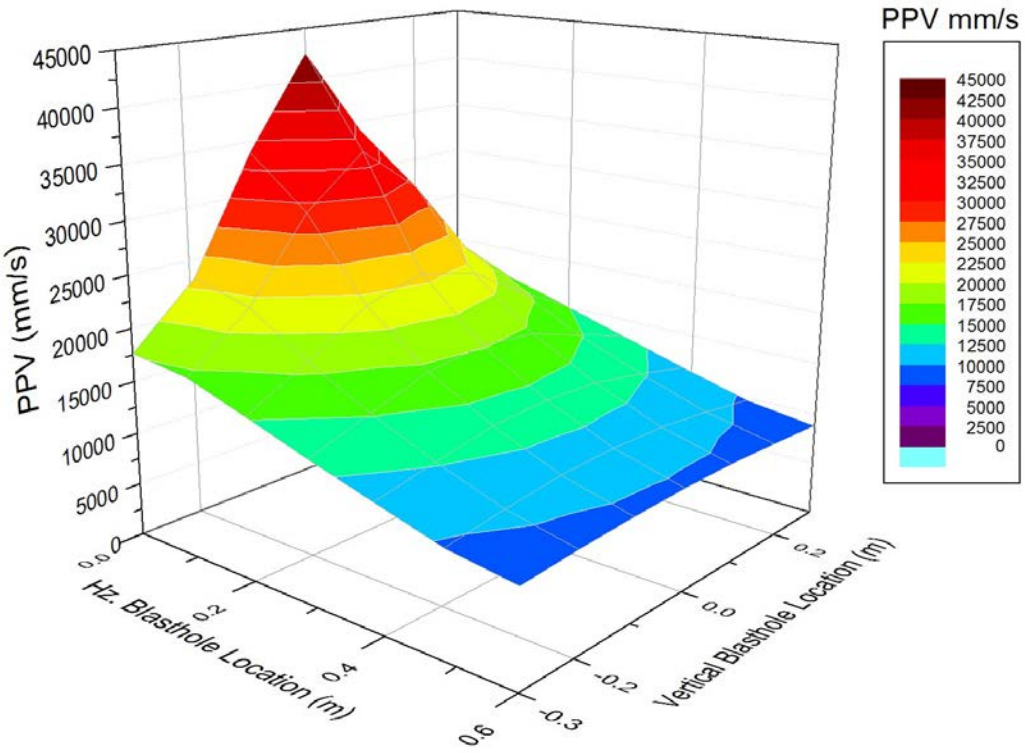

Figure 7.7 Near-field *PPV* modeled – 3D surface – Dyno AP™

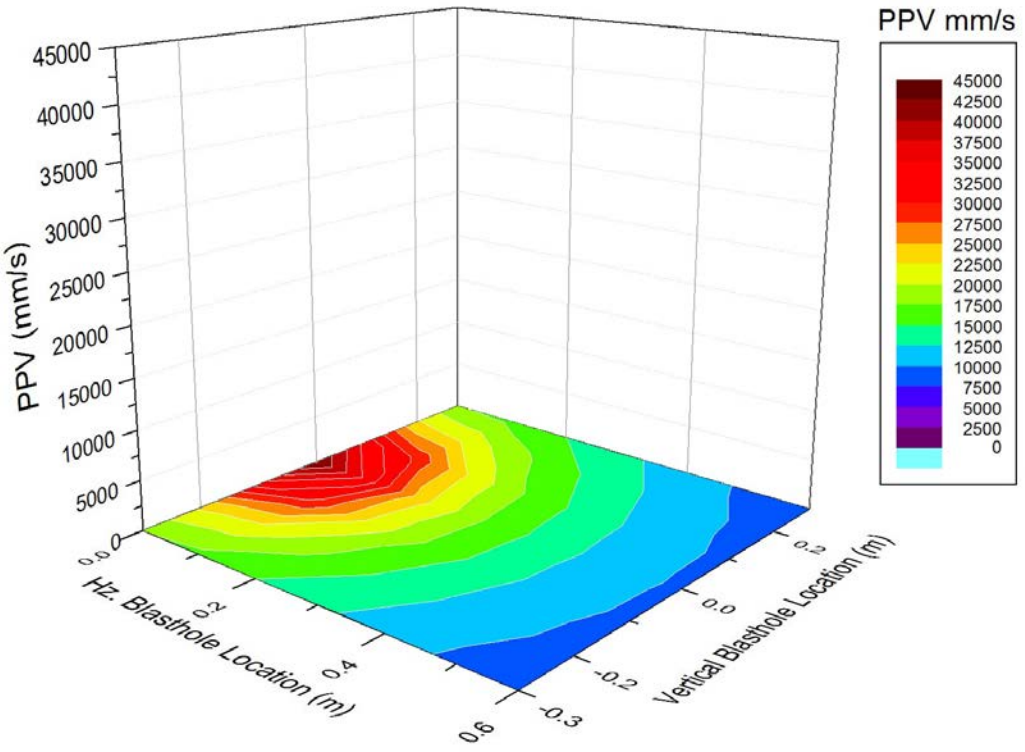

Figure 7.8 Near-field *PPV* modeled – 2D projection – Dyno AP™

The height of the column charge corresponds in all cases to the length of the blasthole of 4.3m. By reducing this height to a very small value (a few millimeters), one could obtain results right next to an infinitesimal small explosive charge, allowing for the determination of *PPV* values along the entire column of explosive. Although this test did not form part of the analysis, it could well be used to calibrate the model using laboratory size blasting samples.

7.3 Blasthole Interaction Analysis

The interacting detonating charges can also be analyzed from the modeling results. For example, two or more charges detonated with the same time delay could be used to assess the radius of interaction of each blasthole charge, thus aiding in determining the burden and spacing that could potentially optimize fragmentation and minimize damage inflicted to the perimeter of the excavation. Figure 7.9 and Figure 7.10 show the three-dimensional surface contour and its two-dimensional surface projection for two interacting charges, with 58cm spacing between them. The explosive considered was Dyno AP™. For this example, it was assumed that the samples are detonated at the same nominal delay, and so, there is no phase shift between the waveforms of both blastholes.

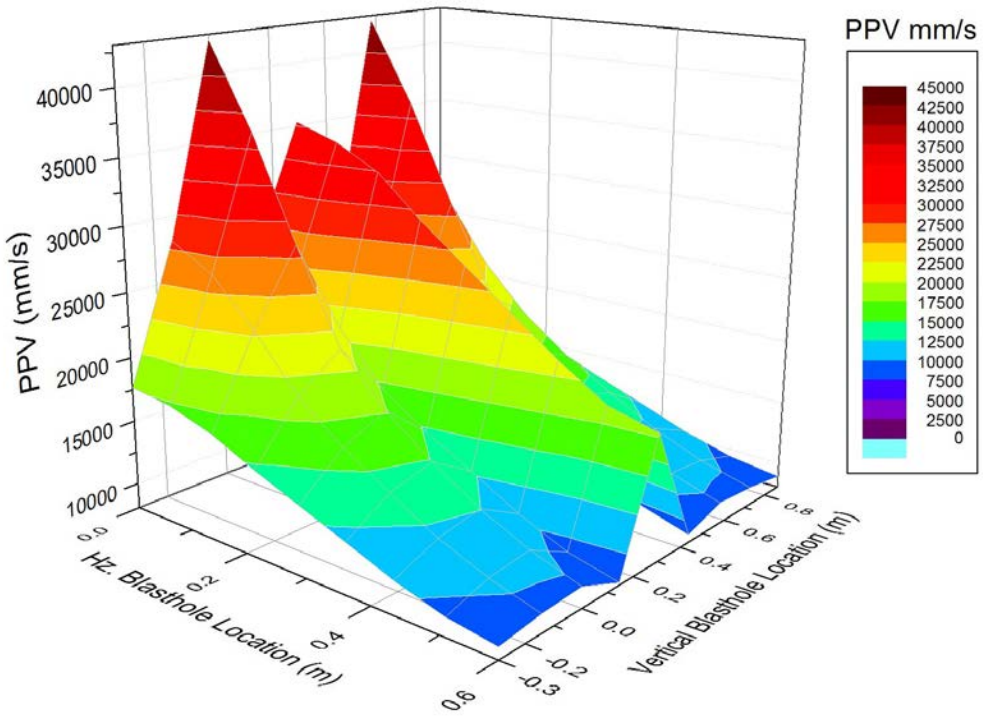

Figure 7.9 Blasthole Interaction – 3D surface – Dyno AP™

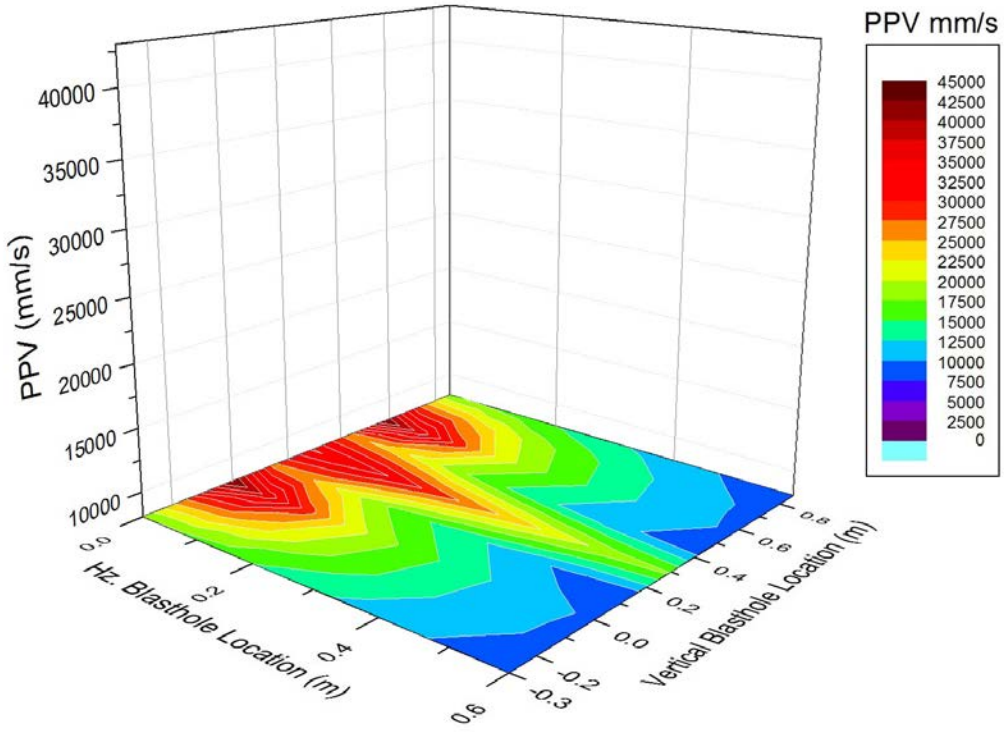

Figure 7.10 Blasthole Interaction – 2D projection – Dyno AP™

7.4 Other Applications of the Model

7.4.1 Blasthole Distribution Analysis

An extension of the previous subchapter would include determination of the *PPV* predictions for different types of explosive considering their distribution as employed in a round. With the model, *PPV* predictions can be determined at any given location, either within the face or in such cases where the seismic vibration has to pass through a point of diffraction, and thus, potential negative implications at any given location could be assessed.

7.4.2 Surface and Underground Blasts

The model was originally designed and implemented for drift and tunnel development, but may well be utilized to assess underground and surface production blasting, where the geometric conditions of the excavations are similar to that of the original design. The POIs (geophones) could be located in the same plane of the blasting round or at 90^{o} from it, as shown in Figure 7.11. In this sense, blastholes can be positioned at any given location, while their length and linear charge densities are user defined. Currently the model is limited to parallel blastholes but could be modified to allow for the analysis at any given orientation.

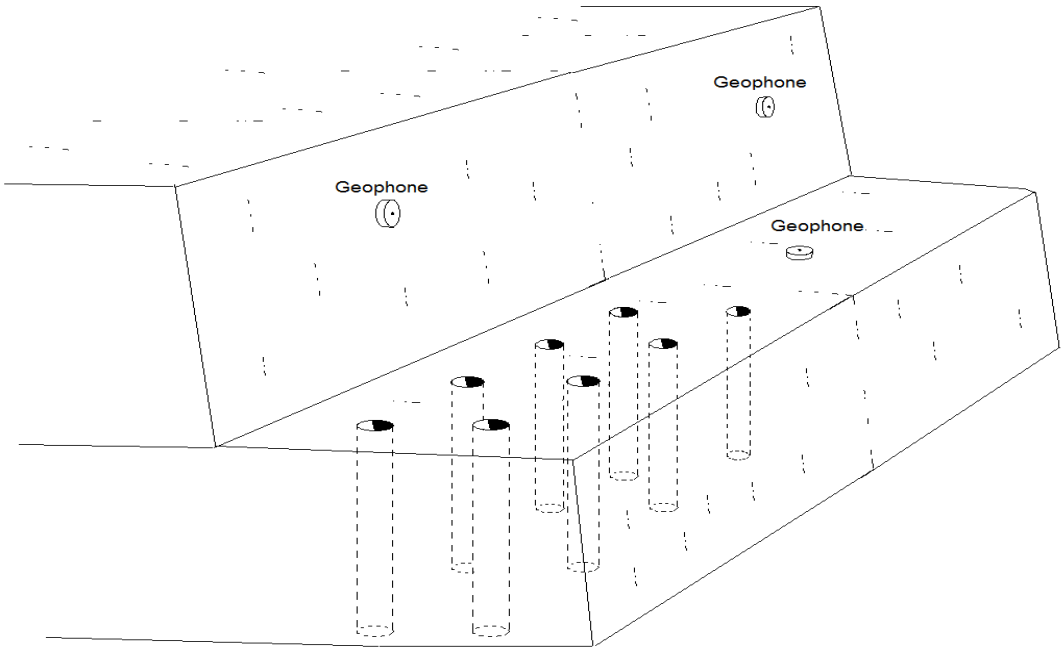

Figure 7.11 Application to a surface blast situation

7.4.3 Pyrotechnic Caps Delay Scatter

With the model, one could determine, for example, the implications of two or more blastholes detonating at the same nominal delay, with the addition of some time delay, in order to emulate the scatter existing among pyrotechnic caps similar to those of Figure 3.26. Ideally, it would be desirable to avoid linear superposition of waveforms originating with different nominal delay numbers, in order to reduce the *PPV* levels. This exercise can be easily performed with this model.

7.5 Limitations of the Model

The model considers that the location of the geophone or point of interest is either immediately at the face of the blasthole, or on a wall oriented 90^{o} with respect to the blasting round face. It determines the shortest distance to the geophone, however, the model is constrained to a specific geometry by having to determine the distance to the geophone necessarily passing through the point of diffraction located at the face-wall

intersection, and from there to the point where the geophone has been installed. This might not always be the case, for example, for some of the perimeter blastholes located at the boundaries of the blast pattern.

Also, depending on the blast sequencing of an actual blasting round, for some of the modeled waveform packets of certain blastholes, the direct path from the packet location to the point of diffraction would not be possible; this would be due to the fact that previous detonated blastholes have opened a void, also known as screening influence (Blair, 2007). For these cases, an actual seismic vibration will be forced to go around this newly created opening. The model provides no consideration for an indirect path of the seismic wave but could potentially be modified to factor in this effect. This can be done, for example, by taking into consideration the current open void (based on the detonation sequence) and the semi-perimeter of an ellipse as the distance that the seismic wave should travel from the packet location to the *POD*. In this case, twice the semi-major axis of the ellipse would be the distance from the packet centroid to the *POD*, and the diameter of the open void would be twice the semi-minor axis.

The blastholes are considered parallel to each other and parallel to the strike orientation of the drift or tunnel. The reality though, is that blastholes normally present some intentional or designed deviation as well as unintentional or unavoidable deviation. For example, in a standard blast pattern, the perimeter blastholes are normally drilled in an outward orientation with a wider angle to maintain the planned area. Since the drilling equipment requires room to position the drill, if these perimeter blastholes are not drilled with a wider angle, the size of the excavation will be reduced as subsequent rounds are blasted. Potential upgrades could include non-parallel blastholes, but this is beyond the scope of this research.

8 CONCLUSIONS

Analysis of *PPV* versus time data and assessment of rock mass quality at the sites investigated has experimentally confirmed that as rock mass quality decreases, the rate of decay of the seismic vibration amplitude increases. That is, if the distance travelled by the seismic vibration is the same for two dissimilar rock mass qualities, then the amplitude of the particle velocity for the lower rock mass quality will experience a more rapid decay or damping over that distance.

Similarly, it was experimentally demonstrated that a rock mass of poorer quality generates lower vibration frequencies, and also dampens the higher vibration frequencies faster, as the wave travels through that particular medium, allowing only the lower frequencies to remain. This becomes especially evident when comparing the frequency content of two dissimilar rock mass qualities, such as those existing at the Musselwhite Mine (90 *RMR*) versus those at the SSX Mine (35 *RMR*), where observed peak vibration frequencies were approximately 1100Hz and 150Hz, respectively.

The high-frequency geophones installed in close proximity to the explosive charges indicate that, at such a short range, the high frequency amplitude components of the particle velocity have greater influence than the lower frequencies. Peak velocities of greater than 60% that of the original *PPV* are measured within the 500-1000Hz range, when a *PPV* versus time record for a good rock mass is analyzed. These results represent a step forward, in respect of the fact that the values that have been commonly observed in the great majority of literature to date have been in the order of 5-50Hz (where the values were obtained at greater distances from the explosive source and utilized lower frequency range geophones).

From analysis of the field measurements, a *PPV* versus *SD* relation for various rock mass qualities was developed. This relation confirmed that the more competent the rock mass quality, the higher the *PPV* required for fragmenting and displacing the rock, and at the same time showed a progressively lower extent of overbreak with improving rock mass quality.

Blasting generates ground vibrations that are predominant at the natural vibration frequencies of the rock. The research has produced useful empirical data on the predominant frequencies associated with various rock mass qualities, as determined in close proximity to a given drift development blast. This data could provide some of the input parameters required to assess various ground support elements employed, for example, shotcrete and rock bolts, using numerical modeling tools or other methods, in order to determine dynamic response under a variety of rock mass conditions. Numerical codes such as PFC3D could perform static and dynamic strength analysis of pseudo-materials subjected to vibrational shaking with user defined loading amplitudes and frequencies.

Also, when safety is a principle consideration, should blast monitoring become a regular feature of mining operations, and given that *PPV* and frequency content are related to rock mass quality, this information could be used to produce much deeper, more thorough assessments and interpretations of the quality of the rock mass and its need for an appropriate type of support system.

The time scatter in long period (LP) pyrotechnic blasting caps suggests that utilizing the total weight of explosive per delay would likely yield erroneous *SD* factor results. There was very little evidence in this research of constructive interference (productive interaction) between blastholes with same nominal delay, such that the vibration waves would eventually yield higher peak magnitudes of particle velocity, compared to the peak magnitudes for individual blastholes with the same nominal delay time, when this type of blasting cap is utilized.

The use of electronic detonators might have greatly simplified the analysis of the seismic records if each blasthole would have been assigned a different delay number. This would have helped reduced uncertainty with regard to the locations of some of the blastholes since the delay scatter for this electronic detonator is assumed to be negligible. By

recognizing the delay time in the seismic records, the recorded *PPV* could be easily assigned to a particular blasthole location.

The model results were used to demonstrate that two blastholes with exactly the same nominal delay time could generate partial destructive interference of their seismic waveforms, measured at the geophone location, due solely to the spatial location within the round. And so, even though two or more blastholes could detonate at exactly the same time, it is possible that this is not reflected in the particle velocity seismic records as an increase in overall peak value.

Overbreak measurement, as determined through the *ELOS* method, involves values that in some cases are perceived to be quite small even in the presence of a wedge type breakout of rather large size, owing to the fact that the total volume of the estimated overbreak is normalized by the planned excavation surface, and thus yielding an average of the overbreak thickness. *ELOS* represents the average depth of the excess of broken material measured normal to the excavation surface. An alternative to the method employed in this research could have been to present simply the total volume of overbreak, without normalizing it to the original volume or surface area being excavated; in this case, it would not be possible to compare the overbreak volume against different excavation sizes.

The semi-empirical model was validated against Hustrulid-Lu (Equation 29), however, the model is not restricted to the near-field particle velocity determination, as in Hustrulid-Lu's equation. This is due to the fact that the model utilizes a waveform instead of discrete numerical values, and can incorporate the delay in arrival times of each and every packet of the blasthole. One of the major contributions of this research is its wide range of applications to different blasting problems, as the solutions obtained using the model and the equations and methodologies provided therein shows.

The model was used to demonstrate the effects of the sampling rate to accurately record *PPV* measurements, where an error on the order of 9% could be made if using 4,096

samples per second, and on the order of 1% if using 16,384 samples per second, as compared with an infinite sampling rate. It is clear that the sampling rate should be set as high as is possible for the instrument in use, but that the rate should also depend on the number of channels being recorded simultaneously, as well as the memory availability of the monitoring equipment.

The proposed methodology (and its subsequent application) addresses the problem of the reduction of the particle velocity of a wave after it has passed a point of diffraction at the face-wall interface. It is expected that the energy of the seismic waves is reduced after passing the point of diffraction at this interface, and the methodology accounts for part of this reduction by using a portion (the vertical projection) of the original *PPV* value. This portion of the original *PPV* value is obtained directly from the value of the angle formed from the location of the incidence ray to the location of the *POD* at the interface.

As the proposed semi-empirical formulation (Eq. 45) incorporates the distance of each and every packet within the blasthole, there is no need to define a unique distance value for determination of the *SD* factor, as in the far-field case. The equation also accounts for the delay in the arrival time of every seismic waveform originating at its packet location, for both the near-field and far-field cases. In essence, it incorporates into one formula, the near- and far-field effects as separate body and surface wave propagation components.

The model incorporates various constants, which can be set at their basic, uncalibrated values, i.e., 1, for simplicity but which can also be determined in the calibration process for the chosen number of blast rounds as monitored (the greater the number of blast rounds, the greater the accuracy of the calibration). In this way, the model provides for a great deal of flexibility to the end user. Calibration of these empirical constants does, however, increase complexity, as these constants need to be defined. In Chapter 5, there is a brief explanation of some of the tests that can be performed in order to determine these constants. Due to cost constraints, not all the values for the input parameters were determined from field measurements. Where field data was not available, values for the input parameters were obtained using existing literature data. In this case, there is little

value in performing cross-correlation analysis between the modeled and measured *PPV* values. The general recommendation is to keep in mind that the accuracy of the determination of the values for the empirical constants directly affects the reliability of the predicted *PPV* values. The more data collected the better. However, there is additional cost to gathering more and more data. Greater accuracy must be weighed against the cost of collecting that data.

In the model's application chapter (7), various examples were undertaken with the proposed model, accounting for explosive type and interaction between charges in a blasting round. These are basic applications that most blasting engineers should perform systematically. With the new approach, other types of analysis in which similar geometric conditions (as in a drift or tunnel development round) could also be analyzed, such as underground and surface production blasting, expanding its potential even further.

The model presents some limitations regarding the estimation of the distance from a blasthole's packet to the geophone location, hence affecting the *PPV* determined from the model. This is due to the fact that the whole blasting sequence is not taken into consideration by the model, and in order to incorporate it into a future proposal, consideration for the loss of part of the original seismic vibration energy should be made. This could be done by estimating the total travel distance of the seismic waves, as they must travel around the void produced by the detonation of previous blastholes, in accord with the blasting sequence.

9 RECOMMENDED FUTURE WORK

This research has shown that future advances in this new methodology could be made as follows:

- The proposed modeling tool requires the input of different equation constants, some of which were obtained from literature and subsequently adapted to the constants specific to the proposed model. It is imperative that the determination of the particular set of constants used by the model should be generated from a series of blast monitoring campaigns, applicable to one or more rock mass qualities. Some of these constants should be readily available, such as the rock mass body and surface propagation velocities, whereas others, such as the *f1* to *f3* factors, would have to be obtained from multi-variable statistical analysis of a number of monitored blasts. Once these empirically determined constants are obtained, the accuracy of the model results would be expected to increase.

- As a result of the concussion produced by the detonation of explosive charges, a given rock mass vibrates at many of its natural vibration frequencies. Although the proposed model can determine the particle velocity waveforms for a number of different frequencies, in this research only the particle velocity that results from application of the single predominant vibration frequency was tested. A multi-frequency analysis could potentially yield more accurate results, although certainly this will also increase the model's complexity. This complexity would include, for example, a determination of the propagation velocity for each range of frequencies being analyzed. To be rigorous in this matter, it would also be necessary to determine the *PPV* equation constants for each frequency range since, for example, the rate of decay and the propagation velocity is different for different frequencies.

- The proposed model assumes that the blastholes are drilled perpendicular to the surface of the face of the blasting round, whereas the reality is that not all the blastholes are drilled in this way. Some of the blastholes, specifically perimeter or contour blastholes including lifters, are drilled at an angle to increase the dimensions of the excavation. It is obvious that the maximum surface increase will be at the end of the blastholes in these cases, to provide sufficient room to

accommodate the drilling equipment. It is also to be expected that by incorporating the actual drillhole direction into the model, *PPV* prediction accuracy should also increase.

- Among the limitations evident in the model is the fact that as each blasthole detonates, it creates a void through which seismic waves cannot propagate. The modeling design assumed that travelled distance is determined from the straight path between a particular packet location and the point of diffraction. The reality, though, is that the seismic wave must travel around this newly created void. A simple solution to this problem might be to compute the travelled path from the packet to the point of diffraction using the perimeter of an ellipse, in which twice the semi-major axis would correspond to the straight line formed by the detonating packet and the point of diffraction, and twice the semi-minor axis would correspond to the diameter of the void being formed. In this way, the semi-perimeter of an ellipse would correspond to the actual travelled distance from a particular packet centroid to the point of diffraction.

REFERENCES

Adamson, W. R., Scherpenisse C. R., and Diaz, J. C. (1999). The use of blast monitoring/modelling technology for the optimisation of development blasting. In Proceedings Explo ’99, (The Australasian Institute of Mining and Metallurgy: Melbourne). pp 35-42.

Ambraseys, N.N., and Hendron, A.J. (1968). Dynamic behavior of rock masses, in Rock mechanics in engineering practice. Stagg, K.G., and Zieniewicz, O.C (eds.), New York, John Whey. pp. 203–236.

Anonymous (2011). The Bureau of Labor Statistics of the U.S. Department of Labor. Accident Classification by Industry.

Anonymous (2000). 17th Edition Blasters. Handbook (ISEE, 2000)).

Barton, N.R., Lien, R., and Lunde, J. (1974). Engineering classification of rock masses for the design of tunnel support. Rock Mech. Vol. 6(4), pp. 189-239.

Barton, N., Lien, L., and Lunde, J. (1974). Analysis of rock mass quality and support practice in tunneling and a guide for estimating support requirements. Internal Report of Norwegian Geotechnical Institute, Oslo, Norway, pp. 6–9.

Bauer, A., and Calder, P.N., (1978). Open Pit and Blasting Seminar. Mining Engineering Department, Queens University, Kingston, Ontario.

Bernard, E.S., and Pireher, M. (2010). The use of Round Determinate panels for the assessment of flexure performance of fiber reinforced concrete, Cement and Aggregates, ASTM.

Bieniawski, Z.T. (1973). Engineering Classification of Jointed Rock masses, Transaction South African Institution of Civil Engineers, Vol. 15. pp. 335-344.

Bieniawski, Z.T. (1976). Rock mass classification in rock engineering. In Exploration for rock engineering, proc. of the symp., (ed. Z.T. Bieniawski) Vol. 1, Cape Town: Balkema. pp. 97-106.

Bieniawski, Z.T. (1989). Engineering rock mass classifications. New York: Wiley.

Baird, G.P., Blair, D.P., and Jiang, J.J. (1992). Particle motions on the surface of an elastic half-space due to a vertical column of explosives. West Aust. Conf. Mining Geomech. pp. 367-374, Kalgoorlie, Australia.

Blair, D.P., and Minchinton, A. (1996). On the damage zone surrounding a single blasthole, Proceedings of Rock fragmentation by blasting, FRAGBLAST-5, (Ed) Mohanty, Montreal, Quebec, Canada, 23-24 August. pp. 121-130.

Blair, D.P. (2004). The frequency content of ground vibration. International Journal of Blasting and Fragmentation. 8: pp. 151–176.

Blair, D.P. (2008). Non-linear superposition models of blast vibration. International Journal of Rock Mechanics & Mining Sciences 45. pp. 235–247.

Bogdanoff, I. (1995). Vibration measurements in damage zone in tunnel blasting. Proceedings of Rock fragmentation by blasting, FRAGBLAST-5, (Ed) Mohanty, Montreal, Quebec, Canada, 23-24 August. pp. 177-185.

Breslin, J.A. (2010). One Hundred Years of Federal Mining Safety and Health Research. NIOSH's Information Circular 9520.

Clark, L. M. (1998). "Minimizing Dilution in Open Stope Mining with a Focus on Stope Design and Narrow Vein Longhole Blasting". MASc. Thesis, Faculty of Graduate Studies, Department of Mining and Mineral Process Engineering.

CMRI (1993), Vibration standards, Central Mining Research Institute, Dhanbad.

Cooper, P. W. (1996). Explosives Engineering, New York: Wiley-VCH. ISBN 0-471-18636-8.

Crandell, F.J. (1949). Ground Vibration due to Blasting and its Effect upon Structures", J. Boston Soc. Civ. Engineers, Apr. pp. 222-245.

Cunningham, C.V.B. (1983). The Kuz-Ram Model for Predicting Fragmentation from Blasting, Proceedings of the First International Symposium on Fragmentation by Blasting, Lulea Sweden. August 22–26. pp. 439–453.

Deere, D.U., Hendron, A.J., Patton, F.D. and Cording, E.J. (1967). Design of surface and near surface construction in rock. In Failure and breakage of rock, proc. 8th U.S. symp.

rock mech., (ed. C. Fairhurst). New York: Soc. Min. Engrs, Am. Inst. Min. Metall. Petrolm Engrs. pp. 237-302.

Dey, K. (2004). Investigation of blast-induced rock damage and development of predictive models in horizontal drivages. PhD Thesis, Indian School of Mines, Dhanbad.

Dick, R.A., Fletcher, L.R., and D'Andrea, D. V. (1983). Explosives and Blasting Procedures Manual. U.S. Bureau of Mines, Report IC 8925.

Du Pont, E.I. De Nemours and Co. (1977). Blasters handbook. 16th edition, Delaware.

Dowding, C.H. (1985). Blast vibration monitoring and control. New Jersey, Prentice-Hall, Englewood Cliffs, NJ, USA.

Duvall, W. I., and Atchison, T. C. (1957), Rock Breakage by Explosives", U.S. Bureau of Mines RI 5356.

Duvall, W.I. (1961). Design Criteria for Portable Seismographs. U.S. Bureau of Mines RI, 5708. 6 pages.

Edwards, A.T., and Northwood, T.D. (1960). Experimental studies of effects of blasting on structures, The Engineer. p. 211.

Forsyth, W.W. (1993). A discussion on the blast induced overbreak around underground excavations. Rock Fragmentation by Blasting FRAGBLAST-4. pp. 161-166.

Green, R.E. (1984). Vibration damage from blasts and tremors. Proceedings of the South African National Group on Rock Mechanics Conference Monitoring for Safety in Geotechnical Engineering. pp. 89-104.

Hoek, E., and Brown, E.T. (1980). Underground Excavations in Rock. London: Institution of Mining and Metallurgy. 527 pages.

Holmberg, R., and Persson, P.A. (1978). Swedish approach to contour blasting. Proceedings of the Fourth Conference on explosive and blasting techniques, Society of Explosives Engineers, February 1-3, New Orleans, USA. pp. 113-127.

Holmberg, R., and Persson, P.A. (1979). Design of Tunnel Perimeter Blasthole Patterns to Prevent Rock Damage, Proceedings, Tunnelling 1979, March 12-16, Ed. Jones M.J., Institution of Mining and Metallurgy, London, UK.

Holmberg, R., and Persson, P.A. (1980). “Design of tunnel perimeter blasthole patterns to prevent rock damage”, Trans. Ins. Min. Metall., London Vol. 89. pp. A37-40.

Holmberg, R., and Hustrulid, W. (1981) Swedish Cautious Blast Excavation at the CSM/ONWI test site in Colorado, Proceedings of the Seventh Conference on Explosives and Blasting Technique. Phoenix, AZ, USA.

Holmberg, R. (1993). Recent developments in control rock damage. Rock Fragmentation by Blasting, Rossmanith (ed.), A.A. Balkema, Rotterdam. pp. 197-198.

Huang J.-W., Bellefleur, G., and Milkereit, B. (1989). Seismic wave attenuation due to scattering and leaky mode mechanisms in heterogeneous reservoirs. Joint convention of CSPG, CSEG and CWLS, Calgary, Alberta.

Hustrulid, W., and Lu, W. (2002). Some general design concepts regarding the control of blast induced damage during rock slope excavation. Fragblast 7, Beijing, China, August, pp. 595-604.

Indian Standard Institute (1973). Criteria for safety and design of structures subjected to underground blast. ISI Bull; IS-6922.

Knopoff, L. (1964). Q: Reviews of Geophysics. 2, 625-660.

Kolsky, H. (1963). Stress waves in solids. New York, Dover.

Koopmans, R., and Hughes, R.W. (1985). Determination of near field excavation disturbance in crystalline rock. Mater. Res. Soc. Symp. Proc.; Vol/Issue: 50; Materials Research Society international symposium, Stockholm, Sweden. pp. 567-576.

Langefors, U., Kihlstrom, B., and Westerberg H. (1958). Ground vibrations in blasting. Water Power.

Langefors, U., and Kilstrom, B. (1973). The Modern Techniques of Rock Blasting. John Wiley and sons. pp. 34 - 73.

Martin L., Seymour, B., Clark, C., Stepan, M., Pakalnis, R., Roworth, M. and Caceres, C. (2010). An analysis of flexural strength and crack width for fiber-reinforced shotcrete used in weak rock mines”. SME 2010, Phoenix, Nevada.

Murthy, V.M.S.R., Dey, K., and Raitani, R. (2003). Prediction of overbreak in underground tunnel blasting - A case study. Journal of Canadian Tunneling Canadien. pp. 109-115.

Naismith, W.A. (1982). The influence of large scale surface blasting on the stability of underground coal mines. First International Congress on Rockbursts and Seismicity in Mines. Gay, N.C., and Wainwright, E.H. (eds.). The South African Institute of Mining and Metallurgy.

Nicholls, H.R., Johnson, C.F., and Duvall, W.I. (1971). Blasting Vibrations and Their Effects on Structures. U.S. Bureau of Mines Bulletin 656. 105 pages.

Pakalnis, R. (2010). Design of underground mine openings utilizing shotcrete. Kencana Mine Presentation, Spokane Research Laboratory, April 8-9.

Palmström, A. (1982). The volumetric joint count - a useful and simple measure of the degree of rock jointing. Proc. 4th congr. Int. Assn Engng Geol., Delhi Vol. 5. pp. 221-228.

Paventi, M. (1995). Rock Mass Characteristics and Damage at the Birchtree Mine. PhD. Thesis, McGill University, 445 pages.

Pavlovic, V. D., and Velickovic, Z. S. (1998), Measurement of the Seismic Wave Propagation Velocity in the Real Medium. The scientific journal FACTA UNIVERSITATIS, Vol. 1, No. 5. pp. 63-73.

Persson, P.A. (1997). The relation between strain energy, rock damage, fragmentation and throw in rock blasting. The International Journal of Blasting and Fragmentation. Vol. 1 No. 1, pp. 99-109.

Pusch, R., and Stanfors, R. (1993). Disturbance of rock around blasted tunnels. In: H.P. Rossmanith (ed.), Rock Fragmentation by Blasting, A.A. Balkema, Rotterdam. pp. 153-159.

Rupert, G.B., and Clark, G.B. (1977). Criteria for the proximity of surface blasting to underground coal mines. Proceedings, 18th US. Symposium on Rock Mechanics. June. pp. 3C3-1 to 3C3-1O.

Scoble, M.J., Cullen, M., and Makuch, A. (1987). Experimental studies of factors relating to destress blasting. Proceedings, 28th US Symposium on Rock Mechanics. Am. Inst. Mining Engineers, Univ. of Arizona. pp. 901-908.

Singh, P.K., and Vogt, W. (1998). Ground vibration: prediction for safe and efficient blasting. Erzmetall; 51 (10): pp. 677-684.

Siskind, D.E., Stagg, M.S., Kopp, J.W., and Dowding, C.H. (1980b). Structure response and damage produced by ground vibration from surface mine blasting. U.S. Bureau of Mines RI 8507. 74 pages.

Siskind, D. (1985). Blast Vibration measurements near and on structure foundations. U.S. Bureau of Mines RI 8969, 1985. 20 pages.

Siskind, D.E., Crum, S.V., Otterness, R.E., and Kopp, J.W. (1989). Comparative study of blasting vibrations from Indiana surface coal mines. U.S. Bureau of Mines RI 9226. 41 pages.

Siskind, D. (2000). Vibrations from Blasting. 1st Edition. Published by International Society of Explosives Engineers, Cleveland, OH, USA, 2000. 120 pages.

Spathis, A.T. (2009). A brief review of the measurement, modelling and management of vibrations produced by blasting, 9th International Symposium on Rock Fragmentation by Blasting, Granada, Spain.

Stagg, M.S., and Engler, A.J. (1980). Measurement of blast-induced ground vibration and seismograph calibration. U.S. Bureau of Mines RI 8506. 62 pages.

Svanholm, B. O., Persson, P. A., and Larsson, B. (1977). Smooth blasting for reliable underground openings. In Rockstore 77: Storage in excavated rock caverns, proc. 1st Int. Symp., Stockholm, (ed. M. Bergman), pp. 573-579. Oxford: Pergamon.

Thoenen, J. R., and Windes, S. L. (1937). Earth vibrations from quarry blasting. Progress Report No. 1, Bureau of Mines RI 3353.

Thoenen, J. R., and Windes, S. L. (1938). Earth vibrations caused by mine blasting, Progress Report No. 2, Bureau of Mines RI 3407.

Thoenen, J. R., and Windes, S. L. (1942). "Seismic effects of quarry blasting," Bureau of Mines Bulletin 442. 1942.

Wetherelt, A., Hunt, P., and Pepper, J. (2003). Peak particle velocity modelling. Proceedings of EFEE Second World Conference on Explosives and Blasting Technique. Prague, Czech Republic, pp. 81-88.

Yang, R.L., Rocque, P., Katsabanis, P., and Bawden, W.F. (1994). Measurement and analysis of near-field blast vibration and damage. Geotechnical and Geological Engineering, Vol. 12. pp. 169-182.

Zhou, X.J., and McNeary, R.L. (2007). Modeling of shotcrete under ASTM C-1550 with PFC3. In proceedings 1st Canada-U.S. Rock Mechanics Symposium: Meeting Society's Challenges and Demands. pp. 1533-1539.

APPENDICES

APPENDIX A – ROCK MASS QUALITY LOGS

Level: 4700
Type: cross cut
ID: No.1
Strike: 20º
Back Support: Type I
Date: Sept 13th, 2006

Back

West Wall

East Wall

Title: **4700 Cross Cut No.1**
Level: 4700 ft
ID: 1
Strike: 20º
Date: 13-Sep-06

Rock Type
Norite

Support

WEST WALL	BACK	EAST WALL
1 strap	Type I	1 strap

Q INDEX WEST WALL

Rx Strength	100MPa
Blk Size (RQD/Jn)	4.75
Jnt Strength (Jr/Ja)	0.63
Jw/SRF	1.00
TOTAL	**2.99**

Q INDEX BACK

Rx Strength	100MPa
Blk Size (RQD/Jn)	9.80
Jnt Strength (Jr/Ja)	0.42
Jw/SRF	1.00
TOTAL	**4.12**

Q INDEX EAST WALL

Rx Strength	100MPa
Blk Size (RQD/Jn)	6.65
Jnt Strength (Jr/Ja)	0.42
Jw/SRF	1.00
TOTAL	**2.79**

RMR CHARACTERIZATION WEST WALL

STRENGTH	R4	12
RQD	80%-85%	15
SPACING	3"-6"+	12
CONDITION	SLT-OPN	12-6
GRNWTR	DRY	10
	RATING	**61-55%**
STRUCTURE		
	DESIGN	**60%**

RMR CHARACTERIZATION BACK

STRENGTH	R4	12
RQD	80%-85%	15
SPACING	6"-1'+	17
CONDITION	SLT-OPN	12-6
GRNWTR	DRY	10
	RATING	**66-60%**
STRUCTURE	**FLAT JNT**	**-10%**
	DESIGN	**55%**

RMR CHARACTERIZATION EAST WALL

STRENGTH	R4	12
RQD	80%-85%	15
SPACING	6"-1'-	15
CONDITION	SLT-OPN	12-6
GRNWTR	DRY	10
	RATING	**64-58%**
STRUCTURE		
	DESIGN	**60%**

Structure

Strike (deg)	Dip (deg)	Persistence (m)	Spacing min (cm)	Spacing max (cm)	Occurrence x times	Notes
295	84	5	5	30	3	
38	85	3	5	30	6	
55	66	3	5	30	4	
10	24	1.5	30	30	7	

Other Notes:
Loose material bagging screen
Only back screened
Big slabs came out on East and West wall/structurally controlled
mm to cm openness
soft to strong JS condition
Type I support
Jnt sets 3 plus random

Figure A. 1 Back, right and left wall pictures and rock mass classification logs – Stillwater Mine – Cross cut 1

Level: 4700
Type: cross cut
ID: No.2
Strike: 20°
Back Support: Type I
Date: Sept 13th, 2006

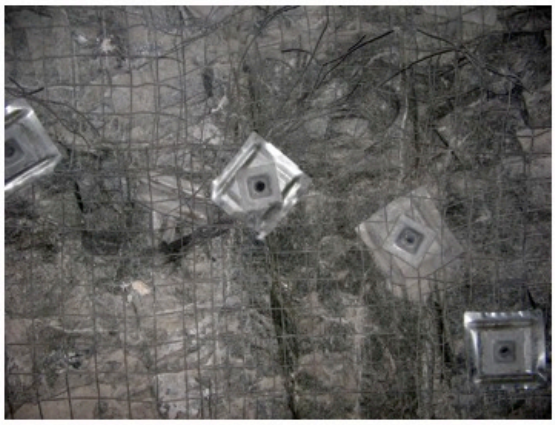

Back

West Wall

East Wall

Title: **4700 Cross Cut No.2**
Level: 4700 ft
ID: 3
Strike: 20°
Date: 13-Sep-06

Support

WEST WALL	BACK	EAST WALL
Type I	Type I	Type I

Q INDEX WEST WALL

Rx Strength	100MPa
Blk Size (RQD/Jn)	9.80
Jnt Strength (Jr/Ja)	0.63
Jw/SRF	1.00
TOTAL	**6.17**

Q INDEX BACK

Rx Strength	100MPa
Blk Size (RQD/Jn)	9.80
Jnt Strength (Jr/Ja)	0.42
Jw/SRF	1.00
TOTAL	**4.12**

Q INDEX EAST WALL

Rx Strength	100MPa
Blk Size (RQD/Jn)	9.80
Jnt Strength (Jr/Ja)	0.42
Jw/SRF	1.00
TOTAL	**4.12**

RMR CHARACTERIZATION WEST WALL

STRENGTH	R4	12
RQD	80%-85%	15
SPACING	6"-1'+	17
CONDITION	SLT-OPN	12-6
GRNWTR	DRY	10
	RATING	**66-60%**
STRUCTURE		
	DESIGN	**65%**

RMR CHARACTERIZATION BACK

STRENGTH	R4	12
RQD	80%-85%	15
SPACING	6"-1'+	17
CONDITION	SLT-OPN	12-6
GRNWTR	DRY	10
	RATING	**66-60%**
STRUCTURE	**FLAT JNT**	**-10%**
	DESIGN	**55%**

RMR CHARACTERIZATION EAST WALL

STRENGTH	R4	12
RQD	80%-85%	15
SPACING	6"-1'+	17
CONDITION	SLT-OPN	12-6
GRNWTR	DRY	10
	RATING	**66-60%**
STRUCTURE		
	DESIGN	**65%**

Structure

Strike (deg)	Dip (deg)	Persistence (m)	Spacing min (cm)	Spacing max (cm)	Occurrence x times	Notes
27	85	4	30	30	4	
270	67	4	30	30	4	
105	86	4	30	100	4	
105	26	4	30	30	5	

Other Notes:
Loose material bagging screen
Only back screened
Big slabs came out on East and West wall/structurally controlled
mm to cm openness
soft to strong JS condition
Type I support
Jnt sets 3 plus random

Figure A. 2 Back, right and left wall pictures and rock mass classification logs – Stillwater Mine – Cross cut 2

Level: 4700
Type: cross cut
ID: No.3
Strike: 20º
Back Support: Type I
Date: Sept 13th, 2006

Back

West Wall

East Wall

Title: **4700 Cross Cut No.3**
Level: 4700 ft
ID: 3
Strike: 20º
Date: 13-Sep-06

Rock Type
Norite

Support

WEST WALL	BACK	EAST WALL
Type I	Type I	Type I

Q INDEX WEST WALL

Rx Strength	100MPa
Blk Size (RQD/Jn)	9.80
Jnt Strength (Jr/Ja)	0.63
Jw/SRF	1.00
TOTAL	**6.17**

Q INDEX BACK

Rx Strength	100MPa
Blk Size (RQD/Jn)	9.80
Jnt Strength (Jr/Ja)	0.42
Jw/SRF	1.00
TOTAL	**4.12**

Q INDEX EAST WALL

Rx Strength	100MPa
Blk Size (RQD/Jn)	9.80
Jnt Strength (Jr/Ja)	0.42
Jw/SRF	1.00
TOTAL	**4.12**

RMR CHARACTERIZATION WEST WALL

STRENGTH	R4	12
RQD	80%-85%	15
SPACING	6"-1'+	17
CONDITION	SLT-OPN	12-6
GRNWTR	DRY	10
	RATING	**66-60%**
STRUCTURE		
	DESIGN	**65%**

RMR CHARACTERIZATION BACK

STRENGTH	R4	12
RQD	80%-85%	15
SPACING	6"-1'+	17
CONDITION	SLT-OPN	12-6
GRNWTR	DRY	10
	RATING	**66-60%**
STRUCTURE	**FLAT JNT**	**-10%**
	DESIGN	**55%**

RMR CHARACTERIZATION EAST WALL

STRENGTH	R4	12
RQD	80%-85%	15
SPACING	6"-1'+	17
CONDITION	SLT-OPN	12-6
GRNWTR	DRY	10
	RATING	**66-60%**
STRUCTURE		
	DESIGN	**65%**

Structure

Strike (deg)	Dip (deg)	Persistence (m)	Spacing min (cm)	Spacing max (cm)	Occurrence x times	Notes
27	85	4	30	30	4	
270	67	4	30	30	4	
105	86	4	30	100	4	
105	26	4	30	30	5	

Other Notes:
Loose material bagging screen
Only back screened
Big slabs came out on East and West wall/structurally controlled
mm to cm openness
soft to strong JS condition
Type I support
Jnt sets 3 plus random

Figure A. 3 Back, right and left wall pictures and rock mass classification logs – Stillwater Mine – Cross cut 3

Level: 4700
Type: Footwall Lateral
ID: No.1
Strike: 285º
Back Support: Type I
Date: Sept 13th, 2006

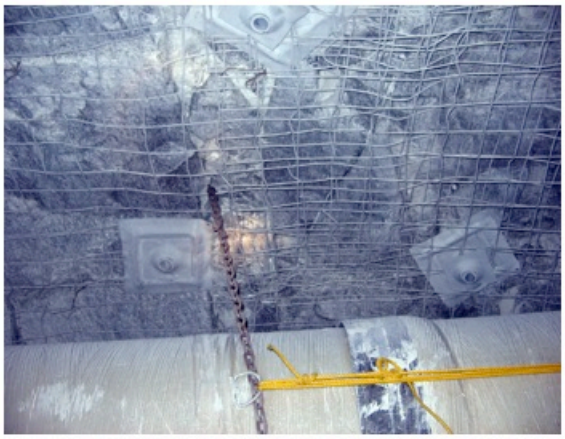

Back

North Wall

South Wall

Title: **4700 Footwall Lateral No.1**
Level: 4700 ft
ID: 1
Strike: 285°
Date: 13-Sep-06

Rock Type
Norite

Support

WEST WALL	BACK	EAST WALL
Type I	Type I	Type I

Q INDEX NORTH WALL

Rx Strength	100MPa
Blk Size (RQD/Jn)	13.55
Jnt Strength (Jr/Ja)	1.26
Jw/SRF	1.00
TOTAL	**17.07**

Q INDEX BACK

Rx Strength	100MPa
Blk Size (RQD/Jn)	13.55
Jnt Strength (Jr/Ja)	1.26
Jw/SRF	1.00
TOTAL	**17.07**

Q INDEX SOUTH WALL

Rx Strength	100MPa
Blk Size (RQD/Jn)	13.55
Jnt Strength (Jr/Ja)	1.26
Jw/SRF	1.00
TOTAL	**17.07**

RMR CHARACTERIZATION NORTH WALL

STRENGTH	R4	12
RQD	90%	20
SPACING	1'+	20
CONDITION	Tight/Slt Tight	18
GRNWTR	DRY	10
	RATING	**80%**
STRUCTURE		
	DESIGN	**80%**

RMR CHARACTERIZATION BACK

STRENGTH	R4	12
RQD	90%	20
SPACING	1'+	20
CONDITION	Tight	18
GRNWTR	DRY	10
	RATING	**80%**
STRUCTURE	**FLAT JNT**	**-10%**
	DESIGN	**70%**

RMR CHARACTERIZATION SOUTH WALL

STRENGTH	R4	12
RQD	90%	20
SPACING	1'+	20
CONDITION	Tight	18
GRNWTR	DRY	10
	RATING	**80%**
STRUCTURE		
	DESIGN	**80%**

Structure

Strike (deg)	Dip (deg)	Persistence (m)	Spacing min (cm)	Spacing max (cm)	Occurrence x times	Notes
35	86	3	30	30	5	
135	34	3	100	100	4	
278	88	4	100	100	5	
150	77	2.5	200	200	4	

Other Notes:
Joints tight/slt tight
>1mm open
soft to strong JS condition
Type I support
Good Blasting

Figure A. 4 Back, right and left wall pictures and rock mass classification logs – Stillwater Mine – Footwall lateral 1

Level: 4700
Type: Footwall Lateral
ID: No.2
Strike: 285°
Back Support: Type I
Date: Sept 13th, 2006

Back

North Wall

South Wall

Title: **4700 Footwall Lateral No.2**
Level: 4700 ft
ID: 2
Strike: 285°
Date: 13-Sep-06

Rock Type
Norite

Support

WEST WALL	BACK	EAST WALL
Type I	Type I	Type I

Q INDEX NORTH WALL

Rx Strength	100MPa
Blk Size (RQD/Jn)	13.55
Jnt Strength (Jr/Ja)	1.26
Jw/SRF	1.00
TOTAL	**17.07**

Q INDEX BACK

Rx Strength	100MPa
Blk Size (RQD/Jn)	13.55
Jnt Strength (Jr/Ja)	1.26
Jw/SRF	1.00
TOTAL	**17.07**

Q INDEX SOUTH WALL

Rx Strength	100MPa
Blk Size (RQD/Jn)	13.55
Jnt Strength (Jr/Ja)	1.26
Jw/SRF	1.00
TOTAL	**17.07**

RMR CHARACTERIZATION NORTH WALL

STRENGTH	R4	12
RQD	90%	18
SPACING	in-1'+	18
CONDITION	Tight	15
GRNWTR	DRY	10
	RATING	**73%**
STRUCTURE		
	DESIGN	**75%**

RMR CHARACTERIZATION BACK

STRENGTH	R4	12
RQD	90%	18
SPACING	in-1'+	18
CONDITION	Tight	15
GRNWTR	DRY	10
	RATING	**73%**
STRUCTURE	**FLAT JNT**	**-10%**
	DESIGN	**65%**

RMR CHARACTERIZATION SOUTH WALL

STRENGTH	R4	12
RQD	90%	18
SPACING	in-1'+	18
CONDITION	Tight	15
GRNWTR	DRY	10
	RATING	**73%**
STRUCTURE		
	DESIGN	**75%**

Structure

Strike (deg)	Dip (deg)	Persistence (m)	Spacing min (cm)	Spacing max (cm)	Occurrence x times	Notes
87	64	4	10	30	4	Controlling
95	90	3	60	60	4	
12	89	4	60	60	5	
80	25	3	100	100	4	

Other Notes:
Joints tight
>1mm open
soft to strong JS condition
Type I support
Overall Blasting: semi-good
Down portion bad
Good at back

Figure A. 5 Back, right and left wall pictures and rock mass classification logs – Stillwater Mine – Footwall lateral 2

Level: 4700
Type: Footwall Lateral
ID: No.3
Strike: 285º
Back Support: Type I
Date: Sept 13th, 2006

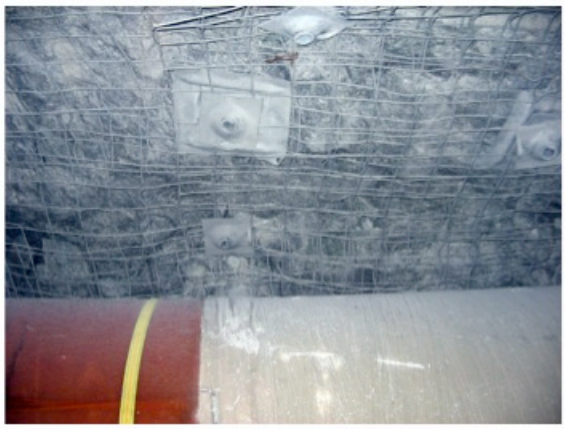

Back

North Wall

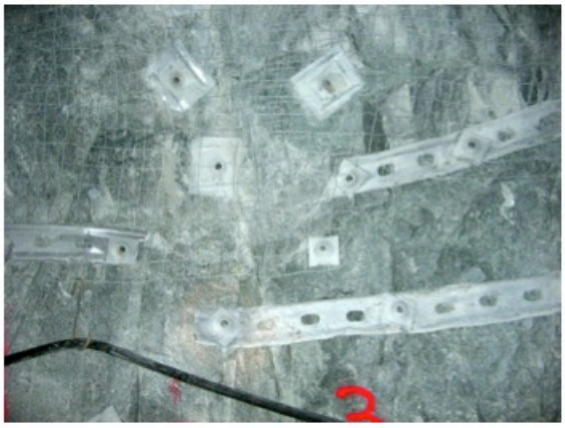

South Wall

Title: **4700 Footwall Lateral No.3**
Level: 4700 ft
ID: 3
Strike: 285º
Date: 13-Sep-06

Rock Type
Norite

Support

WEST WALL	BACK	EAST WALL
Type I	Type I	Type I

Q INDEX NORTH WALL

Rx Strength	100MPa
Blk Size (RQD/Jn)	13.55
Jnt Strength (Jr/Ja)	1.26
Jw/SRF	1.00
TOTAL	**17.07**

Q INDEX BACK

Rx Strength	100MPa
Blk Size (RQD/Jn)	13.55
Jnt Strength (Jr/Ja)	1.26
Jw/SRF	1.00
TOTAL	**17.07**

Q INDEX SOUTH WALL

Rx Strength	100MPa
Blk Size (RQD/Jn)	13.55
Jnt Strength (Jr/Ja)	1.26
Jw/SRF	1.00
TOTAL	**17.07**

RMR CHARACTERIZATION NORTH WALL

STRENGTH	R4	12
RQD	90%	18
SPACING	in-1'+	18
CONDITION	Tight/Slt Open	12
GRNWTR	DRY	10
	RATING	**70%**
STRUCTURE		
	DESIGN	**70%**

RMR CHARACTERIZATION BACK

STRENGTH	R4	12
RQD	90%	18
SPACING	in-1'+	18
CONDITION	Tight/Slt Open	12
GRNWTR	DRY	10
	RATING	**70%**
STRUCTURE		
	DESIGN	**70%**

RMR CHARACTERIZATION SOUTH WALL

STRENGTH	R4	12
RQD	90%	18
SPACING	in-1'+	18
CONDITION	Tight/Slt Open	12
GRNWTR	DRY	10
	RATING	**70%**
STRUCTURE		
	DESIGN	**70%**

Structure

Strike (deg)	Dip (deg)	Persistence (m)	Spacing min (cm)	Spacing max (cm)	Occurrence x times	Notes
107	83	4	60	60	4	
14	88	4	100	100	3	
118	75	2	10	30	5	Controlling

Other Notes:
Joints tight/slt open
soft to strong JS condition
Type I support
Overall Blasting: good
Good N, S and Back
Big chunck came down top portion
Also some underbreak at top portion

Figure A. 6 Back, right and left wall pictures and rock mass classification logs – Stillwater Mine – Footwall lateral 3

Level: 4700
Type: Footwall Lateral
ID: No.4
Strike: 285º
Back Support: Type I
Date: Sept 13th, 2006

Back

North Wall

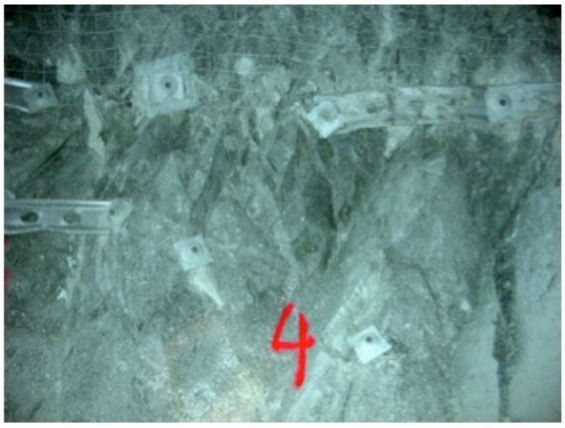

South Wall

Title: **4700 Footwall Lateral No.4**
Level: 4700 ft
ID: 4
Strike: 285°
Date: 13-Sep-06

Rock Type
Norite

Support

WEST WALL	BACK	EAST WALL
Type I	Type I	Type I

Q INDEX NORTH WALL

Rx Strength	100MPa
Blk Size (RQD/Jn)	6.65
Jnt Strength (Jr/Ja)	1.26
Jw/SRF	1.00
TOTAL	**8.38**

Q INDEX BACK

Rx Strength	100MPa
Blk Size (RQD/Jn)	6.65
Jnt Strength (Jr/Ja)	1.26
Jw/SRF	1.00
TOTAL	**8.38**

Q INDEX SOUTH WALL

Rx Strength	100MPa
Blk Size (RQD/Jn)	6.65
Jnt Strength (Jr/Ja)	1.26
Jw/SRF	1.00
TOTAL	**8.38**

RMR CHARACTERIZATION NORTH WALL

STRENGTH	R4	12
RQD	80%-85%	15
SPACING	in-1'	13
CONDITION	Slt Open	9
GRNWTR	DRY	10
	RATING	**59%**
STRUCTURE		
	DESIGN	**60%**

RMR CHARACTERIZATION BACK

STRENGTH	R4	12
RQD	80%-85%	15
SPACING	in-1'	13
CONDITION	Slt Open	9
GRNWTR	DRY	10
	RATING	**59%**
STRUCTURE		
	DESIGN	**60%**

RMR CHARACTERIZATION SOUTH WALL

STRENGTH	R4	12
RQD	80%-85%	15
SPACING	in-1'	13
CONDITION	Slt Open	9
GRNWTR	DRY	10
	RATING	**59%**
STRUCTURE		
	DESIGN	**60%**

Structure

Strike (deg)	Dip (deg)	Persistence (m)	Spacing min (cm)	Spacing max (cm)	Occurrence x times	Notes
150	73	2	10	30	4	Controlling
230	82	4	30	60	4	Controlling
77	87	4	100	100	4	
355	86	3	30	30	2	Random

Other Notes:
Joints slt open
soft to strong JS condition
Type I support
Overall Blasting: semi-good
Semi good top portion N and S
Semi bad bottom portion N and S

Figure A. 7 Back, right and left wall pictures and rock mass classification logs – Stillwater Mine – Footwall lateral 4

Level: 4700
Type: Footwall Lateral
ID: No.5
Strike: 285º
Back Support: Type I
Date: Sept 13th, 2006

Back

North Wall

South Wall

Title: **4700 Footwall Lateral No.5**
Level: 4700 ft
ID: 5
Strike: 285º
Date: 13-Sep-06

Rock Type
Norite

Support

WEST WALL	BACK	EAST WALL
Type I	Type I	Type I

Q INDEX NORTH WALL

Rx Strength	100MPa
Blk Size (RQD/Jn)	13.55
Jnt Strength (Jr/Ja)	1.26
Jw/SRF	1.00
TOTAL	**17.07**

Q INDEX BACK

Rx Strength	100MPa
Blk Size (RQD/Jn)	13.55
Jnt Strength (Jr/Ja)	1.26
Jw/SRF	1.00
TOTAL	**17.07**

Q INDEX SOUTH WALL

Rx Strength	100MPa
Blk Size (RQD/Jn)	13.55
Jnt Strength (Jr/Ja)	1.26
Jw/SRF	1.00
TOTAL	**17.07**

RMR CHARACTERIZATION NORTH WALL

STRENGTH	R4	12
RQD	80%-85%	15
SPACING	1'-3'	20
CONDITION	Tight/Slt Open	12
GRNWTR	DRY	10
	RATING	**69%**
STRUCTURE		
	DESIGN	**70%**

RMR CHARACTERIZATION BACK

STRENGTH	R4	12
RQD	80%-85%	15
SPACING	1'-3'	20
CONDITION	Tight/Slt Open	12
GRNWTR	DRY	10
	RATING	**69%**
STRUCTURE		
	DESIGN	**70%**

RMR CHARACTERIZATION SOUTH WALL

STRENGTH	R4	12
RQD	80%-85%	15
SPACING	1'-3'	20
CONDITION	Tight/Slt Open	12
GRNWTR	DRY	10
	RATING	**69%**
STRUCTURE		
	DESIGN	**70%**

Structure

Strike (deg)	Dip (deg)	Persistence (m)	Spacing min (cm)	Spacing max (cm)	Occurrence x times	Notes
188	75	3	100	100	4	
0	86	3	30	100	4	
75	83	3	30	100	4	Controlling
298	83	3	30	100	3	

Other Notes:
Joints tight/slt open
soft to strong JS condition
Type I support
Overall Blasting: semi-good
Fair top portion N
Good back and S

Figure A. 8 Back, right and left wall pictures and rock mass classification logs – Stillwater Mine – Footwall lateral 5

Title: 4700 Footwall Lateral No.6
Level: 4700 ft
ID: 6
Strike: 288°
Date: 14-Sep-06

Rock Type
Norite

Support

WEST WALL	BACK	EAST WALL
Type I	Type I	Type I

Q INDEX NORTH WALL

Rx Strength	100MPa
Blk Size (RQD/Jn)	9.80
Jnt Strength (Jr/Ja)	0.63
Jw/SRF	1.00
TOTAL	**6.17**

Q INDEX BACK

Rx Strength	100MPa
Blk Size (RQD/Jn)	9.80
Jnt Strength (Jr/Ja)	0.63
Jw/SRF	1.00
TOTAL	**6.17**

Q INDEX SOUTH WALL

Rx Strength	100MPa
Blk Size (RQD/Jn)	9.80
Jnt Strength (Jr/Ja)	0.63
Jw/SRF	1.00
TOTAL	**6.17**

RMR CHARACTERIZATION NORTH WALL

STRENGTH	R4	12
RQD	80%-85%	15
SPACING	in-1'	13
CONDITION	Tight/Slt Open	12
GRNWTR	DRY	10
	RATING	**62%**
STRUCTURE		
	DESIGN	**60%**

RMR CHARACTERIZATION BACK

STRENGTH	R4	12
RQD	80%-85%	15
SPACING	in-1'	13
CONDITION	Tight/Slt Open	12
GRNWTR	DRY	10
	RATING	**62%**
STRUCTURE	**FLAT JNT**	**-10%**
	DESIGN	**50%**

RMR CHARACTERIZATION SOUTH WALL

STRENGTH	R4	12
RQD	80%-85%	15
SPACING	in-1'	13
CONDITION	Tight/Slt Open	12
GRNWTR	DRY	10
	RATING	**62%**
STRUCTURE		
	DESIGN	**60%**

Structure

Strike (deg)	Dip (deg)	Persistence (m)	Spacing min (cm)	Spacing max (cm)	Occurrence x times	Notes
200	69	4	5	30	4	
120	90	3	60	70	5	
140	50	3	30	60	4	
96	13	4	100	100	4	
297	33	3	30	60	3	

Other Notes:
Joints tight/slt open
soft to strong JS condition
Type I support
Overall Blasting: Good
Semi good N
Good Back and S

Figure A. 9 Back, right and left wall rock mass classification logs – Stillwater Mine – Footwall lateral 6

Title: 4700 Footwall Lateral No.7
Level: 4700 ft
ID: 7
Strike: 285°
Date: 14-Sep-06

Rock Type
Norite

Support

WEST WALL	BACK	EAST WALL
Type I	Type I	Type I

Q INDEX NORTH WALL

Rx Strength	100MPa
Blk Size (RQD/Jn)	6.65
Jnt Strength (Jr/Ja)	0.63
Jw/SRF	1.00
TOTAL	**4.19**

Q INDEX BACK

Rx Strength	100MPa
Blk Size (RQD/Jn)	6.65
Jnt Strength (Jr/Ja)	0.63
Jw/SRF	1.00
TOTAL	**4.19**

Q INDEX SOUTH WALL

Rx Strength	100MPa
Blk Size (RQD/Jn)	6.65
Jnt Strength (Jr/Ja)	0.63
Jw/SRF	1.00
TOTAL	**4.19**

RMR CHARACTERIZATION NORTH WALL

STRENGTH	R4	12
RQD	75%-80%	14
SPACING	in-in-1'	11
CONDITION	Slt Open	9
GRNWTR	DRY	10
	RATING	**56%**
STRUCTURE		
	DESIGN	**55%**

RMR CHARACTERIZATION BACK

STRENGTH	R4	12
RQD	75%-80%	14
SPACING	in-in-1'	11
CONDITION	Slt Open	9
GRNWTR	DRY	10
	RATING	**56%**
STRUCTURE		
	DESIGN	**55%**

RMR CHARACTERIZATION SOUTH WALL

STRENGTH	R4	12
RQD	75%-80%	14
SPACING	in-in-1'	11
CONDITION	Slt Open	9
GRNWTR	DRY	10
	RATING	**56%**
STRUCTURE		
	DESIGN	**55%**

Structure

Strike (deg)	Dip (deg)	Persistence (m)	Spacing min (cm)	Spacing max (cm)	Occurrence x times	Notes
124	50	2.5	10	30	5	Controlling
272	49	3	30	30	4	
146	56	3	10	30	6	
105	81	3.5	30	30	3	Controlling

Other Notes:
Joints slt open
soft to strong JS condition
Type I support
Overall Blasting: semi-good
Semi bad top portion N and N Back
Good S

Figure A. 10 Back, right and left wall rock mass classification logs – Stillwater Mine – Footwall lateral 7

Level: 4700
Type: Footwall Lateral
ID: No.8
Strike: 285º
Back Support: Type I
Date: Sept 14th, 2006

Back

North Wall

South Wall

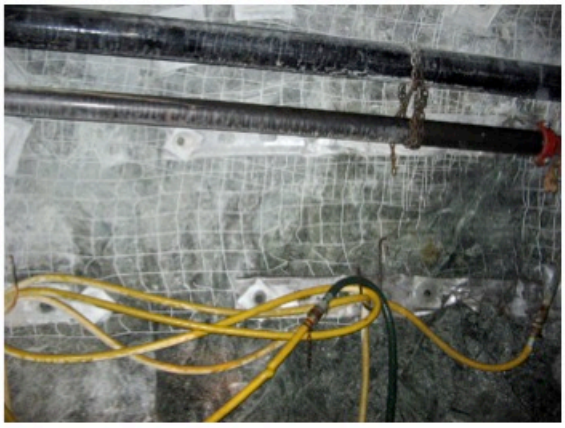

Title: **4700 Footwall Lateral No.8**
Level: 4700 ft
ID: 8
Strike: 285°
Date: 14-Sep-06

Rock Type
Norite

Support

WEST WALL	BACK	EAST WALL
Type I	Type I	Type I

Q INDEX NORTH WALL

Rx Strength	100MPa
Blk Size (RQD/Jn)	6.65
Jnt Strength (Jr/Ja)	0.63
Jw/SRF	1.00
TOTAL	**4.19**

Q INDEX BACK

Rx Strength	100MPa
Blk Size (RQD/Jn)	9.80
Jnt Strength (Jr/Ja)	0.63
Jw/SRF	1.00
TOTAL	**6.17**

Q INDEX SOUTH WALL

Rx Strength	100MPa
Blk Size (RQD/Jn)	6.65
Jnt Strength (Jr/Ja)	0.63
Jw/SRF	1.00
TOTAL	**4.19**

RMR CHARACTERIZATION NORTH WALL

STRENGTH	R4	12
RQD	80%-85%	15
SPACING	in-1'	13
CONDITION	Tight/Slt Open	12
GRNWTR	DRY	10
	RATING	**62%**
STRUCTURE		
	DESIGN	**60%**

RMR CHARACTERIZATION BACK

STRENGTH	R4	12
RQD	85%	17
SPACING	1'	15
CONDITION	Tight/Slt Open	12
GRNWTR	DRY	10
	RATING	**66%**
STRUCTURE		
	DESIGN	**65%**

RMR CHARACTERIZATION SOUTH WALL

STRENGTH	R4	12
RQD	80%-85%	15
SPACING	in-1'	13
CONDITION	Tight/Slt Open	12
GRNWTR	DRY	10
	RATING	**62%**
STRUCTURE		
	DESIGN	**60%**

Structure

Strike (deg)	Dip (deg)	Persistence (m)	Spacing min (cm)	Spacing max (cm)	Occurrence x times	Notes
147	69	3	30	30	4	Controlling
137	86	3	30	30	4	Controlling
218	87	3	30	30	4	
347	88	3.5	30	30	3	
140	31	3	30	30	3	
298	38	3	30	30	3	

Other Notes:
Joints tight/slt open
soft to strong JS condition
Type I support
Overall Blasting: semi-bad
Semi bad top and bottom portion N
Semi bad top portion S
Good back

Figure A. 11 Back, right and left wall pictures and rock mass classification logs – Stillwater Mine – Footwall lateral 8

Level: 4700
Type: Footwall Lateral
ID: No.9
Strike: 285º
Back Support: Type I
Date: Sept 14th, 2006

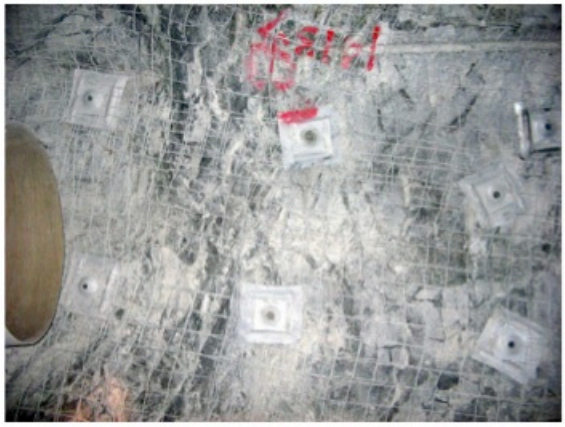

Back

North Wall

South Wall

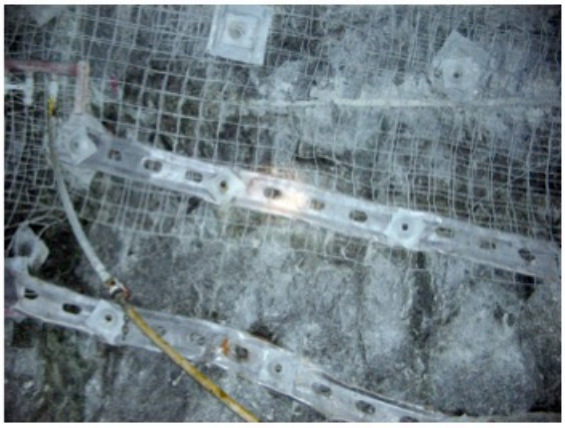

Title: **4700 Footwall Lateral No.9**
Level: 4700 ft
ID: 9
Strike: 285°
Date: 14-Sep-06

Rock Type
Norite

Support

WEST WALL	BACK	EAST WALL
Type I	Type I	Type I

Q INDEX NORTH WALL

Rx Strength	100MPa
Blk Size (RQD/Jn)	7.60
Jnt Strength (Jr/Ja)	0.63
Jw/SRF	1.00
TOTAL	**4.79**

Q INDEX BACK

Rx Strength	100MPa
Blk Size (RQD/Jn)	7.60
Jnt Strength (Jr/Ja)	0.63
Jw/SRF	1.00
TOTAL	**4.79**

Q INDEX SOUTH WALL

Rx Strength	100MPa
Blk Size (RQD/Jn)	7.60
Jnt Strength (Jr/Ja)	0.63
Jw/SRF	1.00
TOTAL	**4.79**

RMR CHARACTERIZATION NORTH WALL

STRENGTH	R4	12
RQD	80%-85%	15
SPACING	in-1'	13
CONDITION	Tight/Slt Open	12
GRNWTR	DRY	10
	RATING	**62%**
STRUCTURE		
	DESIGN	**60%**

RMR CHARACTERIZATION BACK

STRENGTH	R4	12
RQD	80%-85%	15
SPACING	in-1'	13
CONDITION	Tight/Slt Open	12
GRNWTR	DRY	10
	RATING	**62%**
STRUCTURE		
	DESIGN	**60%**

RMR CHARACTERIZATION SOUTH WALL

STRENGTH	R4	12
RQD	80%-85%	15
SPACING	in-1'	13
CONDITION	Tight/Slt Open	12
GRNWTR	DRY	10
	RATING	**62%**
STRUCTURE		
	DESIGN	**60%**

Structure

Strike (deg)	Dip (deg)	Persistence (m)	Spacing min (cm)	Spacing max (cm)	Occurrence x times	Notes
355	54	3.5	30	30	3	Controlling
120	83	3	30	30	4	Controlling
143	63	3	10	30	4	Controlling
15	81	3	60	60	3	

Other Notes:
Joints tight/slt open
soft to strong JS condition
Type I support
Overall Blasting: semi-bad
Semi bad top and bottom portion N
Semi bad top portion S
Semi bad back

Figure A. 12 Back, right and left wall pictures and rock mass classification logs – Stillwater Mine – Footwall lateral 9

Level: 4700
Type: Footwall Lateral
ID: No.10
Strike: 285º
Back Support: Type I
Date: Sept 14th, 2006

Back

North Wall

South Wall

Title: **4700 Footwall Lateral No.10**
Level: 4700 ft
ID: 10
Strike: 285º
Date: 14-Sep-06

Rock Type
Norite

Support

WEST WALL	BACK	EAST WALL
Type I	Type I	Type I

Q INDEX NORTH WALL

Rx Strength	100MPa
Blk Size (RQD/Jn)	4.75
Jnt Strength (Jr/Ja)	0.63
Jw/SRF	1.00
TOTAL	**2.99**

Q INDEX BACK

Rx Strength	100MPa
Blk Size (RQD/Jn)	4.75
Jnt Strength (Jr/Ja)	0.63
Jw/SRF	1.00
TOTAL	**2.99**

Q INDEX SOUTH WALL

Rx Strength	100MPa
Blk Size (RQD/Jn)	4.75
Jnt Strength (Jr/Ja)	0.63
Jw/SRF	1.00
TOTAL	**2.99**

RMR CHARACTERIZATION NORTH WALL

STRENGTH	R4	12
RQD	75%-80%	13
SPACING	in-in-1'	11
CONDITION	Tight/Slt Open	12
GRNWTR	DRY	10
	RATING	**58%**
STRUCTURE		
	DESIGN	**60%**

RMR CHARACTERIZATION BACK

STRENGTH	R4	12
RQD	75%-80%	13
SPACING	in-in-1'	11
CONDITION	Tight/Slt Open	12
GRNWTR	DRY	10
	RATING	**58%**
STRUCTURE		
	DESIGN	**60%**

RMR CHARACTERIZATION SOUTH WALL

STRENGTH	R4	12
RQD	75%-80%	13
SPACING	in-in-1'	11
CONDITION	Tight/Slt Open	12
GRNWTR	DRY	10
	RATING	**58%**
STRUCTURE		
	DESIGN	**60%**

Structure

Strike (deg)	Dip (deg)	Persistence (m)	Spacing min (cm)	Spacing max (cm)	Occurrence x times	Notes
124	90	3	30	30	4	Controlling
248	40	3	30	30	4	Controlling
4	87	2	10	30	6	
125	57	3.5	30	30	3	Controlling
342	89	3	30	30	3	
210	90	2	10	30	6	

Other Notes:
Joints tight/slt open
soft to strong JS condition
Type I support
Overall Blasting: semi-good
Semi good top and bottom portion N and S
Semi good back
Underbreak piece N wall

Figure A. 13 Back, right and left wall pictures and rock mass classification logs – Stillwater Mine – Footwall lateral 10

Level: 4700
Type: Footwall Lateral
ID: No.11
Strike: 285º
Back Support: Type I
Date: Sept 14th, 2006

Back

North Wall

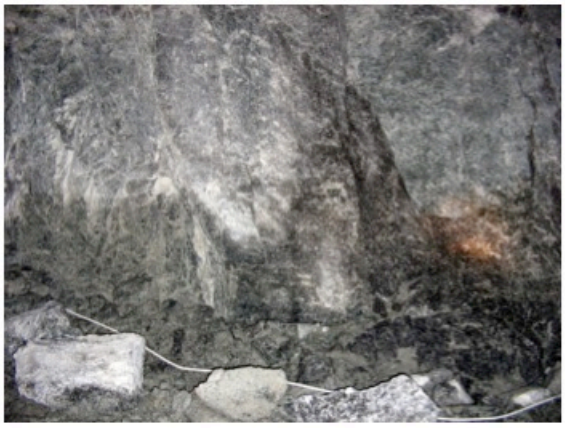

South Wall

Title: **4700 Footwall Lateral No.11**
Level: 4700 ft
ID: 11
Strike: 285°
Date: 14-Sep-06

Rock Type
Norite

Support

WEST WALL	BACK	EAST WALL
Type I	Type I	Type I

Q INDEX NORTH WALL

Rx Strength	100MPa
Blk Size (RQD/Jn)	6.65
Jnt Strength (Jr/Ja)	0.63
Jw/SRF	1.00
TOTAL	**4.19**

Q INDEX BACK

Rx Strength	100MPa
Blk Size (RQD/Jn)	6.65
Jnt Strength (Jr/Ja)	0.63
Jw/SRF	1.00
TOTAL	**4.19**

Q INDEX SOUTH WALL

Rx Strength	100MPa
Blk Size (RQD/Jn)	6.65
Jnt Strength (Jr/Ja)	0.63
Jw/SRF	1.00
TOTAL	**4.19**

RMR CHARACTERIZATION NORTH WALL

STRENGTH	R4	12
RQD	75%-80%	13
SPACING	in-in-1'	11
CONDITION	Slt Open	9
GRNWTR	DRY	10
	RATING	**55%**
STRUCTURE		
	DESIGN	**55%**

RMR CHARACTERIZATION BACK

STRENGTH	R4	12
RQD	75%-80%	13
SPACING	in-in-1'	11
CONDITION	Slt Open	9
GRNWTR	DRY	10
	RATING	**55%**
STRUCTURE		
	DESIGN	**55%**

RMR CHARACTERIZATION SOUTH WALL

STRENGTH	R4	12
RQD	75%-80%	13
SPACING	in-in-1'	11
CONDITION	Slt Open	9
GRNWTR	DRY	10
	RATING	**55%**
STRUCTURE		
	DESIGN	**55%**

Structure

Strike (deg)	Dip (deg)	Persistence (m)	Spacing min (cm)	Spacing max (cm)	Occurrence x times	Notes
7	73	3	10	30	5	Controlling
343	81	3	30	60	3	Controlling
128	83	2.5	10	30	5	
157	79	4	10	30	6	Controlling
235	74	3	10	30	5	Controlling

Other Notes:
Joints slt open
soft to strong JS condition
Type I support
Overall Blasting: semi-bad
Semi bad top and bottom portion N and S
Semi good back

Figure A. 14 Back, right and left wall pictures and rock mass classification logs – Stillwater Mine – Footwall lateral 11

Level: 4700
Type: Footwall Lateral
ID: No.12
Strike: 285º
Back Support: Type I
Date: Sept 14th, 2006

Back

North Wall

South Wall

Title: **4700 Footwall Lateral No.12**
Level: 4700 ft
ID: 12
Strike: 285°
Date: 14-Sep-06

Rock Type
Norite

Support

WEST WALL	BACK	EAST WALL
Type I	Type I	Type I

Q INDEX NORTH WALL

Rx Strength	100MPa
Blk Size (RQD/Jn)	4.75
Jnt Strength (Jr/Ja)	0.42
Jw/SRF	1.00
TOTAL	**2.00**

Q INDEX BACK

Rx Strength	100MPa
Blk Size (RQD/Jn)	6.65
Jnt Strength (Jr/Ja)	0.42
Jw/SRF	1.00
TOTAL	**2.79**

Q INDEX SOUTH WALL

Rx Strength	100MPa
Blk Size (RQD/Jn)	5.70
Jnt Strength (Jr/Ja)	0.42
Jw/SRF	1.00
TOTAL	**2.39**

RMR CHARACTERIZATION NORTH WALL

STRENGTH	R4	12
RQD	70%-75%	12
SPACING	in-6in	8
CONDITION	Tight	15
GRNWTR	DRY	10
	RATING	**57%**
STRUCTURE		
	DESIGN	**55%**

RMR CHARACTERIZATION BACK

STRENGTH	R4	12
RQD	75%	14
SPACING	in-6in	8
CONDITION	Tight	15
GRNWTR	DRY	10
	RATING	**59%**
STRUCTURE		
	DESIGN	**60%**

RMR CHARACTERIZATION SOUTH WALL

STRENGTH	R4	12
RQD	70%-75%	12
SPACING	in-6in	8
CONDITION	Tight	15
GRNWTR	DRY	10
	RATING	**57%**
STRUCTURE		
	DESIGN	**55%**

Structure

Strike (deg)	Dip (deg)	Persistence (m)	Spacing min (cm)	Spacing max (cm)	Occurrence x times	Notes
332	78	2.5	10	30	5	Controlling
324	89	3	10	30	6	
112	70	4	60	60	4	
130	82	4	10	30	5	Controlling
255	83	3	30	30	4	
35	78	3.5	30	30	3	

Other Notes:
Joints tight
soft to strong JS condition
Type I support
Overall Blasting: semi-good
Semi good top and bottom portion N and S
Good back

Figure A. 15 Back, right and left wall pictures and rock mass classification logs – Stillwater Mine – Footwall lateral 12

Level: 4700
Type: Footwall Lateral
ID: No.13
Strike: 285º
Back Support: Type I
Date: Sept 14th, 2006

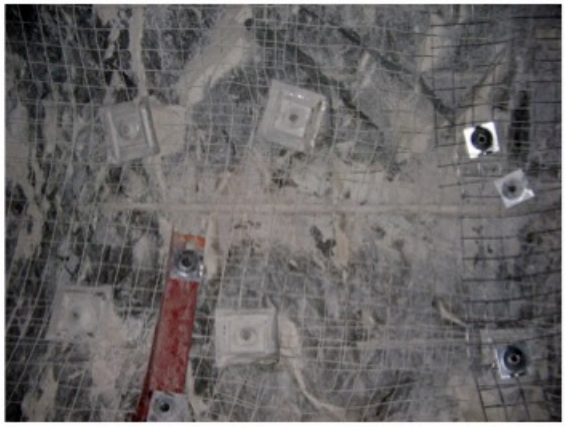

Back

North Wall

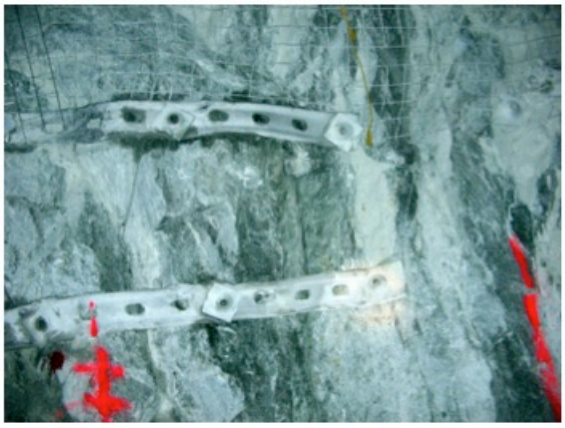

South Wall

Title: **4700 Footwall Lateral No.13**
Level: 4700 ft
ID: 13
Strike: 285°
Date: 14-Sep-06

Rock Type
Norite + sub vertical dyke (1.5' wide)
Dyke: Lower portion of North Wall

Support

WEST WALL	BACK	EAST WALL
Type I	Type I	Type I

Q INDEX NORTH WALL

Rx Strength	100MPa
Blk Size (RQD/Jn)	7.60
Jnt Strength (Jr/Ja)	0.63
Jw/SRF	1.00
TOTAL	**4.79**

Q INDEX BACK

Rx Strength	100MPa
Blk Size (RQD/Jn)	7.60
Jnt Strength (Jr/Ja)	0.63
Jw/SRF	1.00
TOTAL	**4.79**

Q INDEX SOUTH WALL

Rx Strength	100MPa
Blk Size (RQD/Jn)	7.60
Jnt Strength (Jr/Ja)	0.63
Jw/SRF	1.00
TOTAL	**4.79**

RMR CHARACTERIZATION NORTH WALL

STRENGTH	R4	12
RQD	80%	15
SPACING	in-1'	13
CONDITION	Tight	15
GRNWTR	DRY	10
	RATING	**65%**
STRUCTURE		
	DESIGN	**65%**

RMR CHARACTERIZATION BACK

STRENGTH	R4	12
RQD	80%	15
SPACING	in-1'	13
CONDITION	Tight	15
GRNWTR	DRY	10
	RATING	**65%**
STRUCTURE		
	DESIGN	**65%**

RMR CHARACTERIZATION SOUTH WALL

STRENGTH	R4	12
RQD	80%	15
SPACING	in-1'	13
CONDITION	Tight	15
GRNWTR	DRY	10
	RATING	**65%**
STRUCTURE		
	DESIGN	**65%**

Structure

Strike (deg)	Dip (deg)	Persistence (m)	Spacing min (cm)	Spacing max (cm)	Occurrence x times	Notes
300	84	2.5	30	30	4	Controlling
40	90	3.5	30	30	5	Controlling
120	72	3	30	30	4	Controlling
0	90	4	30	30	4	Controlling
87	83	3.5	30	30	5	
147	90	3.5	30	30	4	Controlling

Other Notes:
Joints tight
soft to strong JS condition
Type I support
Overall Blasting: semi-good
Semi bad N
Good S and Back
South wall loaded w/trim pouder
Dynosplit D

Figure A. 16 Back, right and left wall pictures and rock mass classification logs – Stillwater Mine – Footwall lateral 13

Level: 4700
Type: Footwall Lateral
ID: No.14
Strike: 285º
Back Support: Type I
Date: Sept 14th, 2006

Back

North Wall

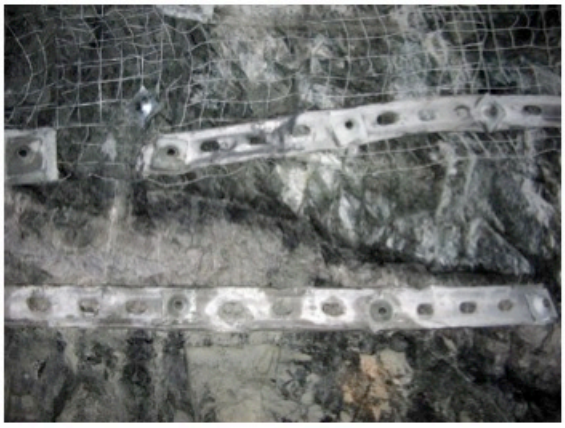

South Wall

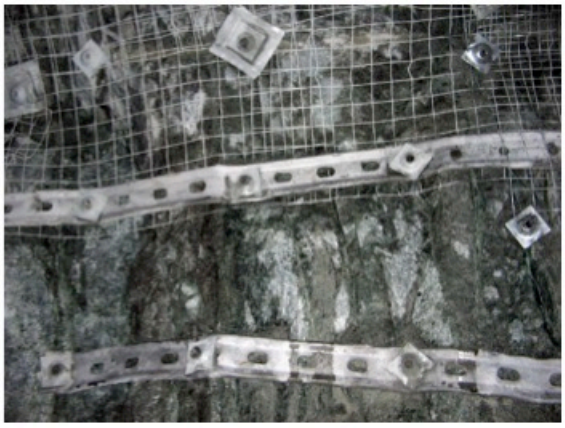

Title: **4700 Footwall Lateral No.14**
Level: 4700 ft
ID: 14
Strike: 285°
Date: 14-Sep-06

Rock Type
Norite + sub vertical dyke (1.5' wide)
Dyke: Mid height of North Wall

Support

WEST WALL	BACK	EAST WALL
Type I	Type I	Type I

Q INDEX NORTH WALL

Rx Strength	100MPa
Blk Size (RQD/Jn)	5.70
Jnt Strength (Jr/Ja)	0.84
Jw/SRF	1.00
TOTAL	**4.79**

Q INDEX BACK

Rx Strength	100MPa
Blk Size (RQD/Jn)	5.70
Jnt Strength (Jr/Ja)	0.84
Jw/SRF	1.00
TOTAL	**4.79**

Q INDEX SOUTH WALL

Rx Strength	100MPa
Blk Size (RQD/Jn)	5.70
Jnt Strength (Jr/Ja)	0.84
Jw/SRF	1.00
TOTAL	**4.79**

RMR CHARACTERIZATION NORTH WALL

STRENGTH	R4	12
RQD	75%-80%	13
SPACING	3in-6in	10
CONDITION	Tight	15
GRNWTR	DRY	10
	RATING	**60%**
STRUCTURE		
	DESIGN	**60%**

RMR CHARACTERIZATION BACK

STRENGTH	R4	12
RQD	75%-80%	13
SPACING	3in-6in	10
CONDITION	Tight	15
GRNWTR	DRY	10
	RATING	**60%**
STRUCTURE		
	DESIGN	**60%**

RMR CHARACTERIZATION SOUTH WALL

STRENGTH	R4	12
RQD	75%-80%	13
SPACING	3in-6in	10
CONDITION	Tight	15
GRNWTR	DRY	10
	RATING	**60%**
STRUCTURE		
	DESIGN	**60%**

Structure

Strike (deg)	Dip (deg)	Persistence (m)	Spacing min (cm)	Spacing max (cm)	Occurrence x times	Notes
123	82	3	30	30	5	Controlling
272	81	3.5	30	30	4	Controlling
162	85	3	10	20	6	Controlling
297	43	4	30	30	4	
218	63	2.5	10	20	6	
85	45	3	30	30	4	Controlling

Other Notes:
Joints tight
soft to strong JS condition
Type I support
Overall Blasting: Good
Good N, S and Back
North wall loaded w/trim pouder
Dynosplit D

Figure A. 17 Back, right and left wall pictures and rock mass classification logs – Stillwater Mine – Footwall lateral 14

Level: 4700
Type: Footwall Lateral
ID: No.15
Strike: 285º
Back Support: Type I
Date: Sept 14th, 2006

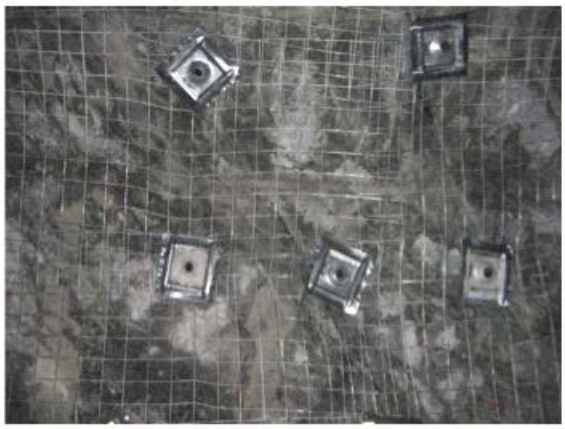

Back

North Wall

South Wall

Title: **4700 Footwall Lateral No.15**
Level: 4700 ft
ID: 15
Strike: 285°
Date: 15-Sep-06

Rock Type
Norite + sub vertical dyke (1.5' wide)
Dyke: Mid height of North Wall

Support

WEST WALL	BACK	EAST WALL
Type I	Type I	Type I

Q INDEX NORTH WALL

Rx Strength	100MPa
Blk Size (RQD/Jn)	12.00
Jnt Strength (Jr/Ja)	0.84
Jw/SRF	1.00
TOTAL	**10.08**

Q INDEX BACK

Rx Strength	100MPa
Blk Size (RQD/Jn)	12.00
Jnt Strength (Jr/Ja)	0.84
Jw/SRF	1.00
TOTAL	**10.08**

Q INDEX SOUTH WALL

Rx Strength	100MPa
Blk Size (RQD/Jn)	12.00
Jnt Strength (Jr/Ja)	0.84
Jw/SRF	1.00
TOTAL	**10.08**

RMR CHARACTERIZATION NORTH WALL

STRENGTH	R4	12
RQD	80%	15
SPACING	1'-2'	17
CONDITION	Tight	15
GRNWTR	DRY	10
	RATING	**69%**
STRUCTURE		
	DESIGN	**70%**

RMR CHARACTERIZATION BACK

STRENGTH	R4	12
RQD	80%	15
SPACING	1'-2'	17
CONDITION	Tight	15
GRNWTR	DRY	10
	RATING	**69%**
STRUCTURE		
	DESIGN	**70%**

RMR CHARACTERIZATION SOUTH WALL

STRENGTH	R4	12
RQD	80%	15
SPACING	1'-2'	17
CONDITION	Tight	15
GRNWTR	DRY	10
	RATING	**69%**
STRUCTURE		
	DESIGN	**70%**

Structure

Strike (deg)	Dip (deg)	Persistence (m)	Spacing min (cm)	Spacing max (cm)	Occurrence x times	Notes
176	62	3.5	30	30	4	Controlling
214	76	3.5	60	60	4	
60	73	3	30	60	4	Controlling
88	43	3	30	60	3	Controlling
174	88	3	30	60	4	Controlling
63	75	3	30	60	4	Controlling

Other Notes:
Joints tight. Infilling mm-cm
soft to strong JS condition
Type I support
Overall Blasting: semi good
Semi-good N and Back
Good S
S and N wall loaded with Dynosplit D
Wedges came down from N wall and back

Figure A. 18 Back, right and left wall pictures and rock mass classification logs – Stillwater Mine – Footwall lateral 15

Level: 7170
Type: cross cut 11
ID: No.1
Strike: 47º
Back Support: Type I
Date: Nov 7th, 2006

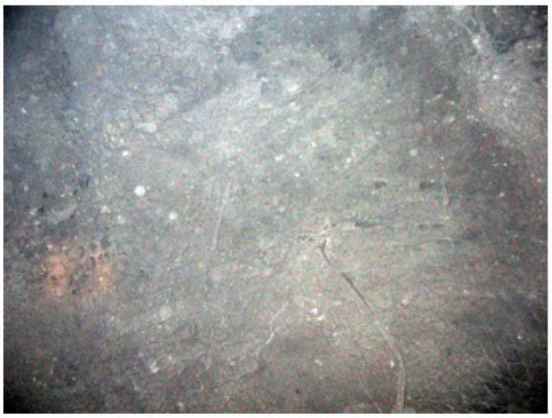

Back

SW Wall

NE Wall

Title: **Z7-7170 Cross Cut No.11**
Level: 7170 ft
ID: 1
Strike: 47º
Date: 07-Nov-06

Rock Type

Best description: Black mud
highly foliated and weathered sedimentary rock

Support

NE WALL	BACK	SW WALL
Type I	Type I	Type I

Q INDEX NE WALL

Rx Strength	30-50MPa
Blk Size (RQD/Jn)	1.90
Jnt Strength (Jr/Ja)	0.16
SRF	1.00
TOTAL	**0.30**

Q INDEX BACK

Rx Strength	30-50MPa
Blk Size (RQD/Jn)	1.90
Jnt Strength (Jr/Ja)	0.16
SRF	1.00
TOTAL	**0.30**

Q INDEX SW WALL

Rx Strength	2MPa
Blk Size (RQD/Jn)	Backfill
Jnt Strength (Jr/Ja)	Backfill
SRF	Backfill
TOTAL	**Backfill**

RMR CHARACTERIZATION NE WALL

STRENGTH	R2	5
RQD	20%-40%	8
SPACING	0.1"-0.5"+	5
CONDITION	SLT-OPN	9-6
GRNWTR	DRY	10
	RATING	**37-33%**
STRUCTURE		
	DESIGN	**35%**

RMR CHARACTERIZATION BACK

STRENGTH	R2	5
RQD	20%-40%	8
SPACING	0.1"-0.5"+	5
CONDITION	SLT-OPN	9-6
GRNWTR	DRY	10
	RATING	**37-33%**
STRUCTURE		
	DESIGN	**35%**

RMR CHARACTERIZATION SW WALL

STRENGTH		
RQD		
SPACING		
CONDITION		
GRNWTR		
	RATING	
STRUCTURE		
	DESIGN	

Structure

Strike (deg)	Dip (deg)	Persistence (m)	Spacing min (cm)	Spacing max (cm)	Occurrence x times	Notes
268	38	1.5	0.1	1	30	
172	20	1	0.1	1	30	

Other Notes:
Lots of loose material bagging screen
Many splisets can't always be properlly installed
Soil type of rock. Can be mushed with hands
mm openess
soft JS condition, smooth, wavy, highly foliated
Type I support, 7ft splitsets with mesh
Blast results: Poor NE (5ft overbreak) wall and fair back (3ft overbreak)
0.8m overbreak Back

Figure A. 19 Back, right and left wall pictures and rock mass classification logs – SSX Mine – Cross cut 11-1

Level: 7170
Type: cross cut 11
ID: No.2
Strike: 47º
Back Support: Type I
Date: Nov 7th, 2006

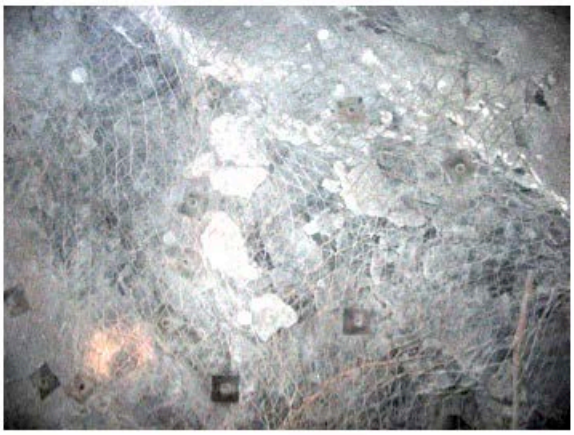

Back

SW Wall

NE Wall

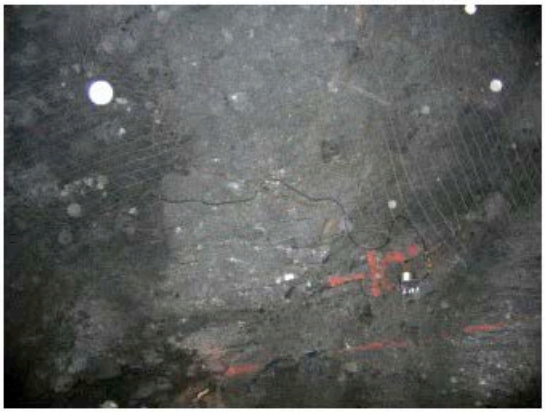

Title: **Z7-7170 Cross Cut No.11**
Level: 7170 ft
ID: 2
Strike: 47º
Date: 07-Nov-06

Rock Type

Best description: Black mud
highly foliated and weathered sedimentary rock

Support

NE WALL	BACK	SW WALL
Type I	Type I	Type I

Q INDEX NE WALL

Rx Strength	30-50MPa
Blk Size (RQD/Jn)	1.90
Jnt Strength (Jr/Ja)	0.16
SRF	1.00
TOTAL	**0.30**

Q INDEX BACK

Rx Strength	30-50MPa
Blk Size (RQD/Jn)	1.90
Jnt Strength (Jr/Ja)	0.16
SRF	1.00
TOTAL	**0.30**

Q INDEX SW WALL

Rx Strength	2MPa
Blk Size (RQD/Jn)	CRF Backfill
Jnt Strength (Jr/Ja)	CRF Backfill
SRF	CRF Backfill
TOTAL	**CRF Backfill**

RMR CHARACTERIZATION NE WALL

STRENGTH	R2	5
RQD	20%-40%	8
SPACING	0.1"-0.5"+	5
CONDITION	SLT-OPN	9-6
GRNWTR	DRY	10
	RATING	**37-33%**
STRUCTURE		
	DESIGN	**35%**

RMR CHARACTERIZATION BACK

STRENGTH	R2	5
RQD	20%-40%	8
SPACING	0.1"-0.5"+	5
CONDITION	SLT-OPN	9-6
GRNWTR	DRY	10
	RATING	**37-33%**
STRUCTURE		
	DESIGN	**35%**

RMR CHARACTERIZATION SW WALL

STRENGTH		
RQD		
SPACING		
CONDITION		
GRNWTR		
	RATING	
STRUCTURE		
	DESIGN	

Structure

Strike (deg)	Dip (deg)	Persistence (m)	Spacing min (cm)	Spacing max (cm)	Occurrence x times	Notes
78	75	1.0	0.1	0.1	30	Same JS
252	25	1.5	0.1	0.1	30	changes strike
84	36	1.0	0.1	1.0	30	and dip in 1.5ft
						due to foliation

Other Notes:
Lots of loose material bagging screen
Many splisets can't always be properlly installed
Soil type of rock. Can be mushed with hands
mm openess
soft JS condition, smooth, wavy, highly foliated
Type I support, 7ft splitsets with mesh
Blast results: Poor NE (5ft overbreak) wall and poor back (3ft overbreak)
Last row of drilled blastholes are not loaded w/explosives
in most rounds blast damage surpassed last drillhole row

Figure A. 20 Back, right and left wall pictures and rock mass classification logs – SSX Mine – Cross cut 11-2

Level: 7170
Type: cross cut 11
ID: No.3
Strike: 47º
Back Support: Type I
Date: Nov 7th, 2006

Back

SW Wall

NE Wall

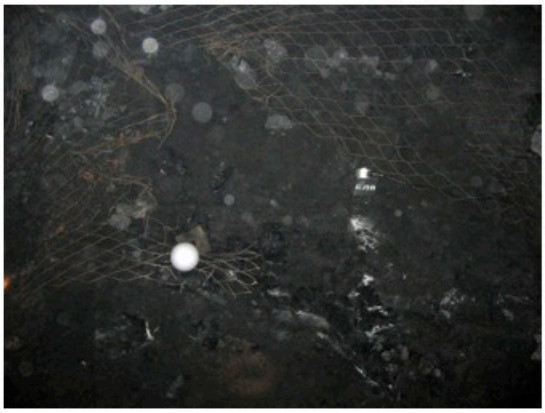

Title: **Z7-7170 Cross Cut No.11**
Level: 7170 ft
ID: 3
Strike: 47°
Date: 07-Nov-06

Rock Type

Best description: Black mud
highly foliated and weathered sedimentary rock

Support

NE WALL	BACK	SW WALL
Type I	Type I	Type I

Q INDEX NE WALL

Rx Strength	30-50MPa
Blk Size (RQD/Jn)	1.90
Jnt Strength (Jr/Ja)	0.16
SRF	1.00
TOTAL	**0.30**

Q INDEX BACK

Rx Strength	30-50MPa
Blk Size (RQD/Jn)	1.90
Jnt Strength (Jr/Ja)	0.16
SRF	1.00
TOTAL	**0.30**

Q INDEX SW WALL

Rx Strength	2MPa
Blk Size (RQD/Jn)	CRF Backfill
Jnt Strength (Jr/Ja)	CRF Backfill
SRF	CRF Backfill
TOTAL	**CRF Backfill**

RMR CHARACTERIZATION NE WALL

STRENGTH	R2	5
RQD	20%-40%	8
SPACING	0.1"-0.5"+	5
CONDITION	SLT-OPN	9-6
GRNWTR	DRY	10
	RATING	**37-33%**
STRUCTURE		
	DESIGN	**35%**

RMR CHARACTERIZATION BACK

STRENGTH	R2	5
RQD	20%-40%	8
SPACING	0.1"-0.5"+	5
CONDITION	SLT-OPN	9-6
GRNWTR	DRY	10
	RATING	**37-33%**
STRUCTURE		
	DESIGN	**35%**

RMR CHARACTERIZATION SW WALL

STRENGTH		
RQD		
SPACING		
CONDITION		
GRNWTR		
	RATING	
STRUCTURE		
	DESIGN	

Structure

Strike (deg)	Dip (deg)	Persistence (m)	Spacing min (cm)	Spacing max (cm)	Occurrence x times	Notes
248	55	1.5	1.0	1.0	30	Same JS
						changes strike
						and dip in 1.5ft
						due to foliation

Other Notes:
Lots of loose material bagging screen
Many splisets can't always be properlly installed
Soil type of rock. Can be mushed with hands
mm openess. Black mud w/calcite pockets
soft JS condition, smooth, wavy, highly foliated
Type I support, 7ft splitsets with mesh, difficult to maintain bolt spacing
Blast results: Very poor NE (7ft overbreak) wall and fair back (3ft overbreak)
Last row of drilled blastholes are not loaded w/explosives
in most rounds blast damage surpassed last drillhole row

Figure A. 21 Back, right and left wall pictures and rock mass classification logs – SSX Mine – Cross cut 11-3

Level: 7170
Type: cross cut 11
ID: No.4
Strike: 47º
Back Support: Type I
Date: Nov 7th, 2006

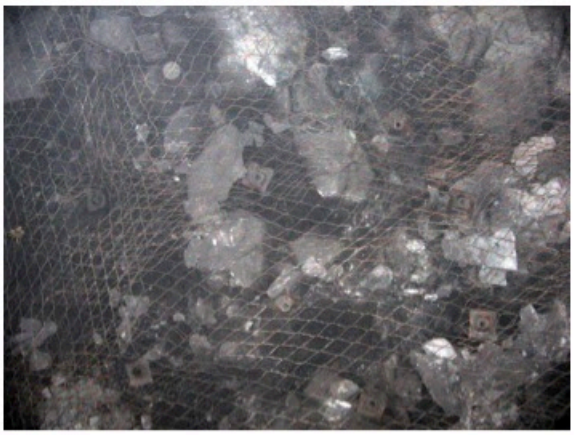

Back

SW Wall

NE Wall

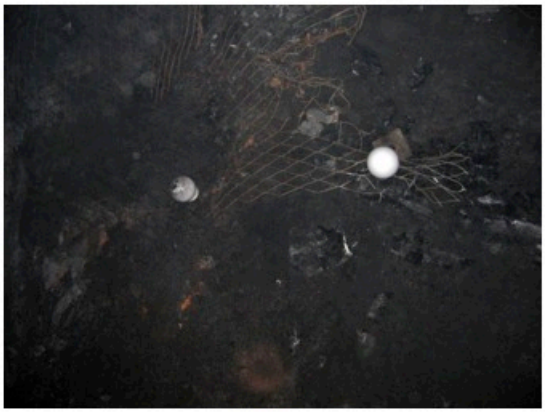

Title: **Z7-7170 Cross Cut No.11**
Level: 7170 ft
ID: 4
Strike: 47º
Date: 07-Nov-06

Rock Type

Best description: Black mud
highly foliated and weathered sedimentary rock

Support

NE WALL	BACK	SW WALL
Type I	Type I	Type I

Q INDEX NE WALL

Rx Strength	30-50MPa
Blk Size (RQD/Jn)	1.90
Jnt Strength (Jr/Ja)	0.16
SRF	1.00
TOTAL	**0.30**

Q INDEX BACK

Rx Strength	30-50MPa
Blk Size (RQD/Jn)	1.90
Jnt Strength (Jr/Ja)	0.16
SRF	1.00
TOTAL	**0.30**

Q INDEX SW WALL

Rx Strength	2MPa
Blk Size (RQD/Jn)	CRF Backfill
Jnt Strength (Jr/Ja)	CRF Backfill
SRF	CRF Backfill
TOTAL	**CRF Backfill**

RMR CHARACTERIZATION NE WALL

STRENGTH	R2	5
RQD	20%-40%	8
SPACING	0.1"-0.5"+	5
CONDITION	SLT-OPN	9-6
GRNWTR	DRY	10
	RATING	**37-33%**
STRUCTURE		
	DESIGN	**35%**

RMR CHARACTERIZATION BACK

STRENGTH	R2	5
RQD	20%-40%	8
SPACING	0.1"-0.5"+	5
CONDITION	SLT-OPN	9-6
GRNWTR	DRY	10
	RATING	**37-33%**
STRUCTURE		
	DESIGN	**35%**

RMR CHARACTERIZATION SW WALL

STRENGTH		
RQD		
SPACING		
CONDITION		
GRNWTR		
	RATING	
STRUCTURE		
	DESIGN	

Structure

Strike (deg)	Dip (deg)	Persistence (m)	Spacing min (cm)	Spacing max (cm)	Occurrence x times	Notes
78	21	1.5	1.0	1.0	30	Same JS
180	38	1.0	1.0	1.0	30	changes strike
143	87	1.0	1.0	1.0	30	and dip in 1.5ft
						due to foliation

Other Notes:
Lots of loose material bagging screen
Many splisets can't always be properlly installed, round showed better results
Soil type of rock. Can be mushed with hands
mm openess. Black mud w/calcite pockets
soft JS condition, smooth, wavy, highly foliated
Type I support, 7ft splitsets with mesh, difficult to maintain bolt spacing
Blast results: Fair NE (2.5ft overbreak) wall and fair back (2ft overbreak)
Last row of drilled blastholes are not loaded w/explosives
in most rounds blast damage surpassed last drillhole row

Figure A. 22 Back, right and left wall pictures and rock mass classification logs – SSX Mine – Cross cut 11-4

Level: 7170
Type: cross cut 11
ID: No.5
Strike: 47º
Back Support: Type I
Date: Nov 7th, 2006

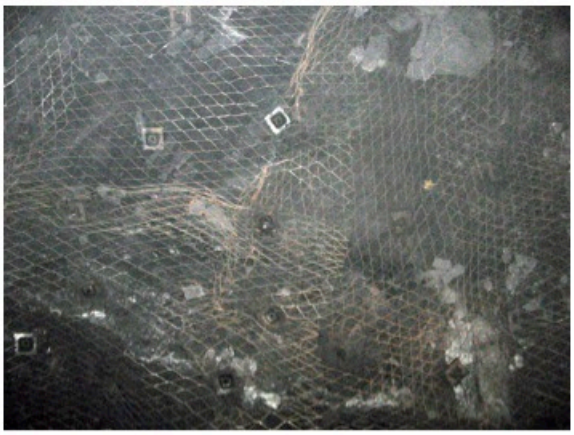

Back

SW Wall

NE Wall

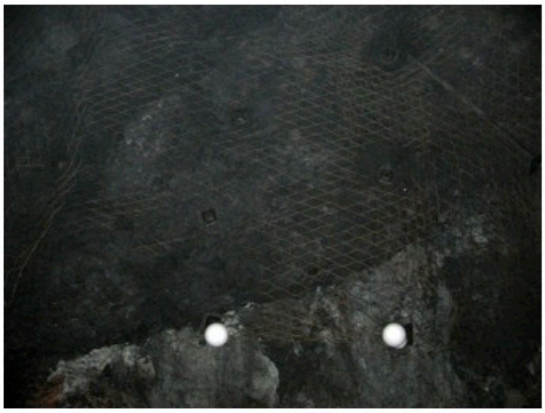

Title: **Z7-7170 Cross Cut No.11**

Level: 7170 ft
ID: 5
Strike: 47º
Date: 07-Nov-06

Rock Type

Best description: Black mud
highly foliated and weathered sedimentary rock

Support

NE WALL	BACK	SW WALL
Type I	Type I	Type I

Q INDEX NE WALL

Rx Strength	30-50MPa
Blk Size (RQD/Jn)	1.90
Jnt Strength (Jr/Ja)	0.10
SRF	1.00
TOTAL	**0.19**

Q INDEX BACK

Rx Strength	30-50MPa
Blk Size (RQD/Jn)	1.90
Jnt Strength (Jr/Ja)	0.16
SRF	1.00
TOTAL	**0.30**

Q INDEX SW WALL

Rx Strength	2MPa
Blk Size (RQD/Jn)	CRF Backfill
Jnt Strength (Jr/Ja)	CRF Backfill
SRF	CRF Backfill
TOTAL	**CRF Backfill**

RMR CHARACTERIZATION NE WALL

STRENGTH	R2	5
RQD	20%-40%	8
SPACING	0.1"-0.5"+	5
CONDITION	SLT-OPN	9-6
GRNWTR	DRY	10
	RATING	**37-33%**
STRUCTURE		
	DESIGN	**35%**

RMR CHARACTERIZATION BACK

STRENGTH	R2	5
RQD	20%-40%	8
SPACING	0.1"-0.5"+	5
CONDITION	SLT-OPN	9-6
GRNWTR	DRY	10
	RATING	**37-33%**
STRUCTURE		
	DESIGN	**35%**

RMR CHARACTERIZATION SW WALL

STRENGTH		
RQD		
SPACING		
CONDITION		
GRNWTR		
	RATING	
STRUCTURE		
	DESIGN	

Structure

Strike (deg)	Dip (deg)	Persistence (m)	Spacing min (cm)	Spacing max (cm)	Occurrence x times	Notes
50	81	1.5	0.1	1.0	30	Same JS
						changes strike
						and dip in 1.5ft
						due to foliation

Other Notes:
Lots of loose material bagging screen
Many splisets can't always be properlly installed, round showed better results
Soil type of rock. Can be mushed with hands
mm openess. Black mud w/calcite pockets
soft JS condition, smooth, wavy, highly foliated
Type I support, 7ft splitsets with mesh, difficult to maintain bolt spacing
Blast results: Poor NE (6ft overbreak) wall and poor back (5.5ft overbreak)
Last row of drilled blastholes are not loaded w/explosives
in most rounds blast damage surpassed last drillhole row

Figure A. 23 Back, right and left wall pictures and rock mass classification logs – SSX Mine – Cross cut 11-5

Level: 720mL
Type: C Block East
ID: No.1
Strike: 345º
Back Support: Type I
Date: May 15th, 2008

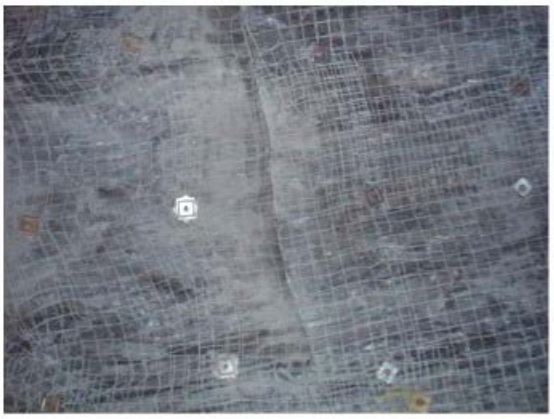

Back

East Wall

West Wall

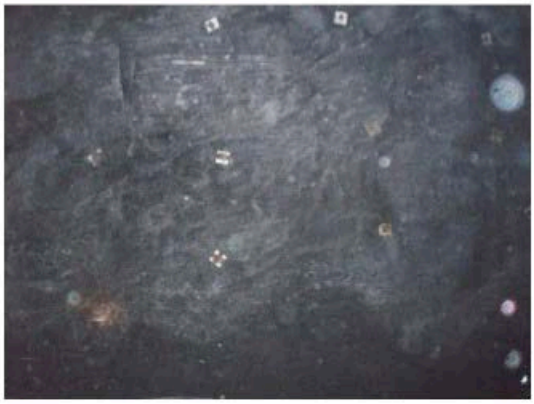

Title: **720L C Block East**
Level: 720mL
ID: 1
Strike: N15W
Date: 13-May-08

Rock Type

Best description: E Very Competent Ground

Support

E WALL	BACK	W WALL
Type II upper corner	Type II	Type II upper corner

Q INDEX E WALL

Rx Strength	100-150MPa
Blk Size (RQD/Jn)	45.00
Jnt Strength (Jr/Ja)	4.00
SRF	1.00
TOTAL	**180.00**

Q INDEX BACK

Rx Strength	100-150MPa
Blk Size (RQD/Jn)	45.00
Jnt Strength (Jr/Ja)	4.00
SRF	1.00
TOTAL	**180.00**

Q INDEX W WALL

Rx Strength	100-150MPa
Blk Size (RQD/Jn)	45.00
Jnt Strength (Jr/Ja)	4.00
SRF	1.00
TOTAL	**180.00**

RMR CHARACTERIZATION NE WALL

STRENGTH	R4+	13
RQD	90+	20
SPACING	2m+	28
CONDITION	Tight	20
GRNWTR	DRY	10
	RATING	**91%**
STRUCTURE		
	DESIGN	**90%**

RMR CHARACTERIZATION BACK

STRENGTH	R4+	13
RQD	90+	20
SPACING	2m+	28
CONDITION	Tight	20
GRNWTR	DRY	10
	RATING	**91%**
STRUCTURE		
	DESIGN	**90%**

RMR CHARACTERIZATION SW WALL

STRENGTH	R4+	13
RQD	90+	20
SPACING	2m+	28
CONDITION	Tight	20
GRNWTR	DRY	10
	RATING	**91%**
STRUCTURE		
	DESIGN	**90%**

Structure

Strike (deg)	Dip (deg)	Persistence (m)	Spacing min (cm)	Spacing max (cm)	Occurrence x times	Notes
254	86	4+	-	200+	2	JS
327	58	N/A	-	30	1000	Foliation

Other Notes:
No material bagging screen
2m+ spaced JS structures
very tight
hard rough slt wavy
Type II support, resin rebar rx bolts with mesh
only placed at the back and upper corners of both walls
0.3cm (visual) overbreak, 5 half barrels only at the back

Figure A. 24 Back, right and left wall pictures and rock mass classification logs – Musselwhite Mine – Footwall lateral 1

Title: **3471 Development Panel**

Level: 1700ft
ID: 1
Strike: 210°
Date: 29-Mar-07

Rock Type

Intercalated limestone and mudstone

Commonly well layered with layer thickness highly variable

Support

WEST WALL	BACK	EAST WALL
Shotcrete/split set/mesh	Shotcrete/split set/mesh	Shotcrete/split set/mesh

Q INDEX WEST WALL

Rx Strength	100MPa
Blk Size (RQD/Jn)	6.25
Jnt Strength (Jr/Ja)	0.50
SRF	1.00
TOTAL	**3.13**

Q INDEX BACK

Rx Strength	100MPa
Blk Size (RQD/Jn)	6.25
Jnt Strength (Jr/Ja)	0.50
SRF	1.00
TOTAL	**3.13**

Q INDEX EAST WALL

Rx Strength	100MPa
Blk Size (RQD/Jn)	6.25
Jnt Strength (Jr/Ja)	0.50
SRF	1.00
TOTAL	**3.13**

RMR CHARACTERIZATION WEST WALL

STRENGTH	R3+	7
RQD	75%	13
SPACING	5-10cm	10
CONDITION	Tight/sltly open	15
GRNWTR	DRY	10
	RATING	**55%**
STRUCTURE		
	DESIGN	**55%**

RMR CHARACTERIZATION BACK

STRENGTH	R3+	7
RQD	75%	13
SPACING	5-10cm	10
CONDITION	Tight/sltly open	15
GRNWTR	DRY	10
	RATING	**55%**
STRUCTURE		
	DESIGN	**55%**

RMR CHARACTERIZATION EAST WALL

STRENGTH	R3+	7
RQD	75%	13
SPACING	5-10cm	10
CONDITION	Tight/sltly open	15
GRNWTR	DRY	10
	RATING	**55%**
STRUCTURE		
	DESIGN	**55%**

Structure

DDR (deg)	Dip (deg)	Persistence (m)	Spacing min (cm)	Spacing max (cm)	Occurrence x times	Notes
160	60	2.5	30	30	4	
220	85	3.5	60	60	6	
215	84	2.5	30	60	3	
185	45	3	30	60	5	
180	10	3	30	60	5	

Other Notes:
Joints varying from tight to slightly open. Infilling mm-cm
soft to medium strong JS condition
Shotcrete for both walls and back
Overall Blasting: semi good
6ff split set + mesh
4' x 4' pattern

Figure A. 25 Back, right and left wall rock mass classification logs – Turquoise Ridge JV Mine – Footwall lateral 1

APPENDIX B – PARTICLE VELOCITY AND FREQUENCY CONTENT - CASE STUDIES

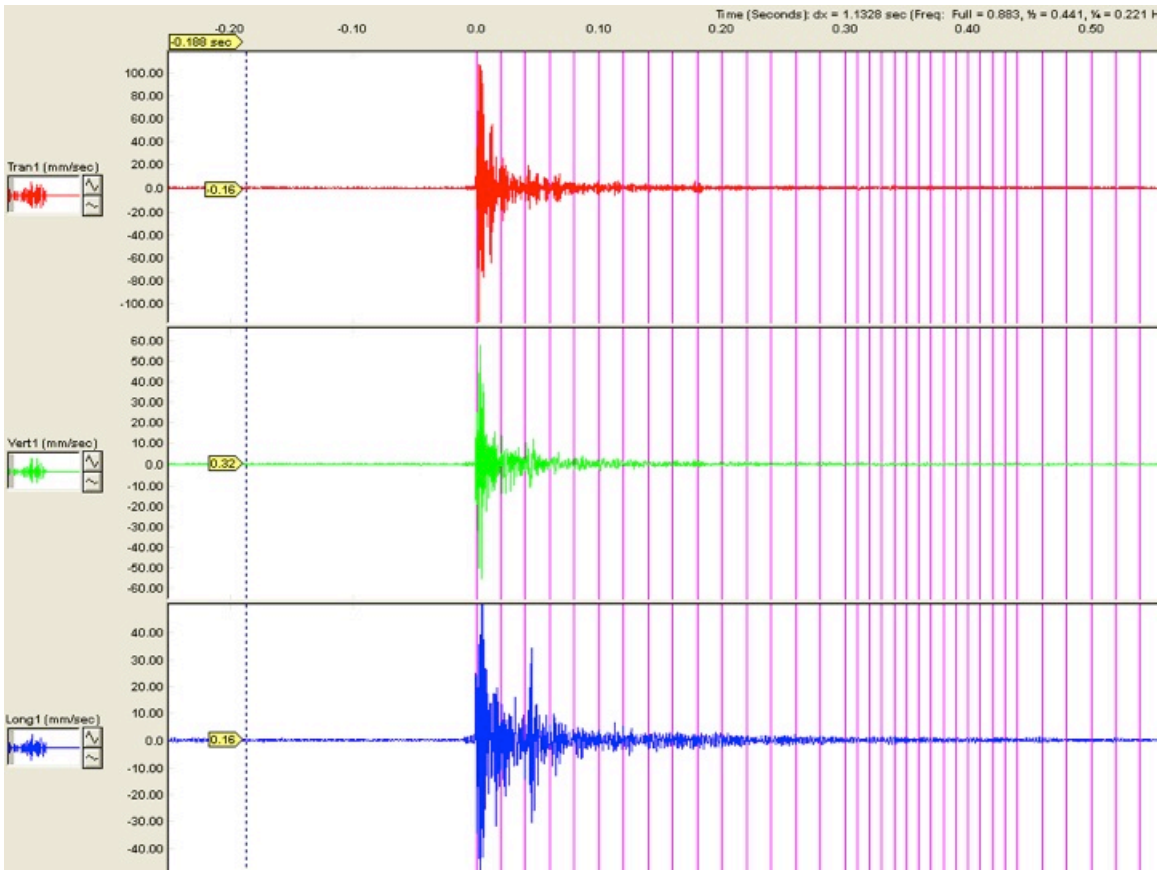

Figure B. 1 Particle velocity record – Transversal, vertical and longitudinal – Musselwhite Mine

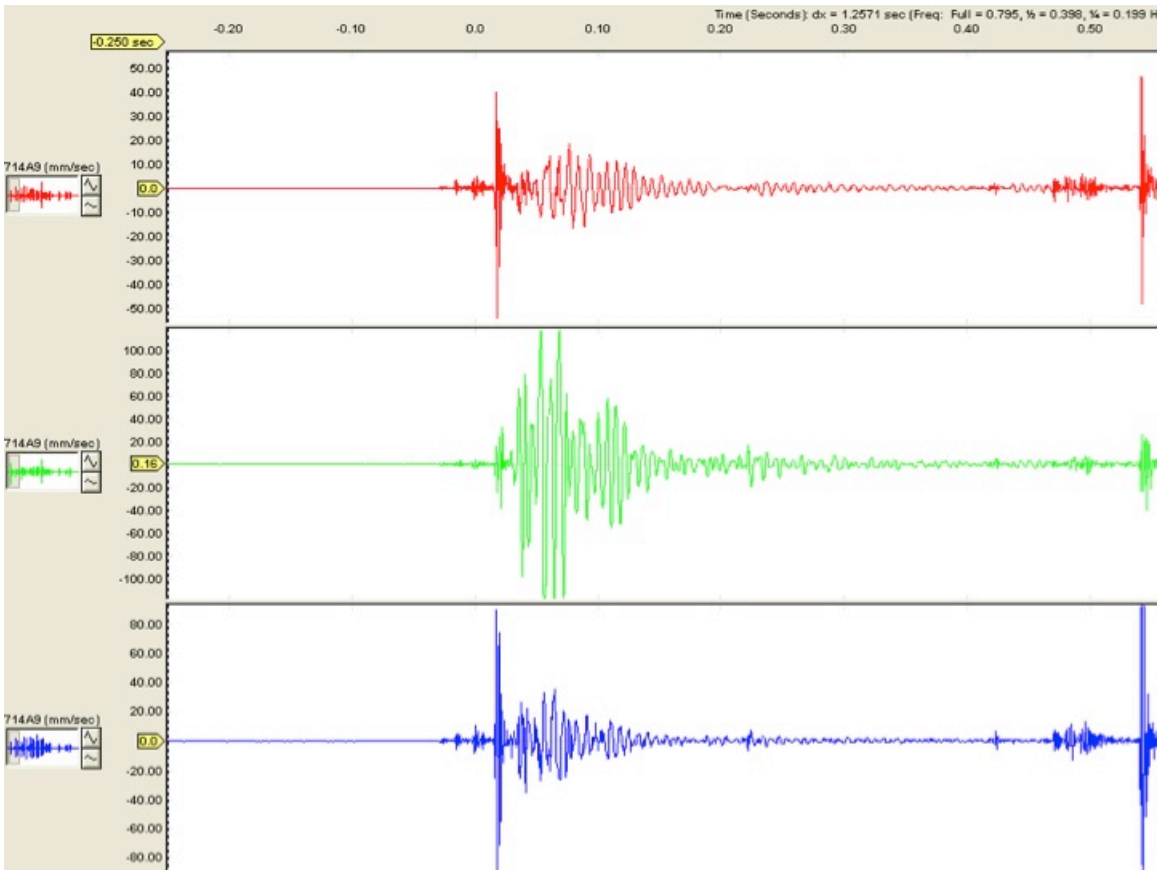

Figure B. 2 Particle velocity record – Transversal, vertical and longitudinal – Stillwater Mine

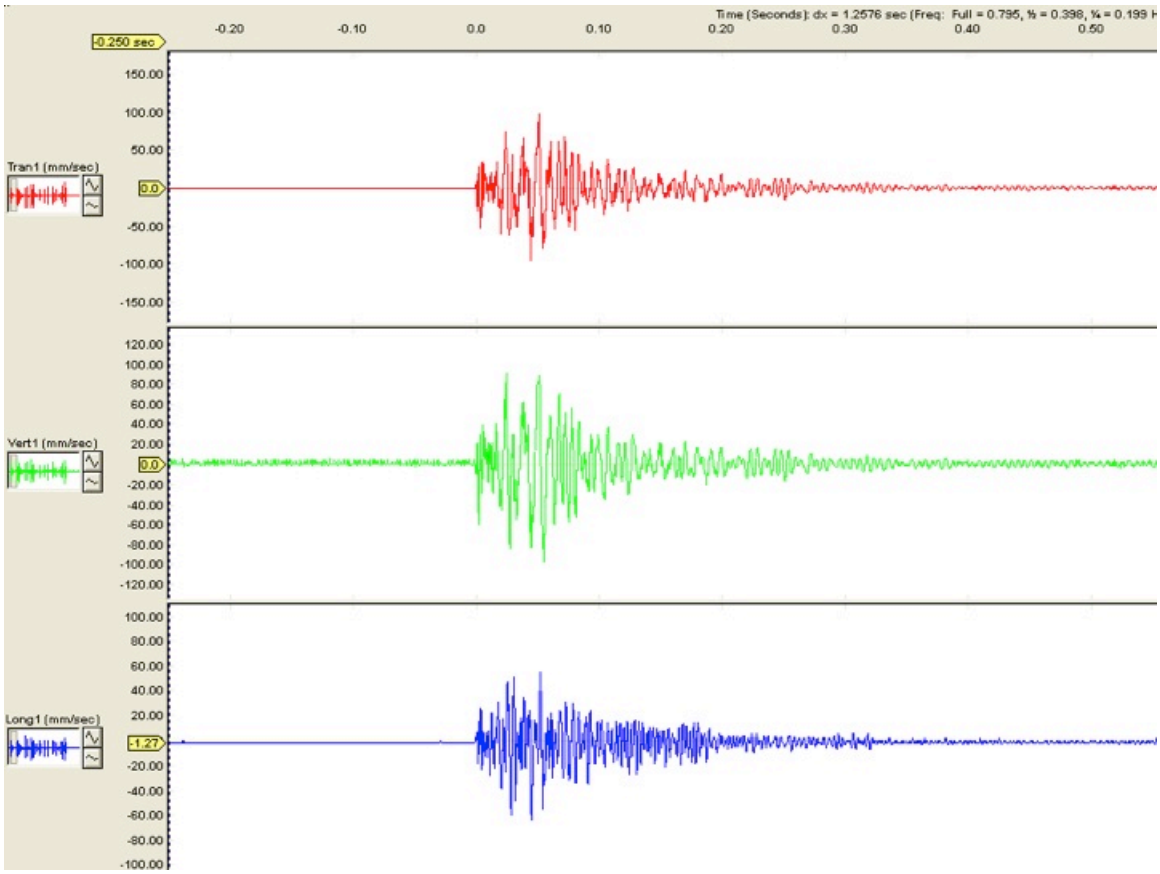

Figure B. 3 Particle velocity record – Transversal, vertical and longitudinal – Turquoise Ridge JV Mine

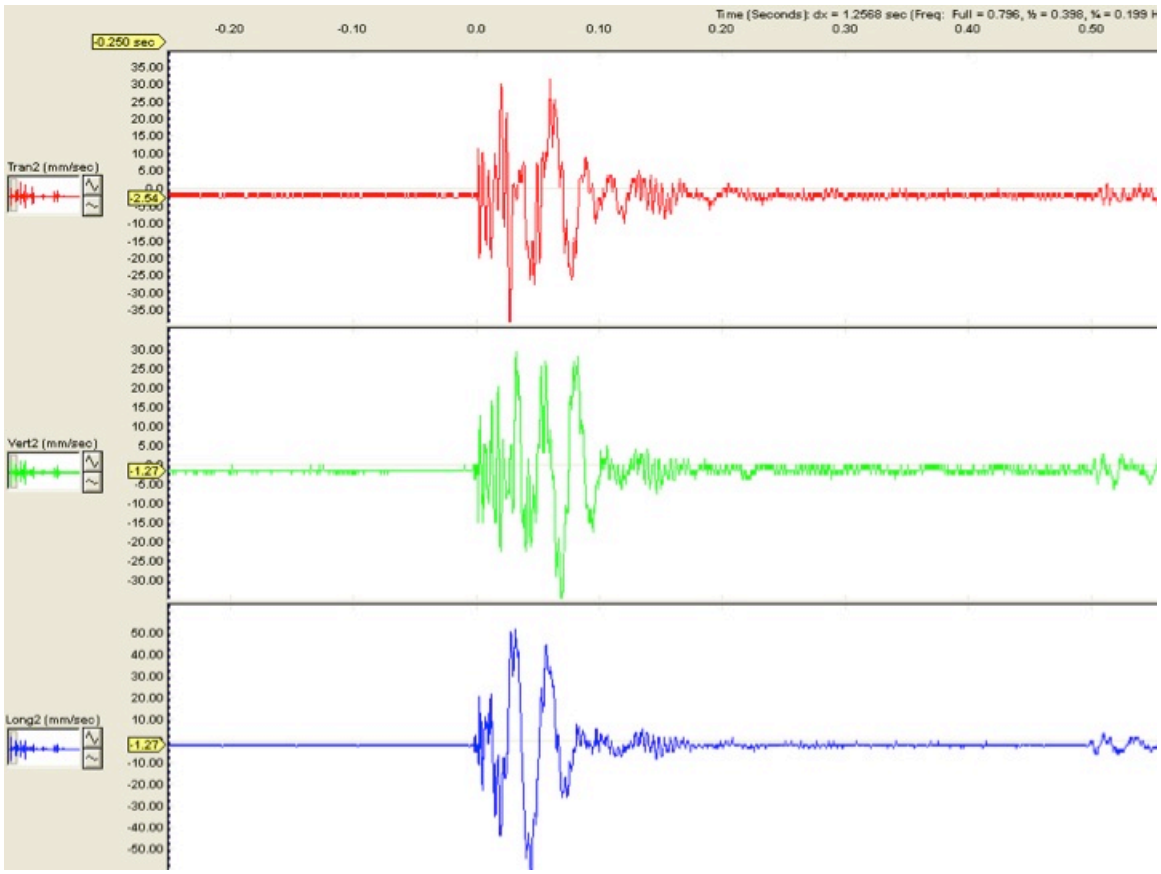

Figure B. 4 Particle velocity record – Transversal, vertical and longitudinal – SSX Mine

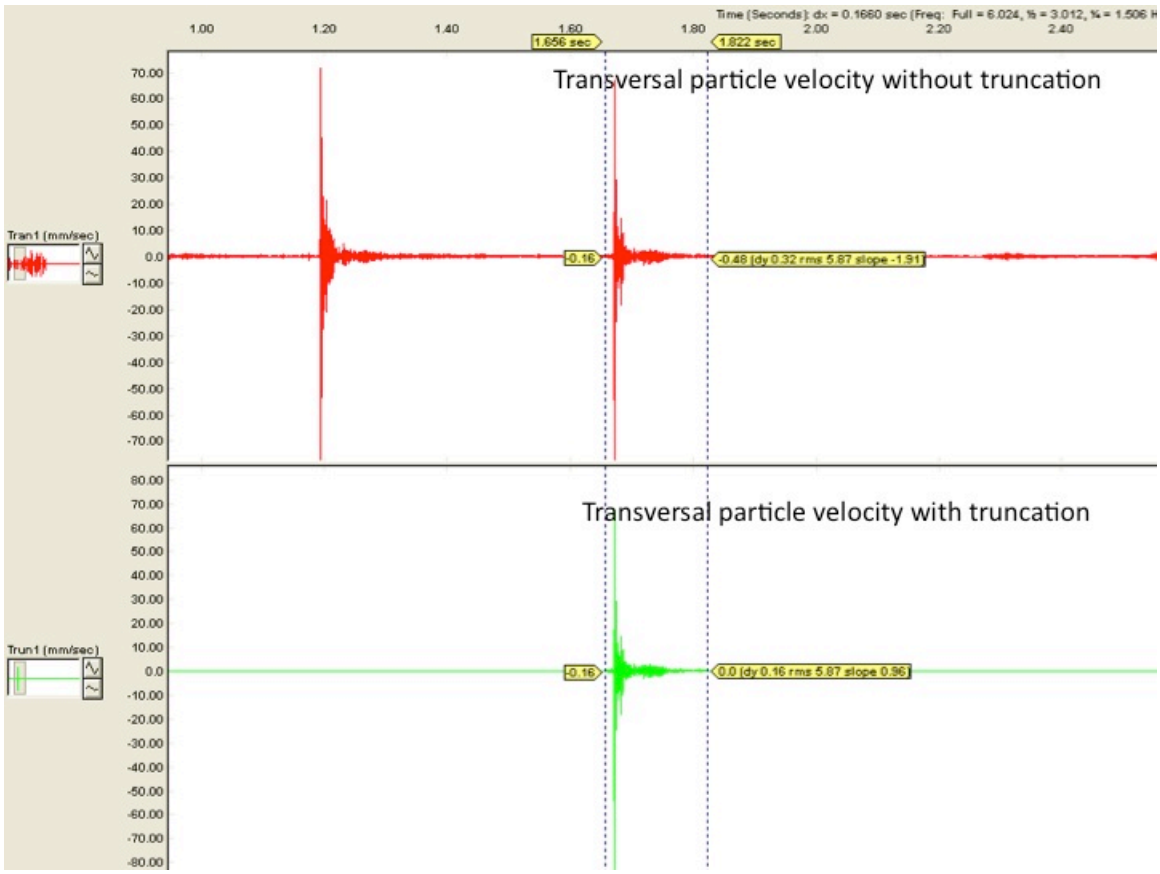

Figure B. 5 Original (Trans1) and truncated transversal particle velocity records (Trun1) – Musselwhite Mine

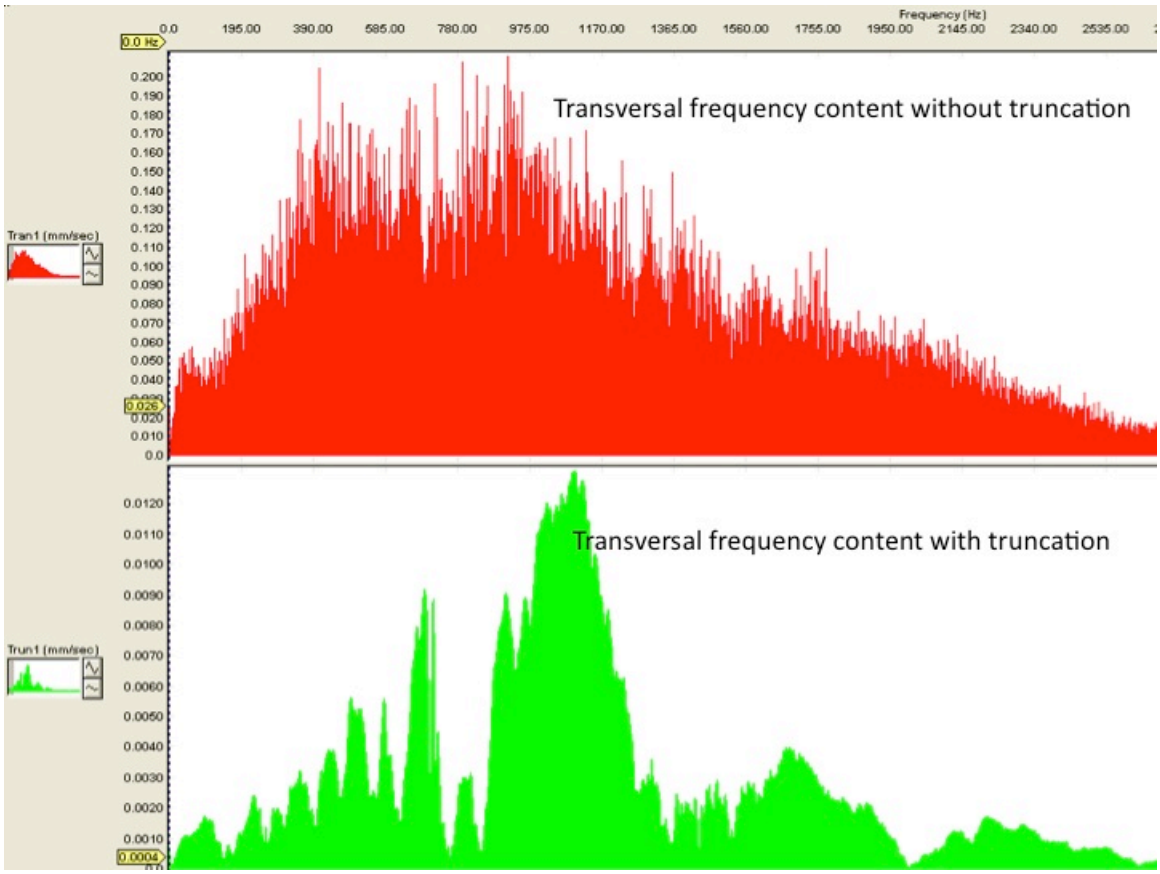

Figure B. 6 Frequency content of original (Trans1) and truncated transversal particle velocity records (Trun1) – Musselwhite Mine

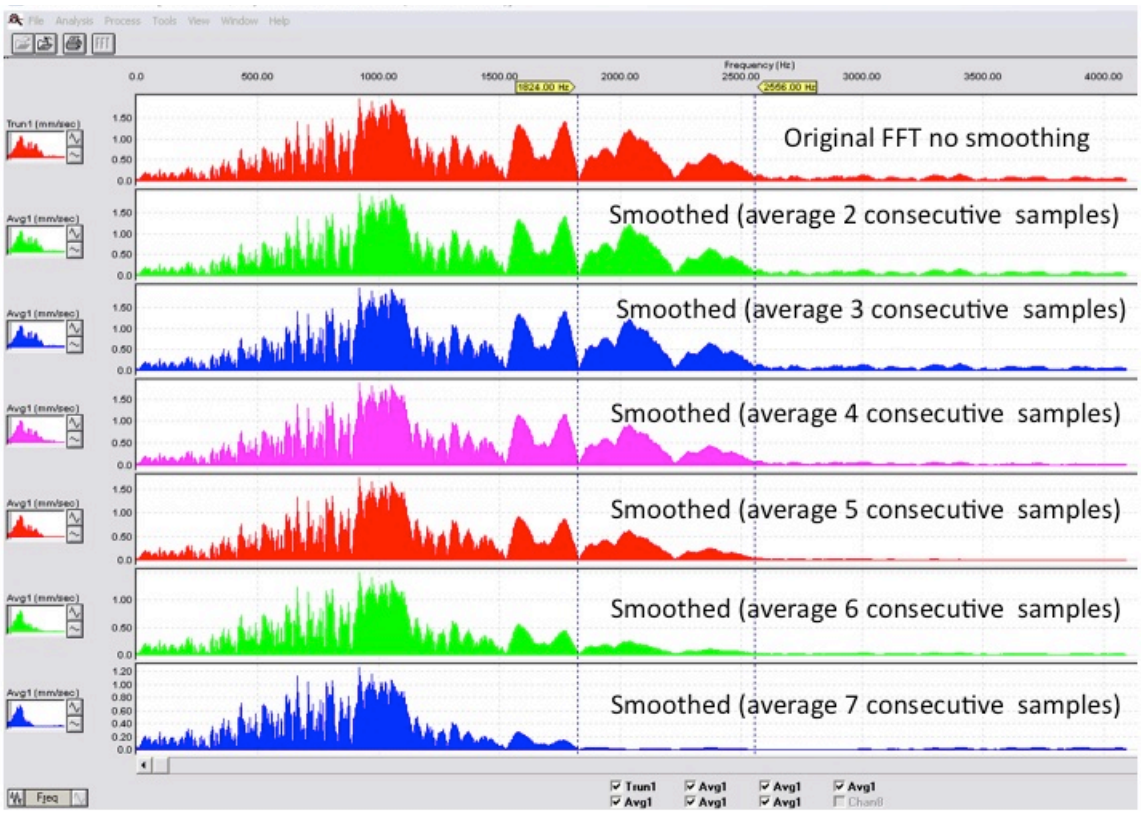

Figure B. 7 Frequency content of truncated unsmoothed and smoothed (average of 2, 3, 4, 5, 6 and 7 consecutive samples) transversal particle velocity records – Musselwhite Mine

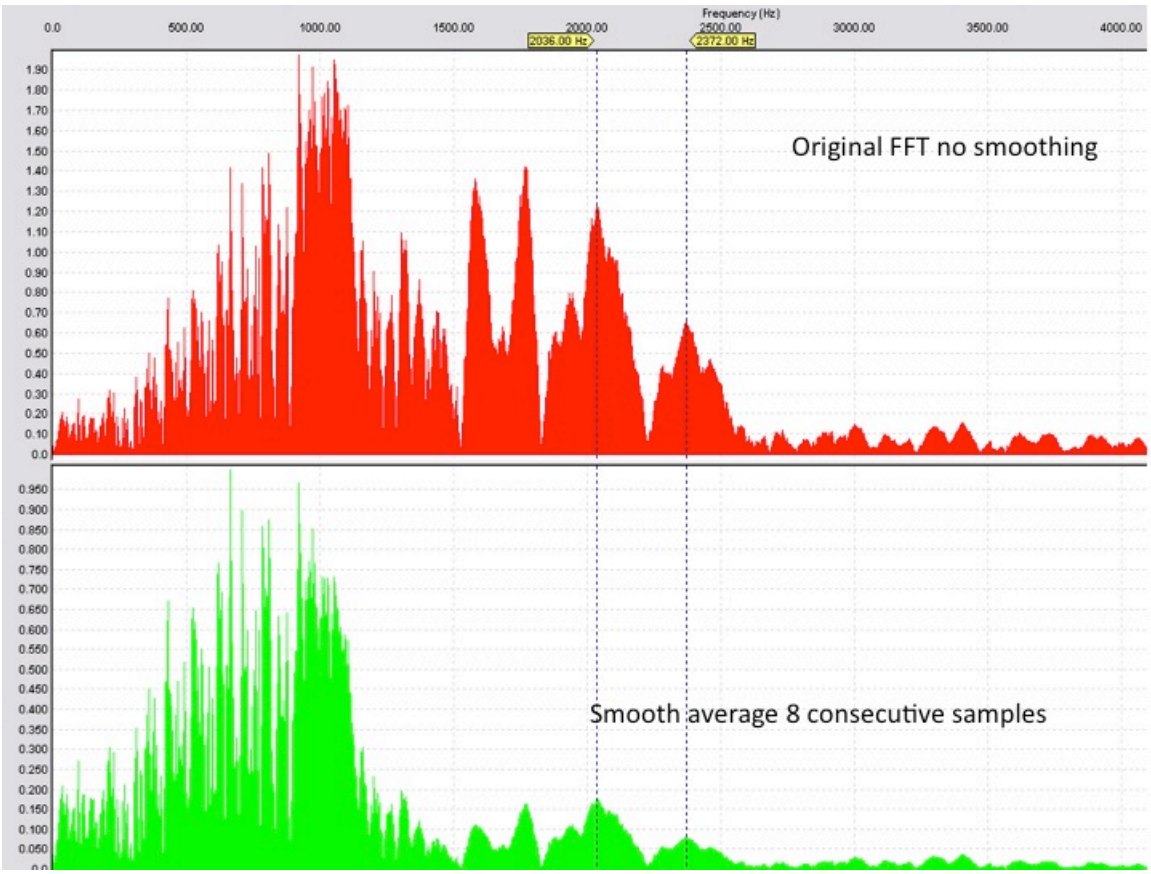

Figure B. 8 Frequency content of truncated unsmoothed and smoothed (average of 8 consecutive samples) transversal particle velocity records – Musselwhite Mine

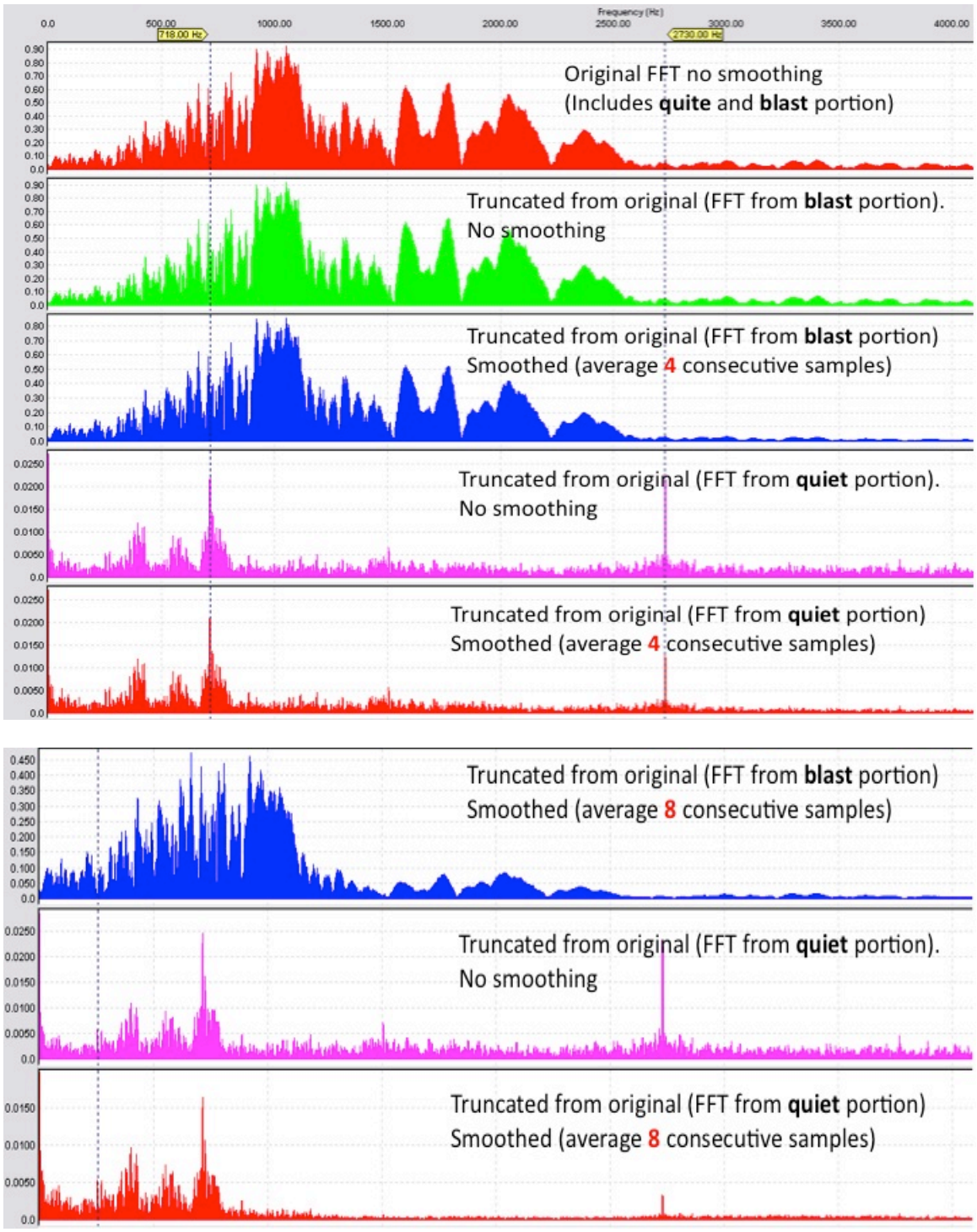

Figure B. 9 Frequency content of truncated unsmoothed and smoothed blast and quiet portion (average of 4 and 8 consecutive samples) of the transversal particle velocity records – Musselwhite Mine

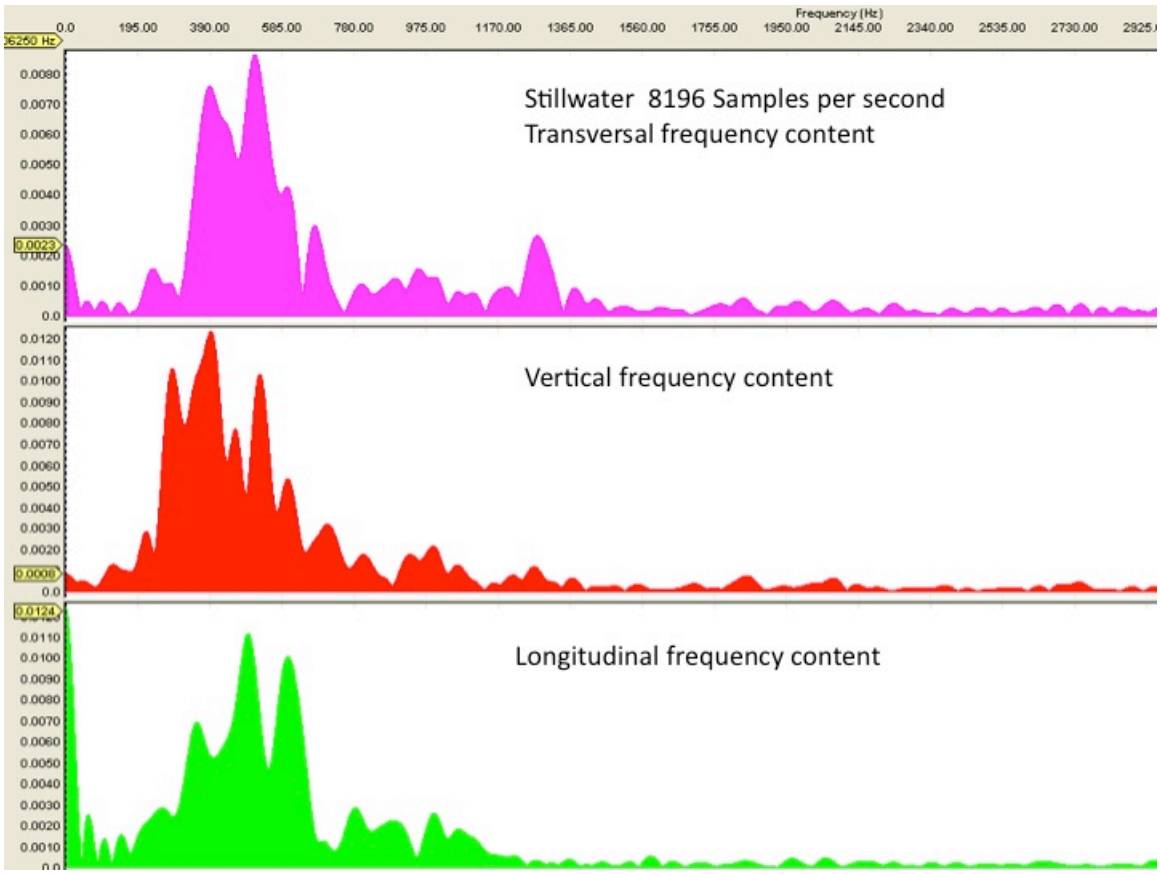

Figure B. 10 Frequency content of transversal, vertical and longitudinal particle velocity records – #0 delay – Stillwater Mine

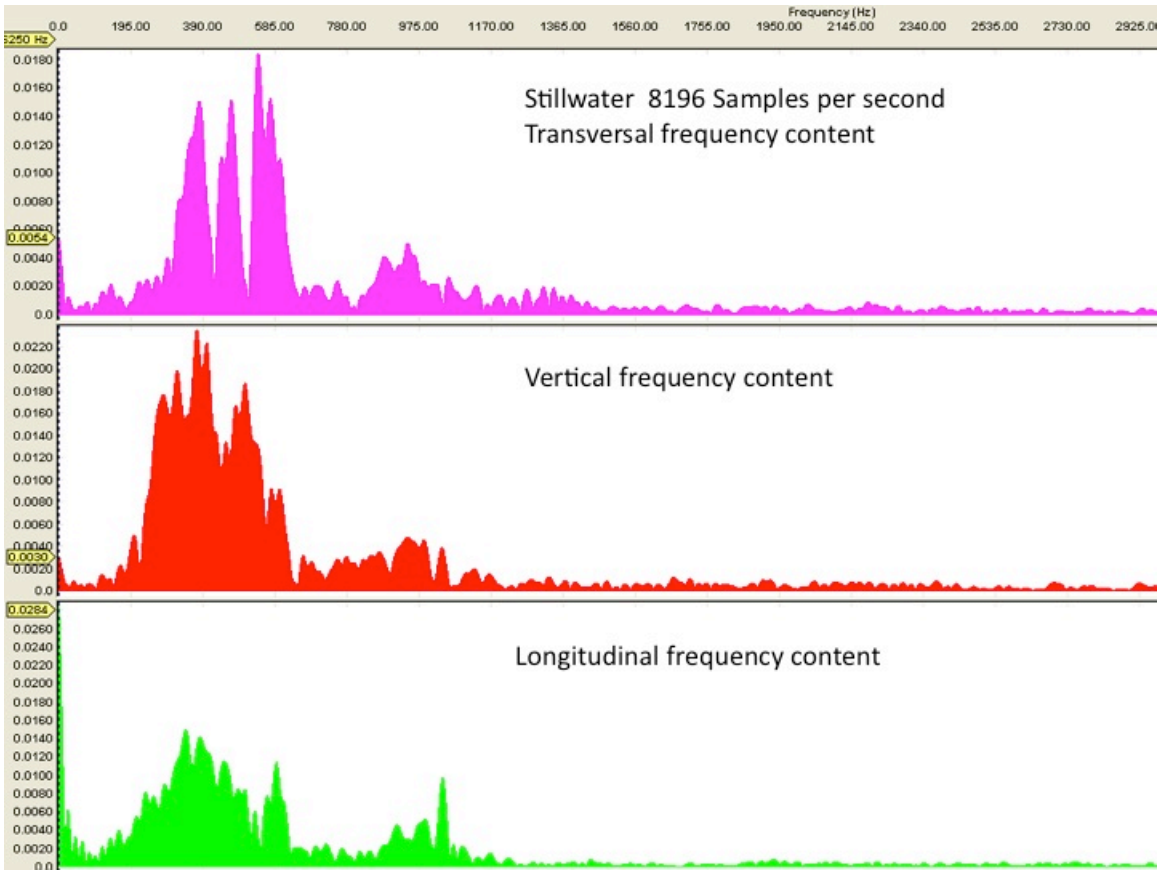

Figure B. 11 Frequency content of transversal, vertical and longitudinal particle velocity records – #2 (1/2) delay – Stillwater Mine

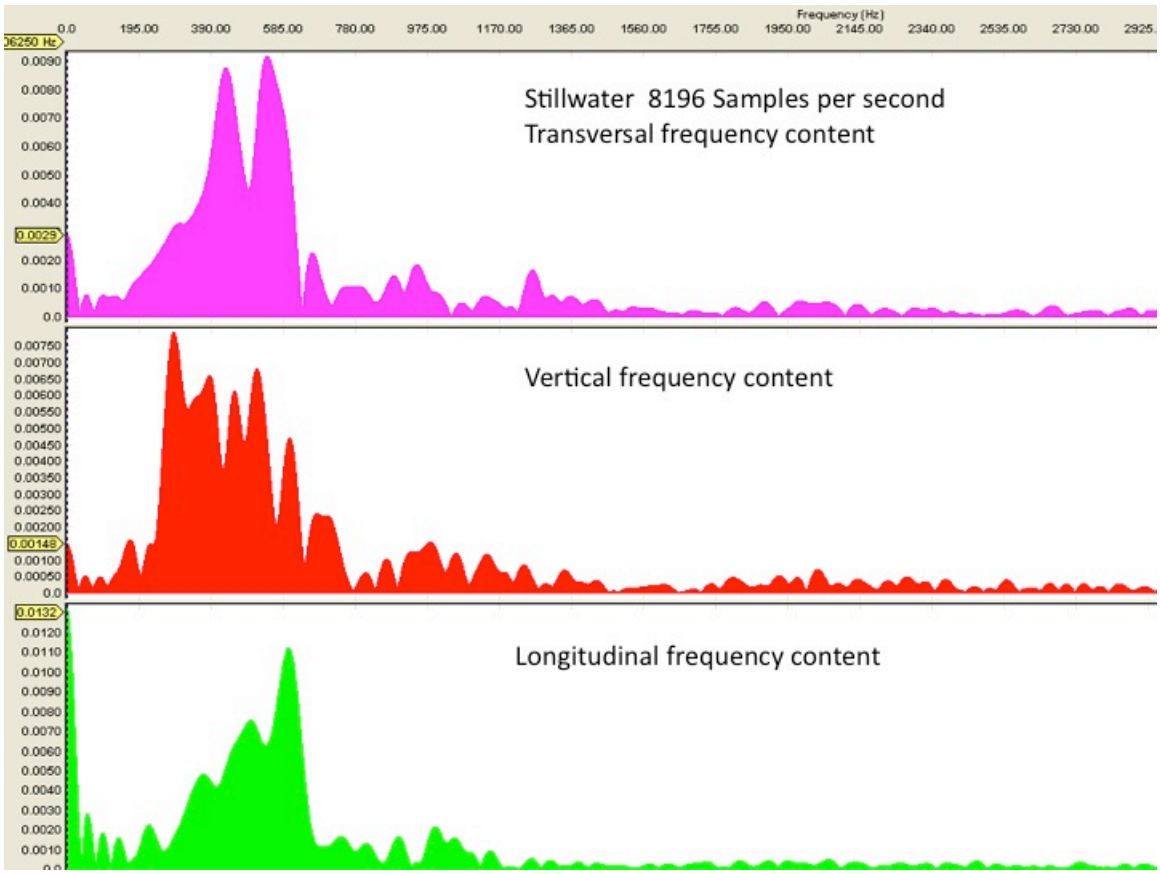

Figure B. 12 Frequency content of transversal, vertical and longitudinal particle velocity records – #2 (2/2) delay – Stillwater Mine

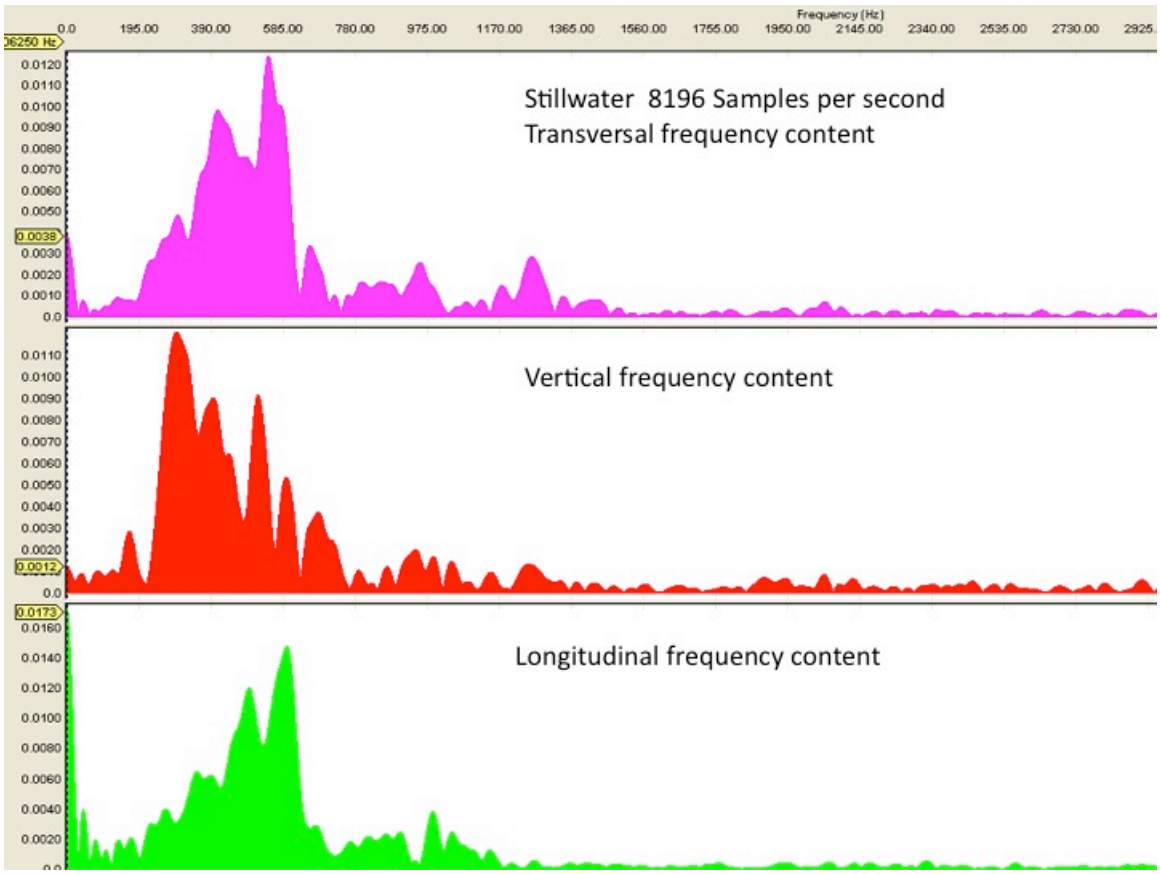

Figure B. 13 Frequency content of transversal, vertical and longitudinal particle velocity records – #3 (1/2) delay – Stillwater Mine

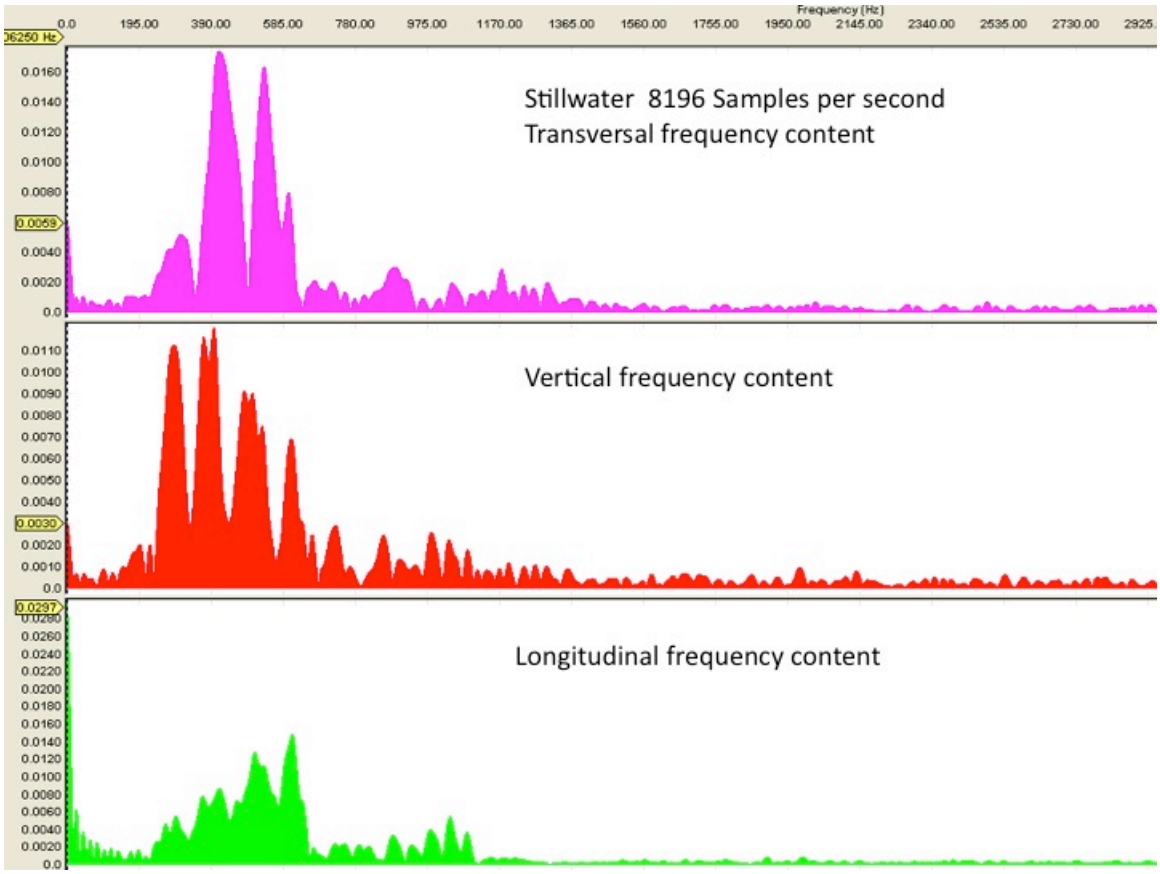

Figure B. 14 Frequency content of transversal, vertical and longitudinal particle velocity records – #3 (2/2) delay – Stillwater Mine

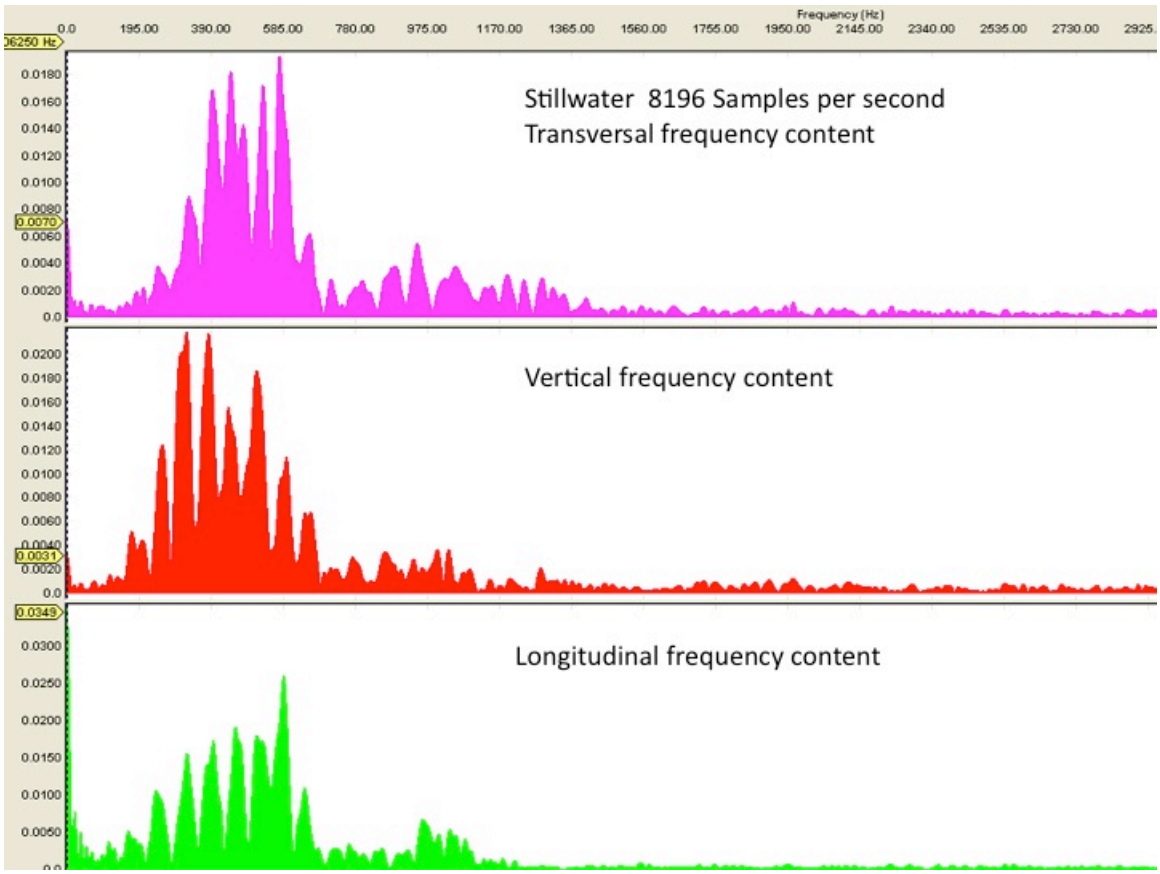

Figure B. 15 Frequency content of transversal, vertical and longitudinal particle velocity records – #4 (1/2) delay – Stillwater Mine

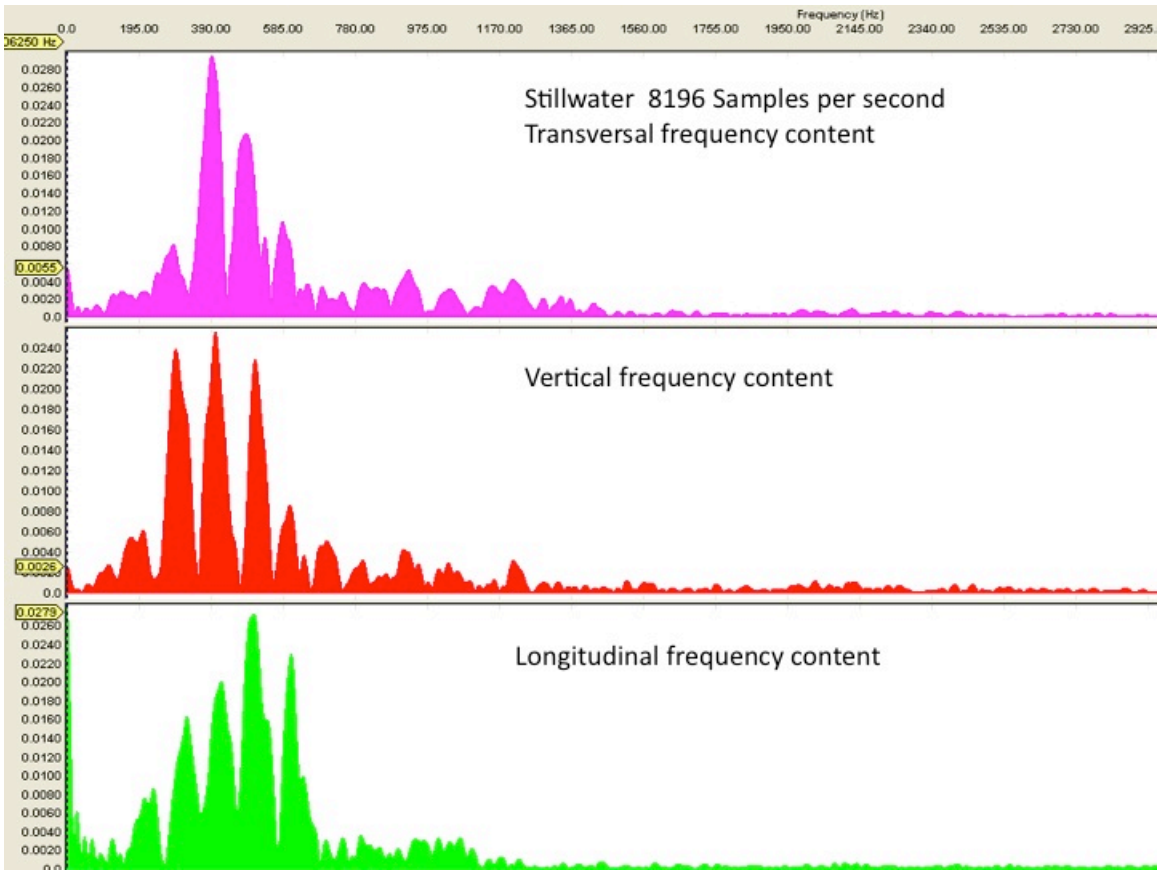

Figure B. 16 Frequency content of transversal, vertical and longitudinal particle velocity records – #4 (2/2) delay – Stillwater Mine

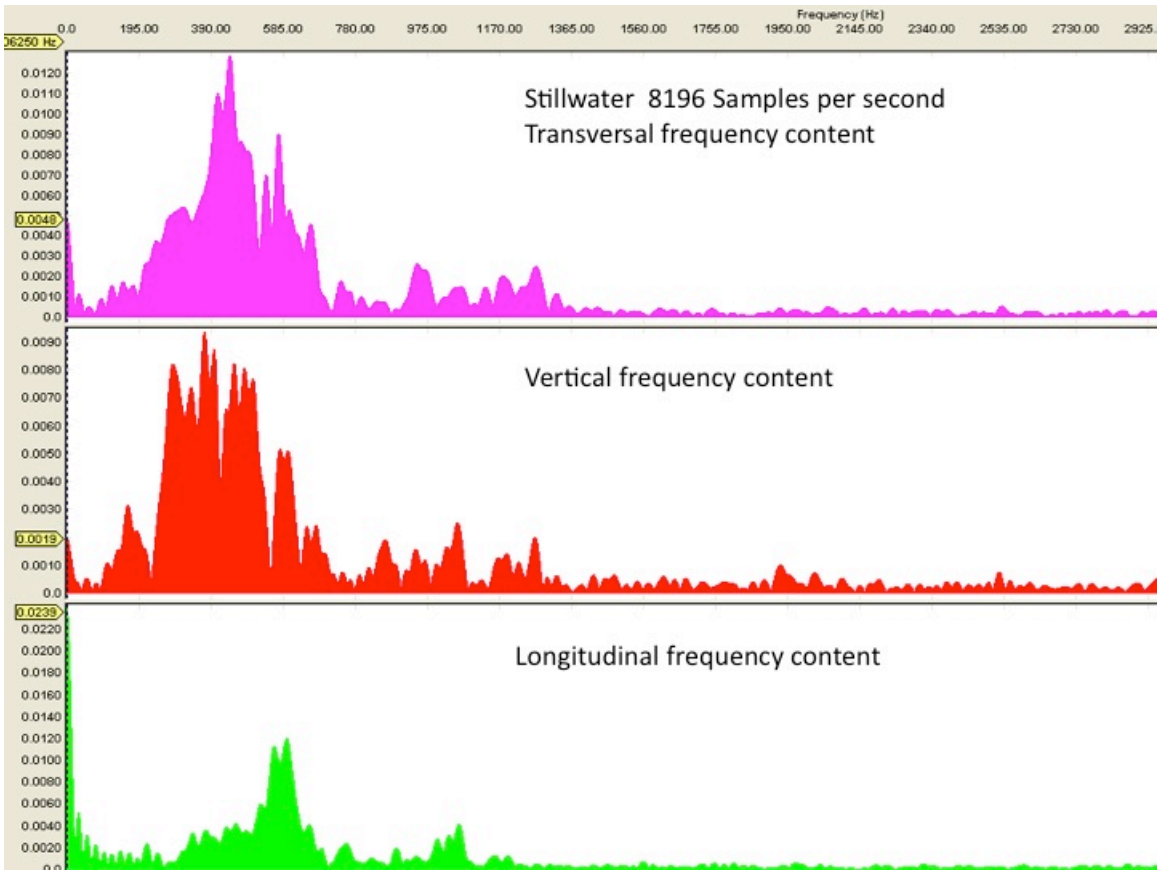

Figure B. 17 Frequency content of transversal, vertical and longitudinal particle velocity records – #5 (1/2) delay – Stillwater Mine

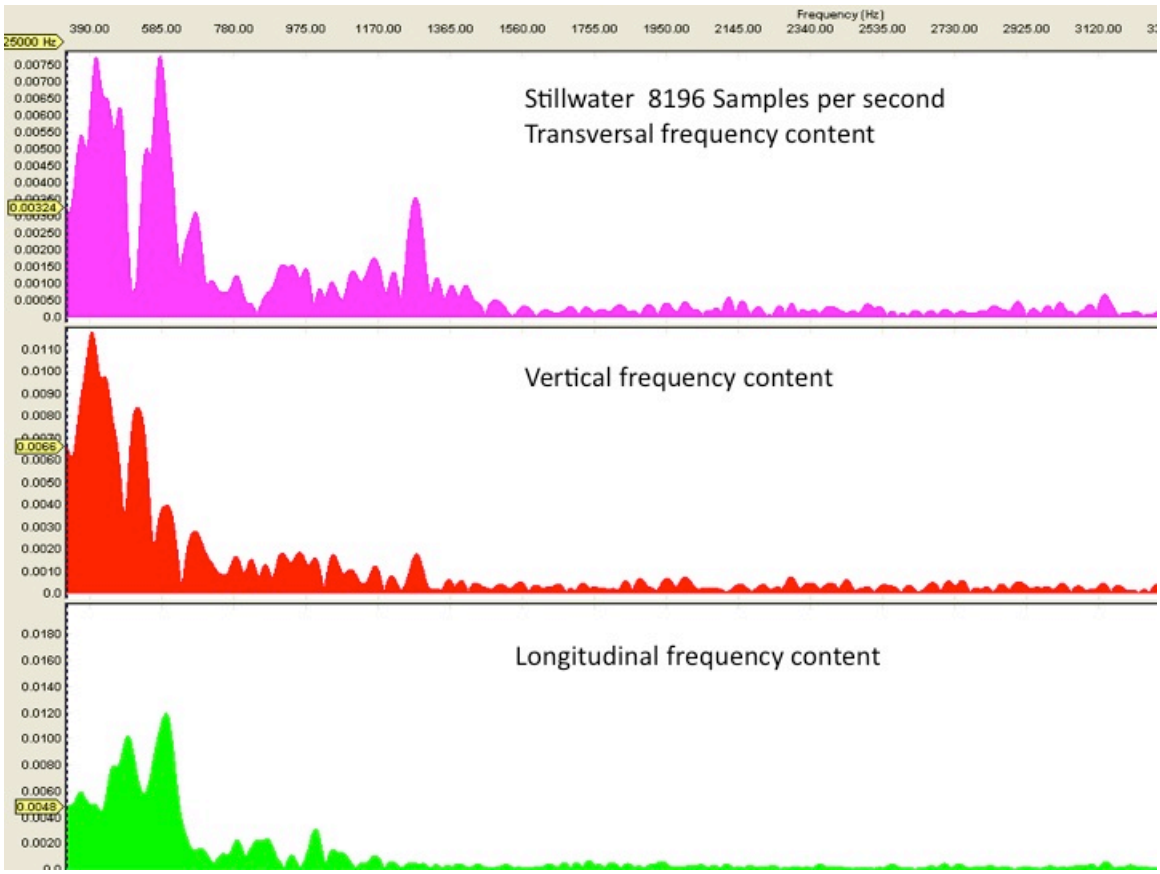

Figure B. 18 Frequency content of transversal, vertical and longitudinal particle velocity records – #5 (2/2) delay – Stillwater Mine

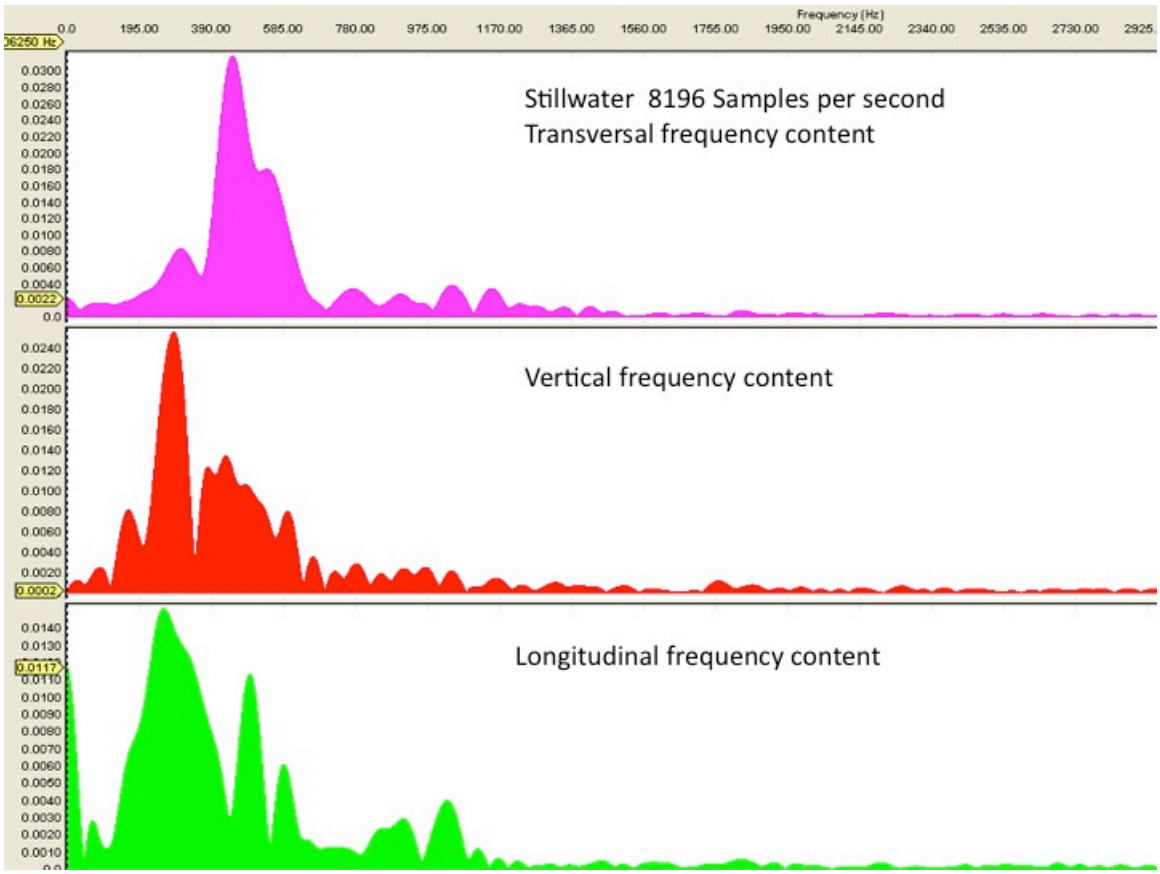

Figure B. 19 Frequency content of transversal, vertical and longitudinal particle velocity records – #6 (1/2) delay – Stillwater Mine

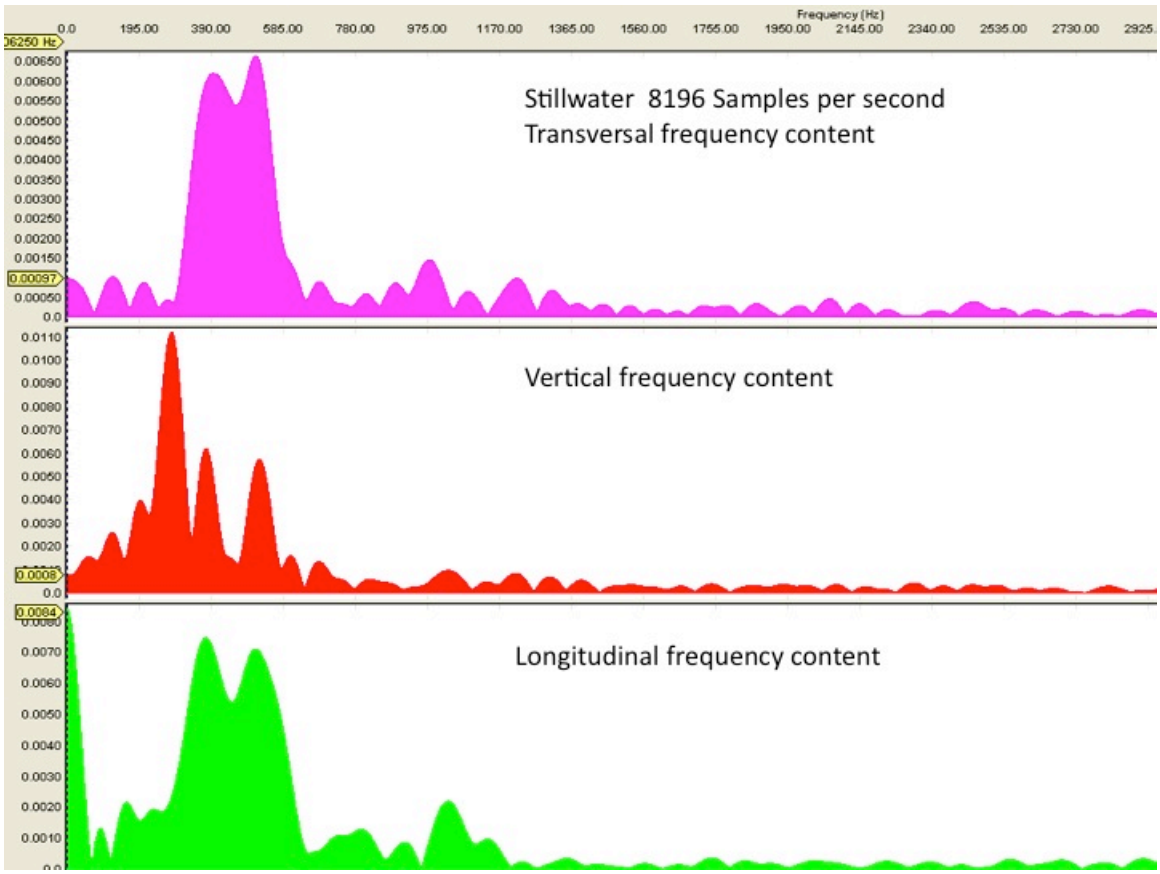

Figure B. 20 Frequency content of transversal, vertical and longitudinal particle velocity records – #6 (2/2) delay – Stillwater Mine

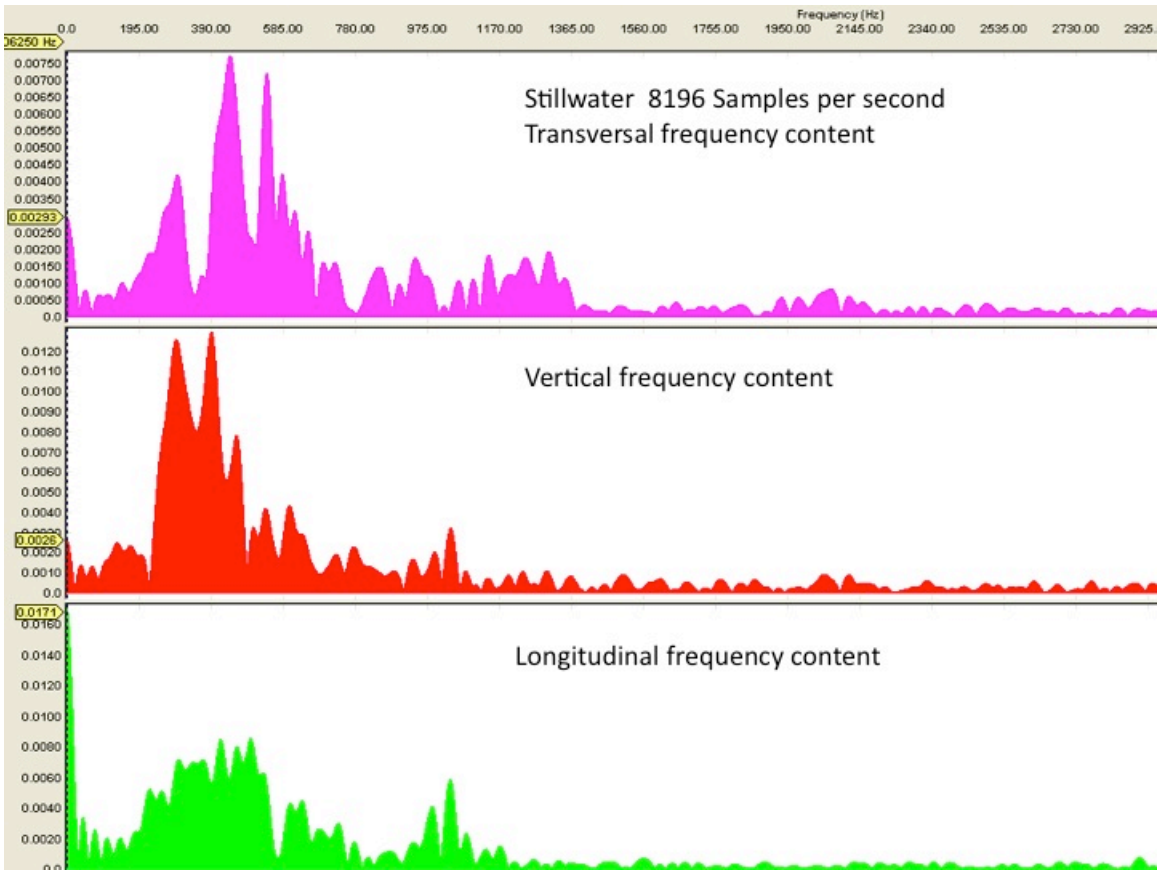

Figure B. 21 Frequency content of transversal, vertical and longitudinal particle velocity records – #7 (1/2) delay – Stillwater Mine

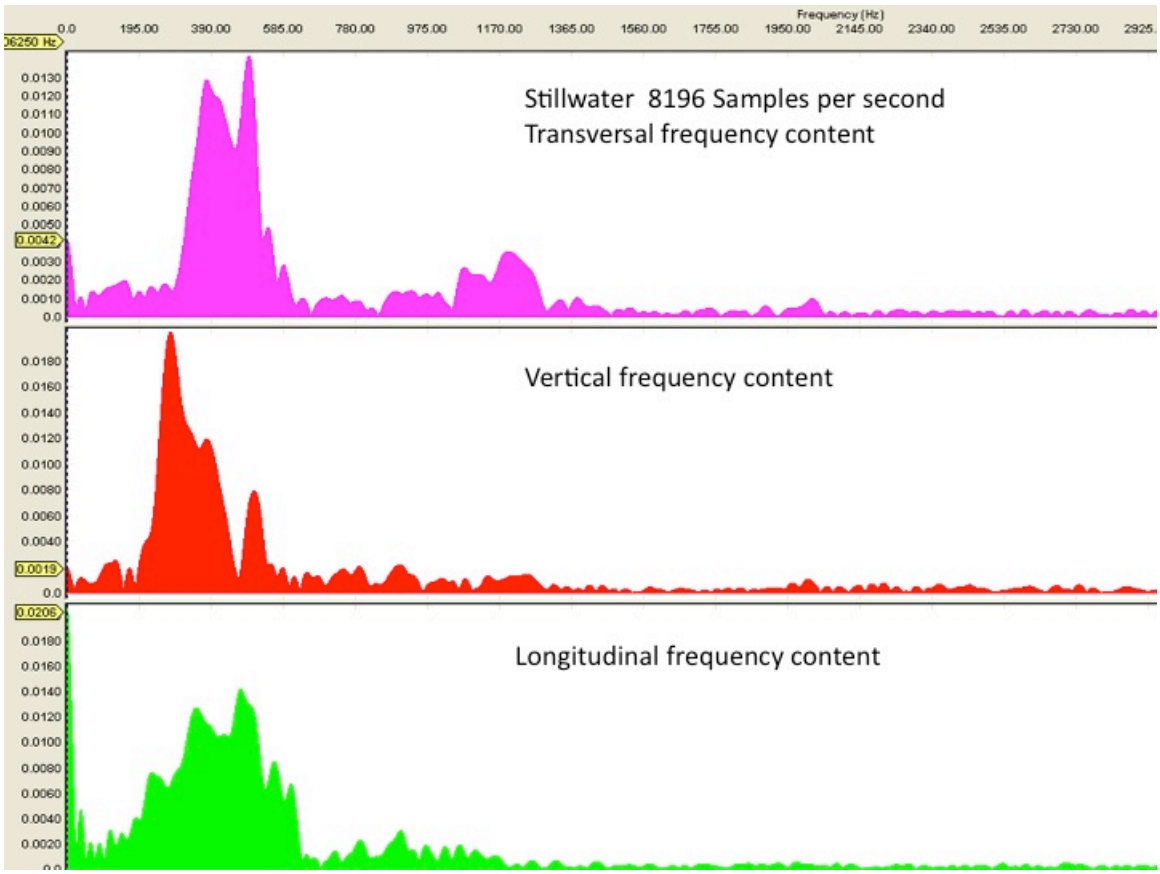

Figure B. 22 Frequency content of transversal, vertical and longitudinal particle velocity records – #7 (2/2) delay – Stillwater Mine

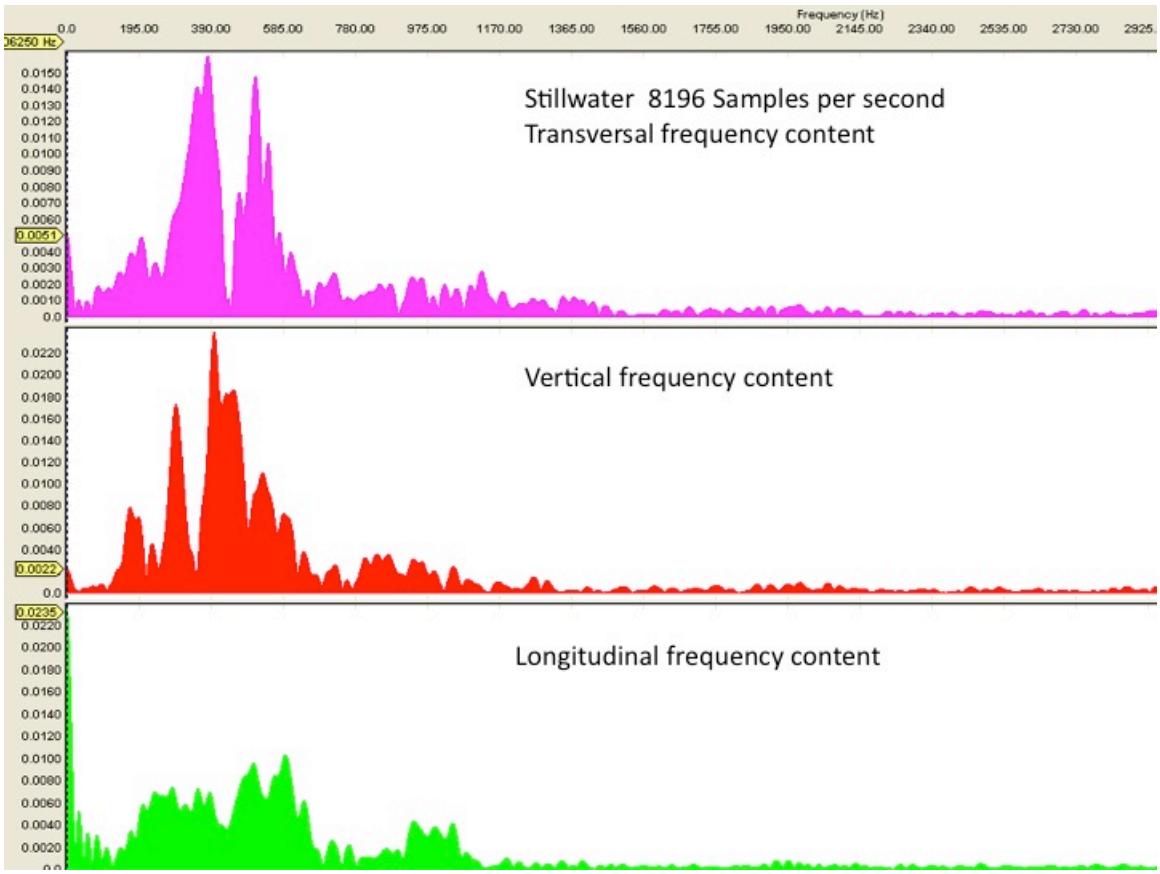

Figure B. 23 Frequency content of transversal, vertical and longitudinal particle velocity records – #8 (1/2) delay – Stillwater Mine

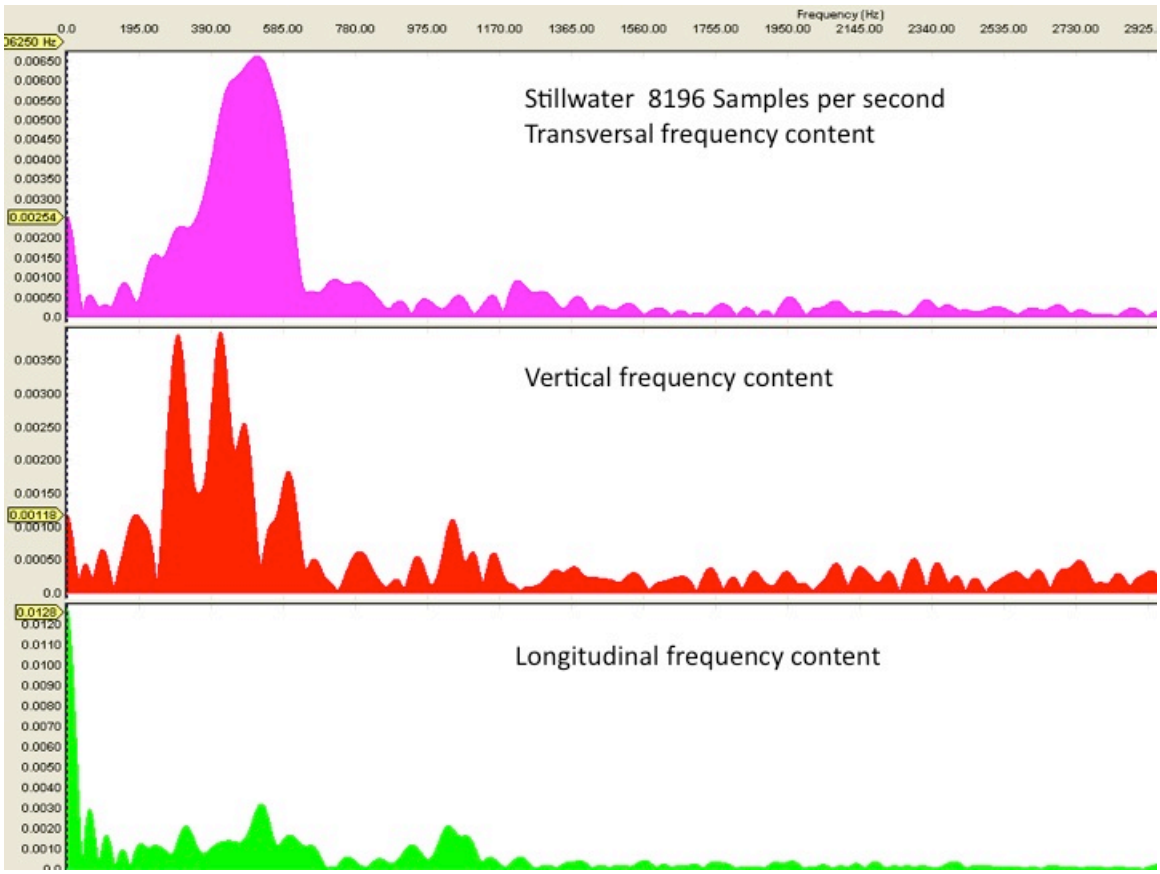

Figure B. 24 Frequency content of transversal, vertical and longitudinal particle velocity records – #8 (2/2) delay – Stillwater Mine

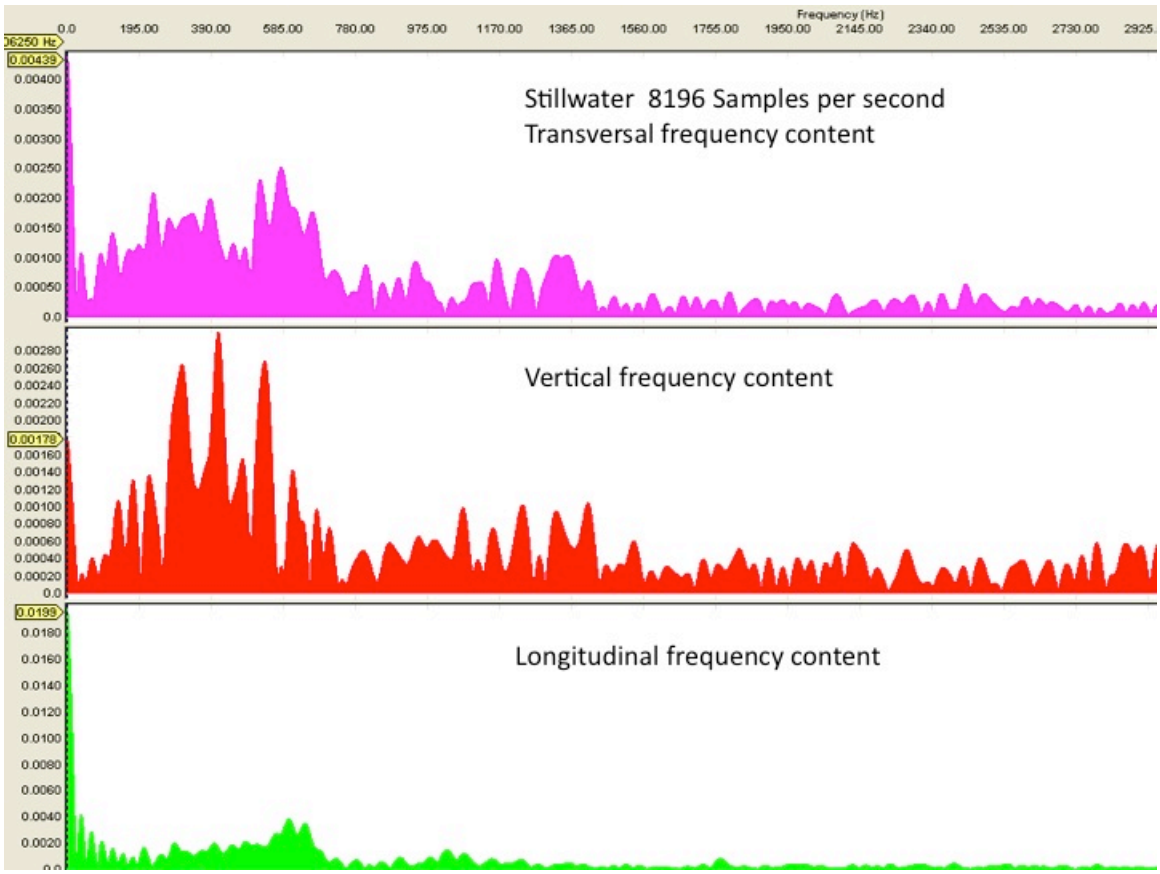

Figure B. 25 Frequency content of transversal, vertical and longitudinal particle velocity records – #9 (1/2) delay – Stillwater Mine

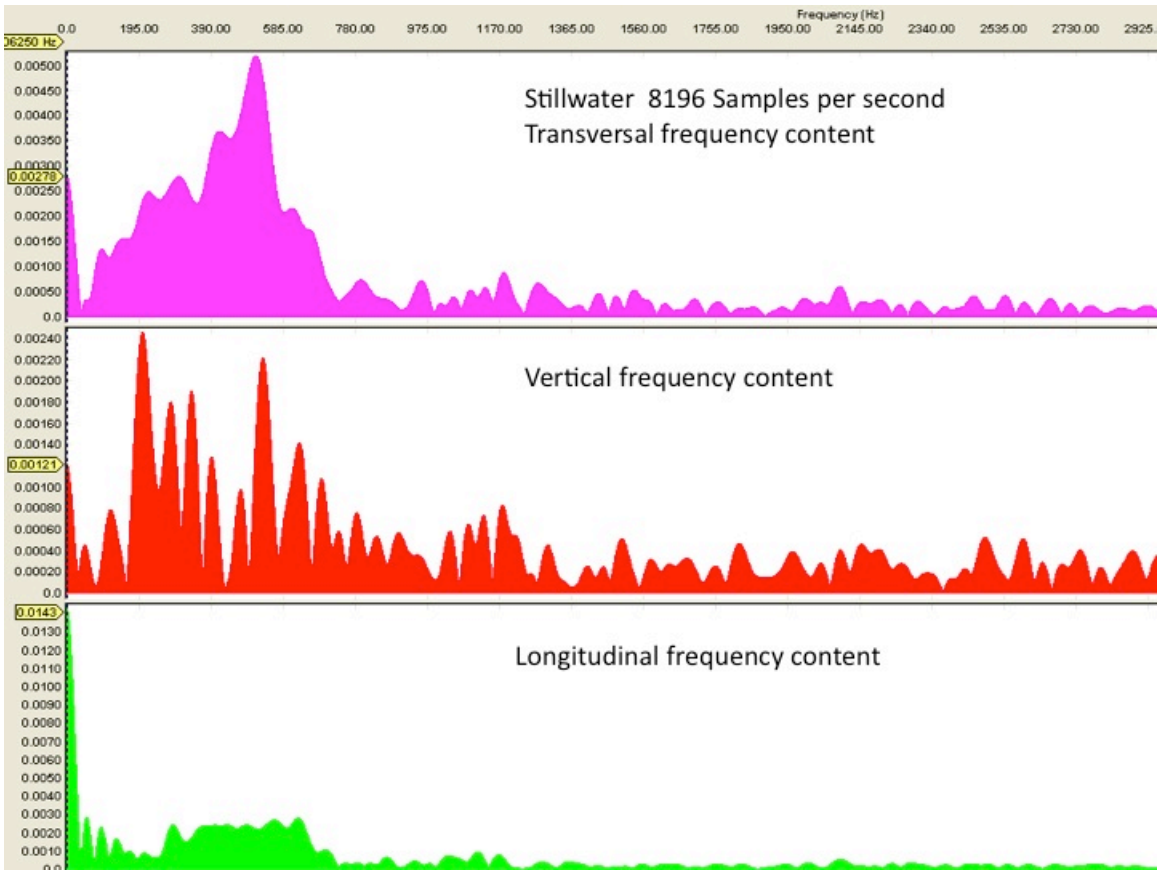

Figure B. 26 Frequency content of transversal, vertical and longitudinal particle velocity records – #9 (2/2) delay – Stillwater Mine

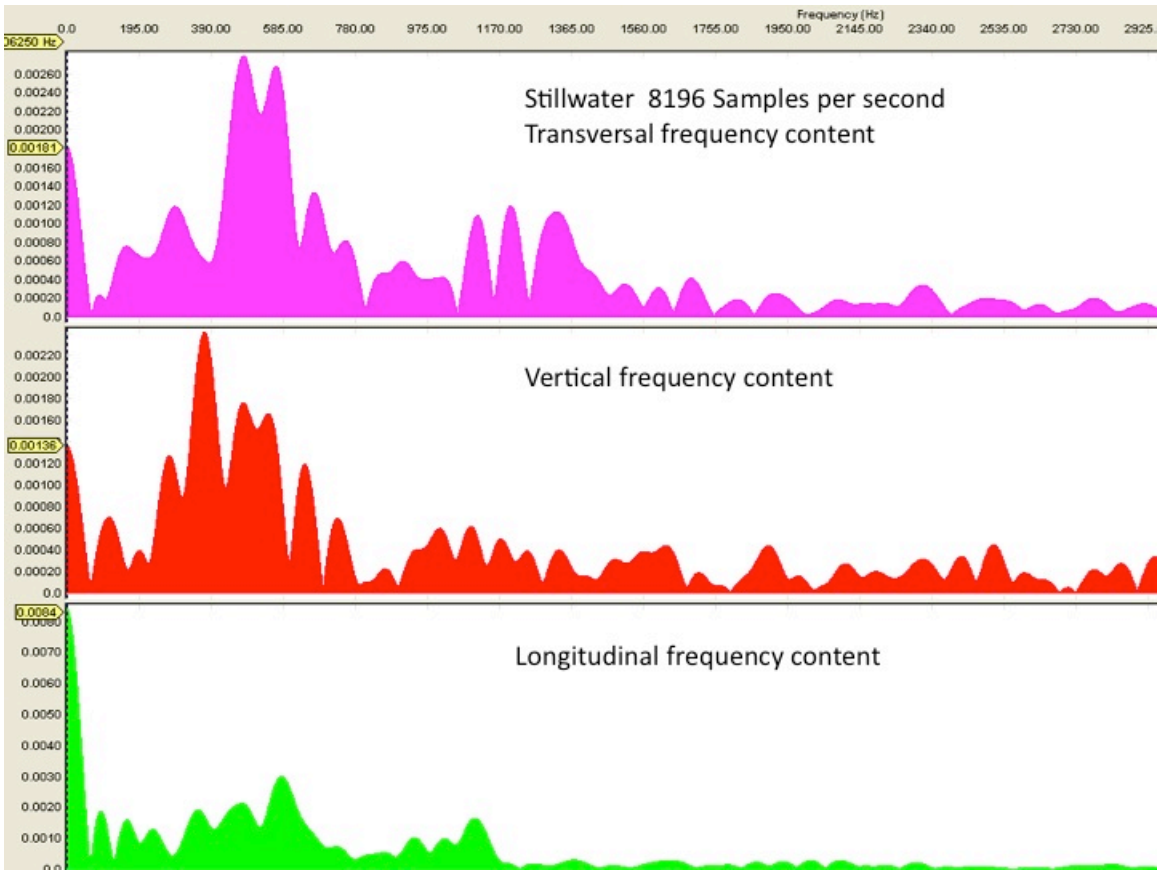

Figure B. 27 Frequency content of transversal, vertical and longitudinal particle velocity records – #11 delay – Stillwater Mine

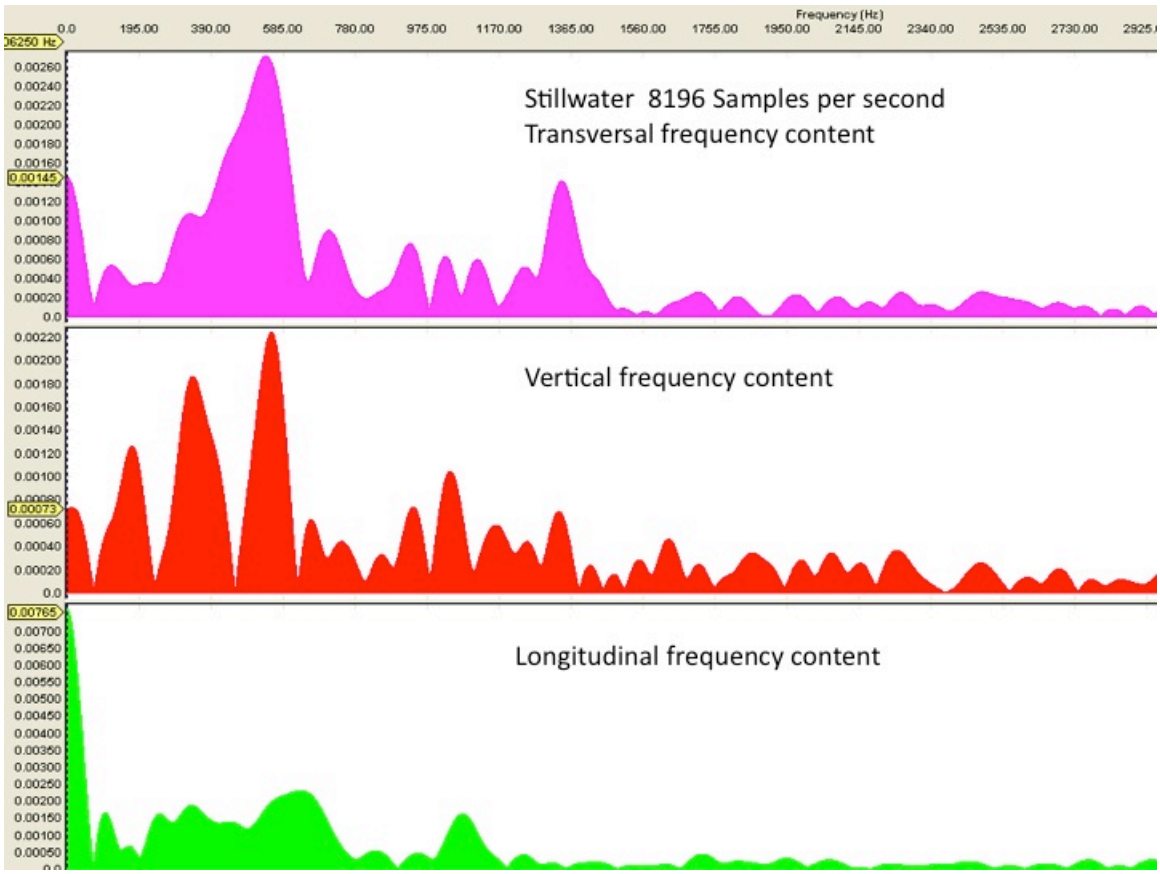

Figure B. 28 Frequency content of transversal, vertical and longitudinal particle velocity records – #12 delay – Stillwater Mine

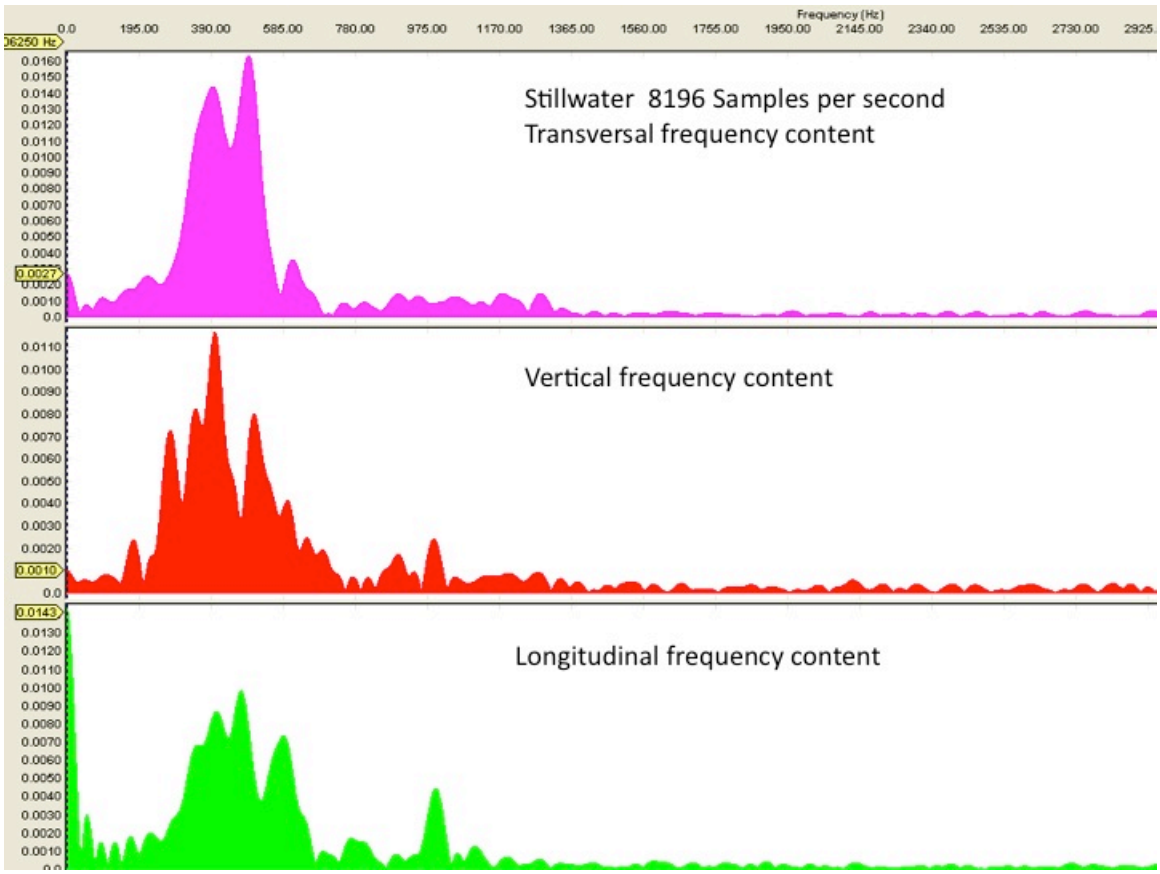

Figure B. 29 Frequency content of transversal, vertical and longitudinal particle velocity records – #13 delay – Stillwater Mine

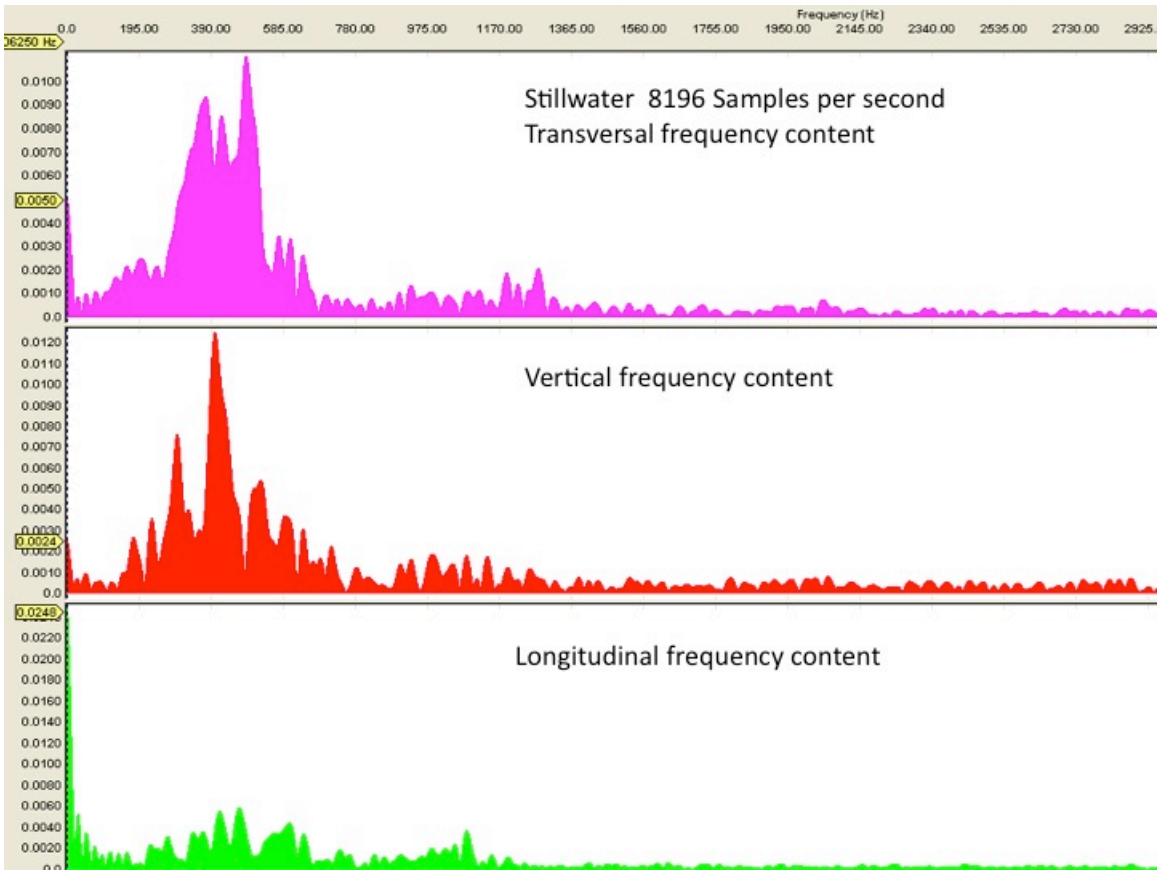

Figure B. 30 Frequency content of transversal, vertical and longitudinal particle velocity records – #14 delay – Stillwater Mine

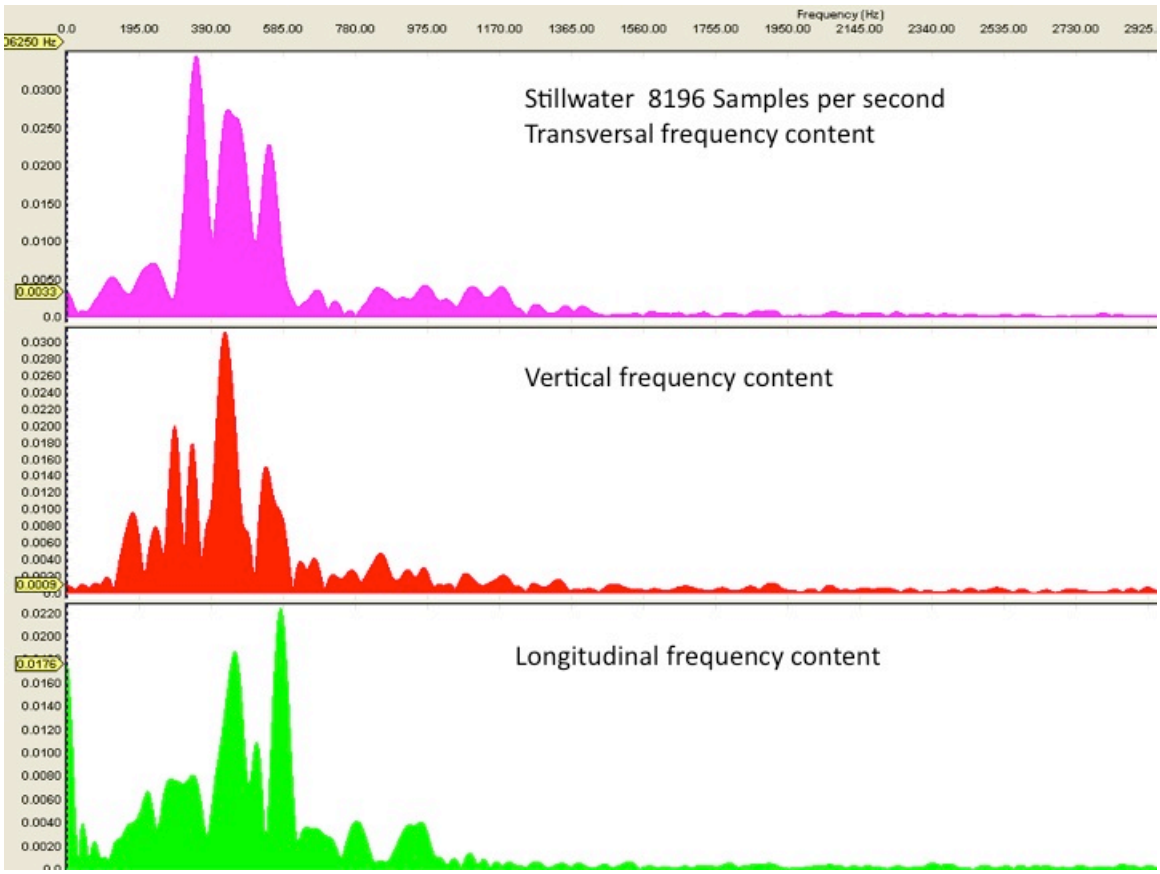

Figure B. 31 Frequency content of transversal, vertical and longitudinal particle velocity records – #15 (1/2) delay – Stillwater Mine

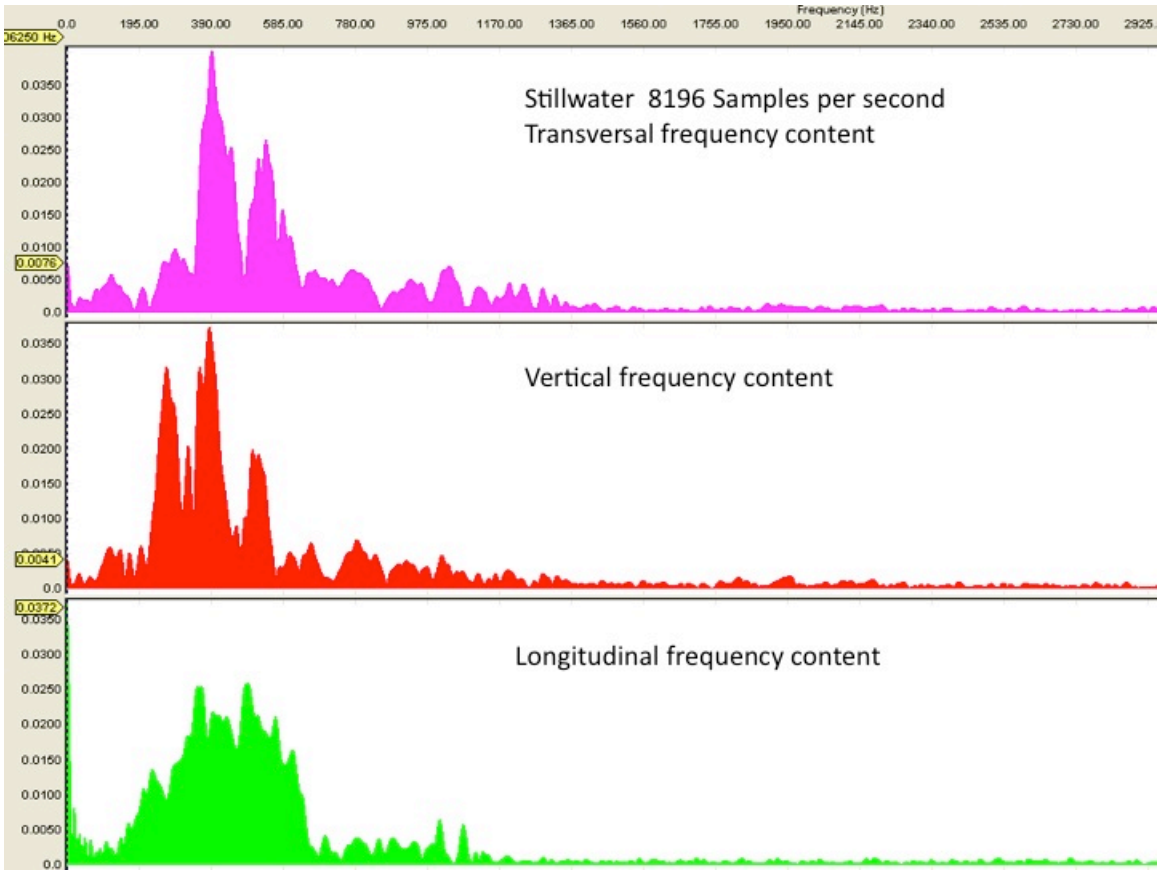

Figure B. 32 Frequency content of transversal, vertical and longitudinal particle velocity records – #15 (2/2) delay – Stillwater Mine

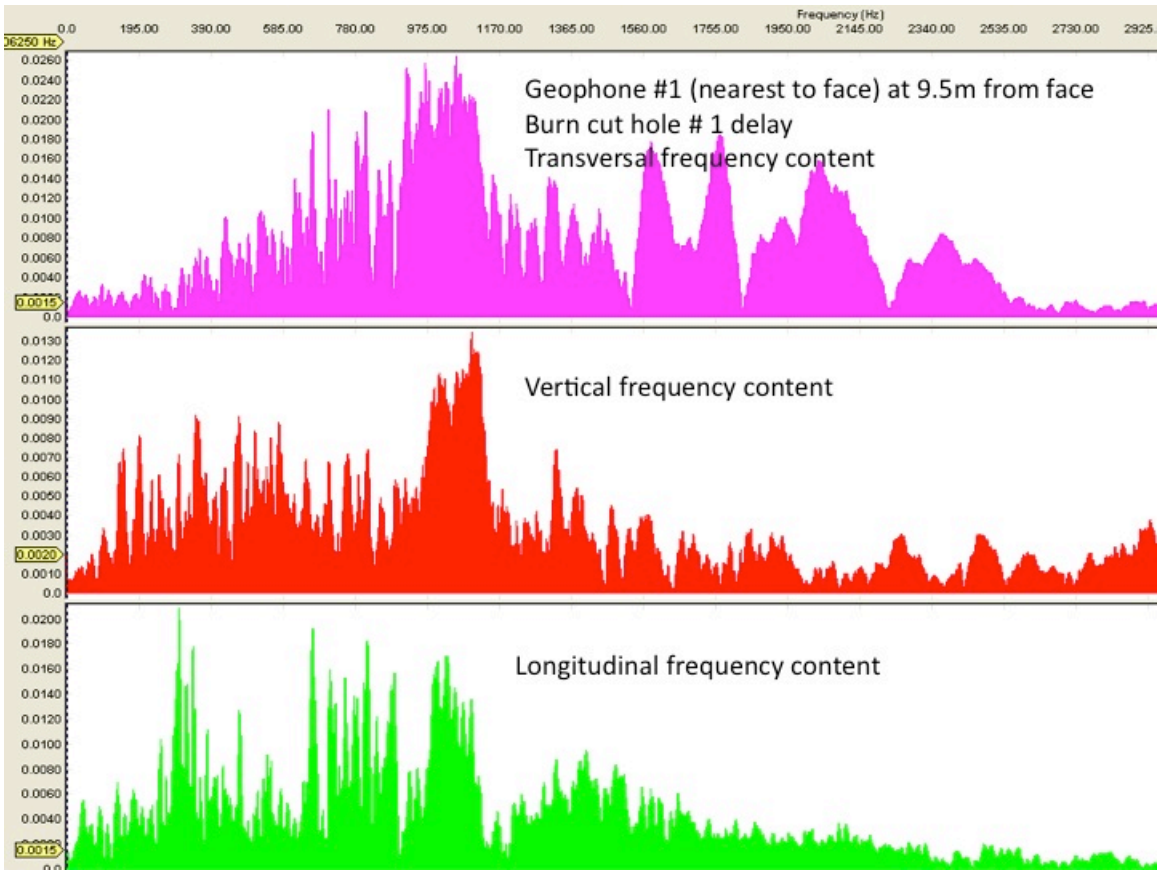

Figure B. 33 Frequency content of transversal, vertical and longitudinal particle velocity records – #1 delay at 9.5m from face – Musselwhite Mine

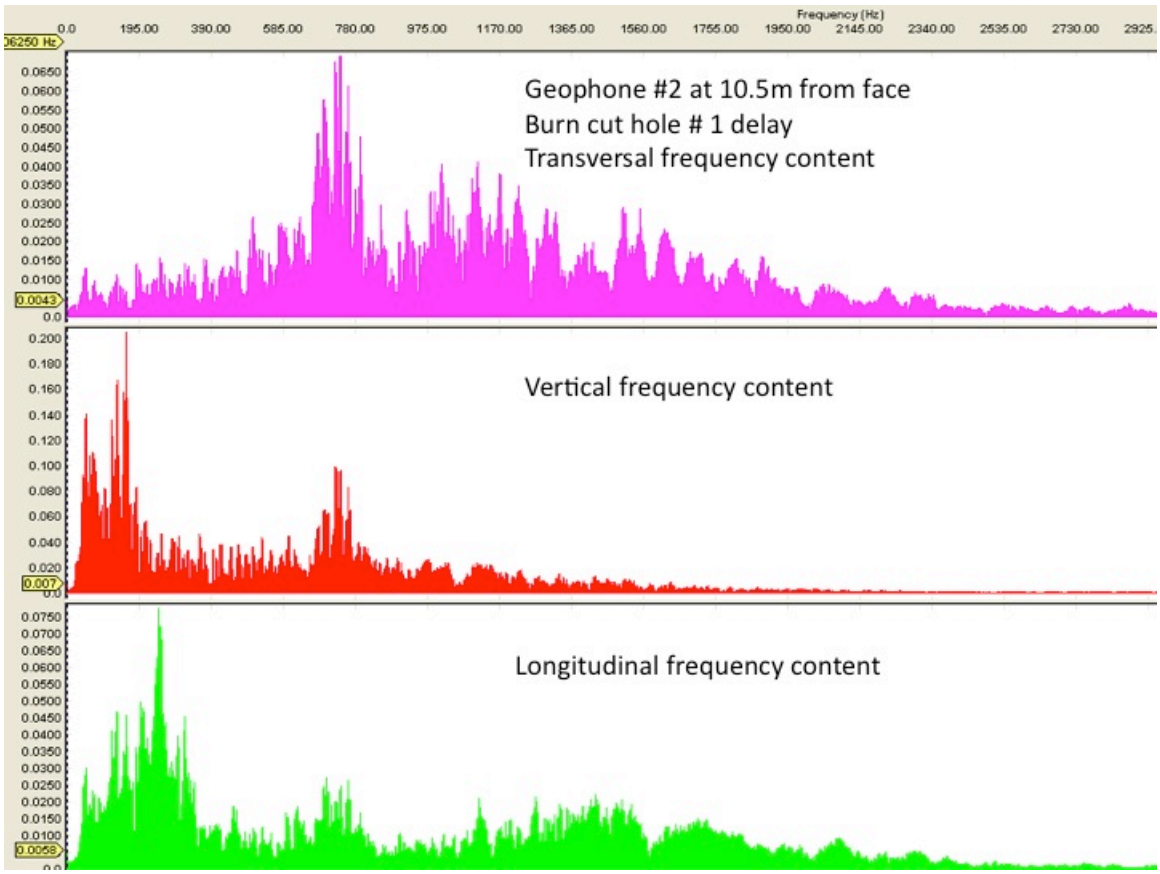

Figure B. 34 Frequency content of transversal, vertical and longitudinal particle velocity records – #1 delay at 10.5m from face – Musselwhite Mine

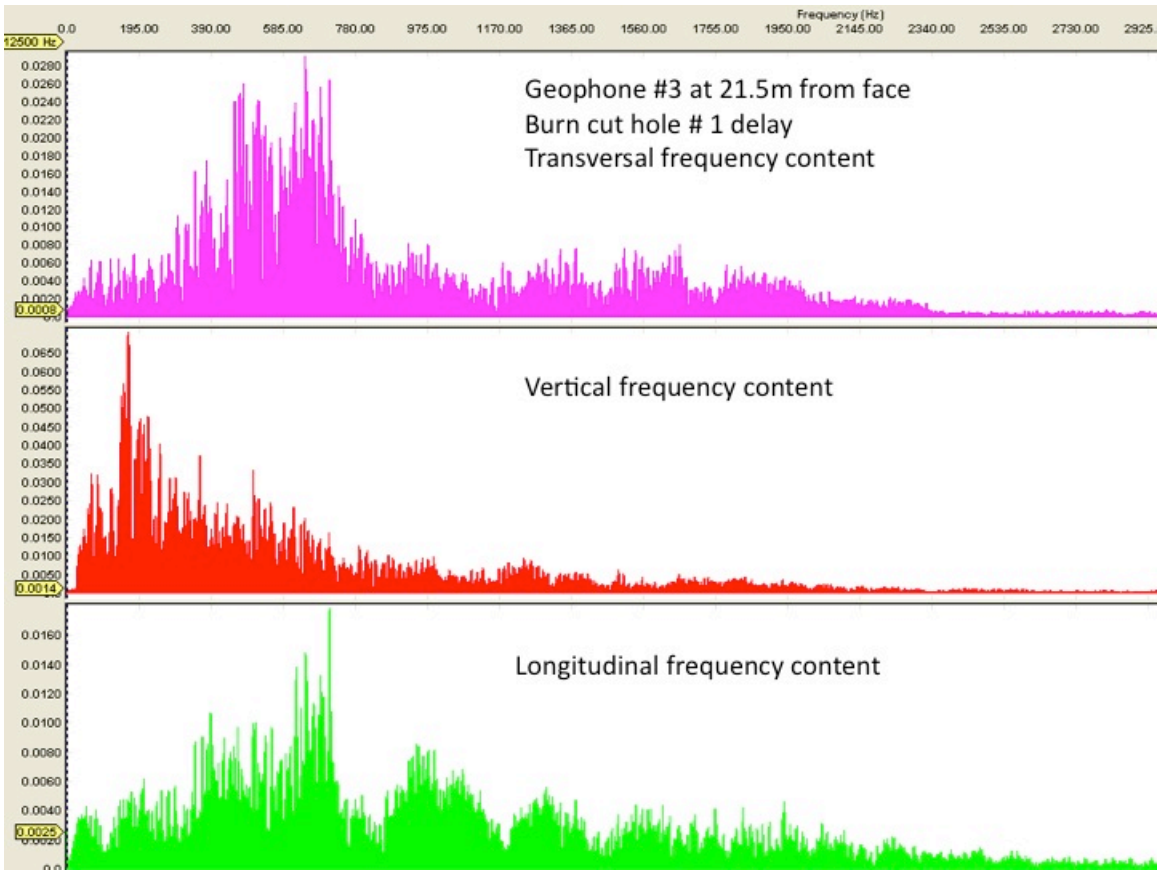

Figure B. 35 Frequency content of transversal, vertical and longitudinal particle velocity records – #1 delay at 21.5m from face – Musselwhite Mine

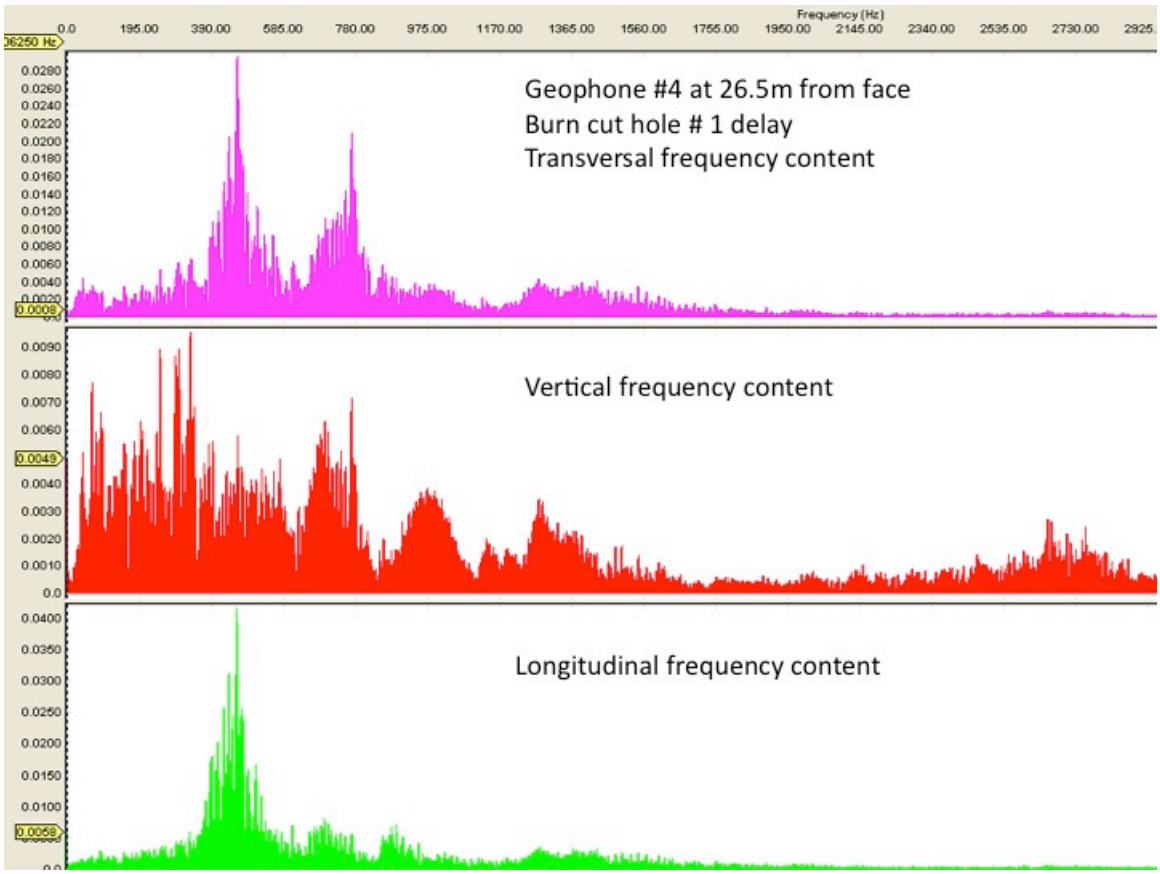

Figure B. 36 Frequency content of transversal, vertical and longitudinal particle velocity records – #1 delay at 26.5m from face – Musselwhite Mine